

Seat belt control : from modeling to experiment

Citation for published version (APA):

Laan, van der, E. P. (2009). *Seat belt control : from modeling to experiment*. [Phd Thesis 1 (Research TU/e / Graduation TU/e), Mechanical Engineering]. Technische Universiteit Eindhoven.
<https://doi.org/10.6100/IR653932>

DOI:

[10.6100/IR653932](https://doi.org/10.6100/IR653932)

Document status and date:

Published: 01/01/2009

Document Version:

Publisher's PDF, also known as Version of Record (includes final page, issue and volume numbers)

Please check the document version of this publication:

- A submitted manuscript is the version of the article upon submission and before peer-review. There can be important differences between the submitted version and the official published version of record. People interested in the research are advised to contact the author for the final version of the publication, or visit the DOI to the publisher's website.
- The final author version and the galley proof are versions of the publication after peer review.
- The final published version features the final layout of the paper including the volume, issue and page numbers.

[Link to publication](#)

General rights

Copyright and moral rights for the publications made accessible in the public portal are retained by the authors and/or other copyright owners and it is a condition of accessing publications that users recognise and abide by the legal requirements associated with these rights.

- Users may download and print one copy of any publication from the public portal for the purpose of private study or research.
- You may not further distribute the material or use it for any profit-making activity or commercial gain
- You may freely distribute the URL identifying the publication in the public portal.

If the publication is distributed under the terms of Article 25fa of the Dutch Copyright Act, indicated by the "Taverne" license above, please follow below link for the End User Agreement:

www.tue.nl/taverne

Take down policy

If you believe that this document breaches copyright please contact us at:

openaccess@tue.nl

providing details and we will investigate your claim.

Seat Belt Control

From modeling to experiment

Ewout van der Laan



Stellingen

behorende bij het proefschrift

Seat Belt Control From modeling to experiment

1. Geregelde gordelsystemen moeten een focus zijn van restraint systeem ontwikkelaars.
dit proefschrift
2. Sensoren voor het afschatten van letsel tijdens een botsing zijn duur, niet praktisch of bestaan nog niet. De effectiviteit van restraint systemen kan echter bijzonder verbeterd worden met dit type sensoren.
dit proefschrift
3. De termen actieve en passieve veiligheid zijn niet eenduidig. Beter kan men spreken van primaire en secundaire veiligheidssystemen.
dit proefschrift
4. De introductie van de frontale airbag heeft de risico's vergroot van het niet-gebruiken van een autogordel.
5. De impact-factor van een tijdschrift is een zeer misleidende index bij het beoordelen van de kwaliteit van wetenschappelijk onderzoek. Eén van de vele redenen hiervoor is dat de index (statistisch gezien) weinig kenmerkend is voor de individuele publicatie.
6. De bonusregeling voor topmanagers is een voorbeeld van een slecht teruggekoppeld systeem.
7. De creativiteit van wetenschappers leidt soms tot vermakelijke publicaties: 'The investigation (...) revealed that the most likely candidate for the injury was a tobacco pipe, which was probably being held in one hand and was broken apart by the deploying airbag and projected into the face of the driver.'
Walz, F.H., Mackay, M., Gloor. B., 'Airbag Deployment and Eye Perforation by a Tobacco Pipe'. J Trauma, 38(4), 1995, p. 498-501.
8. 'De wiskundige kennis van vwo'ers sluit onvoldoende aan bij de eisen van natuurwetenschappelijke studies in het hoger onderwijs.' Dit geldt helaas ook in toenemende mate voor hun taal- en grammaticakennis.
'Aspirant-bèta student struikelt al over de sinus', NRC Handelsblad, 9 juni 2009.

9. Promoveren betekent letterlijk *vooruitbewegen*; ironisch genoeg bestaat het merendeel ervan uit stilzitten.
10. Het is niet alleen collegiaal en hygiënisch om te douchen voordat je naar je werk gaat. Je krijgt er meestal ook de beste ideeën.
11. Niet alles wat in de krant staat is waar. Alles wat niet waar is, staat op internet.
12. Niet alleen vanwege Stelling 9 is het is aan te raden veel te sporten tijdens het promotietraject.
13. One cannot think well, love well or sleep well, if one has not dined well.
Virginia Woolf
14. Mensen zijn vaak het drukst in hun vrije tijd.
15. Iedereen wil graag bijzonder zijn. Dat is precies de reden waarom we allemaal op elkaar lijken.
Theo Maassen
16. Gedurende de financiële crisis hebben veel banken hun krediet verspeeld door het niet meer te verlenen.
17. De meeste kritische opmerkingen over dit proefschrift zijn over en niet onder de gordel.

Ewout van der Laan
Eindhoven, oktober 2009

Seat Belt Control

From modeling to experiment



The research reported in this thesis is supported by TNO Science and Industry, the Netherlands.

disc

The research reported in this thesis is part of the research program of the Dutch Institute of Systems and Control (DISC). The author has successfully completed the educational program of the Graduate School DISC.

A catalogue record is available from the Eindhoven University of Technology Library

Laan, Ewout P. van der

Seat Belt Control. From modeling to experiment / by E.P. van der Laan. – Eindhoven : Technische Universiteit Eindhoven, 2009. Proefschrift. – ISBN-13: 978-90-386-2086-2

Subject headings: vehicle safety / restraint systems / seat belt / modeling / model predictive control / state estimation

Copyright © 2009 by E.P. van der Laan. All rights reserved.

This thesis was prepared with the L^AT_EX₂ ϵ documentation system

Cover design: Dovile Jurgelenaite, Lithuania

Reproduction: PrintPartners Ipskamp B.V., Enschede, the Netherlands

Seat Belt Control

From modeling to experiment

PROEFSCHRIFT

ter verkrijging van de graad van doctor
aan de Technische Universiteit Eindhoven,
op gezag van de rector magnificus, prof.dr.ir. C.J. van Duijn,
voor een commissie aangewezen door het College voor Promoties,
in het openbaar te verdedigen
op maandag 7 december 2009 om 16.00 uur

door

Ewout Peter van der Laan

geboren te Borne

Dit proefschrift is goedgekeurd door de promotor:

prof.dr.ir. M. Steinbuch

Copromotor:

dr.ir. A.G. de Jager

CONTENTS

	NOMENCLATURE	vii
1	INTRODUCTION	1
	1.1 Motor Vehicle Safety	1
	1.2 Thoracic Injury Biomechanics	5
	1.3 Seat Belt Systems	10
	1.4 Research Objective	15
	1.5 Control Problem Formulation	16
	1.6 Contributions and Outline	18
2	MODELING FOR CONTROL DESIGN	21
	2.1 Introduction	21
	2.2 System Boundary	22
	2.3 Approach	23
	2.4 The Reference Model	27
	2.5 Sensitivity Analysis	35
	2.6 The Design Model	39
	2.7 Validation	43
	2.8 The Linear Time Invariant Model	49
	2.9 Discussion	56
3	MODEL PREDICTIVE CONTROL STRATEGY	57
	3.1 Introduction	58
	3.2 Control Strategy	59
	3.3 Design of the Local Feedback Controller	65
	3.4 Setpoint Optimization	70
	3.5 Prediction of Vehicle Motion	77
	3.6 Combined Model Predictive Controller	81
	3.7 Results with the Reference Model	84
	3.8 Discussion	85

4	SMART SENSORS FOR THORACIC INJURIES ESTIMATION	87
4.1	Introduction	87
4.2	Vehicular Occupant Sensors.	88
4.3	The Kalman Filter	93
4.4	The Linearized Extended Kalman Filter	98
4.5	Discussion	100
5	A SEMI-ACTIVE BELT FORCE ACTUATOR	101
5.1	Introduction	101
5.2	Actuator Requirements	102
5.3	Design Concept	105
5.4	Dynamic Modeling of the Hydraulic System	109
5.5	Actuator Design	122
5.6	Identification and Control Design	127
5.7	Towards Closed-loop Sled Experiments	140
5.8	Discussion	154
6	CONCLUSIONS AND RECOMMENDATIONS	155
6.1	Conclusions	155
6.2	Recommendations	159
A	DESIGN MODEL	161
B	ACTUATOR DESIGN	165
	BIBLIOGRAPHY	169
	SUMMARY	177
	SAMENVATTING	179
	DANKWOORD	181
	CURRICULUM VITAE	183

NOMENCLATURE

Roman lowercase

<i>symbol</i>	<i>description</i>	<i>unit</i>
<i>a</i>	acceleration	g
<i>c</i>	dimensions in the occupant model	m
<i>d</i>	damping coefficients in constitutive relations	Ns/m
	diameter	m
<i>e</i>	error variable	
<i>f</i>	state equation function	
	frequency	Hz
<i>g</i>	output equation function	
	gravity constant	m/s ²
<i>h</i>	parameters of the polynomial basis function	
<i>k</i>	stiffness coefficients in constitutive relations	N/m
<i>ℓ</i>	belt elongation	m
<i>m</i>	mass	kg
<i>n</i>	order of polynomial basis function	-
<i>n_y</i>	measurement noise	
<i>n_x</i>	process noise	
<i>p</i>	optimization variable	
<i>q</i>	generalized coordinate	m, rad
<i>r</i>	position vector	
<i>s</i>	laplace operator	
<i>t</i>	time	s
<i>u</i>	control input variable	
<i>v</i>	measurable variable	
	velocity	m/s
<i>w</i>	input variable	
<i>x</i>	state variable	
	position	m
<i>y</i>	model output variable	
<i>z</i>	performance variable	

Roman uppercase

<i>symbol</i>	<i>description</i>	<i>unit</i>
A	state system matrix	
	area	m^2
A_{\max}	injury criterion for spinal acceleration	g
B	input system matrix	
C	state output matrix	
C_d	discharge coefficient for orifices	
D	input output matrix	
	scaling factor in VC criterion	mm
D_{\max}	chest deflection injury criterion	mm
E	energy	J
	bulk modulus of fluid	J
F	force	N
I	moment of inertia	
J	performance index	
K	gain of local feedback controller \mathcal{K}	
L	constraints on relative occupant position	m
	length of the cylinder	m
M	moment	
N	number of measured samples	-
P	transfer function of LTI model \mathcal{P}	
	pressure	bar
	(mechanical) power	W
Q	covariance matrix of process noise	
Q^{nc}	nonconservative or generalized forces	
R	covariance matrix of measurement noise	
S	sensitivity function	
	constraints on relative occupant velocity	m/s
T	kinetic energy function	
	sample time	s
	complementary sensitivity function	
	temperature	
	duration	s
U	voltage	
V	control volume	
	potential energy function	J

Greek

<i>symbol</i>	<i>description</i>	<i>unit</i>
α	wrapped belt angle	rad
β	weighting constants	-
γ	auxiliary optimization variable	
δ	virtual variation	
ε	relative displacement of a constitutive relation	m, rad
	belt strain	-
ϵ	robustness function in vehicle prediction	
ζ		
η	perturbation signal in sensitivity analysis	
θ	rotation of the bodies in the occupant model	rad
κ	belt position wrt pulley	m
λ	eigenvalue	rad/s
μ	dynamic or absolute viscosity	Ns/m ²
	friction coefficient	-
μ_o	permeability constant	Tm/A
ν	kinematic viscosity	mm ² /s
ξ	saturation function for the spool position	m
ρ	density	kg/m ³
σ	singular value	
τ	auxiliary time variable	s
ϕ	nonlinear constraint function of occupant responses	
φ	nonlinear objective function of occupant responses	
ψ	vehicle displacement function	m
ω	frequency	rad/s
Φ	volumetric flow rate	m ³ /s
Λ	primal controlled system	
Γ	belt actuator system	
Σ	physical system or plant	

Mathematical notation

<i>symbol</i>	<i>description</i>
\mathbf{w}	column vector
w	scalar
A	matrix
A^T	transpose of matrix A
\dot{w}	derivative of w wrt time

$w(k+1 k)$	prediction of $w(k+1)$ at time k
\hat{w}	estimation of w
\bar{w}	operating point or trajectory
\tilde{w}	approximation of w
w_q	derivative of w wrt q
$\frac{d}{dt}$	derivative wrt t
$\frac{\partial}{\partial t}$	partial derivative wrt t
$[w_1 \ w_2]$	row vector
$[a, b]$	closed interval between a and b
$\{a, b, c\}$	the set consisting of a , b , and c
\in	is an element of
\mathbb{N}	set of natural numbers including zero
\mathbb{R}	set of real numbers
$\ \dots\ $	norm
\Rightarrow	implication
$f : a \mapsto b$	the function f maps element a to element b
$Pr(E)$	probability that event E occurs
\vec{w}	vector in coordinate frame
$\vec{a} \cdot \vec{b}$	inner product between vector \vec{a} and \vec{b}
Δ	difference operator
\propto	proportional to
$:=$	definition

Calligraphic

\mathcal{C}	controller of the CRC system
\mathcal{D}	design model of the system Σ
\mathcal{F}	controller for the torso acceleration of the sled
\mathcal{G}	actuator model
\mathcal{H}	controller for the actuator
\mathcal{O}	observer algorithm
\mathcal{K}	local feedback controller
$\hat{\mathcal{K}}$	low-performance local feedback controller
\mathcal{L}	observer gain
\mathcal{M}	MPC controller
\mathcal{P}	linear reduced order model of the system Σ
\mathcal{P}_f	linear full order model of the system Σ
\mathcal{R}	reference model of the system Σ
$\hat{\mathcal{R}}$	modified reference model
\mathcal{S}	sled setup model

Acronyms

AIS	Abbreviated Injury Scale
CFR	Constant Force Restraints
CRC	Continuous Restraint Control
CFC	Channel Filter Class
CTI	Combined Thoracic Injury criterion
CVS	Crash Victim Simulation
EU15	Members of the European Union between 1995-2004
EU27	Members of the European Union between 2007-2009
FMVSS	Federal Motor Vehicle Safety Standards
GPS	Global Positioning System
IC	Injury Criteria
LP	Linear Program
LTI	Linear Time-Invariant
LTV	Linear Time-Varying
MADYMO	MAThematical DYnamic MOdel
MAIS	Maximum AIS
MB	Multi-Body
MM	Modulus Margin
MPC	Model Predictive Control
NCAP	New Car Assessment Programme
NHTSA	National Highway Transport Safety Association
ODB	Offset Deformable Barrier
PM	Phase Margin
PSD	Power Spectral Density
RB	Rigid Barrier
SA	Sensitivity Analysis
SAE	Society of Automotive Engineers
SLL	Switching Load Limiter
TOAIS	Thoracic AIS
VC	Viscous Criterion

1

INTRODUCTION

Abstract / In this chapter, an introduction on vehicle safety is given, accompanied by an overview of current safety measures used for the protection of a vehicle occupant. The injury mechanisms of the human thorax are shortly discussed, and it is elucidated how seat belt systems influence these mechanisms. Finally, a discussion on the limitations of conventional seat belts leads to the formulation of the research objective.

1.1 Motor Vehicle Safety

Transportation with motor vehicles has become unarguably safer over the last decades. To illustrate this, the number of annual road fatalities¹ in the period 1970-2000 in the EU15 has decreased from 78 to 41 thousand, and 28 thousand fatalities are reported for 2007. On the other hand, the distance that people travel each year in a passenger car has more than doubled in the same period and countries, namely from 4.6 to 10 thousand kilometers per person per year (European Commission for Energy and Transport, 2009). The numbers for the United States indicate a similar trend (National Center for Statistics and Analysis, 2009).

Although this decrease in the fatality rate is promising, it is generally agreed upon that safety in road transportation has to and will remain a focus of automotive research for several reasons. In the first place, still a little more than 40 thousand persons are killed yearly in road transportation (both in USA and in EU27), and 1.27 million world-wide in 2004. This makes road traffic injuries currently one of the top three causes of death for people aged between 5 and 44 years (World Health

¹A fatality means that the person died within 30 days after the incident.

Organization, 2009). Another reason is that more than 90% of the fatalities occur in low- and middle-income countries, which have less than half of the total number of registered vehicles. Looking at future trends, it is expected that in these countries the vehicle fleet will explosively grow in the coming decade, especially in the fast-growing economies of China, India, Brazil and Russia; for example, the total number of registered cars in China use rose with 24% in 2008². This will lead to a significant increase in world-wide road fatalities. This is also indicated by the World Health Organization, that predicts that the number of fatalities will almost be doubled by 2030 (World Health Organization, 2009). Hence both the present statistical numbers as future expected trends require that automotive safety research has to be pushed even more.

1.1.1 Safety Measures

To understand how safety measures can be made more effective, it is useful to break the vehicle accident down into different phases. In the field of automotive safety research, typically three (chronological) phases are used, being the phase of the (i) accident avoidance, (ii) occupant protection, and (iii) rescue. They are also known as the pre-crash, crash and post-crash phase, but these terms can be somewhat confusing. During each phase, a number of safety measures is active, concerned with the vehicle, the occupant or the environment. For example, they concern the vehicle crashworthiness and crash prevention, the driver performance and behavior, and the highway construction and medical treatment. In Figure 1.1, a matrix with a number of safety measures is shown, organized in the three phases and three applications fields described above.

Also indicated in this figure are the instances of primary and secondary collision. The primary collision refers to the moment that the vehicle impacts against an opponent (another vehicle, object, pedestrian, road etcetera). This collision typically results in the secondary collision, which is defined as the moment when the occupant makes contact with an element within the vehicle, e.g., the vehicle interior, the airbag, knee bolster, windshield, or seat belt. During the secondary collision, the vehicle's injury reducing systems such as the airbag, the seat belt and the head restraints, are paramount. They are better known as *restraint systems*, as they assist in restraining the occupant during a crash.

A note on the terminology used within vehicle safety research is opportune here. Accident avoidance systems are often indicated by the term active safety, whereas passive safety is generally used to reflect the occupant protection systems. How-

²National Bureau of Statistics of China (NBSC) [online], <http://www.stats.gov.cn/english/> (last access: August 2009)

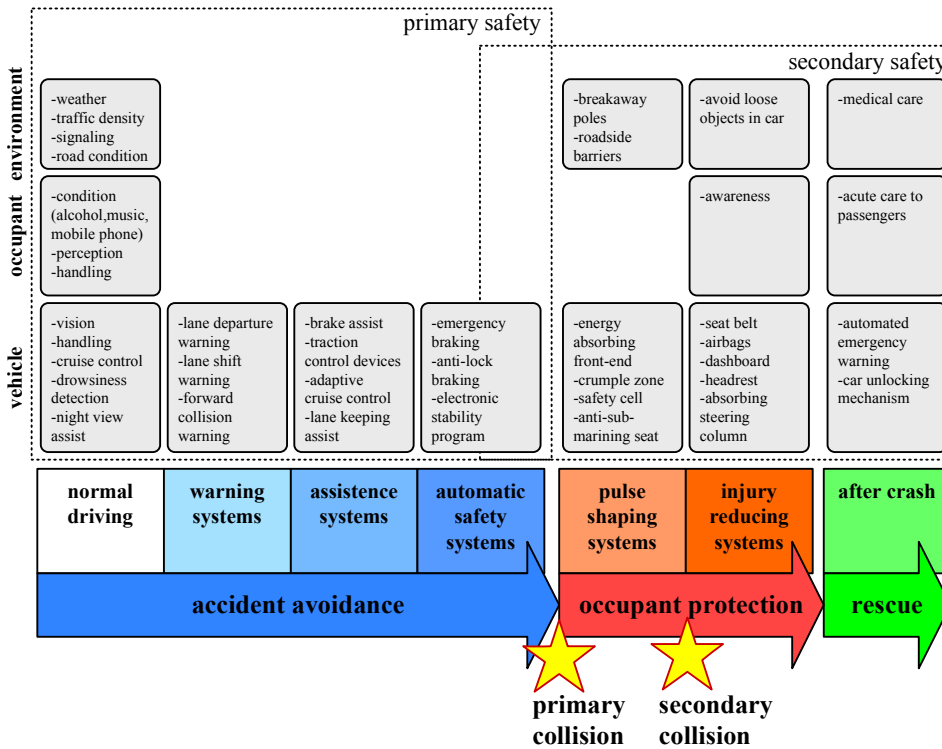


Figure 1.1 / An overview of the safety measures typically found in today’s motor vehicles, organized in the three crash phases and in the three fields where the measures are applied to.

ever, the terms passive and active safety can be confusing, e.g. a passive safety device may suggest that they are no active elements, while active restraint systems refer to passive safety. Throughout this entire thesis these terms are therefore avoided. Primary safety is a more unambiguous term, and is used to indicate all the safety measures to prevent or reduce the severity of the primary collision. Secondary safety measures then, obviously, refer to all the actions taken to reduce the severity of the secondary collision. The third term in this context is integrated safety, which reflects the interaction of primary safety sensors with secondary safety measures. For example, pre-crash sensors gather information about the vehicle behavior just before impact and enable the reversible pretensioner.

In the past decade, there has been a noticeable increase in the development of *primary safety measures*. This has mainly been made possible through advancements in the sensor technology, and the increased integration of electronic devices with the vehicle’s steering, braking and warning systems. Nowadays, some very effective

collision avoidance systems are becoming a standard in passenger vehicles. World-wide vehicle safety experts agree that a significant further reduction in fatalities and injuries can also be achieved by *secondary safety measures* (van Schijndel-de Nooij and Wismans, 2008). With almost 1.3 million injury-related accidents that happen yearly in EU27 (SafetyNet, 2009), the need for ongoing research in this area, especially also in the area of restraint systems, is indisputable. Examples of recent improvement of the restraint systems are: airbags located in head restraints and inflatable side-panel beams in case of a side impact, moving head restraints in case of a rear-impact, and size-adaptive airbags for various occupants. Although these systems are a useful addition to the occupant protection systems, major improvements can still be made in the area of the vehicle's restraint systems.

1.1.2 Scope of the Thesis

The function of a safety measure depends on the accident scenario, e.g. a roll-over crash requires a specific protection, children are injured differently than adults, and the airbag trigger time has to change for out-of-position occupants. Hence, it is important to target a specific scenario when improving restraint systems.

In this thesis, the scenario with statistically the largest risk on a fatality is chosen. In the EU18, in 53% of the fatalities, the mode of transport of the victim is a passenger car, as opposed to a (motor)cycle, pedestrian, moped, lorry, bus, coach etcetera. For the United States, this number is 73%. Moreover, persons of 16 year and older represent 95% of all fatalities in the USA and EU18. Concerning the collision type, 54% of occupant fatalities occurred in vehicles that sustained frontal damage (National Center for Statistics and Analysis, 2009; SafetyNet, 2009).

Restraint systems are typically most effective for a part of the body. Approximately 25-30% of all motor vehicle related deaths and disabling injuries can be directly attributed to thoracic injury (Nirula and Pintar, 2008), and can be marked as a contributive factor in around 70% of the cases (Kent et al., 2002; Nahum and Melvin, 1993). When only frontal collisions are considered, these numbers may even be higher, as the head and neck are the most injured body regions in rear and side impacts. Additionally, since the introduction of the airbag, fatalities due to neck and head injuries have significantly decreased, which makes the thoracic region of more importance (Berthet and Vezin, 2006). Summarizing, the scope of this thesis is on protection of the thoracic region, for adult occupants in a passenger car, involved in a frontal impact.

Thoracic injury protection can only be made safer, when there is a clear understanding of the mechanisms that result in severe injuries or fatalities. Relevant aspects of thoracic injuries are therefore presented in the next section.

1.2 Thoracic Injury Biomechanics

In the design of vehicle occupant protection systems, the risk of injury is assessed with models for the human being, e.g. mechanical models (crash test dummies) or mathematical models. A thorough knowledge of human injury biomechanics is required to develop these models. Injury biomechanics refer to the research area that studies the injury process and develops ways to reduce or eliminate injuries that can occur in an impact environment (Viano et al., 1989).

The injury process can be understood by the load-injury model. A mechanical load is exerted on the human body as a result of an impact, and this leads to a biomechanical response. The magnitude of the biomechanical responses can be influenced by the safety measures as presented in Section 1.1.1. Injury mechanisms describe how these responses may lead to an injury, and the severity of the injury is quantified by an injury criterion (Wismans et al., 2000).

1.2.1 Thoracic Injury Mechanisms

During the sudden vehicle deceleration in a frontal crash event, impact forces are applied to the thorax. This is mainly due to contact with the shoulder belt, the airbag and, in case of severe crashes, also with the vehicle interior. These forces result in a deceleration and compression of the thorax. The compression generally cause *skeletal* injuries, as the bending forces are large enough to fracture the ribs and sternum. These fractured ribs can on their turn pierce the lungs (Berthet and Veizin, 2006). On the other hand, the deceleration generally cause *soft tissue* injury, e.g. ruptured aortic veins (Wismans et al., 2000). Skeletal injuries, like fractured ribs and sternum, are most common (King, 2004). The injury mechanisms described here are caused by blunt impact and occur most frequently. Injuries by penetration impact from loose objects are less common.

The severity of injury seems to depend on the amount of energy the thorax must absorb, and the duration of mechanical loading. The type of injury depends on the magnitude of loading and also on the rate of loading, since human tissues have a viscoelastic nature. To assess the risk of injury during an impact, it is convenient to have a method to estimate the injury severity level.

1.2.2 Thoracic Injury Severity

In 1969, emergency room physicians have developed an injury scale, called the Abbreviated Injury Scale (AIS), to quantify the level of severity of an injury (Committee on Injury Scaling, 2008). In Table 1.1, the AIS severity levels for the human

thorax region are explained. For example, AIS4 refers to injuries that are severe but not life threatening for an average person, and a severity of AIS3+ indicates that the injury is categorized as 3, 4, 5 or 6. The combined highest injury severity level of all body regions is indicated by the Maximum AIS (MAIS) score.

Table 1.1 / The Abbreviated Injury Scale (AIS), applied to thoracic injuries.

AIS	Severity Level	Thoracic injury
0	no injury	-
1	minor	1 rib fracture
2	moderate	2-3 rib fractures
3	serious	4+ rib fractures one side; lung bruises
4	severe	4+ ribs fractures both sides; heart bruises
5	critical	chest ruptures; aortic wounds
6	unsurvivable	
9	unknown	

An important problem is to find a correct relationship between the injury severity and the mechanical load that is applied. This problem is difficult, since the relationship has to be obtained through i) testing with cadavers and post-mortem human subjects, which lack muscle tension, ii) crash reconstruction, in which the loading conditions have to be estimated, and iii) volunteer tests, which are generally far below the tolerance level. The problem is further complicated because of the large biological variation between the mechanical properties of human tissue, e.g. due to differences in age and gender. It is therefore primarily a statistical problem, for which *injury risk functions* are introduced. They relate the probability of a certain injury severity with a mechanical loading parameter, based on extensive experimental testing.

1.2.3 Thoracic Injury Criteria

Biomechanical engineers are typically not capable of assessing the injury severity like a physician. Engineers prefer quantitative relations, in this case between the biomechanical responses that cause the injury. The relation between biomechanical responses and injury severity is described by the injury criterion (IC), and they can be used to determine the injury risk functions. In the following, a list of IC is presented that are widely accepted to assess thoracic trauma for adults in frontal impacts (Berthet and Vezin, 2006; King, 2000, 2004), see also Table 1.2:

A_{max} In a classic work by Neathery (1975), it was suggested that there is a good correlation between injury level and spinal acceleration. This led in the USA to an injury threshold for spinal acceleration, specified in the Federal Motor Vehicle Safety Standards (FMVSS) no. 208, issued by NHTSA (1998). It demands that the resultant acceleration at the center of mass of the upper thorax, a_{spine} , of the 50th percentile Hybrid III male dummy may not exceed 60 g in 48-km/h frontal impact tests against a rigid barrier for more than 3 ms continuously. This threshold value indicates a 20% risk to AIS4+ chest injury. The criterion is indicated as the A_{max} criterion, given by

$$A_{\text{max}} := \max_t \left(\min_{\tau \in [0,3] \text{ ms}} |a_{\text{spine}}(t + \tau)| \right) \quad (1.1)$$

This IC is based on research that was performed before the introduction of restraint systems like pretensioners, load limiters, and air bags. Although the acceleration is a proper indication for the forces that are exerted on the body, this IC is not used anymore in EuroNCAP consumer tests (EuroNCAP, 2008). The IIHS and USNCAP test agencies still include this IC in their vehicle tests, although they mention in their protocol that the meaningfulness of this IC is limited (IIHS, 2008; Office of Crashworthiness Standards, 1996). On the other hand, there are still studies, e.g. based on an experimental data analysis by Kallieris et al. (1998), that explicitly conclude that the spinal acceleration (at first vertebrae T1) is a suitable thoracic injury predictor.

D_{max} The first injury assessment recommendation for the rib cage and underlying organs was also developed by Neathery (1975), and it is based on the maximum chest deflection of the thorax. In particular, the IC is defined as the peak chest deflection, D_{max} , given by

$$D_{\text{max}} := \max_t (\Delta x_{\text{chest}}(t)) \quad (1.2)$$

where the deflection, $\Delta x_{\text{chest}}(t)$, is measured between sternum and spine. The United Nations Economic Commission for Europe issues regulations on the protection of occupants of motor vehicles in the event of a frontal impact, known as the UN-ECE R94 (Economic Commission for Europe, 2007). They propose a limit of 50 mm for D_{max} , which corresponds to a 42% risk on AIS4+ injury (Mertz et al., 1991). The limits proposed in the R94 document are also adhered to by the EuroNCAP agency. The current FMVSS 208 demands a chest deflection of no more than 76 mm for the 50th percentile Hybrid III male dummy, which result in 95% risk on AIS3+.

VC Viano and Lau (1983) defined an IC that also includes the rate of deformation of the thorax, called the Viscous Criterion (VC). In their study, it was argued that the VC is the best criterion for determining soft tissue injury. The

VC is based on the outcome of a series of tests with cadavers and post-mortem human subjects. The VC value equals the maximum value of the product of chest compression, $C(t)$, which is defined as the normalized chest deflection $\Delta x_{\text{chest}}(t)$, and the time derivative of the chest deflection, denoted by $V(t) = \Delta v_{\text{chest}}(t)$. Hence

$$\text{VC} := \max_t \left(\Delta v_{\text{chest}}(t) \cdot \frac{\Delta x_{\text{chest}}(t)}{D} \right) \quad (1.3)$$

The scaling factor D is given by SAE J1727 regulations, namely $D = 144, 176$ and 195 mm for the 5%, 50% and the 95% percentile Hybrid III dummies respectively (Safety Test Instrumentation Standards Committee, 1996). The limit value in the UN-ECE R94 regulation is $\text{VC} \leq 1.0$ m/s, which corresponds to a 25% risk on AIS4+ injury. A value of 1.3 m/s has a 50% chance on AIS4+ injury (Viano and Lau, 1983). FMVSS 208 issues no limit values.

Table 1.2 / Thoracic injury criteria and their associated biomechanical responses, and the tolerance levels for the Hybrid III dummy.

IC	Biomechanical responses	Tolerance level	Injury risk
A_{max}	spinal acceleration (a_{spine})	60 g (FMVSS 208)	20% AIS4+
D_{max}	chest deflection (Δx_{chest})	50 mm (ECE-R94) 76 mm (FMVSS 208)	42% AIS4+ 95% AIS3+
VC	derivative of chest deflection (Δv_{chest}) & chest deflection	1.0 m/s (ECE-R94)	25% AIS4+

1.2.4 Thoracic Injury Reduction Systems

Having established the injury mechanisms, the vehicle components have to be identified that are most likely to cause injuries during the crash event. Changing the design of these components may lead to a reduction of the risk on thoracic injuries.

The seat belt obviously influences the thoracic biomechanical responses. The belt tries to restrain the occupant in the seat, thereby exerting large forces and deforming the chest with the possibility of serious injury. In literature, the relation between thoracic trauma in frontal impact and the amount of seat belt loading has been established extensively, see e.g. Cesari and Bouquet (1994); Crandall et al. (1997); Horsch et al. (1991); Lobdell (1973); Mertz et al. (1991); Morgan et al. (1994); Neathery (1975) and references therein. These studies show that a proper belt loading may result in a significantly lower injury risk to the thorax.

Therefore, the influence of the seat belt is paramount in the mitigation of thoracic injuries.

The second important restraint system, the airbag, is a so-called supplementary restraint system, since it is only effective when it is used in addition to the shoulder belt. Accident statistics presented by NHTSA (2001) support this, see Figure 1.2, in which TOAIS refers to thoracic AIS. The numbers in this graph indicate that the seat belt is eminent in reducing injuries: the effectiveness of protection is very poor when only the airbag is used. In the cases where the occupant did use a belt, the total restraint effectiveness increases slightly when an airbag is deployed. For severe thoracic injuries (TOAIS3+), the airbag decreases the total restraint effectiveness. This can be explained by the fact that solely severe neck and head injuries are significantly reduced by the airbag, hence the airbag is less effective as a thoracic protection device (Kent et al., 2005).

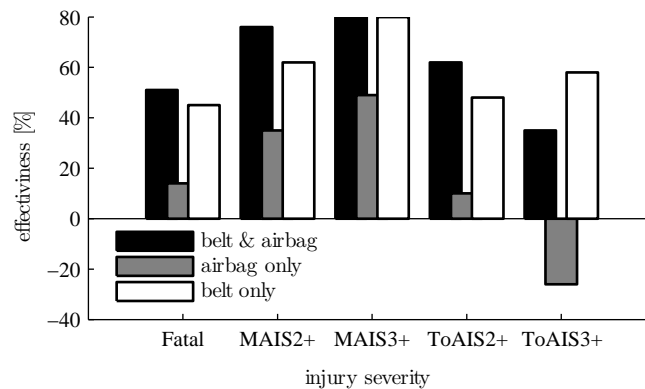


Figure 1.2 / Restraint effectiveness for AIS2+, AIS3+ and fatal injuries for frontal and near frontal crashes (NHTSA, 2001).

As the first column in the figure shows, airbags do reduce the probability of death in (near) frontal collisions, but the effect is small compared with seat belts. This is also concluded by Viano (1995), who found that the additional contribution of airbags to fatality reduction in drivers with seat belts is approximately 5-8%. Currently, the only major improvement in airbag design can be made in the discrimination between crashes that require deployment or not (Kent et al., 2005).

It is concluded that an improvement of the seat belt system is the most effective way in reducing thoracic injuries of adult occupant in frontal vehicle impacts. To eliminate the influence of the airbag on the injury mitigation, the airbag is omitted from the system descriptions in the remainder of this thesis. To elucidate where the belt system can be made more effective in mitigating injuries, a background on seat belts is given in the next section.

1.3 Seat Belt Systems

1.3.1 Overview

In 1959, Volvo was the first car manufacturer to install the front-seat three-point seat belt as standard equipment in their Volvo Amazon³. Today, exactly 50 years later, the three-point belt or safety belt, as depicted in Figure 1.3, can be found in the vast majority of the passenger cars in the Western world. The primary function of the seat belt is to restrain the occupant during impact to prevent seat ejection. The secondary function is to make optimal use of space between the occupant and vehicle interior to decelerate the occupant, a phase called ride-down (Huston, 2001). Below follows a short explanation of the most important components of the today's belt system (Håland, 2006; Seiffert and Wech, 2007).

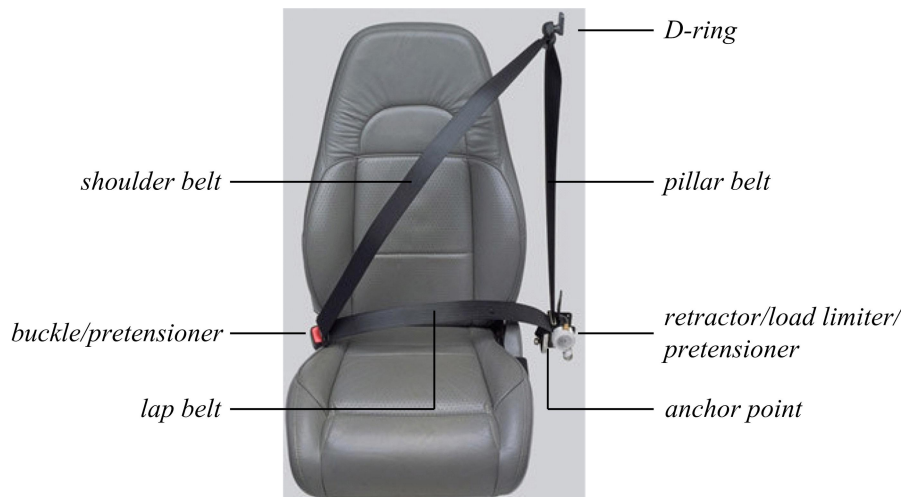


Figure 1.3 / A conventional three-point seat belt system found in today's passenger cars. Copyright Delphi, Inc., image adapted with permission.

The three-point seat belt The three-point seat belt has a layout as shown in Figure 1.3. The belt runs from the vehicle's B-pillar to the D-ring, it then goes over the torso of the occupant to the buckle, and then to the anchor point. The three belt segments are called pillar belt, shoulder belt and lap belt, as indicated in the figure. An important aspect of the belt is its webbing, which determines the strain behavior under loading conditions. Restraint suppliers express the belt webbing characteristics by the relative

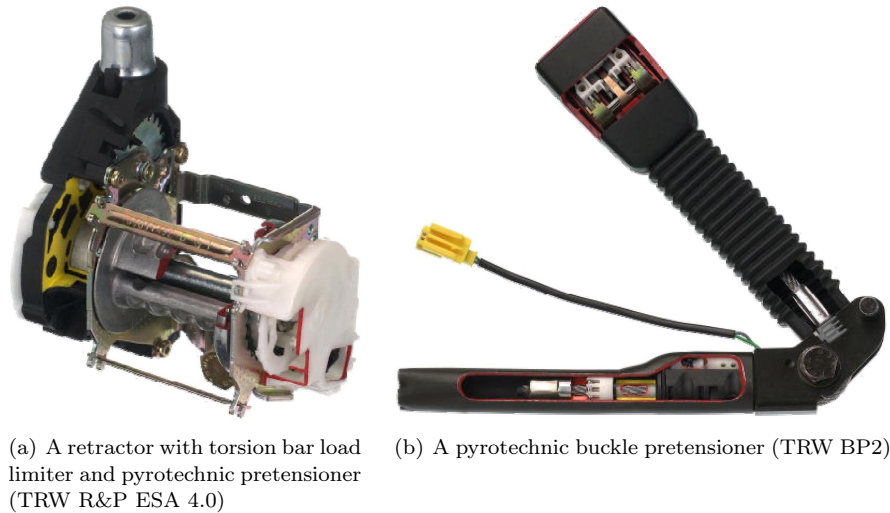
³Volvo Cars milestones 1927 - 2007 [online], <http://www.volvocars.com/int1/corporation/Heritage/History/Pages/default.aspx?item=1> (last access: August 2009)

percentage of elongation at a tension force of 10 kN (but also forces of 2500 lbs. are used). Conventional belt webbing typically has a stiffness between 10-20%, a thickness of 1-1.5 mm and a width of 48-51 mm.

The retractor This part is sometimes known as the inertia-reel, and is located in the lower part of the B-pillar. The function of the retractor is twofold. Firstly, when the belt is unbuckled, the webbing is reeled in by a rewinding spring connected to the retractor spool. This spring also removes the worst slack from the belt when in use, such that the belt aligns properly over the occupant without being uncomfortable. The second function is the locking mechanism. The retractor locks the belt whenever the vehicle senses a crash, for example by acceleration sensors. In addition to this, the locking mechanism is also activated when the occupant pulls the belt faster than normal, which gives the occupant a feeling of confidence in the safety belt.

The load limiter The load limiter or shoulder belt force limiter has probably been the most important improvement since the introduction of the safety belt. The device is typically integrated within the retractor, and its function is to ensure that the loading forces on the occupant are limited. The load limiting force is typically obtained by torsion of the steel bar. When the belt force is lower than the load limit, there is no pay-out of the belt. Belt forces that are higher than the limit level make the torsion bar twist, and the webbing will unwind from the spool. The torsion bar characteristics determine the load-deformation profile, which has typically a constant limit level of 2-6 kN in today's passenger vehicles (Håland, 2006). Since the introduction of the load limiter, studies showed that the risk on thoracic injuries is drastically reduced, especially the D_{\max} IC (Foret-Bruno et al., 2001). An example of a load limiter integrated in the retractor is shown in Figure 1.4(a).

The pretensioner During the first milliseconds of the crash, it is desirable that as much slack is removed from the belt as possible. Slack in the shoulder belt allows the occupant to move forward at the start of the crash, which limits the available space for the ride-down and complicates airbag trigger timing. Slack in the lap belt increases the risk of *submarining*, the phenomenon of sliding underneath the belt. Since the retractor spring force is too weak (for reasons of comfort) to achieve slack removal, pretensioner devices have been developed. Originally, they consisted of mechanical springs, but nowadays, they have a pyrotechnical mechanism. Pretensioners are located in the buckle and/or the retractor, and they apply a restraining force of 1.5-2 kN within milliseconds after the crash. They can retract 100-150 mm of belt, dependent on the amount of initial slack. Retractor pretensioners were introduced in 1983 by Mercedes-Benz, and the buckle pretensioner by Volvo in 1989. In Figure 1.4, both types are shown.



(a) A retractor with torsion bar load limiter and pyrotechnic pretensioner (TRW R&P ESA 4.0) (b) A pyrotechnic buckle pretensioner (TRW BP2)

Figure 1.4 / Copyright TRW Automotive, Inc., images reproduced with permission.

1.3.2 Design Limitations

The described seat belt system is very effective in restraining the occupant and in reducing injury risks, however, there are two design aspects that significantly limit its performance. The first one is the asymmetry of the shoulder belt, which runs diagonally over the torso. Especially in oblique, lateral and roll-over crashes, there is a risk that the occupant slides out of the belt. The 4- or 5-point belt does a much better job in this aspect, but so far, it can only be found in child restraint seats and vehicles used in motor sports.

The second aspect concerns the flexibility of the seat belt system. Every scenario requires - ideally - a specific setting. The load limiter has usually a fixed level of operation, which cannot address the great variety in occupant weight, position, biomechanical tolerance, belt usage and crash severity. This problem was for the first time explicitly written down by Mackay (1994). Also Iyota and Ishikawa (2003), for example, found that smaller and larger occupants are more likely to be injured than the averaged sized occupants for which the restraints are designed. Foret-Bruno et al. (1998) showed that chest deflection injury tolerances decrease with age, and belt loadings should be adapted accordingly. As a third example, Adomeit et al. (1997) concluded that injury risks can be significantly reduced, when the belt force is adjusted to the vehicle closing speed.

In the majority of the vehicles, it is not yet possible to optimize the force level

for the actual crash scenario, and the design will be a tradeoff to maintain sufficient performance in all possible scenarios. Moreover, the level is in practice often chosen such that it gives as much protection as possible in the standardized scenarios. These scenarios are used in consumer vehicle tests or prescribed by directive standards, e.g. the FMVSS issued by NHTSA (1998). This fundamental shortcoming of current safety belts makes that not every vehicle occupant is optimally protected in every possible situation that can occur in real-world crashes. To overcome this shortcoming and to improve occupant safety, research has recently focused on developing adaptive seat belt systems.

1.3.3 Force Adaptive Seat Belt Systems

Adaptive seat belts are able to adjust their configuration during, or before, the secondary collision. In this way, the protection could be made optimal for a specific occupant, occupant position, vehicle, or crash (Mackay et al., 1994). This flexibility allows improving the occupant's response for the actual situation. The need to develop intelligent, real-time controlled restraint systems has also been recognized in the roadmap for future passive safety technology (Wismans, 2007).

In this thesis, the term adaptive seat belts is adhered to, but different names can be found in literature (Wismans, 2003). They are also called smart, intelligent or active seat belts, although these terms do not systematically refer to different systems. Differences can, however, be seen in the approaches that are used, and three types of adaptive systems can be distinguished

- **Constant Force Restraint (CFR)**. A constant load limiting level is set before, or in the first milliseconds of the crash. The level is typically based on occupant characteristics such as mass or size.
- **Switching Load Limiter (SLL)**. During the crash, the load limiter can switch to a different load limit level. The switching moment can generally be chosen freely, and the level is typically lowered from 4 to 2 kN. They are also known as dual stage load limiters.
- **Continuous Restraint Control (CRC)**. The restraint force in the seat belt can be prescribed at multiple time instances during the crash, depending on the update frequency of the load limiting device.

In Table 1.3, a number of studies is listed, that have investigated the influence of adaptive seat belts on thoracic injury mitigation. It has been shown that a proper constant belt force level, chosen before the primary collision, significantly improves

thoracic injury mitigation. SLL systems are able to lower the risk of thoracic injury even more, compared to CFR systems. Current state-of-the-art seat belt systems, implemented in luxury class consumer passenger cars, have switching load limiters, or load limiters with declining or progressive levels, see TRW or KSS⁴. However, these adaptive systems are still not optimal, as their flexibility is limited.

A huge step in injury reduction is made with the CRC seat belt system, where the belt force is continuously manipulated during impact. In two similar studies by Crandall et al. (2000) and Kent et al. (2007), an optimal time-varying belt force, found through optimization with an elementary chest model, is applied in open-loop. The solution presented by Hesselning (2004) is more robust, since the belt force is applied in a feedback configuration, and optimal values are obtained by solving a control problem. In this way, injury level reductions can be achieved of 10-50 %, for different body regions and various dummy sizes. Hence, the (feedback) CRC system is preferable by far, since it will result in significant lower injury risks, especially for occupants or collisions that deviate from the average on which the regulations are based and the tests are designed.

Table 1.3 / Various adaptive safety belt approaches, which adjust their configuration to the operating environment.

Approach	Literature reference
CFR	Holding et al. (2001); Mertz et al. (1995); Miller (1996); Musiol et al. (1997); Paulitz et al. (2006); Shin et al. (2007).
SLL	Clute (2001); Iyota and Ishikawa (2003); Kawaguchi et al. (2003); Yeh et al. (2005).
CRC	Cooper et al. (2004); Crandall et al. (2000); Hesselning (2004); Hesselning et al. (2006a,b); Kent et al. (2007).

It is recognized that a CRC seat belt system focuses on the reduction of only a small part of the total number of road transport fatalities. As outlined in Section 1.1.2, roughly half of the fatalities involve a passenger car, and another half of these fatal accidents resulted from a frontal impact. Furthermore, thoracic injuries are a direct cause of death in 30% of the fatalities, and a contributive in 70% of the cases. Hence, the number of fatalities could be reduced by 9-20% at best. Moreover, the methods and solutions presented in this thesis may also apply – perhaps to a lesser extent – to other crash scenarios, e.g. roll-over crashes or rear impacts. The CRC seat belt system may also help to improve other safety measures such as the airbag, and reduce the number of severely injured occupants.

⁴TRW Automotive Inc. [online], http://www.trw.com/sub_system/seat_belt_systems/load_limiters, Key Safety Systems (KSS), Inc. [online], <http://www.keysafetyinc.com/seatbelts.asp> (last access: August 2009)

1.4 Research Objective

The foregoing introduction on vehicle safety and injury biomechanics serves to argue where improvements in occupant protection are most effective in terms of fatality reduction. Section 1.1.2 defined the scope of this research, and Section 1.3.3 concluded that a CRC system for the seat belt would be most effective in this respect. These conclusions are summarized in the following research objective:

Design a system that prescribes the seat belt force in a conventional 3-point seat belt arrangement, such that the thoracic injury criteria in (1.1)-(1.3) are minimized, without increasing other injury criteria. The system is applied to adult front-seat occupants involved in a frontal impact with a passenger car, in which the airbag is disabled.

Hesseling (2004) has proposed two interesting and attractive approaches to achieve this objective. In the first approach, the problem is formulated as a tracking control problem, where biomechanical responses of the occupant are measured and forced to follow a reference trajectory. This trajectory results in a minimum risk of injury, while satisfying certain constraints. Through simulation studies, Hesseling showed promising results in terms of stability, tracking error, and reduction of injury criteria. However, the reference trajectories are constructed assuming full a priori knowledge of the crash pulse, constraints and occupant characteristics, which is clearly not realistic. In the second approach, an optimization strategy called model predictive control (MPC) is used to derive optimal restraint settings. However, the optimization procedure presented in the study by Hesseling is not likely to be solved in real-time, and still requires knowledge of the future vehicle motion during impact.

Hence, there is currently a number of assumptions that hinder the actual implementation of the CRC system in a vehicle:

- *a priori* knowledge of the crash pulse is available;
- there are no restrictions on the manipulation of the seat belt force, i.e. an ideal restraint actuator is available;
- all required measurement data, such as biomechanical occupant responses, are available in real-time;
- the algorithms are computationally feasible in order to meet the real-time requirements.

These assumptions need to be dealt with before the next generation of passenger vehicles can be equipped with a seat belt CRC system. In this thesis, a possible solution will be presented to meet the outlined research objective.

1.5 Control Problem Formulation

In this section, the research objective and assumptions presented in the previous section are formulated as a control problem.

Figure 1.5 presents a very general and abstract layout of the CRC system for the seat belt. The block Σ reflects the system consisting of an occupant, the seat, the vehicle interior, and a conventional three-point belt. This system is subjected to an (arbitrary) full frontal impact, represented by an acceleration field acting on the vehicle interior, the seat and the belt attachment points. It is common practice in automotive safety research to use the longitudinal acceleration of the B-pillar of the vehicle to represent the acceleration field. It is referred to as $a_{\text{veh}}(t)$, and it enters the system Σ as a disturbance.

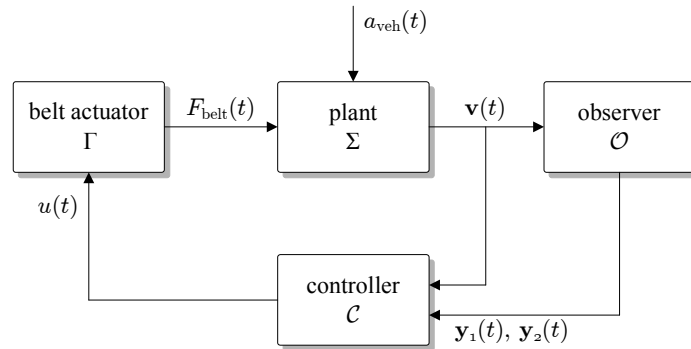


Figure 1.5 / General layout of the control problem.

The force in the pillar belt, denoted by $F_{\text{belt}}(t)$, is generated by a belt force actuator, Γ , instead of the conventional load limiter. This device applies a force to the belt according to a reference signal u , the control variable, and hence $\Gamma : u(t) \mapsto F_{\text{belt}}(t)$. The inputs to the system Σ are collected in vector $\mathbf{w}(t)$

$$\mathbf{w}(t) = [F_{\text{belt}}(t) \quad a_{\text{veh}}(t)]^T \quad (1.4)$$

The control variable $u(t)$ is generated by a numerical algorithm, referred to as controller \mathcal{C} , which aims at minimizing one or more of the thoracic injury criteria (1.1) - (1.3). The minimal combined risk of injury is defined by a weighting of these thoracic injury criteria, formulated by a performance index J . The criteria, and thus index J , are a (nonlinear) function φ of the biomechanical occupant responses. These biomechanical responses are listed in Table 1.2, and they are

collected in a variable $\mathbf{y}_1(t)$, hence

$$\mathbf{y}_1(t) = [a_{\text{spine}}(t) \quad \Delta x_{\text{chest}}(t) \quad \Delta v_{\text{chest}}(t)]^T \quad (1.5)$$

In addition, constraints apply to certain responses, referred to by variable $\mathbf{y}_2(t)$. Namely, the available space in the vehicle compartment is limited, which poses a constraint on the relative occupant displacement. It is chosen to put a constraint on the forward displacement of the sternum relative to the vehicle, $\Delta x_{\text{ribs}}(t)$, hence

$$\mathbf{y}_2(t) = [\Delta x_{\text{ribs}}(t)] \quad (1.6)$$

Also, the belt actuator may have a limited performance, which limits the trajectory of $u(t)$. Both constraints are represented by a vector constraint function, ϕ . Minimization of J is now achieved by forcing the responses $\mathbf{y}_1(t)$ to follow an optimal trajectory through manipulation of $u(t)$, while satisfying the constraint $\phi(\mathbf{y}_2(t), u(t)) \leq 0$.

The biomechanical responses $\mathbf{y}_1, \mathbf{y}_2$ may not be available from measurement data during a real-world crash. That is because not all of the required sensors to measure the above described responses do currently exist, whereas many of the available sensors are too expensive, too inaccurate or have too low a bandwidth. For example, current sensors to detect the position of the occupant are typically based on vision systems, which are expensive, not well-integrated in the vehicle, have a low bandwidth and are not crash resistant. Therefore, it would be useful to develop an observer algorithm, \mathcal{O} , that is able to reconstruct the responses based on measurement data that is already available in the vehicle, or can be obtained with cheap and fast sensors. These measurable signals are collected in variable $\mathbf{v}(t)$, hence the observer is given by $\mathcal{O} : \mathbf{v}(t) \mapsto \mathbf{y}_1(t), \mathbf{y}_2(t)$. The measurements are generated by the system Σ , so $\Sigma : \mathbf{w}(t) \mapsto \mathbf{v}(t)$.

In this thesis, the observer \mathcal{O} and actuator Γ will be developed, and the system Σ will be defined. With these, the control problem can be formulated. Using the aforementioned notations, the controller \mathcal{C} has to solve the following optimization problem:

$$\begin{aligned} \min_u \quad J &= \varphi(\mathbf{y}_1(t)) \\ \text{subject to} \quad 0 &\geq \phi(\mathbf{y}_2(t), u(t)) \\ \mathcal{O} &: \mathbf{v}(t) \mapsto \mathbf{y}_1(t), \mathbf{y}_2(t) \\ \Sigma &: \mathbf{w}(t) \mapsto \mathbf{v}(t) \\ \Gamma &: u(t) \mapsto F_{\text{belt}}(t) \end{aligned} \quad (1.7)$$

in which it is reasonable to assumed that all initial conditions are zero, i.e. $\mathbf{y}_1(0) = \mathbf{y}_2(0) = \mathbf{w}(0) = \mathbf{v}(0) = u(0) = 0$.

Given the outlined control problem, it is desirable to have a mathematical model of the systems Γ and Σ , as will be argued hereunder. The models are useful for:

Control design. The controller \mathcal{C} that solves problem (1.7), has to contain knowledge on the systems Σ and Γ , and the functions φ , ϕ . Therefore, a model of these systems is desirable, such that a controller can be designed that achieves disturbance rejection and optimizes the performance according to the specifications in (1.7);

Prediction. An optimal trajectory \mathbf{y}_1 has to be found that minimizes J , without violating the constraints on \mathbf{y}_2 and $u(t)$. Since the crash event is finite, the optimal trajectory can be found through a prediction of these responses. This requires a *prediction model*, that has the variables \mathbf{y}_1 , \mathbf{y}_2 as outputs and the future control effort u as inputs;

Observation. The observer algorithm \mathcal{O} is designed such that it uses the measurements \mathbf{v} to estimate responses \mathbf{y}_1 and \mathbf{y}_2 . A commonly used method to design such an observer is to use an *observer model* that describes the relation between \mathbf{v} and the required output responses. The model can be employed to reconstruct or estimate the signals of the system that are not directly measurable;

Simulation. The models can be used for testing of the system behavior in different crash scenarios.

One must be able to execute the prediction and observer model with a low computational effort, since they are used in a procedure that has to meet real-time requirements.

1.6 Contributions and Outline

Given the control and modeling problem sketched in the previous section, the main results of this thesis can be summarized as follows:

- i) a mathematical model of the system Σ , consisting of an occupant, the vehicle interior, and a conventional three-point belt. The model describes the relation between variables \mathbf{y}_1 , \mathbf{y}_2 and \mathbf{v} , and the vehicle acceleration a_{veh} and control effort u . The model is suitable for use on online control optimization strategies, and can be used for the design of a thoracic injury observer system;

- ii) a control strategy \mathcal{C} that is able to determine optimal seat belt settings on-line, without a priori crash information, while aiming at a minimum risk of injury for the occupant in an arbitrary frontal crash;
- iii) an observer system \mathcal{O} that supplies estimates of the biomechanical responses \mathbf{y}_1 and constraint responses \mathbf{y}_2 , as required by the control algorithm, based on measurements \mathbf{v} from low-cost, fast sensors;
- iv) an actuator Γ that is able to realize the restraining force in the pillar belt, according to the requirements of the control strategy.

The thesis is organized along the above list of contributions. In Chapter 2, a number of relatively simple mathematical models is developed, based on complex, realistic models that have been extensively validated against real-world crashes. The approach to handle the constrained control and predictive problems is treated in Chapter 3, given ideal sensors and a perfect actuator. Subsequently, the observer system is proposed and developed in Chapter 4. The design, construction and a first step towards the experimental evaluation of a belt force actuator are presented in Chapter 5. This thesis concludes in Chapter 6 with a discussion on the obtained results, and with a presentation of an outlook on future motor vehicle safety research.

2

MODELING FOR CONTROL DESIGN

Abstract / In this chapter, a systematic approach is presented to obtain manageable models of a dummy in a vehicle interior, subject to a frontal crash. Two types of models are constructed, viz. a nonlinear, low-order model and a linear time-invariant model. The models are validated against a reference model, which has a high fidelity to the real world. The occupant models contain the control-relevant dynamics of thoracic and neck body region for a range of high-speed, frontal impact scenarios.

2.1 Introduction

In Section 1.5, it was argued that continuous controlled seat belt systems require the development of a set of (mathematical) models. The aim of this chapter is to develop these models, which describe the system consisting of an occupant, vehicle interior and a three-point seat belt subject to a frontal impact. The purpose of these models is to employ them for controller and observer design, and the models are therefore referred to as *design models*, \mathcal{D} . The design models must be able to be executed with a low computational effort, as they have to predict relevant responses in real-time. This means that the degree of complexity in the model has to be limited, and only dominant phenomena should be included in the model. With the modeling goal being defined, the next step in the modeling process is to define the boundaries of the system to be modeled (Bosgra, 2004).

This chapter is largely based on E.P. van der Laan et al. (2009b), Control Oriented Modeling of Occupants in Frontal Impacts, *International Journal of Crashworthiness*, 14(4), p. 323-337, and E.P. van der Laan et al. (2007a), Control Oriented Modeling of Vehicular Occupants and Restraint Systems. In *Proceedings of the Conference of the International Research Council on the Biomechanics of Impact (IRCOBI)*, 19-21 Sep, Maastricht, the Netherlands, p. 47-58

2.2 System Boundary

The system to be modeled is already shortly discussed in Section 1.5. The system reflects that part of the real world that describes the effect of the pillar belt force on thoracic injuries of a seated, belted vehicular driver, subject to a frontal impact. Throughout the impact, the driver has no contact with the airbag or vehicle steering wheel or dashboard, as argued in Section 1.4. Hence, the system consists of an occupant, a seat, a three-point belt arrangement, a belt force actuator, belt attachment points and a floor board. The design of the belt actuator, Γ , will be presented in Chapter 5, so no statements can yet be made on its input-output behavior. The belt actuator is therefore not included in the modeling process.

The system to be modeled is referred to as Σ , see also Section 1.5. The input signals to Σ are the force in the pillar belt, F_{belt} , and the vehicle acceleration, a_{veh} . The input variable for the design models is denoted by vector \mathbf{w} , as in (1.4)

$$\mathbf{w}(t) = [F_{\text{belt}}(t) \quad a_{\text{veh}}(t)]^T \quad (2.1)$$

The output variables are given by the measurement variable \mathbf{v} and biomechanical responses \mathbf{y}_1 and \mathbf{y}_2 . Concerning the measurements variables \mathbf{v} , the observer system \mathcal{O} will estimate \mathbf{y}_1 and \mathbf{y}_2 based on \mathbf{v} . It is expected that the spinal acceleration, a_{spine} , and chest deflection, Δx_{chest} and Δv_{chest} , can be estimated with a model of the thorax and belt, given that the sternum acceleration and shoulder belt force is known. Estimating the sternal displacement, Δx_{ribs} , from acceleration data is prone to errors, and can be avoided if a position measurement is available. For this, a sensor is used that measures the displacement of the belt at the belt actuator, referred to as the *belt rollout*. This is summarized in the following assumption:

Assumption 2.1 / *Measurements of the belt rollout, x_{belt} , and the acceleration of the sternum, a_{ribs} , can be used to estimate or reconstruct \mathbf{y}_1 and \mathbf{y}_2 , given knowledge on the system Σ and measurements of system inputs F_{belt} and a_{veh} .*

This choice for these sensors is assumed here in this chapter, but a thorough discussion on this topic is given in Chapter 4. The two sensor outputs are part of measurement variable \mathbf{v} , and collected in vector \mathbf{y}_3 as follows

$$\mathbf{y}_3(t) = [x_{\text{belt}}(t) \quad a_{\text{ribs}}(t)]^T \quad (2.2)$$

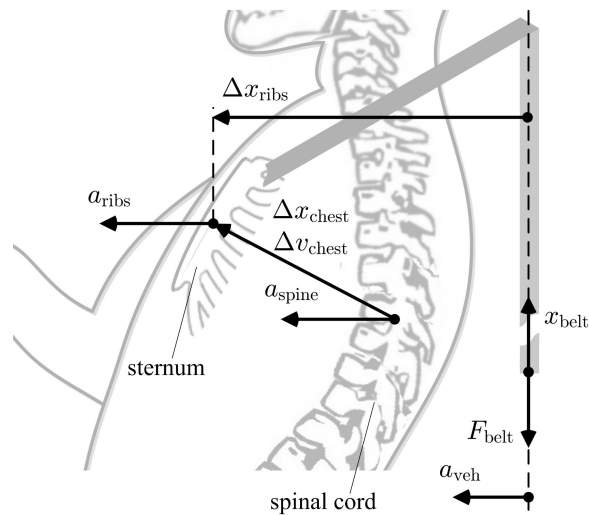
The combined model output variable is now defined by \mathbf{y} , hence

$$\begin{aligned} \mathbf{y} &= [\mathbf{y}_1 \quad \mathbf{y}_2 \quad \mathbf{y}_3]^T \\ &= [a_{\text{spine}} \quad \Delta x_{\text{chest}} \quad \Delta v_{\text{chest}} \mid \Delta x_{\text{ribs}} \mid x_{\text{belt}} \quad a_{\text{ribs}}]^T \end{aligned} \quad (2.3)$$

with \mathbf{y}_1 and \mathbf{y}_2 given by Equations 1.5 and 1.6, respectively. The model outputs \mathbf{y} are also listed in Table 2.1 and depicted on a human thorax in Figure 2.1.

Table 2.1 / Output responses \mathbf{y} of the design model.

Symbol	Description
a_{spine}	forward acceleration of the spinal cord
Δx_{chest}	chest deflection
Δv_{chest}	derivative of chest deflection
Δx_{ribs}	forward sternum displacement, wrt vehicle interior
x_{belt}	belt rollout at the retractor
a_{ribs}	forward sternum acceleration

**Figure 2.1** / Location of the output responses of the design model.

2.3 Approach

Generally, there are two ways of arriving at models of a physical system (van den Hof, 2006). First, using measurements of the variables of the system, a model can be constructed by identifying relations that match the measured data as well as possible. This procedure is called system identification, and the resulting model is identified purely on the basis of data, so without taking the physical structure into account (black box identification). In the light of this research, real world crash data may be used, but the availability of this data is limited, and it would involve a lot of engineering judgement. As an alternative, input-output data from existing, validated models may be used. However, this black-box procedure makes it difficult to adapt the model to various occupant types, to a different vehicle interior, or to changes in the belt layout. Also, the identification has to be redone

when additional outputs are required, and finally, it provides no insight in the underlying system dynamics.

Another method is pure physical modeling (white box), where the relations are obtained using *first-principles of physics*. This method is favorable, as it provides a lot of flexibility. In literature, many examples of this type of occupant models can be found, but they are not directly suitable for use in the proposed CRC system. The next section gives a short overview of existing human body (or dummy) models subject to impact.

2.3.1 Computational Modeling of Biomechanical Systems

A huge amount of attempts has been made to describe the basic dynamics of an occupant ever since McHenry proposed one of the first very elementary models in 1963 (McHenry, 1963). Available present-day crash occupant models are used for crash victim simulation (CVS), and they aim, in general, at an extremely accurate and complete description of the occupant and its interaction with the vehicle. Such complex models consist of rigid multibody (RMB) or finite element (FE) models, or a combination of both. MADYMO[®], (TNO Madymo B.V., 2005), is a well-known example of the latter. The complexity of these models makes them less suitable for our purposes.

Also many less complex vehicle-occupant-restraint models can be found in literature. An overview of existing occupant modeling tools is given by Huston (1987); Prasad (1984); Prasad and Chou (1989) for crash-victim models up to 1990. A more recent overview is given by Prasad (1997), Wismans et al. (2005) and Cheng et al. (2005). The models presented in those studies properly describe the most relevant phenomena.

The model developed by Crandall et al. (2000) is a very elementary two-mass injury model of the thorax, interacting with a seat-belt, see Figure 2.2(a). Their model does not include a belt model and is too simple to model the diversity in scenarios.

The occupant-seat models developed by Habib (2001) and Paulitz et al. (2006) are very similar.

These three-body models are used to demonstrate the potential of adaptive restraint systems. The influence of different belt forces on head, chest and pelvis acceleration is examined, see Figure 2.2(b) and Figure 2.2(e). However, the models lack a chest model to predict Δx_{chest} , and do not have sufficient accuracy and flexibility.

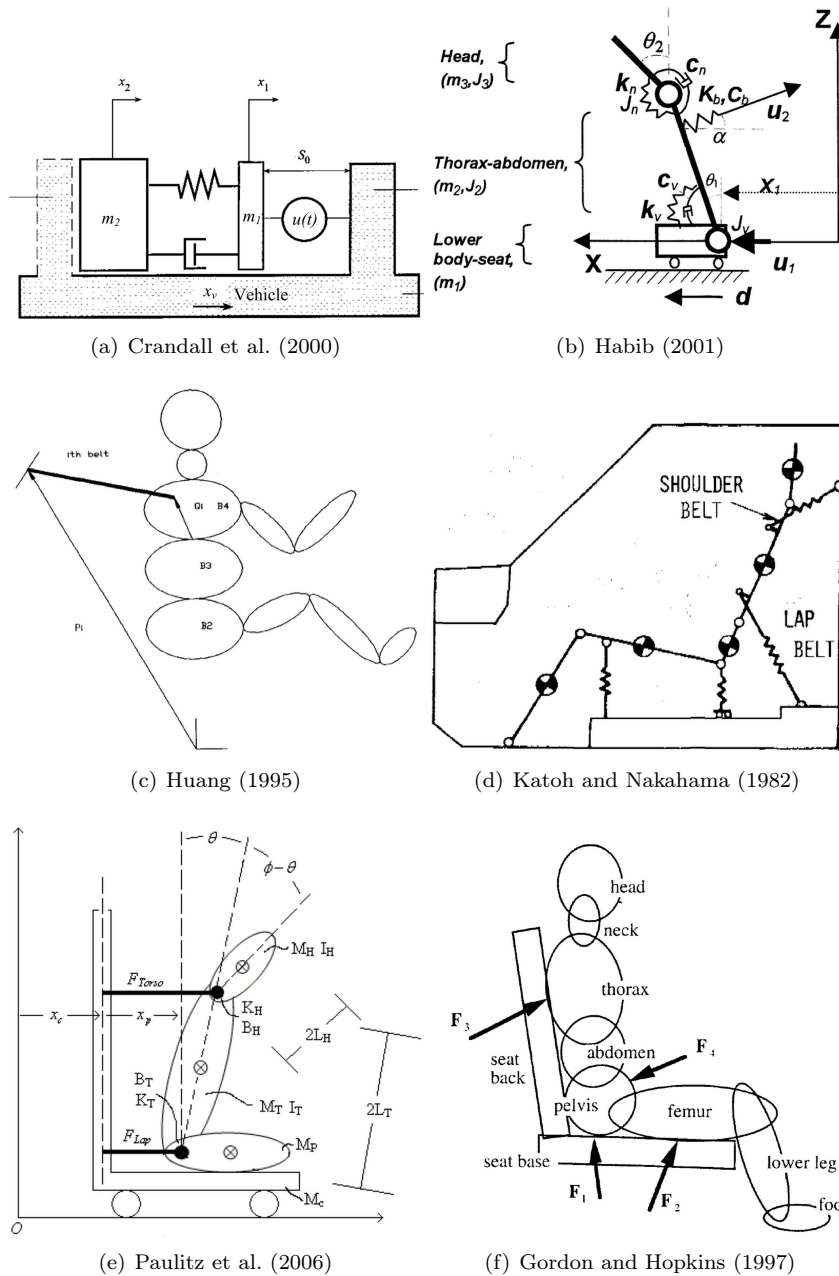


Figure 2.2 / Representation of various simple biomechanical occupant models with belt restraining force for frontal impact simulation.

In a paper by Gordon and Hopkins (1997), dummy model parameters are obtained from validated models and measured kinematic data. The resulting model is suitable for our purposes, but a shoulder belt and a chest model need to be added, see Figure 2.2(f).

Huang (1995) formulated a nonlinear mathematical model of a human body constrained by a seat and a restraint system, see Figure 2.2(c). The model is a three dimensional system with 15 bodies, and although the design methodology is suitable, the model is too complex for use here.

Finally, Katoh and Nakahama (1982) presented a 5 body model including restraining forces, where the seat belt is modeled as a linear spring, see Figure 2.2(d). The model exhibits desired behavior, but - again - lacks accuracy in the responses. Also, a chest model is not implemented and model parameters are not given.

Concluding, the presented models are not suitable in their present form as a design tool for the proposed CRC seat belt system; a proper chest model is absent, the seat belt is modeled poorly, the accuracy in the output responses is limited, or the models are too complex. Therefore, it is chosen to develop the design models, according to the requirements and system boundaries from Section 2.1, and with the knowledge obtained from this literature study. The advantage of this approach is that it provides a lot of flexibility in choosing the model structure, model complexity, coding software, etcetera. Moreover, it provides insight in the dynamics of vehicle occupants subject to impact.

2.3.2 Multi-fidelity Approach

The outlined modeling problem has led to an approach that is referred to as *multi-fidelity modeling*. Existing complex, high-order CVS models have a (relatively) high fidelity to real-life crash events, indicated by Σ . These models are therefore referred to as *reference models*, \mathcal{R} , and they are coded in commercially available software packages. These accurate models can be employed to derive less complex models, the design models \mathcal{D} , by means of a *sensitivity analysis*. The design models yield less accurate (but hopefully sufficient) responses compared to the reference model, but have a low computational load. The low-order design models are approximated by linear time invariant (LTI) models, \mathcal{P} , which will have the lowest fidelity. These linear models are used to design controller and observer algorithms, and may be used for real-time injury prediction.

In the following sections, a systematic approach to derive a low-order model from a high-order occupant model is presented, see Figure 2.3.

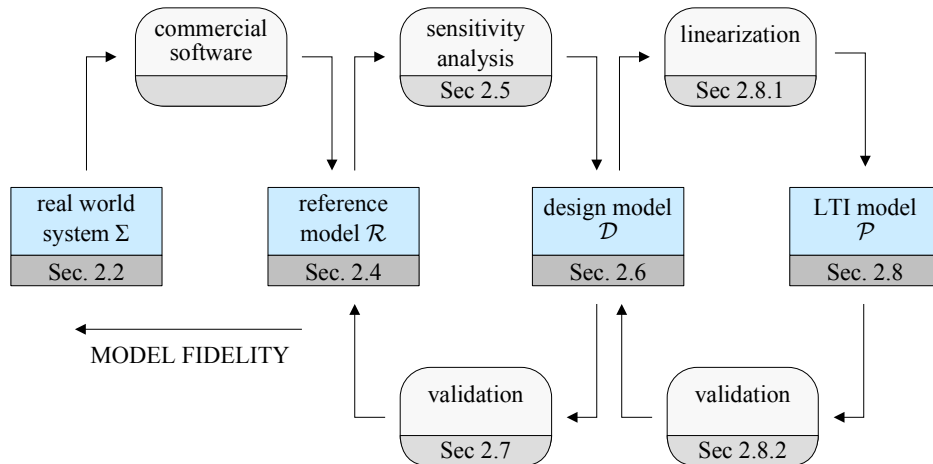


Figure 2.3 / Multi-fidelity modeling approach.

2.4 The Reference Model

A widely used software package for crash victim simulation is MATHematical DY-namic Model (MADYMO[®]), developed by TNO Madymo B.V. (2005). The package includes a large database for CVS, for example it contains a variety of dummy models and impact barriers. The numerical reference model \mathcal{R} used here is the model developed within the European PRISM¹ project (Bosch-Rekvelde et al., 2005), coded in Madymo 6.3. In this section, the most important characteristics of this PRISM model are described, and the quality with respect to real world crash tests is evaluated.

2.4.1 The PRISM Model

The main objective of the PRISM project was to facilitate the development of smart, i.e., adaptive or real-time controlled, restraint systems. In this context, vehicle interior compartment models were developed based on average measures of four vehicles. Here, the interior model is used that originated from four supermini cars (Ford Ka, Citroen C3, Opel Corsa and Daihatsu Cuore). The baseline restraint system consists of frontal airbags and a three-point belt system, including a load limiter and buckle pretensioner. More details on the restraint system settings can be found in Bosch-Rekvelde et al. (2005).

¹PRISM: Proposed Reduction of car crash Injuries through improved SMart restraint development technologies

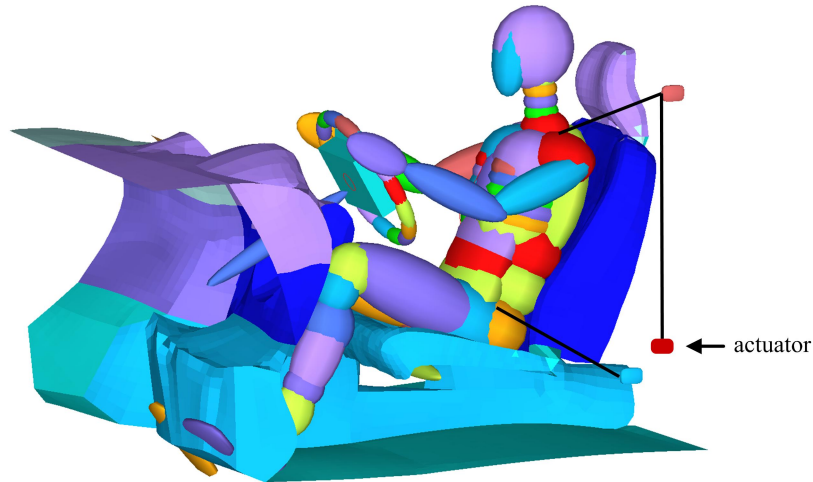


Figure 2.4 / Madymo surface representation of the PRISM reference model \mathcal{R} , consisting of a 50th percentile Hybrid III dummy.

In this study, the 5th, 50th and 95th percentile ellipsoid Hybrid III dummies (v7.1) were settled in the compartment model (TNO Madymo B.V., 2005). Hybrid III (HIII) dummies are, at this moment, the most common frontal impact dummies used by crash testing agencies. The three Hybrid III dummies have a mass of respectively 50, 77 and 100 kg, and a standing height of 1.52, 1.68 and 1.88 m. The ellipsoid multi-body dummy model consists of 37 rigid bodies, 37 kinematic joints, and 26 constitutive equations. These equations relate a force or moment to the relative motion in a kinematic joint, or between two points in general. The multi-body dummy model has 81 degrees of freedom. The dashboard, front interior, airbags and seat are modeled with finite elements, whereas the steering wheel, pedals, seat frame and belt system are represented by rigid bodies. Because of the constitutive relations and the discontinuous contact models, the system is non-smooth and highly nonlinear. The PRISM interior model with a 50th percentile Hybrid III dummy is depicted in Figure 2.4.

The responses from this model are filtered by Channel Frequency Class (CFC) filters. CFC filters are used to process the signals from the measurement data channels of a dummy device. Recommendations for each channel are given by the SAE Recommended Practice J211-1 document, issued by the Society of Automotive Engineers (SAE) (1995). The filters are designated by a number (60, 180, 600 or 1000), indicating the cut-off frequency of a 4th order, zero-phase Butterworth filter.

A number of vehicle crash pulses and measured responses from real-world crash tests is available to assess the quality of the reference model. The vehicle crash pulse, a_{veh} , used in this study is the forward acceleration signal measured at the vehicle's left B-pillar, filtered with a CFC60 filter. Since the focus lies on (high-speed) frontal impacts, it is chosen to use the results from EuroNCAP and US-NCAP frontal crash tests with the aforementioned supermini cars. Three of the available crash pulses are shown in Figure 2.5.

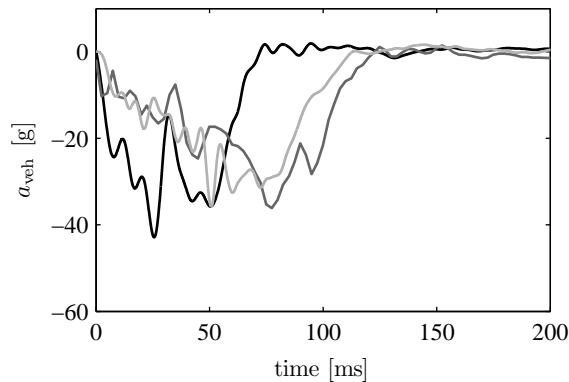


Figure 2.5 / Examples of crash pulses with small family cars, filtered with CFC60. They are obtained from the frontal impact protocols: USNCAP fixed rigid barrier FRB (black), EuroNCAP offset deformable barrier ODB (dark gray) and progressive deformable barrier PDB (light gray).

2.4.2 Quality of the Reference Model

The numerical Hybrid III ellipsoidal dummy is known to represent its physical counterpart properly, and good correlation results are found in component and sled tests (TNO Madymo B.V., 2005). The HIII dummies are well accepted in several standards (FMVSS 208, EVE-R94), and are widely used by global NCAP agencies. The quality of the PRISM model with these dummies is judged by comparing the responses with full scale impact tests. The results of a frontal EuroNCAP impact² with one of the aforementioned supermini cars are given in Figure 2.6, together with the results from the reference model. It shows good correlation for the responses of the chest region, and the head acceleration, a_{head} . Responses related to neck injury criteria are also shown in the figure. The neck axial compressive force, F_a is comparable, however, a mismatch in magnitude can be seen in the neck bending moment, M_y and neck shear force, F_s . Comparable results are found for simulations with other crash pulses, see also van der Laan

²64 km/h, 40% offset, offset deformable barrier (ODB)

et al. (2009a). Therefore, it is concluded that the numerical PRISM model has sufficient fidelity for the chest region, but the neck model has limited accuracy.

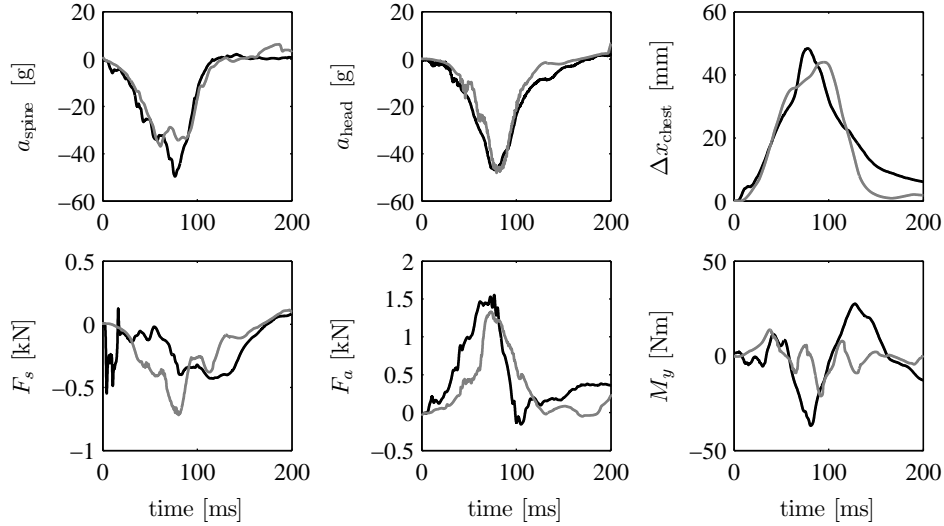


Figure 2.6 / Responses from the PRISM model (black) and real world crash data (gray) with a supermini car in a EuroNCAP full frontal ODB scenario. Responses are filtered with appropriate CFC filters.

2.4.3 Feedback Control of the Reference Model

In the reference model \mathcal{R} presented in Section 2.4.1, the belt restraint system still consists of a conventional load limiter. The occupant will therefore exhibit a different behavior than in the future controlled system. Or formulated in control engineering terms, the internal state of model \mathcal{R} is confined to a different region of the state space. The controller only has to be effective in the region associated with desired occupant behavior, and therefore, the control design model can be less complex. Namely, it does not have to be valid in the large region of the state space, in which the non-linear and non-smooth complex reference model is valid. Hence, it is desirable to analyze the reference model when it exhibits its more or less desired behavior, and derive \mathcal{D} based on this analysis.

This behavior is enforced by an output feedback or tracking controller, see Hesseling (2004). It is recognized that the use of a controller at this point might seem to be a paradox, since one of the research goals is to develop a low-order model, with which controllers can be designed. The controller thus merely serves to enforce the numerical reference model to exhibit a behavior that is close to the future desired behavior, such that the obtained design models are relevant.

A coupling between Matlab/Simulink[®] and MADYMO[®] is used to feedback control the reference model. The control input to the reference model is the belt force, F_{belt} , so the regular load limiter is replaced by a force actuator. From all the responses listed in Table 2.1, it is chosen to control one single output, viz. the spinal acceleration, a_{spine} , for reasons that will become clear in Section 2.4.4. The feedback controller, called local controller $\hat{\mathcal{K}}$, has to ensure that the spinal acceleration follows a more or less desired behavior, $a_{\text{ref}}(t)$. This profile is determined in the next paragraph. In Figure 2.7, a schematic diagram of the feedback controlled restraint system is given, with e the tracking error and a_{veh} the crash pulse.

Since a force is used to control an acceleration, the dominant dynamic low-frequency behavior can be represented by a gain. An integrative feedback controller may then result in a stable closed-loop system. It also introduces low-frequency amplification and high-frequency roll-off in the open-loop system, providing tracking performance, disturbance attenuation and numerical noise reduction of the closed-loop system. The controller function $\hat{\mathcal{K}} : e \mapsto F_{\text{belt}}$ thus reads

$$F_{\text{belt}}(t) = K \cdot \int e(t) dt \quad (2.4)$$

with K a constant.

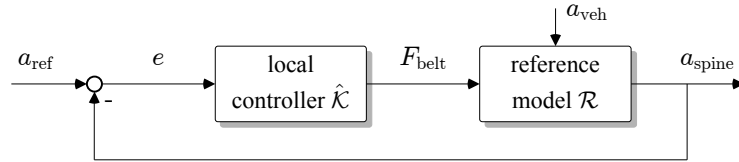


Figure 2.7 / Closed-loop feedback diagram of a controlled restraint system.

2.4.4 Setpoint for the Spinal Acceleration

In this paragraph, the setpoint a_{ref} for the spinal acceleration is presented. The response for the spinal acceleration will be optimal in terms of a minimum A_{max} value, when it equals a constant value, a_{opt} , throughout the duration of the crash. However, the difference between the spinal and vehicle acceleration determines the amount of relative spinal displacement, which is limited by the vehicle interior. This limited space results an upper bound for a_{opt} . Moreover, the spinal acceleration must initially have a (constant) negative slope, j_1 , necessary to limit the amount of backward motion of the occupant. Then, after time $t = t_1$, the acceleration will reach the value a_{opt} , and after time $t = t_2$, it has a constant positive slope j_2 before it reaches zero at time $t = t_3$. Such a profile is sketched in

the left diagram in Figure 2.8, and it can be described by

$$a_{\text{ref}}(t) = \begin{cases} -j_1 t & \forall t = [0, t_1] \\ -a_{\text{opt}} & \forall t = [t_1, t_2] \\ j_2(t - t_3) & \forall t = [t_2, t_3] \\ 0 & \forall t \geq t_3 \end{cases} \quad (2.5)$$

with $j_1 = t_1^{-1}a_{\text{opt}}$, and $j_2 = (t_3 - t_2)^{-1}a_{\text{opt}}$ for reasons of continuity. Additionally, it is required that the desired spinal velocity is zero at time $t \geq t_3$. Assuming that the initial spinal velocity equals the initial vehicle velocity v_o , the value of a_{opt} reads $a_{\text{opt}} = 2v_o(t_3 + t_2 - t_1)^{-1}$. The setpoint is thus fully characterized by three parameters, collected in vector $\mathbf{p} = [t_1 \ t_2 \ t_3]^T$. As mentioned, the upper bound of a_{opt} is dictated by constraints. To show this, define

$$\Delta x_{\text{ref}}(t) := \int_{\tau=0}^t \int_{\tau=0}^t (a_{\text{ref}}(\tau) - a_{\text{veh}}(\tau)) d\tau \quad (2.6)$$

So Δx_{ref} is the *desired* relative displacement of the lumbar spine with respect to the vehicle interior. The initial condition is chosen to be $\Delta x_{\text{ref}}(0) = 0$. An upper bound constraint on Δx_{ref} ensures that the front seat occupant is not moving too close to the steering wheel before the airbag deployment has been completed - causing even more severe injuries. A lower bound constraint prevents the occupant from being pushed backwards through the seat. The values of the bounds are given by $L_1 \leq 0$ and $L_2 \geq 0$, respectively. Finally, it is demanded that the jerks j_1 and j_2 are limited by $j_{\text{max}} > 0$ to obtain a more or less smooth profile, and the value t_3 is bounded by end time constraint T_e .

The optimal setpoint can be found by solving the following optimization problem

$$\begin{aligned} \min_{\mathbf{p}} \quad & a_{\text{opt}} \\ \text{subject to} \quad & L_1 \leq \Delta x_{\text{ref}}(t) \leq L_2 \quad \forall t = [0, t_3] \\ & j_{1,2} \leq j_{\text{max}} \\ & 0 < t_1 < t_2 < t_3 < T_e \\ & (2.5) - (2.6) \end{aligned}$$

for an arbitrary crash pulse $a_{\text{veh}}(t)$, with $t = [0, T_e]$.

The available space for ride-down of the occupant is about 0.30 m in this model, but since no airbag is used, a safe limit of 0.12 m is adhered to. Now the following parameters are used: $L_1 = 0$ m, $L_2 = 0.12$ m, $T_e = 0.15$ s, and $j_{\text{max}} = 2 \cdot 10^4$ ms⁻³. The results for $\Delta x_{\text{ref}}(t)$ and $a_{\text{ref}}(t)$ are shown in Figure 2.8 for a crash pulse a_{veh} that originates from a EuroNCAP crash test with a small passenger car, i.e. 40% ODB frontal impact at 64 km/h (40 mph). The crash pulse is shown as a gray line in the left diagram in Figure 2.8. The optimal solution is given by $\mathbf{p} = [49 \ 111 \ 123]^T$ ms, and $a_{\text{opt}} = 22.9$ g.

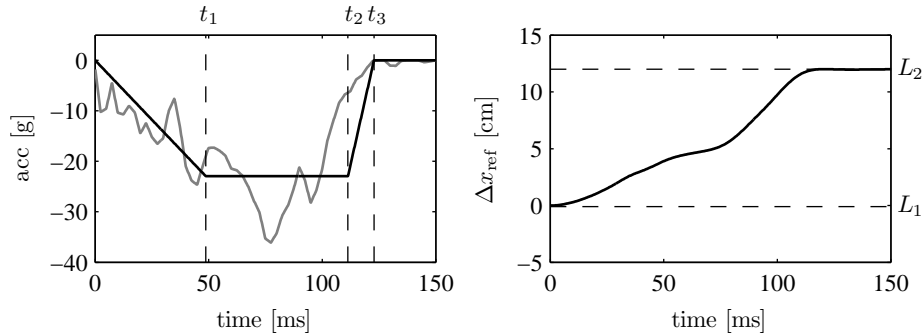


Figure 2.8 / Setpoint a_{ref} (top, black) for a crash pulse a_{veh} (gray, left), and the relative desired chest displacement $\Delta x_{\text{ref}}(t)$ (black, right).

2.4.5 A Simulation Example

A simulation is performed with the closed-loop configuration as sketched in Figure 2.7. The airbags in the reference model are disabled, as argued when defining the system boundary in Section 2.2. The crash pulse from Figure 2.8 acts as a disturbance on the system, and the setpoint is given by a_{ref} , as derived above. The controller $\hat{\mathcal{K}}$ in (2.4) with $K = 5.0 \cdot 10^5$ gave sufficient closed-loop performance and disturbance rejection.

The results of a closed-loop simulation with the reference model \mathcal{R} is presented in Figure 2.9. The left diagram in Figure 2.9 shows the controlled spinal acceleration, and the right diagram shows the belt force required to track the setpoint. The setpoint is tracked accurately and the system exhibits the desired controlled behavior. Note that almost 10 kN is used during a short period of time to control the chest acceleration. This value is fairly high compared to current load limiter values (4-6 kN).

The value K of controller $\hat{\mathcal{K}}$ had to be carefully tuned: a small decrease led to insufficient performance (tracking error), while a small increase led to instability (unbounded output on bounded input). It implies that this controller does not achieve robustness to a (slightly) varying system gain. Moreover, the entire control strategy is not useful here: the parameter vector \mathbf{p} to construct the setpoint can only be obtained with *a priori* crash information, which is obviously not available in a real-world crash event. In Chapter 3, a control strategy is presented that does not require *a priori* knowledge of the crash.

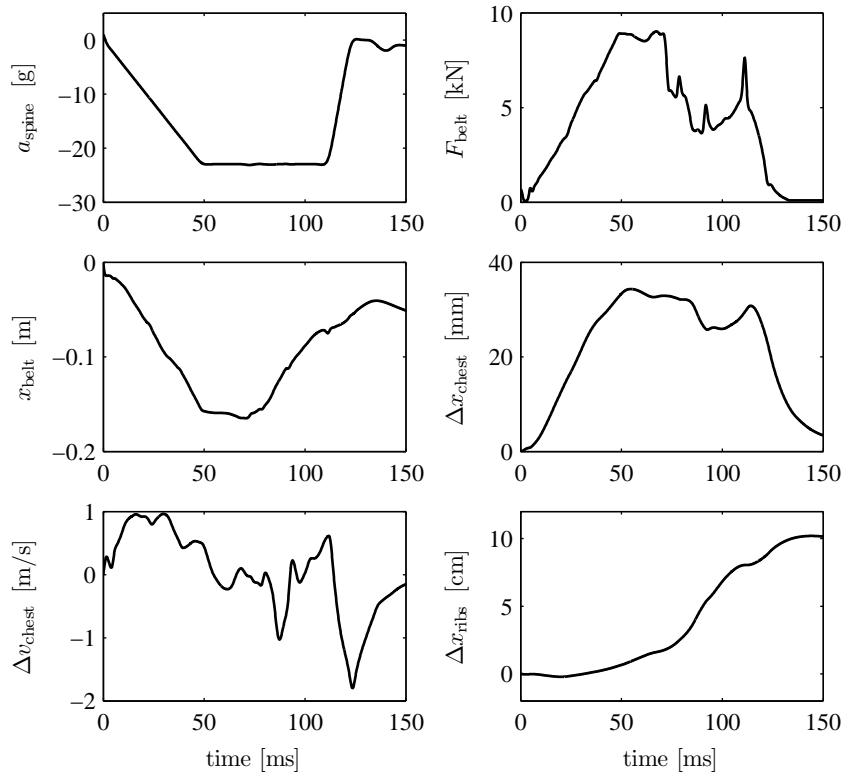


Figure 2.9 / Closed-loop simulation results with the reference model, filtered with appropriate CFC filters.

2.4.6 Conclusion

In this section, a reference model \mathcal{R} is presented that can be used to simulate a real-world frontal crash event. It has been shown that the model has sufficient fidelity to the real world, and thoracic injury responses of a belted occupant can be accurately predicted. The model is put into a feedback control configuration, and this was used to enforce a behavior of the model that is close to the future desired behavior. Therefore, it is concluded that the reference model is suitable for the intended modeling purposes.

2.5 Sensitivity Analysis

This section presents a sensitivity analysis, that is used to identify the most relevant elements in the reference model. With the results of this analysis, the design model can be constructed.

2.5.1 Method

Formally, the notion sensitivity analysis (SA) is used to determine the sensitivity of a target function (a model output) on the input factors, i.e the elements in a complex system that are uncertain or of interest (Saltelli et al., 2004). The model outputs are the six responses listed in Table 2.1. The input factors for the SA are the kinematic and dynamical components of the reference model, more specifically: (i) the degrees of freedom of the joints, (ii) the constitutive equations that describe the stiffness and damping characteristics, (iii) the contact interaction models and (iv) the belt system. Occupant characteristics like mass of the bodies, stature, and posture do not belong to the input factors, as they can directly be implemented in the design model.

The perturbed reference model is indicated by $\hat{\mathcal{R}}$. Simulations with $\hat{\mathcal{R}}$ will not be performed in the closed-loop configuration as in Section 2.4.3, since the feedback controller will smooth out the introduced modifications in the model by modifying F_{belt} . Instead, open-loop simulations are carried out with the obtained belt force F_{belt} from Figure 2.9 and the vehicle acceleration a_{veh} from Figure 2.8. This is referred to as the *nominal scenario*. The perturbed outputs, $\hat{\mathbf{y}}$, of $\hat{\mathcal{R}}$ are compared to the nominal responses, \mathbf{y} , and the perturbation vector $\eta(t) = \mathbf{y} - \hat{\mathbf{y}}$ is analyzed, see Figure 2.10.

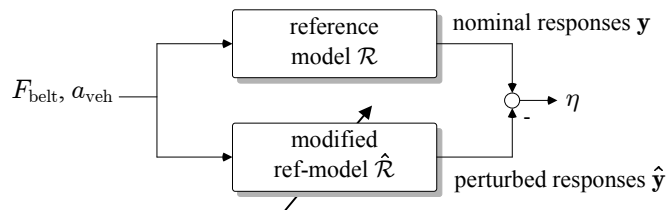


Figure 2.10 / The sensitivity analysis is performed by comparing open-loop responses of the nominal and perturbed reference model.

As target functions, the 2-norm and ∞ -norm on the perturbation signal are used (Skogestad and Postlethwaite, 2005)

$$\|\eta_i\|_2 = \sqrt{\int_{t=0}^{T_e} \eta_i^2(t) dt}, \quad \|\eta_i\|_\infty = \sup_{t \in [0, T_e]} |\eta_i(t)|$$

with T_e the duration of the simulation, and η_i the i^{th} component of column vector η . To draw conclusions on the sensitivity of the target function on the input factors, limit values are defined for every element of $\|\eta\|_\infty$ and $\|\eta\|_2$. These limit values indicate whether a modification perturbs the model outputs insignificantly, so whether or not this modification has to be implemented in the design model.

2.5.2 Results

Degrees of freedom

Since the dummy model is symmetrical and only frontal crashes are considered, it is expected that a 2D model can produce sufficiently accurate injury responses. The influence of the asymmetry of the belt is hereby ignored. Furthermore, it is expected that some of the degrees of freedom in the extremities will not largely influence the thoracic and neck responses. Based on these two assumptions, the total number of degrees of freedom of the multi-body dummy in the reference model, 81, can be drastically reduced.

In the sensitivity analysis of the reference model, individual joints *and* combinations of joints are locked or unlocked and the perturbation signals are evaluated. Adhering to the limit values, a combination of joints is found which is believed to be essential for occupant modeling in frontal impact. For example, it follows that the leg (arm) can not be taken as a single body, since the freedom in the knee (elbow) joint significantly influences all target functions. Moreover, two neck joints are required to allow a forward translation of the head. In the left column of Table 2.2, the 11 joints are shown that need to be included to obtain norm values below the limit values. In the right column, the 11 rigid bodies are shown that are connected by these joints. Since some bodies are lumped, the combined centers of mass, and moments of inertia wrt their center of mass have to be calculated (Steiner's rule).

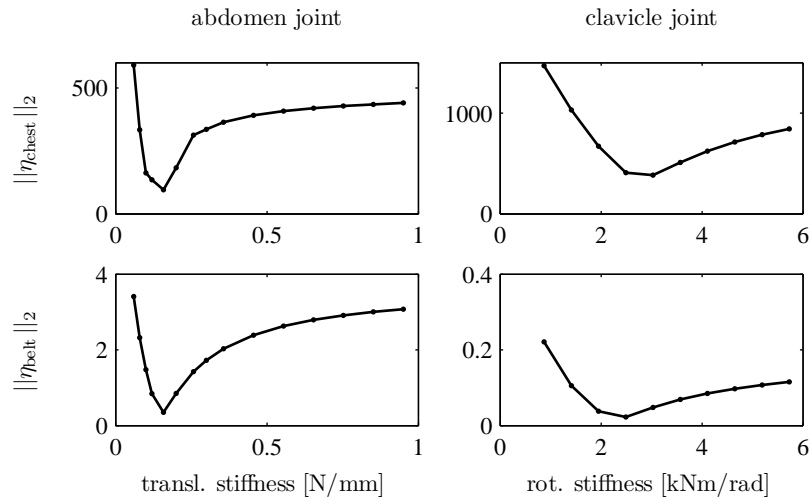
Constitutive relations

After locking several joints, a total of 15 out of 26 constitutive relations remain. Most of them are nonlinear and nonsmooth, sometimes with hysteresis. It is found that removing 6 relations did not violate the norms on the target function. The remaining 9 relations could be replaced with linear, smooth relations, without violating the norm limits. As an example of this procedure, an analysis is performed for the constitutive relations of the abdomen and clavicle joints. The nonlinear relations in these joints are replaced by a linear stiffness with a constant coefficient. The reference model is evaluated for different values of the stiffness and the distribution of the target function is computed. Figure 2.11 shows the 2-norms for the spinal acceleration and belt rollout, $\|\eta_{\text{chest}}\|_2$ and $\|\eta_{\text{belt}}\|_2$ respectively. The

Table 2.2 / Essential joints and body parameters.

Joint	Type	Body	Mass [kg]	Mom. of inertia [10^{-3} kgm ²]
Knee	revol.	Tibia	12.53	426
Hip	spherical	Femur	14.80	217
Abdomen	transl.	Pelvis	17.96	104
Elbow	universal	Abdomen	0.64	10.0
Clavicle	universal	Spine	12.86	140
Ribs	free	Ribs	1.50	20.0
Lumbar spine	revol.	Upper arm	8.18	82.4
NeckPivot	revol.	Lower arm	4.62	91.6
NeckOC	revol.	Neck	0.93	22.1
Attachment	free	Head	4.41	5.16
Actuator	transl.	Actuator	0.01	0.00

lowest error values are obtained with a stiffness of 0.15 N/mm for the abdomen and 3 kNm/rad for the clavicle joint. It is also shown that the responses are very sensitive to the abdomen stiffness. This analysis is performed for all constitutive models, resulting in a modified reference model with only 7 linear constitutive relations. Note that this analysis is, at least, only valid for this crash scenario.

**Figure 2.11** / The 2-norm of η_{chest} and η_{belt} for different values of the abdomen and clavicle joint stiffness.

Contact models

The contact models are largely responsible for the non-smoothness of the system. Additionally, the force-penetration characteristics consist of nonlinear relations with hysteresis. Several contact models are removed or modified to investigate the influence on the dummy behavior. In the considered scenario, the following contacts are disabled: arms-dashboard, feet - lower board, knees-knee bolsters, head-steer, and head-headrest. It is found that 7 remaining contacts are essential in the reference model. Replacing the nonlinear force-penetration relations in these contact models by an linear stiffness and damping with appropriate constant values, did only slightly violate the limits on the error norms. Despite of the slight violation, it is chosen to proceed with these constant values.

The seat belt

The belt stiffness in the reference model is modeled by a nonlinear force-elongation function with hysteresis. Additionally, a friction function is defined between the belt and the buckle, in the D-ring, and on certain locations on the dummy. A sensitivity analysis revealed that the model outputs are sensitive to perturbations in the friction coefficient in the D-ring and buckle. Altering these friction forces largely affects the responses. So the buckle and D-ring friction are included in the design model. Replacing the nonlinear belt characteristics by a linear stiffness of 124 kN/m and a linear damping of 100 Ns/m did only slightly effect the output responses, so the error norms stayed within limits.

2.5.3 Conclusion

A sensitivity analysis is performed that consisted of individual modifications in the reference model \mathcal{R} , and these modifications were subsequently combined. The combined modifications led to a simplified reference model $\hat{\mathcal{R}}$, with output responses that only slightly violated the error norms. The proposed sensitivity analysis method is more attractive than a straightforward optimization of the parameters, since this would be very time-consuming given the complexity of the model, and it would likely result in local minima during the optimization.

The sensitivity analysis made clear that a 2D dummy model with 11 bodies, 11 joints and 14 degrees of freedom generates a perturbation on the nominal responses, of which the 2-norm and ∞ -norm were within predefined limits. Moreover, most of the 17 constitutive equations for the joints, contact models and belt characteristics can be replaced by linear relations. It is emphasized that the conclusions of this analysis only hold for the Hybrid III 50th percentile dummy used in the PRISM reference model, for a specific crash pulse, an *a priori* determined belt force and the chosen target functions.

2.6 The Design Model

A design model, \mathcal{D} , is constructed that is able to generate the responses, listed in Table 2.1, in close agreement with the reference model responses. In this section, the results from the sensitivity analysis are employed to derive a low-order, 2D multi-body dynamical occupant model, with a seat belt, that represents a Hybrid III dummy.

2.6.1 The Occupant Model Parameters

In Figure 2.12, the locations of the body, joints and contacts are shown, together with the seat belt arrangement, the seat and floor board. The large circles represent the centers of gravity of the bodies, and small white circles the joints. The 6 contact models are illustrated by Kelvin elements. The output variables from \mathbf{y} and the input variables from \mathbf{w} are indicated, together with the neck injury responses F_a , F_s and M_y . The coordinate frame is a Cartesian frame $\{O, \vec{e}\}$, with $\vec{e} = [\vec{e}_1 \ \vec{e}_2]^T$ a column of two orthogonal vectors of unit length. In this layout, the vehicle displacement during impact, $x_{\text{veh}}(t)$, is forced upon the seat, belt attachment points and floor board.

The parameters of the 11 bodies in the design model concerning the mass and moment of inertia are directly obtained from the parameters of the reference model, see Table A.1. The centers of gravity of the bodies have an identical initial position as they have in the reference model. Each body has one degree of freedom, except from the ribs body, which has two translational degrees of freedom. With two additional degrees of freedom to position the system with respect to the cartesian coordinate frame, the model has 14 degrees of freedom in total. These generalized coordinates are stacked in a vector $\mathbf{q} = [q_1 \ \dots \ q_{14}]^T$ and their locations are shown in Figure A.1. The model dimensions are illustrated in Figure A.1, and their values are listed in Table A.2.

The joints in the design model are listed in Table 2.2, and they are modeled as kinematically ideal. The joint constitutive relations are implemented as Kelvin elements, with constant stiffness and damping coefficients k and d .

Concerning the contact models, contact is assumed throughout the crash. In this way, the functions in the contact model are made continuous. However, for the contact between occupant's thorax and the seat back, the occupant loses contact with the seat approximately during the second half of the crash. This contact model is therefore made one-sided.

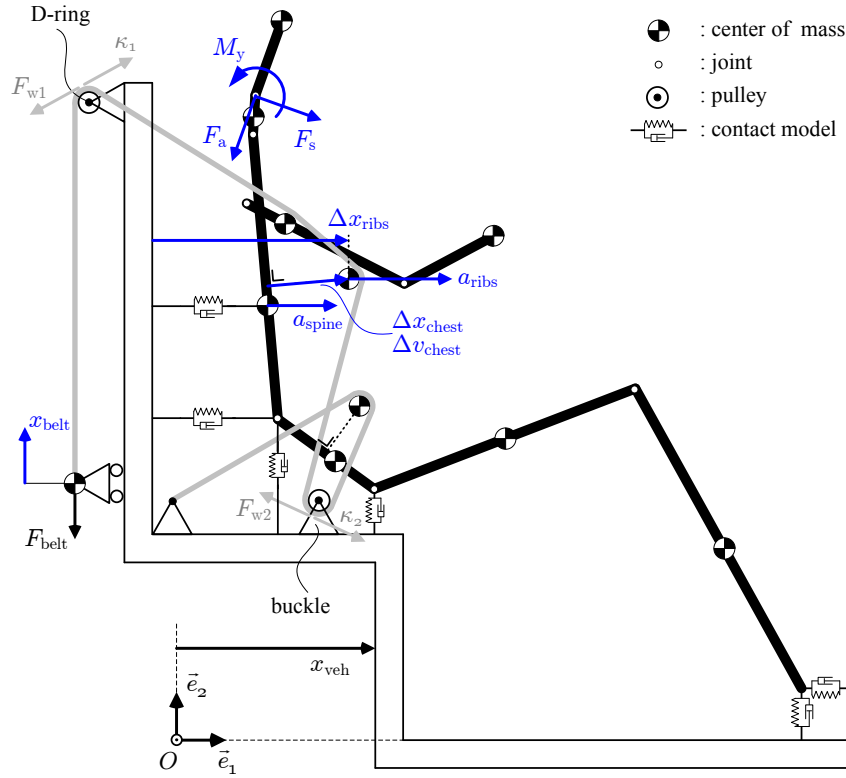


Figure 2.12 / Representation of the initial position of the multi-body design model.

2.6.2 The 3-point Safety Belt

Since the occupant model is two dimensional, the safety belt has also to be represented in two dimensions. The belt runs over rotating pulleys from the actuator body to the D-ring, clavicle, rib, buckle, abdomen and is rigidly connected to the vehicle at the anchor point, see Figure 2.12. The locations of the D-ring, the buckle and the anchor are taken from the reference model. As mentioned earlier, only the D-ring and buckle include friction, given by friction forces F_{w1} and F_{w2} , respectively. The friction forces are defined by the following friction model, see TNO Madymo B.V. (2005):

$$\begin{aligned} F_{w1} &= \text{sgn}(\dot{\kappa}_1) F_{\text{belt}} (1 - e^{-\mu \alpha_1}) \\ F_{w2} &= \text{sgn}(\dot{\kappa}_2) F_{\text{belt}} (1 - e^{-\mu \alpha_2}) e^{-\mu \alpha_1} \end{aligned} \quad (2.7)$$

with $\mu = 0.1$ the friction coefficient, $\kappa_{1,2}(\mathbf{q})$ the displacement of the belt relative to the surface of the D-ring and buckle pulley, $\alpha_{1,2}$ the wrapped angle of the

belt over the pulley, and sgn the signum function. The value of $\alpha_{1,2}$ can be estimated from the reference model. As the variations in $\alpha_{1,2}$ are relatively small and approximately equal, they have been given a fixed value $\alpha_{1,2} = 2.5$ rad, hence $|F_{w1}| = 0.22|F_{\text{belt}}|$, and $|F_{w2}| = 0.17|F_{\text{belt}}|$. To represent the mechanical properties of the belt, a Kelvin element is used with a stiffness $k = 124$ kN/m and a damping coefficient $d = 100$ Ns/m, as given in Section 2.5.2.

2.6.3 Equations of Motion

The Euler-Lagrange's approach, see e.g. Schiehlen (1990), is used to obtain the equations of motion. The Euler-Lagrange equations read

$$\frac{d}{dt} \left(T_{,\dot{\mathbf{q}}} \right) - T_{,\mathbf{q}} + V_{,\mathbf{q}} = (\mathbf{Q}^{\text{nc}})^T \quad (2.8)$$

with

- $T(t, \mathbf{q}, \dot{\mathbf{q}})$ the kinetic energy,
- $V(\mathbf{q})$ the total potential energy function,
- $\mathbf{Q}^{\text{nc}}(\mathbf{q}, \dot{\mathbf{q}}, F_{\text{belt}})$ the vector of generalized forces, and
- the subscript $_{,\mathbf{q}}$ means derivative with respect to vector \mathbf{q} .

The absolute position and rotation vectors of the center of mass of the 11 bodies are given in the Cartesian coordinate frame by vectors $\mathbf{r}_i(\mathbf{q})$ and $\theta_i(\mathbf{q})$, respectively, for $i = 1, \dots, 11$. The total kinetic energy T is given by the scalar

$$T(\mathbf{q}, \dot{\mathbf{q}}, x_{\text{veh}}, \dot{x}_{\text{veh}}) = \frac{1}{2} \sum_{i=1}^{11} m_i \dot{\mathbf{r}}_i^T \dot{\mathbf{r}}_i + I_i \dot{\theta}_i^T \dot{\theta}_i$$

with m_i the mass and I_i the moment of inertia of each body i . The potential energy function V is the sum of the internal and the potential energy. So

$$V(\mathbf{q}) = g \sum_{i=1}^{11} m_i \bar{\mathbf{r}}_i^T \bar{\mathbf{e}}_2 + \frac{1}{2} \sum_{j=1}^{17} k_j \varepsilon_j^2$$

with $\varepsilon_j(\mathbf{q}, \mathbf{q}_o)$ relative displacements corresponding to the constitutive equations $j = 1, \dots, 17$. Here, k_j is the stiffness in this constitutive equation, and g the gravity constant.

Thirdly, the generalized, nonconservative forces consist of the externally applied force, F_{belt} , the friction forces, $F_{w1,2}$, and the damping forces. The damping force is given by $-d_j \dot{\varepsilon}_j$, and the virtual work by $-(d_j \dot{\varepsilon}_j) \delta \varepsilon_j$ with d_j the damping

coefficient. Given that the virtual work by the generalized damping forces is given by $(\mathbf{Q}_d^{\text{nc}})^T \delta \mathbf{q}$, the generalized damping force equals

$$\mathbf{Q}_d^{\text{nc}}(\mathbf{q}, \dot{\mathbf{q}}) = - \sum_{j=1}^{17} (d_j \dot{\varepsilon}_j) \left(\frac{\partial \varepsilon_j}{\partial \mathbf{q}} \right)^T$$

The friction forces $F_{w1,2}$ from (2.7) apply a virtual work to the pulleys, given by $F_{w1,2} \delta \kappa_{1,2}$. Note that κ is the relative displacement of the belt with respect to the pulley. The generalized, nonconservative friction force is hence given by

$$\mathbf{Q}_f^{\text{nc}}(\mathbf{q}, F_{\text{belt}}) = \sum_{j=1}^2 F_{wj} \left(\frac{\partial \kappa_j}{\partial \mathbf{q}} \right)^T$$

Finally, the applied force F_{belt} works on the belt actuator body with coordinate q_{13} , as shown in Figure A.1, so

$$\mathbf{Q}_u^{\text{nc}}(F_{\text{belt}}) = [0 \quad \dots \quad 0 \quad 1 \quad 0]^T F_{\text{belt}}$$

The total nonconservative forces are now a summation of the parts as

$$\mathbf{Q}^{\text{nc}}(\mathbf{q}, \dot{\mathbf{q}}, F_{\text{belt}}) = \mathbf{Q}_d^{\text{nc}}(\mathbf{q}, \dot{\mathbf{q}}) + \mathbf{Q}_f^{\text{nc}}(\mathbf{q}, F_{\text{belt}}) + \mathbf{Q}_u^{\text{nc}}(F_{\text{belt}})$$

The output \mathbf{y} , given in Table 2.1 and (2.3), is formulated in terms of generalized coordinates \mathbf{q} and $\dot{\mathbf{q}}$, and the vehicle acceleration a_{veh} .

The Euler-Lagrange equation in (2.8) is derived symbolically. The symbolic approach allows optimization of uncertain or unknown parameters, and it facilitates a linearization of the equations. The nonlinear, non-autonomous system is described by the following nonlinear, second order ordinary differential equations:

$$\begin{aligned} \ddot{\mathbf{q}}(t) &= \mathbf{f}(\mathbf{q}(t), \dot{\mathbf{q}}(t), \mathbf{w}(t)) \\ \mathbf{y}(t) &= \mathbf{g}(\mathbf{q}(t), \dot{\mathbf{q}}(t), \mathbf{w}(t)) \end{aligned} \tag{2.9}$$

with $\mathbf{y} \in \mathbb{R}^6$ as defined in (2.3), $\mathbf{w} \in \mathbb{R}^2$ as in (1.4), and with $\mathbf{q}, \dot{\mathbf{q}} \in \mathbb{R}^{14}$, and the nonlinear vector functions $\mathbf{f} : (\mathbb{R}^{14} \times \mathbb{R}^{14} \times \mathbb{R}^2) \mapsto \mathbb{R}^{14}$ and $\mathbf{g} : (\mathbb{R}^{14} \times \mathbb{R}^{14} \times \mathbb{R}^2) \mapsto \mathbb{R}^6$. The initial conditions are defined by $\mathbf{q}(0) = \mathbf{q}_o$ and $\dot{\mathbf{q}}(0) = \mathbf{0}$, and their values are given in Table A.2.

2.7 Validation

In this section, simulations with the design models are performed, and the models are validated by comparing the results with the results of the reference models. This is done for different crash pulses and dummy sizes.

2.7.1 Results for the Nominal Scenario

The crash pulse a_{veh} and seat belt force F_{belt} that were used throughout Section 2.4.4-Section 2.5, are chosen as the input to the design model. The equations of motions in (2.8) are solved with these inputs and the earlier mentioned initial conditions, $\mathbf{q}(0) = \mathbf{q}_o$ and $\dot{\mathbf{q}}(0) = \mathbf{0}$, from Table A.2. The output responses in Figure 2.13 show that there is good agreement in spinal acceleration, considering the low complexity of the design model. The chest compression and VC criterion are also very well reproduced. The position of the occupant, Δx_{ribs} differs slightly from 80 ms and onwards.

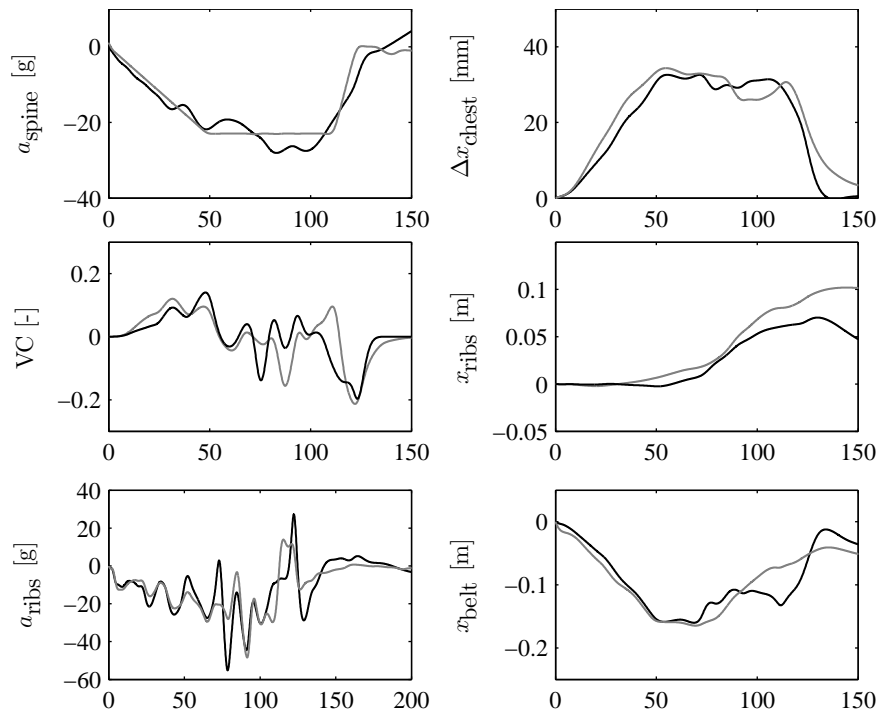


Figure 2.13 / Responses of the 50%-ile reference model (gray) and design model (black) in a 40% ODB frontal impact at 64 km/h (40 mph).

With respect to the measurable outputs, the belt rollout x_{belt} is accurate until 50 ms. This is most likely caused by the different loading and unloading paths in the belt characteristics function, which is not implemented in the design model. Although this effect was not clear from the sensitivity analysis, the results shown here indicate that the ribs displacement is very sensitive to the belt rollout. The sternum acceleration responses a_{ribs} are similar in timing and magnitude.

In Figure 2.14, an elementary 2D representation is given of both design and reference model at time instances $t = 0, 30, 60, \dots, 150$ ms. From this figure, it seems that the lower part of the body does hardly move until 60 ms, but all injury predictors have their maximum value at this point in time. So the seat belt allows only small displacements up till this point, will exerting high loads on the body. When these loads reach their maximum value, the belt restraint load is lowered, and the dummy is allowed to move forward. The nonlinearities in the reference model are likely to be a result of the geometry. Hence, it can be expected that a linearization of the model will give good results.

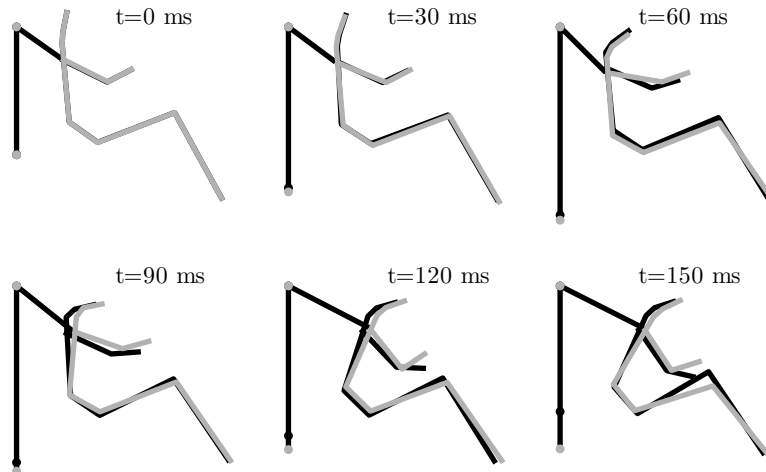


Figure 2.14 / Impression of the position of the design model bodies (gray) and the reference model bodies (black) at 6 time instances.

2.7.2 Results for Neck Injury Criteria

It has been shown that the thoracic injury responses are accurately reproduced by the design model. This indicates that the design model captures the relevant phenomena of a crash event. Therefore, it is investigated here whether neck injury criteria could also be predicted with this design model, although these criteria are not used in the proposed CRC system. The neck injury criterion N_{ij} is generally

accepted to be most relevant criterion in frontal impacts, specifically the tension-flexion (t-f) and tension-extension (t-e) loading condition (Eppinger et al., 1999). The injury predictor is defined as

$$N_{ij} := \max_t \left(\left| \frac{M_y(t) - 0.01778F_s(t)}{M_{yc}} \right| + \left| \frac{F_a(t)}{F_{zc}} \right| \right)$$

in which F_a , F_s and M_y are the neck axial force, the neck shear force and the neck bending moment in the occipital condyle. These 3 outputs are indicated in Figure 2.12. The constants M_{yc} and F_{zc} are dummy dependent, and their values can be found in FMVSS 208 regulations, see (NHTSA, 1998). The results for these two criteria are shown in Figure 2.15 for the design model in the nominal scenario. The injury responses are plotted over time and compared to the reference model responses, and the results show that the responses have similar maxima and timing.

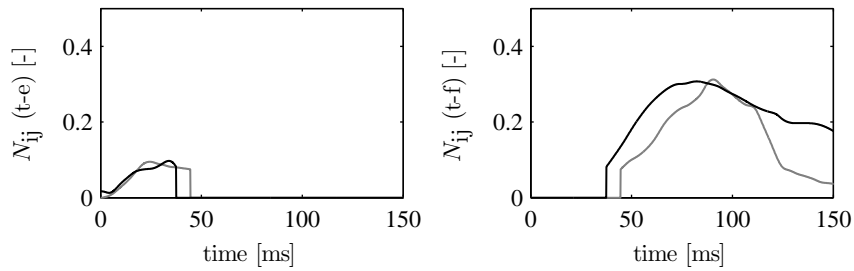


Figure 2.15 / The neck injury criteria N_{ij} of the 50%-ile reference model (gray) and design model (black) in a 40% ODB frontal impact at 64 km/h (40 mph).

2.7.3 Results for Different Frontal Impacts

The specific responses and the overall behavior of the dummy in the design model are comparable to those of the reference model, at least for the nominal scenario. This may be an indication that the design model is a correct simplification of the reference model in that scenario. To validate the model in other scenarios, simulations with 35 different crash pulses are carried out. The pulses are obtained from crashes of a supermini against various barriers, cars and trucks. The initial speed v_o ranges between 10 and 27 ms^{-1} (36 - 100 km/h), and the time at which the minimum vehicle velocity was reached, t_{end} , ranged between 93 and 155 ms.

For every crash pulse a_{veh} , the optimal behavior, i.e. the reference trajectory a_{ref} , is computed according to the method presented in Section 2.4.4. A closed-loop simulation is performed with the reference model to determine the control effort

F_{belt} . This belt force and its corresponding a_{veh} are then applied to the design model, see Figure 2.16.

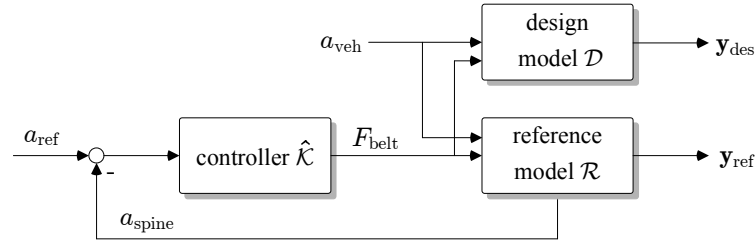


Figure 2.16 / Design model responses are evaluated in *open-loop*, with the input from a *closed-loop* reference model simulation.

In Figure 2.17, the responses from the reference model, y_{ref} , and the design model, y_{des} are compared. It shows the results of a USNCAP crash scenario (56 km/h, 100% overlap, rigid barrier (RB)). As can be observed, the injury responses differ slightly in magnitude, but they are again predicted quite well by the design model. The sternum displacement, however, differs substantially (maximum 4.6 cm), as well as the belt rollout.

The results of the design and reference model for all 35 scenarios are calculated for the same responses as shown in Figure 2.13 and Figure 2.17. A comparison is made with a method called the objective rating tool (Twisk et al., 2007). It uses the time history signals from two systems, usually a real-world crash and a CVS model, and applies rating criteria. These criteria are the Global Peak Value (GPV), the Global Peak Time (GPT) and the Weighted Integrated Factor Method (WiFac), and they use the complete time history of the signals. The GPV and GPT are a measure in which the peak amplitude and the timing of the peak amplitude are compared, respectively. WiFac is a measure of the difference area between two signals.

The criteria are determined for all simulation results, and the outcome is shown in Table 2.3. Generally, these ratings are only applied to responses that are part of IC's. Here, the objective rating tool is also applied to x_{belt} , and x_{ribs} , but since their peak value are of no importance, the GPV and GPT are not determined. The criteria values in the table show that, given the range of impact speeds and crash durations, the overall results are satisfactory. Only the relative displacement of the sternum, Δx_{ribs} , is not well predicted, as was also clear from the figures presented earlier.

Although the amount of test data was limited (35 frontal impact crashes), it is concluded that the developed model is able to predict the basic neck and chest injury trends in many types of high-speed frontal crashes.

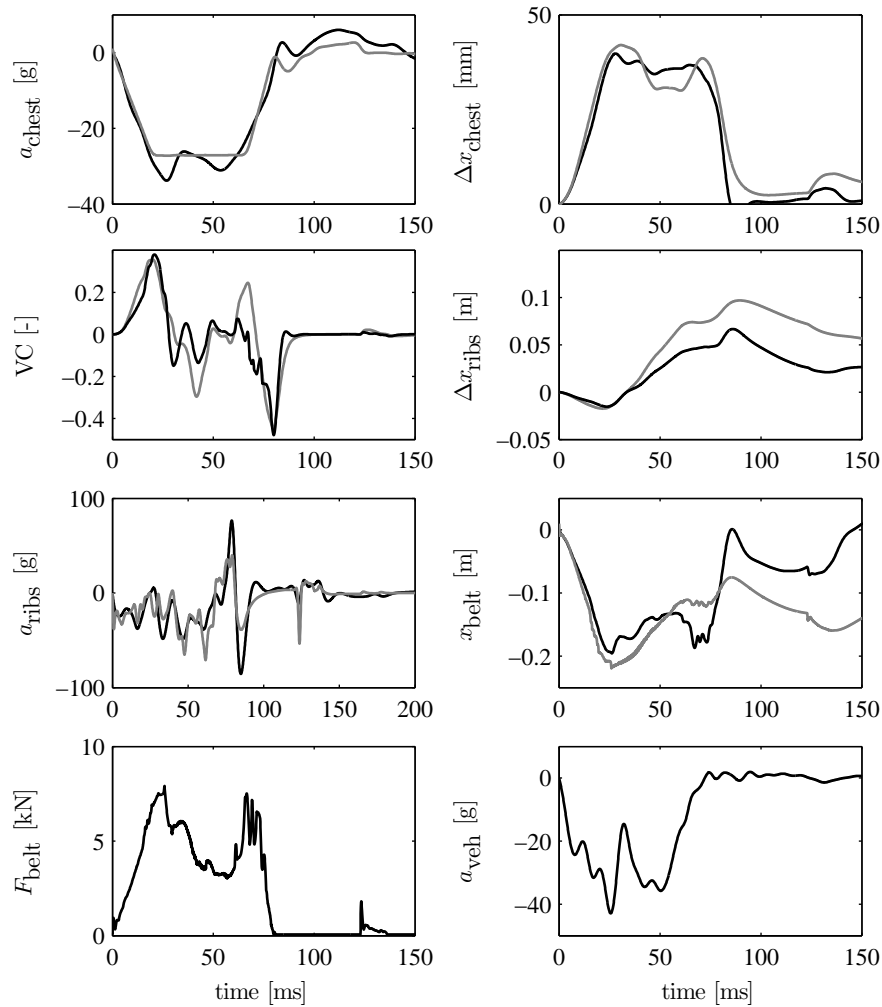


Figure 2.17 / Responses of the 50%-ile reference model (gray) and design model (black) in a RB impact at 56 km/h (35 mph).

2.7.4 Results for 5 and 95 %-ile Hybrid III Dummies

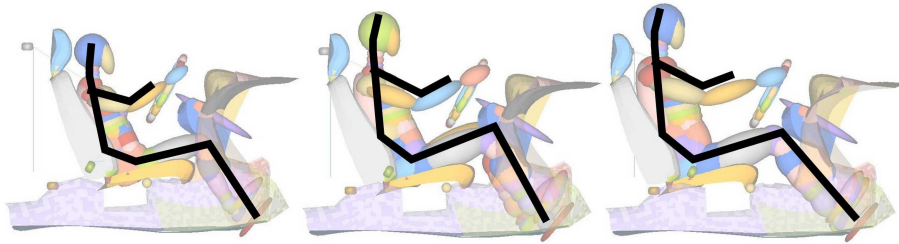
The design model is sufficiently accurate for the 50th %-ile dummy, in terms of prediction of the thoracic injury responses, neck injury responses and measurement responses. To investigate whether this is also the case for other dummies, the average occupant dummy is modified to represent the small female and large male dummy, i.e. the 5%-ile and 95%-ile Hybrid III dummy. These two dummies are

Table 2.3 / Objective Rating Results

response	GPV [%]		GPT [%]		WiFac [%]	
	mean	std	mean	std	mean	std
a_{spine}	86	5	88	9	97	3
Δx_{chest}	93	5	89	13	90	7
Δv_{chest}	85	12	67	22	87	9
VC	70	20	66	18	76	16
$N_{ij} \text{ (t-f)}$	83	8	95	3	75	11
$N_{ij} \text{ (t-e)}$	87	11	96	4	71	10
Δx_{ribs}					67	30
x_{belt}					79	4

settled in the small family car interior from the PRISM project, but the seat position is slightly adapted. This will make the hands fit on the steering wheel, and makes that there is sufficient space for the ride-down of the dummy. The setpoints $a_{\text{ref}}(t)$ are adapted in accordance with the ride-down space, and closed-loop simulations with this modified reference model are performed.

The design model is also modified as follows. The values of the masses, moments of inertia, location of the joints, centers of gravity etcetera can directly be calculated from the reference models. The dimensions, masses and initial positions are listed in Table A.1 and Table A.2. The resulting geometries are shown in Figure 2.18.

**Figure 2.18** / Simplified representation of the 5%-, 50%- and 95%-ile design and reference model.

Next, the constitutive relations in the 5%-ile and 95%-ile reference models are compared to the relations of the 50%-ile dummy model. Based on this, a number of parameters values had to be adjusted, and their values are shown in Table 2.4. It indicates that all values are scaled, except for the damping values of the abdomen, clavicle and neckOC joint. The contact models are unchanged.

Results are shown in Figure A.2(a) and Figure A.2(b). For the 5%-ile and 95%-ile dummies, the spinal acceleration and belt displacement are well approximated, considering the difference in complexity of the models. Also the other injury criteria have similar trends in the time domain. Based on these results, it is concluded that these modified design models also mimic their complex counterparts very satisfactorily. It is emphasized that they are obtained by a relatively easy scaling of the Madymo dummies.

Table 2.4 / Modified constitutive relations (joints) of the design models in SI units

Joint	5%-ile		50%-ile		95%-ile	
	k	d	k	d	k	d
Abdomen	1.0e5	2.0e2	1.5e5	2.5e2	1.0e5	2.6e2
Ribs (x-dir)	1.2e5	4.0e2	2.2e5	6.0e2	2.4e5	8.0e2
Ribs (y-dir)	1.2e5	7.8e2	1.2e5	1.2e3	1.2e5	4.4e3
NeckPivot	1.5e2	1.5	2.3e2	2.5	2.5e2	4.0
NeckOC	1.0e2	1.0	1.6e2	10	2.0e2	1.0

2.8 The Linear Time Invariant Model

In the previous sections, three nonlinear design models \mathcal{D} have been constructed that capture the control-relevant dynamics of \mathcal{R} . As shown in Figure 2.3 in Section 2.3.2, the next step is to approximate \mathcal{D} with linear models, \mathcal{P} .

2.8.1 Linearization by a Taylor Expansion

The three different design models \mathcal{D} represent an average sized dummy, and two extreme dummy sizes, and the models are described by the nonlinear differential equations given in (2.9). Now define a state vector \mathbf{x} as follows $\mathbf{x}(t) := [\mathbf{q}^T(t) \ \dot{\mathbf{q}}^T(t)]^T$ and $\mathbf{x}_0 := [\mathbf{q}_0^T \ \mathbf{0}^T]^T$. With these definitions, the design model from (2.9) can be rewritten in the following standard state space form

$$\begin{aligned} \dot{\mathbf{x}}(t) &= \mathbf{f}_i(\mathbf{x}(t), \mathbf{w}(t)), & \mathbf{x}(0) &= \mathbf{x}_0 \\ \mathbf{y}(t) &= \mathbf{g}_i(\mathbf{x}(t), \mathbf{w}(t)) \end{aligned} \tag{2.10}$$

in which $\mathbf{x} \in \mathbb{R}^{28}$, $\mathbf{y} \in \mathbb{R}^6$, $\mathbf{w} \in \mathbb{R}^2$, $\mathbf{f}_i : \mathbb{R}^{28} \times \mathbb{R}^2 \mapsto \mathbb{R}^{28}$ and $\mathbf{g}_i : \mathbb{R}^{28} \times \mathbb{R}^2 \mapsto \mathbb{R}^6$. The function subscript $i \in \{1, 2, 3\}$ denotes the dummy type, i.e. the 5, 50 and 95 %-ile dummy respectively. Suppose the functions \mathbf{f}_i and \mathbf{g}_i are infinitely differentiable. Then it follows from Taylor's theorem that near a certain state

trajectory $\bar{\mathbf{x}}(t)$ and input trajectory $\bar{\mathbf{w}}(t)$, the functions can be approximated by the following power series

$$\begin{aligned} \mathbf{f}_i(\mathbf{x}, \mathbf{w}) &\approx \mathbf{f}_i(\bar{\mathbf{x}}, \bar{\mathbf{w}}) + \left. \frac{\partial \mathbf{f}_i}{\partial \mathbf{x}} \right|_{\bar{\mathbf{x}}, \bar{\mathbf{w}}} (\mathbf{x} - \bar{\mathbf{x}}) + \left. \frac{\partial \mathbf{f}_i}{\partial \mathbf{w}} \right|_{\bar{\mathbf{x}}, \bar{\mathbf{w}}} (\mathbf{w} - \bar{\mathbf{w}}) + \text{h.o.t.} \\ \mathbf{g}_i(\mathbf{x}, \mathbf{w}) &\approx \mathbf{g}_i(\bar{\mathbf{x}}, \bar{\mathbf{w}}) + \left. \frac{\partial \mathbf{g}_i}{\partial \mathbf{x}} \right|_{\bar{\mathbf{x}}, \bar{\mathbf{w}}} (\mathbf{x} - \bar{\mathbf{x}}) + \left. \frac{\partial \mathbf{g}_i}{\partial \mathbf{w}} \right|_{\bar{\mathbf{x}}, \bar{\mathbf{w}}} (\mathbf{w} - \bar{\mathbf{w}}) + \text{h.o.t.} \end{aligned} \quad (2.11)$$

where h.o.t. refers to higher order terms in $(\mathbf{x} - \bar{\mathbf{x}})$ and $(\mathbf{w} - \bar{\mathbf{w}})$. The output trajectory is defined by $\bar{\mathbf{y}} = \mathbf{g}_i(\bar{\mathbf{x}}, \bar{\mathbf{w}})$. The symbol t is omitted for clarity of reading. The partial derivatives in (2.11) are referred to by the following matrices

$$\begin{aligned} A_f(t) &:= \left. \frac{\partial \mathbf{f}(\mathbf{x}, \mathbf{w})}{\partial \mathbf{x}} \right|_{(\bar{\mathbf{x}}, \bar{\mathbf{w}})} \in \mathbb{R}^{28 \times 28}, & B_f(t) &:= \left. \frac{\partial \mathbf{f}(\mathbf{x}, \mathbf{w})}{\partial \mathbf{w}} \right|_{(\bar{\mathbf{x}}, \bar{\mathbf{w}})} \in \mathbb{R}^{28 \times 2} \\ C_f(t) &:= \left. \frac{\partial \mathbf{g}(\mathbf{x}, \mathbf{w})}{\partial \mathbf{x}} \right|_{(\bar{\mathbf{x}}, \bar{\mathbf{w}})} \in \mathbb{R}^{6 \times 28}, & D_f(t) &:= \left. \frac{\partial \mathbf{g}(\mathbf{x}, \mathbf{w})}{\partial \mathbf{w}} \right|_{(\bar{\mathbf{x}}, \bar{\mathbf{w}})} \in \mathbb{R}^{6 \times 2} \end{aligned} \quad (2.12)$$

For ease of notation, the subscript i is omitted here from the system descriptions, since only the 50%-ile dummy model will be described in the remainder of this section, unless stated otherwise.

A *linear* time-varying model (LTV) of (2.10) can be obtained when the higher order terms in (2.11) are neglected. This linear model will then approximate the state and output vector, denoted by $\tilde{\mathbf{x}}$ and $\tilde{\mathbf{y}}$ respectively. Define the following perturbation variables

$$\mathbf{x}_\delta(t) := \tilde{\mathbf{x}}(t) - \bar{\mathbf{x}}(t), \quad \mathbf{w}_\delta(t) := \mathbf{w}(t) - \bar{\mathbf{w}}(t), \quad \mathbf{y}_\delta(t) := \tilde{\mathbf{y}}(t) - \bar{\mathbf{y}}(t)$$

Note that input \mathbf{w} is not approximated, and is identical to the input of the nonlinear model. Then using (2.11), the system in (2.10) can be approximated by the following linear time-varying model

$$\mathcal{P}_f(t) : \begin{cases} \dot{\mathbf{x}}_\delta &= A_f(t)\mathbf{x}_\delta + B_f(t)\mathbf{w}_\delta, & \mathbf{x}_\delta(0) &= \tilde{\mathbf{x}}(0) - \bar{\mathbf{x}}(0) \\ \mathbf{y}_\delta &= C_f(t)\mathbf{x}_\delta + D_f(t)\mathbf{w}_\delta \end{cases} \quad (2.13)$$

So this linear system maps a perturbation on the input $\mathbf{w}_\delta(t)$ to perturbation $\mathbf{y}_\delta(t)$, given an initial state perturbation $\mathbf{x}_\delta(0)$. When the perturbations on the input and initial state are small, or when the original system in (2.10) is predominantly linear in the entire input and state space, then the system in (2.10) is well approximated by (2.13).

It is chosen to perform the linearization along the trajectories of the nominal scenario, see Figure 2.13. The initial condition is chosen to be identical to the nonlinear system, hence $\mathbf{x}_\delta(0) = 0$. The resulting linear time-varying model is discussed in the following sections.

2.8.2 Time Domain Results

LTI models have been selected from the LTV model in (2.13) at time instances $\tau \in \{5, 10, \dots, 100\}$ ms. The operating trajectories in an LTI model are also time-invariant, and they are now referred to as operating points, $\bar{\mathbf{x}} = \mathbf{x}(\tau)$, $\bar{\mathbf{w}} = [F_{\text{belt}}(\tau) \ a_{\text{veh}}(\tau)]^T$ and $\bar{\mathbf{y}} = \mathbf{y}(\tau)$. This leads, for each of the three dummy types, to 20 linear (LTI) systems and 20 operating points.

Simulations are performed with each LTI model and corresponding perturbed input $\mathbf{w}_\delta(t) = \mathbf{w}(t) - \bar{\mathbf{w}}$ and $\mathbf{x}_\delta(0) = \mathbf{0}$. The output responses are found through $\mathbf{y}(t) = \mathbf{y}_\delta(t) + \bar{\mathbf{y}}$. Simulation results for the LTI model derived at $\tau = 20$ ms are shown in Figure 2.19, together with the responses of the nonlinear design model \mathcal{D} and reference model \mathcal{R} in the nominal scenario. The LTI model responses obtained with the operating point at $\tau = 20$ ms lie the closest to the other two nonlinear model responses.

The results show that all outputs are comparable, except for the displacement responses of the ribs and belt. Given the complexity of the nonlinear reference model, the responses of the LTI model for the chest compression, spinal acceleration and sternum acceleration are remarkably well predicted. The LTI system derived at time instance τ is referred to by $\mathcal{P}_f = \mathcal{P}_f(\tau)$.

2.8.3 Frequency Domain Analysis

The dynamical behavior of a system can conveniently be analyzed in the frequency domain, and control design methods therefore often require systems described in the frequency domain. The LTI system \mathcal{P}_f has a transfer function matrix, $P_f(s)$, given by

$$P_f(s) = C_f(sI - A_f)^{-1}B_f + D_f, \quad \Rightarrow \quad \mathbf{y}(s) = P_f(s)\mathbf{w}(s)$$

where s denotes the Laplace operator, and $\mathbf{y}(s)$ and $\mathbf{w}(s)$ the Laplace transforms of time signals $\mathbf{y}(t)$ and $\mathbf{w}(t)$, respectively. Structural models based on first principles may contain modes with very low or high natural frequencies that are not relevant for control design (Gawronski, 2004). Additionally, it may contain weakly controllable and observable parts that could be removed. Finally, modern control design methods such as \mathcal{H}_∞ lead to controllers that have an order that is at least the plant order, so it is desirable to keep the plant order low (Skogestad and Postlethwaite, 2005). This is done by a model reduction technique based on the eigenvalues.

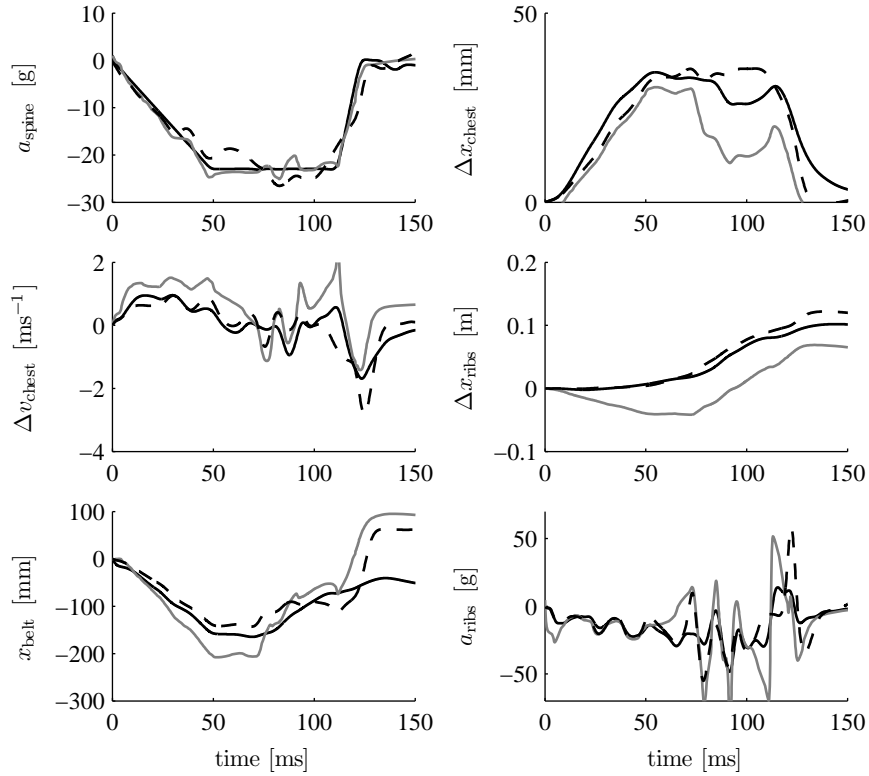


Figure 2.19 / Responses of the 50%-ile reference model (black), design model (black, dashed) and LTI model at time instance $\tau = 20$ ms (gray) in a 40% ODB frontal impact at 64 km/h (40 mph).

Model truncation

The model truncation presented here consists of removing the dynamic components associated with frequencies that lie outside the frequency range of interest. The states of a state-space realization are removed based on the (complex) eigenvalues $\lambda = \sigma + j\omega$ of system matrix A_f . Since the model \mathcal{D} has 14 degrees of freedom, the LTI model has 14 modes, and each mode is associated with a pair of eigenvalues. The natural (undamped) frequency is given by $\omega_{n,i} = 2\pi f_{n,i} = |\lambda_i|$, $i = 1, \dots, 28$. If the eigenvalue pair is complex conjugated, the natural frequencies are identical and the mode is called under-damped. When the eigenvalue pair has distinct, real values, the mode is over-damped. The natural frequencies of the LTI system \mathcal{P}_f are shown in Figure 2.20. There are 9 over-damped modes en 5 under-damped modes, and all modes are stable ($\sigma_i < 0$). Reduction is achieved by simple truncation

of the states that correspond to natural frequencies outside the control relevant frequency band. Crashes typically have durations of no more than 200 ms, so it can be expected that the part of the response with frequency content below 1 Hz can be neglected, and with content higher than 10 kHz will not reflect relevant physical phenomena of an occupant. Therefore, the 5 states *not* corresponding to natural frequencies $1 \leq f_n \leq 10^4$ Hz are removed. After truncation, the reduced LTI system is given by \mathcal{P} as follows

$$\mathcal{P} : \begin{cases} \dot{\mathbf{x}}_\delta(t) &= A\mathbf{x}_\delta(t) + B\mathbf{w}_\delta(t), & \mathbf{x}_\delta(0) = \mathbf{0} \\ \mathbf{y}_\delta(t) &= C\mathbf{x}_\delta(t) + D\mathbf{w}_\delta(t) \end{cases} \quad (2.14)$$

with $A \in \mathbb{R}^{23 \times 23}$, $B \in \mathbb{R}^{23 \times 2}$, $C \in \mathbb{R}^{6 \times 23}$, $D \in \mathbb{R}^{6 \times 2}$, and transfer function matrix $P(s) = C(sI - A)^{-1}B + D$.

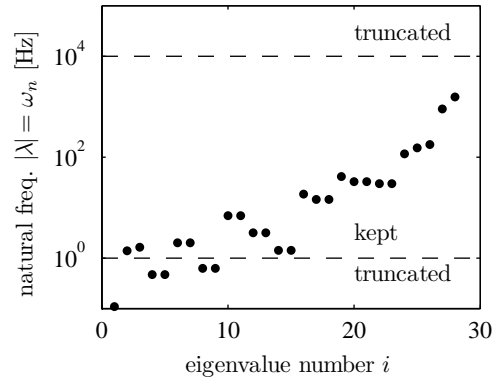


Figure 2.20 / Natural frequencies of the linear time-invariant system \mathcal{P}_f , derived from a linearization of \mathcal{D} .

Frequency Responses Function

Define $P_{(jk)}(s)$ as the element of transfer function matrix $P(s)$ that maps the k^{th} input to the j^{th} output, so $P_{11}(s)$ refers to the transfer from input F_{belt} to output a_{spine} . The transfer function $P_{11}(s)$ is derived for the LTI system $\mathcal{P}_f(\tau)$, for the entire time grid as proposed in Section 2.8.2, and after applying the truncation explained above. Their frequency responses functions (FRF), $P_{11}(j\omega)$, are plotted on time grid τ , given by $\tau \in \{5, 10, \dots, 85\}$.

Figure 2.21(a) shows the FRFs for $\tau \in \{5, 10, \dots, 50\}$ ms, and Figure 2.21(b) for $\tau \in \{55, 60, \dots, 85\}$ ms. They indicate that the FRFs in each individual plot are very similar, but they differ substantially between the plots. This is caused by the belt friction that changes its direction of application from $t \approx 50$ ms onwards,

as can be seen in Figure 2.13 and the friction equation in (2.7). This nonlinearity in the design model causes the change in magnitude of the time-varying transfer function from belt force to spinal acceleration.

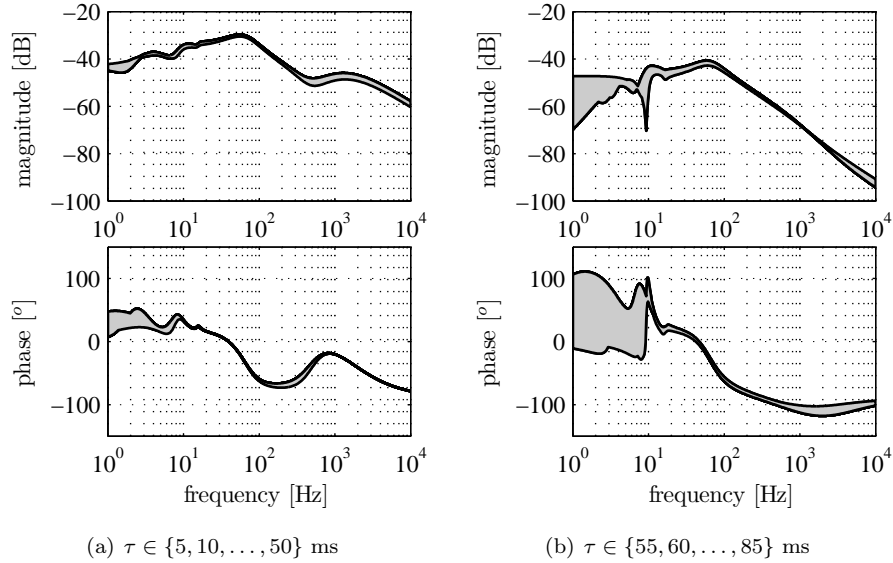


Figure 2.21 / Bode plots of the frequency response function $\mathcal{P}_{11}(j\omega)$ for the 50th percentile dummy, obtained from a linearization around different points of the trajectory at time instances τ .

For frequencies higher than 10 Hz, the FRFs are fairly similar before 50 ms, and after 50 ms. Indeed, the time domain results showed that already one linear *time-invariant* (LTI) model could be used to predict the output responses for the entire crash duration. Therefore, the LTI model (2.14), derived at $\tau = 20$ ms, is used in the design of the CRC control system.

2.8.4 Family of LTI models

Finally, the family of models is derived for the remaining two dummy types, i.e. the 5%-ile and 95%-ile. This means that the state space matrices in (2.12) are derived for \mathbf{f}_i , \mathbf{g}_i with $i = 1, 3$. LTI models are obtained by evaluating the LTV models at $\tau = 20$ ms. Model reduction is applied, so all states are removed associated with natural frequencies outside the frequency band of interest. This results in a 22nd and 23rd order model for the 5%-ile and 95%-ile dummy, respectively. The family

of LTI models is given by

$$\mathcal{P}_i : \begin{cases} \dot{\mathbf{x}}_\delta(t) &= A_i \mathbf{x}_\delta(t) + B_i \mathbf{w}_\delta(t), & \mathbf{x}_\delta(0) = \mathbf{0} \\ \mathbf{y}_\delta(t) &= C_i \mathbf{x}_\delta(t) + D_i \mathbf{w}_\delta(t) \end{cases} \quad (2.15)$$

for $i = 1, 2, 3$. The frequency responses functions $P_{i,j_1}(j\omega)$ are determined, i.e. from the first input, F_{belt} , to all outputs $j = 1, \dots, 6$. The functions are plotted in Figure 2.22, which illustrates that the system gain scales (inversely) with occupant mass. Moreover, the gain of $P_{11}(s)$ differs substantially between the 5%-ile and the 95%-ile dummy, circa 20 dB at 300 Hz. This indicates that a controller that uses this output should adapt to the occupant type to maintain performance.

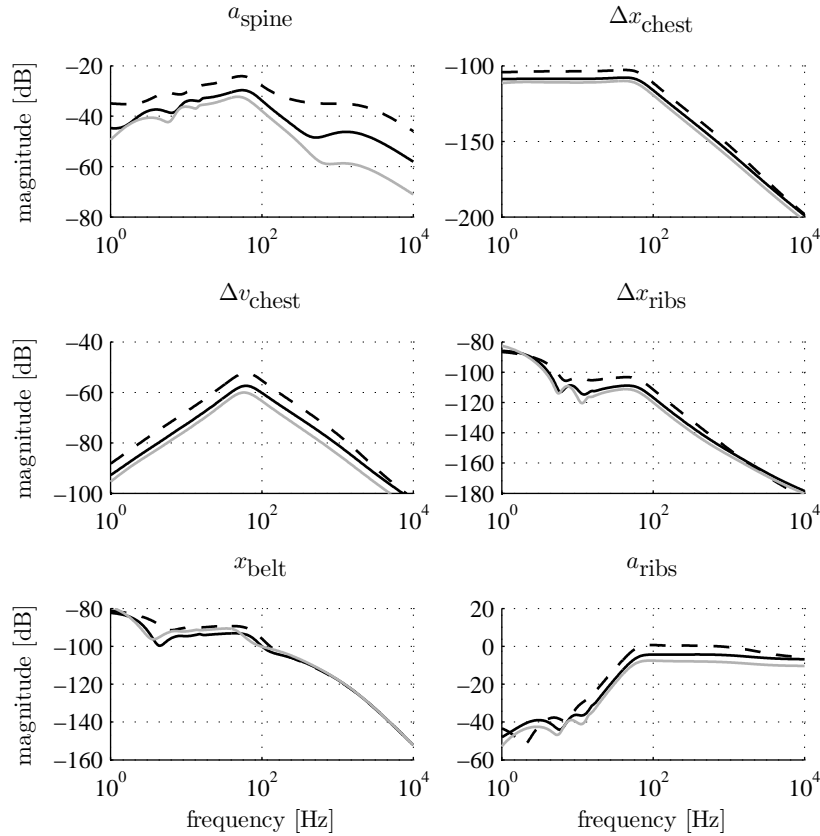


Figure 2.22 / Bode plot of the frequency response function $P_{j_1}(j\omega)$ for the 5%-ile (black, dashed), 50%-ile (black) and 95%-ile (gray) dummy, obtained at the linearization point $\tau = 20$ ms.

2.9 Discussion

Continuous Restraint Control systems (CRC) will in some form be part of the safety systems of future vehicles. It has been recognized that low-order occupant models are essential in the development of these systems; however, simple but accurate models with actuated restraints do not exist. In this chapter, these *design models* have been developed via a multi-fidelity approach.

A complex reference model is used, and a belt force signal is selected such that the complex model exhibits more or less the desired behavior. Next, the sensitivity of several model outputs to modifications in the complex model is analyzed. After an extensive number of tests, it became clear that the dynamics could be well described by only a small number of bodies and by linear, smooth constitutive relations. A two-dimensional model is constructed that consists of 11 rigid bodies with 14 degrees of freedom. The parameters in this model, such as mass, dimension, initial conditions, can directly be obtained from the parameters in the reference model, which makes scaling of the design model straightforward. Most of the parameters of the constitutive relations correspond well to those implemented in the reference model.

A validation study showed that the design model generates the biomechanical responses related to injury predictors for the chest and neck region remarkably well. The models are validated for a broad range of frontal crash scenarios, and for three different adult Hybrid III dummies. After these validations, a linearization of the design models was performed. For all the validation tests, it was shown that the low-order models include the important dynamics of the reference model. Only the belt displacement and sternal displacement did not match very well in some scenarios, since the belt rollout is very sensitive to the seat belt characteristics. The linear visco-elastic belt model used in the design model may be too simple to capture the relevant phenomena. Especially since this response will be used in the observer, see Chapter 4, to estimate biomechanical occupant responses, attention should be directed towards development of a simple, but accurate belt model that includes different loading and unloading paths.

Since the initial belt geometry and initial dummy geometry are identical in both design and reference model, similar trends in the responses could have been expected. It will be relevant to investigate the sensitivity of the responses to mismatches in the initial posture or belt placement. Furthermore, it is assumed that the reference model is a representation of the real world. Although Madymo numerical dummies are nowadays widely used in crash research, validation of the reference model is - in this study - based on a fairly small amount of test data.

3

MODEL PREDICTIVE CONTROL STRATEGY

Abstract / This chapter presents a control strategy for the continuous restraint control system, as discussed in Chapter 1. The control strategy is based on elements of model predictive control and reference management, in which a nonlinear device is added to a primal closed-loop controlled system. The model predictive controller determines an optimal setpoint in terms of injury reduction and constraint satisfaction by solving a constrained optimization problem. Prediction of the vehicle motion, required to predict future constraint violation, is included in the design and is based on past crash data using linear regression techniques. Simulation results with realistic MADYMO models show that, with ideal sensors and actuators, a significant reduction (45%) of the peak spinal acceleration can be achieved, without prior knowledge of the crash. Furthermore, it is shown that the algorithms are sufficiently fast to be implemented on-line.

This chapter is largely based on E.P. van der Laan et al. (2009c), Reference Governors for Controlled Belt Restraint Systems, *Vehicle System Dynamics, in press*, and E.P. van der Laan et al. (2008b), Reference Governors for Controlled Belt Restraint Systems, In *Proceedings of the IEEE International Conference on Vehicular Electronics and Safety (ICVES)*, 22-24 Sep, Columbus, OH, USA, pp. 114-119

3.1 Introduction

In previous studies on continuous restraint control (CRC) systems, the control problem is formulated as a feedback tracking problem, where biomechanical responses of the occupant are measured and forced to follow a desired response. These desired responses are formulated in terms of a reference trajectory, which results in a minimum risk of injury, while satisfying certain constraints. Feedback control is a straightforward choice for continuous restraint control, since - besides performance and stability - it may additionally provide robustness to uncertainties and disturbances, and it has a linearizing effect on nonlinear systems (Skogestad and Postlethwaite, 2005).

Through simulation studies, Hesseling et al. (2006a) showed promising results in terms of tracking errors, and a significant reduction of injury criteria. However, in his study, the reference trajectories are constructed assuming full a priori knowledge of the vehicle crash pulse, which is clearly not realistic. Besides, optimization strategies to derive optimal restraint settings, which have also been proposed by Crandall et al. (2000); Kent et al. (2007), are not likely to be solved in real-time.

To harvest the advantages of using CRC systems, these limitations have to be overcome. This indicates the strong need for the development of a control algorithm that - based on the available measurements - computes the optimal control signals for the restraint actuator. The following requirements should be incorporated:

- (i) the algorithm must be computationally feasible in order to meet the real-time requirements,
- (ii) a priori knowledge of the crash pulse is not available, and
- (iii) the algorithm must be based on on-line measurement data.

This chapter proposes a solution to this challenging control design problem. The main contributions can be summarized as follows: (i) a control strategy is proposed that is able to determine optimal restraint settings *without* a priori crash information, aiming at a minimum risk of injury for the occupant, (ii) algorithms are developed, based on constrained optimization problems, which implement the proposed control strategy and are able to run in real-time, (iii) simulation results with a force controlled seat belt and a MADYMO dummy model are presented that show a significant injury reduction for the thoracic region without a priori crash information.

3.2 Control Strategy

In this section, the control problem is mathematically formulated, and the adopted control strategy is presented.

3.2.1 Formulation of the Control Problem

As proposed in Section 1.4, the control algorithm \mathcal{C} aims at minimizing three thoracic injury criteria (IC), namely A_{\max} , D_{\max} and VC , which are defined in Section 1.2.2. To determine the values of these IC, the vehicle occupant responses $a_{\text{spine}}(t)$, $\Delta x_{\text{chest}}(t)$ and $\Delta v_{\text{chest}}(t)$ are required. These responses are generated by the system Σ , consisting of the vehicle interior, the occupant and the three-point seat belt arrangement.

In addition to minimizing the IC, the controller has to fulfill certain constraints on the forward occupant motion. These constraints will prevent the occupant from hitting the steering wheel - causing even more severe injuries - or being pushed backwards through the seat. It is chosen in this chapter to apply a constraint to the spinal displacement relative to the vehicle interior, Δx_{spine} , hence

$$\Delta x_{\text{spine}}(t) := x_{\text{spine}}(t) - x_{\text{veh}}(t) \quad (3.1)$$

with

$$\begin{aligned} \ddot{x}_{\text{spine}} &= \dot{v}_{\text{spine}} = a_{\text{spine}} \\ \ddot{x}_{\text{veh}} &= \dot{v}_{\text{veh}} = a_{\text{veh}} \end{aligned} \quad (3.2)$$

with a_{spine} as defined in Section 1.2.2, and a_{veh} as defined in Section 1.5.

The constraint for the spinal displacement is given by

$$\bar{L}_1 \leq \Delta x_{\text{spine}}(t) \leq \bar{L}_2, \quad t \geq 0 \quad (3.3)$$

with \bar{L}_1 and \bar{L}_2 appropriate constants related to the position of the seat and steering wheel, respectively. Furthermore, $t = 0$ is defined as the start of the crash event. In Section 1.5, it was proposed to use the relative displacements of the ribs, Δx_{ribs} , in this constraint instead of the spinal cord. However, as will become clear in Section 3.4.3, the inclusion of Δx_{spine} has the advantage that an extremely simple observer model of Σ is required by the control algorithm. For Δx_{ribs} , this would be more involved.

The vehicle crash, $a_{\text{veh}}(t)$, is an exogenous disturbance input to system Σ , as formulated in Section 1.5. The second input to Σ is the seat belt force $F_{\text{belt}}(t)$,

which is generated by the actuator Γ . Input to this actuator system Γ is the control effort, $u(t)$, that is prescribed by the controller \mathcal{C} . Since there is, at this point, no knowledge on the characteristics of the actuator system Γ , the following assumption is proposed:

Assumption 3.1 / *The actuator system Γ from Figure 1.5 is ideal, in the sense that $\Gamma : F_{\text{belt}}(t) = u(t)$.*

Ongoing research in the field of belt restraint actuators makes it plausible that an actuator will be available in the near future that is sufficiently fast and accurate, see e.g. the Wedgetronic Seatbelt, developed by Siemens VDO, or Chapter 5.

In Section 1.5, it was proposed that an observer algorithm will provide the required responses, $\mathbf{y}_1, \mathbf{y}_2$, to the controller. This observer algorithm will be developed in Chapter 4, and therefore it is assumed here that *only* the measurable variables, \mathbf{v} , are directly available to the controller. These variables will be specified in Section 3.2.4.

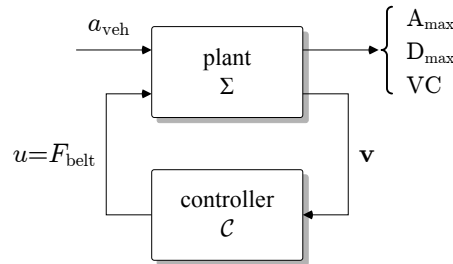


Figure 3.1 / General control scheme, in which the seat belt force is manipulated to minimize thoracic injury criteria of the system Σ , consisting of the vehicle interior, the occupant and a three-point seat belt arrangement.

Figure 3.1 shows the general control scheme, which is reproduced from Figure 1.5. At this point, the focus lies on minimization of only the A_{max} criterion, but minimization of the D_{max} or VC criteria can be added to this problem in a straightforward manner. As a consequence, the control problem at hand can be formulated as follows:

Design a controller \mathcal{C} that prescribes the control input $u = F_{\text{belt}}$ to the system Σ , based on the information of the measurements \mathbf{v} , such that the criterium A_{max} in (1.1) is minimized in real-time, while satisfying the constraint in (3.3). The system Σ is subject to an (arbitrary) crash acceleration pulse a_{veh} .

This constrained optimal control problem can be approached by model predictive control or its ramifications.

3.2.2 Model Predictive Control

Model Predictive Control (MPC) is a widely used control technique, able to handle control problems with input and state constraints, see e.g. Garcia et al. (1989); Maciejowski (2001); Mayne et al. (2000); Morari and Lee (1999). Typically, MPC utilizes an explicit model of the to-be-controlled plant to predict the future output behavior of the plant, on the basis of a measured or estimated current state and a chosen future input sequence. Its prediction capability allows solving an optimal control problem over a finite future horizon, subject to constraints on state and input variables. MPC uses a receding horizon strategy in the sense that from the computed optimal input sequence, only the first control move is actually implemented. At the next sampling time, this optimization problem is solved again on the basis of the updated state variables. Solving the optimization problem on-line is usually a time-consuming process, which is the reason that classical MPC in general requires a formidable computational effort. It is therefore mostly applied to slow or small processes, and clearly not during a vehicle crash. However, more efficient methods to implement MPC algorithms have been considered recently.

In explicit MPC (Bemporad et al., 2002a,b; Tøndel et al., 2003), the optimization problem is solved off-line using multi-parametric programming. This results in a partitioning of the state space into different regions, and each region is associated with its own affine state feedback law. This might offer a solution to meet the real-time requirements, if the determination of the correct region can be computed very fast. However, in many situations the number of regions is large, making the evaluation of the control function still demanding. At the current state of affairs, it is expected that explicit MPC will not be applicable to the complex system at hand, and alternatives have to be considered.

Reference Governors reflect a predictive control method that acts on the setpoint or reference signal, rather than the control signal, and it can be seen as a subclass of MPC (Bemporad, 1998; Bemporad et al., 1997; Gilbert and Kolmanovsky, 2002). The main idea is to add an auxiliary nonlinear device to a primal controlled system, and this device modifies a desired setpoint whenever necessary to avoid (future) constraint violation. A state measurement is used to detect constraint violation, which implies that an additional outer feedback loop is present for constraint satisfaction. Applications of reference management are so far limited to systems with constant reference signals or small disturbances. Since the optimal setpoint for the primal controlled system is not a constant and disturbances on the system are significant, the reference governor method seems less suitable in this context.

No MPC ramification could be found in literature that is directly applicable to the problem sketched in Section 3.2.1, so it will be developed here.

3.2.3 Cascade Control

For the seat belt control system, a cascaded control method is adopted. The cascade controller consists of a local, linear feedback controller and an outer MPC controller, see Figure 3.2. The figure shows a plant with an output y , that is controlled by the local feedback controller. This system consisting of plant and local controller is called the *primal controlled system*, Λ . The local controller is designed to make Λ stable, and to yield good tracking performance of reference r in spite of the presence of disturbances w , i.e. $y \approx r$. The outer controller determines reference r by solving an optimization problem on-line. This controller contains many features of a conventional MPC controller, but is slightly different. For example, there is no feedback of the primal controlled system to the MPC controller, so there are no stability issues in the outer loop.

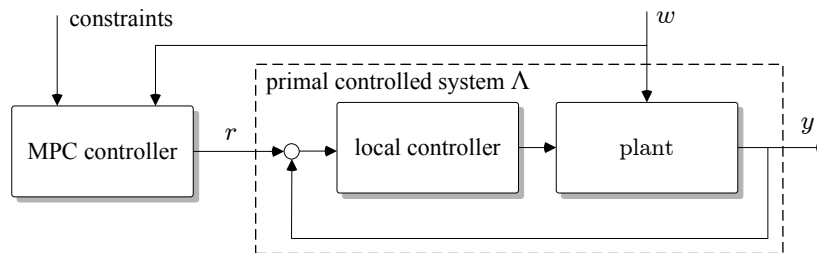


Figure 3.2 / The general layout of the cascaded controller, in which a modified MPC controller acts on a primal controlled system Λ .

The proposed control strategy is particularly appealing, because of its computational efficiency and the separation of stability and performance. The primal controlled system can be seen as the *new* stable plant to be controlled by the MPC controller. This implies that the MPC controller merely has to determine an optimal reference trajectory r such that disturbance w is mitigated, while satisfying the constraints. Hence the MPC controller has to ensure that the performance requirements are fulfilled, while the local controller assures stability. Another advantage of this approach is the following. The optimal response r follows from minimization of a maximum injury criterion value, which will typically result in a flat profile. So the optimal response has *ideally* most of its content in relatively low frequencies. The MPC controller that calculates the setpoints can therefore run at a low update frequency, while applying a zero order hold between the updates. On the other hand, the local controller may run at a different – usually higher – update frequency, which is governed by the plant dynamics.

In the following paragraph, it is explained how the proposed control strategy is tailored to solve the specific control problem outlined in Section 3.2.1.

3.2.4 The Approach and Outline

The approach to implement the cascade controller, \mathcal{C} , is divided into three steps which are described below. Following the control problem formulated in Section 3.2.1, the setpoint $r = a_{\text{ref}}$ should be constructed such that A_{max} in (1.1) is minimized, subject to the dynamics of plant Σ and the inequality constraint in (3.3). The controlled variable is taken to be $y = a_{\text{spine}}$, given the following assumption

Assumption 3.2 / *An accurate estimate of the spinal acceleration a_{spine} is available to the controller during impact, so it is part of measured variable \mathbf{v} .*

This assumption is plausible, given the results presented in van der Laan et al. (2007b), where Kalman filters are used to estimate the spinal acceleration from belt roll-out measurements. The first step concerns the primal controlled system:

1. **Local feedback controller.** Design a local feedback controller, \mathcal{K} , applied to system Σ , that aims at minimizing a performance variable $|z| = |a_{\text{ref}} - a_{\text{spine}}|$.

Now the following is proposed with respect to the local controller:

Assumption 3.3 / *A local feedback controller, \mathcal{K} , can be designed such that the primal controlled system Λ , consisting of plant Σ and controller \mathcal{K} , has ideal tracking performance, at least in the (limited) frequency range of a_{ref} and a_{veh} , hence $\Lambda : a_{\text{spine}}(t) = a_{\text{ref}}(t)$.*

This assumption can also be realized closely, as simulation results with complex and accurate occupant models indeed show excellent tracking behavior, see Section 3.3 and, e.g., Hesselting et al. (2006a); van der Laan et al. (2009b).

When Assumption 3.3 holds, finding the optimal signal a_{spine} in terms of a minimal A_{max} translates to finding an optimal a_{ref} . This optimization problem is solved by the MPC controller \mathcal{M} , see Figure 3.3. The MPC controller has two objectives, performing an optimization and a prediction, and these two algorithms are described separately. This leads to the second step, the *setpoint optimization*:

2. **Setpoint optimization.** Based on a prediction of the future vehicle motion, determine a reference signal a_{ref} that minimizes one or more injury criteria (here A_{max}) and that satisfies the constraint in (3.3).

In this step, a vehicle motion prediction is required. To this end, consider the following

Assumption 3.4 / *The vehicle acceleration pulse, a_{veh} , and the vehicle speed at*

the moment of impact, v_o , are known during impact, and hence part of measured variable \mathbf{v} .

This is a reasonable assumption, since acceleration sensors are present in most consumer cars to detect a crash. The GPS speed estimate or the vehicle's speedometer¹ can be used to determine the speed just before impact. Using this assumption, the last step, i.e. the second algorithm of the MPC controller \mathcal{M} , is formulated as:

3. **Prediction of vehicle motion.** Based on the initial vehicle speed v_o and the entire history of the measured vehicle acceleration a_{veh} , predict the future vehicle motion.

Combining these three steps leads to the overall cascade controller \mathcal{C} as shown in Figure 3.3. Since this scheme typically results in better behavior when executed more often as the crash progresses, it should be computationally extremely efficient, especially given the short duration of the crash. When Figure 3.3 is compared with Figure 3.1, then the signal \mathbf{v} follows from Assumptions 3.2 and 3.4, hence the measurement signal is given by

$$\mathbf{v}(t) = [a_{\text{veh}}(t) \quad a_{\text{spine}}(t) \quad v_o]^T$$

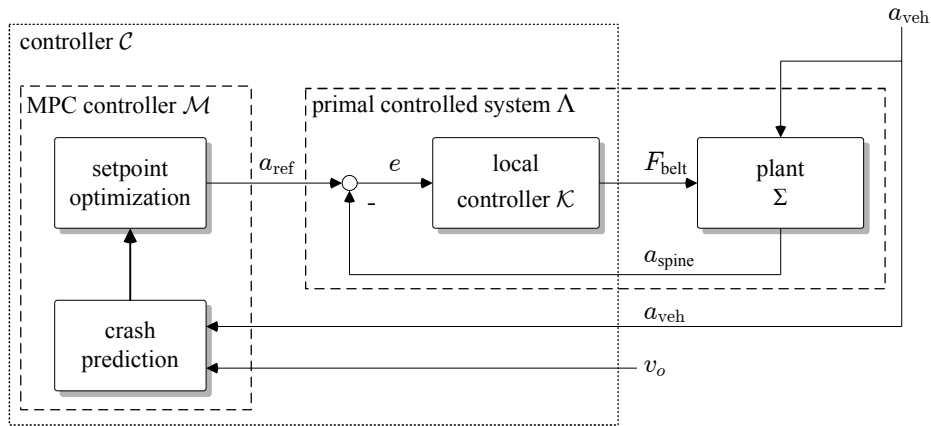


Figure 3.3 / Cascade controller, consisting of a primal controlled loop and an modified MPC controller with crash prediction.

The upcoming three sections discuss these three steps: the design of the local controller is presented in Section 3.3, the setpoint optimization algorithm is treated in Section 3.4, and finally, the crash prediction is dealt with in Section 3.5.

¹this is a good estimate when there is low slip, which is often the case as anti-locking brake systems are available in most consumer vehicles

3.3 Design of the Local Feedback Controller

In this section, the first component of the cascade controller \mathcal{C} is designed, namely the local feedback controller, \mathcal{K} .

3.3.1 Controller Objective

The objective of this controller is to manipulate control variable $F_{\text{belt}}(t)$ using the error variable $e(t)$, such that the controlled variable $a_{\text{spine}}(t)$ accurately follows the reference trajectory $a_{\text{ref}}(t)$, while the system Σ is subject to disturbance variable $a_{\text{veh}}(t)$ and measurement noise $n_y(t)$. In the following, this control objective is specified more precisely by defining performance and robustness criteria. The controller is designed using the LTI control design model \mathcal{P} , which is derived in Section 2.8.3. The LTI model is given by (2.14), and is described by transfer function $P(s)$. Following the notation in Section 2.8.3, the controlled variable is given in the Laplace domain by

$$a_{\text{spine}}(s) = P_{11}(s)F_{\text{belt}}(s) + P_{12}(s)a_{\text{veh}}(s)$$

See Figure 3.4 for a layout of the feedback control scheme with the LTI model, and see Figure 3.5 for the Bode plots. Note that the transfer $P_{12}(s)$ appears dominant over $P_{11}(s)$, however, the magnitude of the first input is significantly larger than the second input.

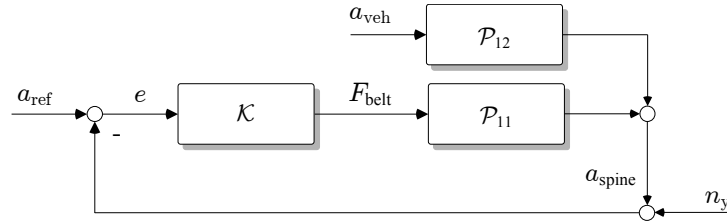


Figure 3.4 / The primal loop with the local feedback controller \mathcal{K} , and the LTI model \mathcal{P} .

The transfer function of \mathcal{K} is given by $\mathcal{K}(s)$, and hence the control variable reads $F_{\text{belt}}(s) = \mathcal{K}(s)(a_{\text{ref}}(s) - n_y(s) - a_{\text{spine}}(s))$. This allows to formulate a performance output $z(s)$ as follows

$$\begin{aligned} z(s) &= a_{\text{ref}}(s) - a_{\text{spine}}(s) \\ &= S(s)a_{\text{ref}}(s) + T(s)n_y(s) - P_{12}(s)S(s)a_{\text{veh}}(s) \end{aligned} \quad (3.4)$$

with the closed-loop transfers

$$S(s) = \frac{1}{1 + \mathcal{K}(s)P_{11}(s)}, \quad T(s) = \frac{\mathcal{K}(s)P_{11}(s)}{1 + \mathcal{K}(s)P_{11}(s)} \quad (3.5)$$

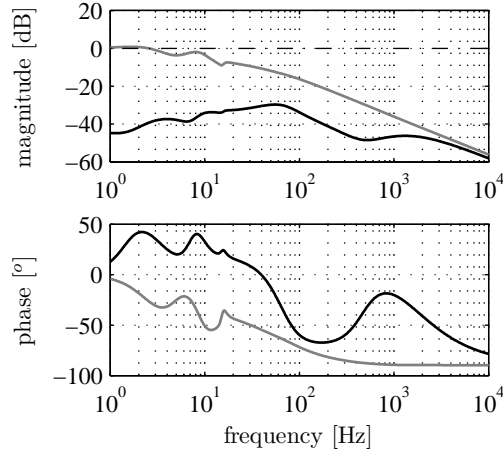


Figure 3.5 / Bode plot of the frequency responses function of the LTI control model \mathcal{P}_{11} (black) and \mathcal{P}_{12} (gray).

3.3.2 Performance and Robustness Criteria

The controller objective is to minimize the performance variable z . It is required that the performance variable satisfies $|z(t)| \leq 0.5$ g for all t . Performance design criteria are usually formulated in the frequency domain, and according to (3.4), they have to be formulated on the closed-loop transfers. However, this requires knowledge of the expected frequency content and magnitude of the signals a_{ref} , a_{veh} and n_y .

Measurements from consumer crash tests are used to determine the properties of these signals. They are sampled at 20 kHz, and the crash acceleration pulse is available unfiltered. The measured spinal acceleration in the crash test is – however – only available after filtering with a CFC180 filter, so this signal is not suitable to determine the noise signal n_y on the output. Therefore, the noise on the unfiltered crash acceleration signal is used, as it arises from a similar acceleration sensor as used to determine dummy acceleration signals.

A part of the noisy time history signal of a_{veh} is shown in Figure 3.6(a), and the cumulative power spectral density (PSD) estimate of the signal is shown in Figure 3.6(b). One can see that the crash pulse satisfies $|a_{\text{veh}}(t)| \leq 50$ g. It is assumed that the vehicle acceleration is zero for $t \geq 150$ ms, and this is used to find that the noise signal roughly satisfies $|n_y(t)| \leq 1$ g, for all t . From the cumulative PSD plot, it can be seen that the power of a_{veh} increases up till 100 Hz. From that point onwards until 600 Hz, the density plot is flat and hence almost no

power is added. In the frequency region 0.6-6 kHz, the cumulative power increases to 100%. It is concluded from this observation that almost all the energy in the vehicle acceleration pulse is present in the signal with frequencies $f \leq 100$ Hz. This conclusion is also supported by that fact that the measured vehicle acceleration is filtered with a CFC180 filter, hence most of the crash energy will have its content below 180 Hz (Society of Automotive Engineers (SAE), 1995). The measurement noise thus has most of its energy in frequencies $f \geq 600$ Hz.

Finally, an example of the setpoint a_{ref} is given in Figure 3.13. Many setpoints have been generated using a variety of crash pulses, and it is plausible to assume that $|a_{\text{ref}}(t)| \leq 30$ g for all t . In Figure 3.6(b), the cumulative PSD estimate is plotted for the signal a_{ref} from Figure 3.13, and it shows that almost all the energy (98%) is present for frequencies $f \leq 10$ Hz.

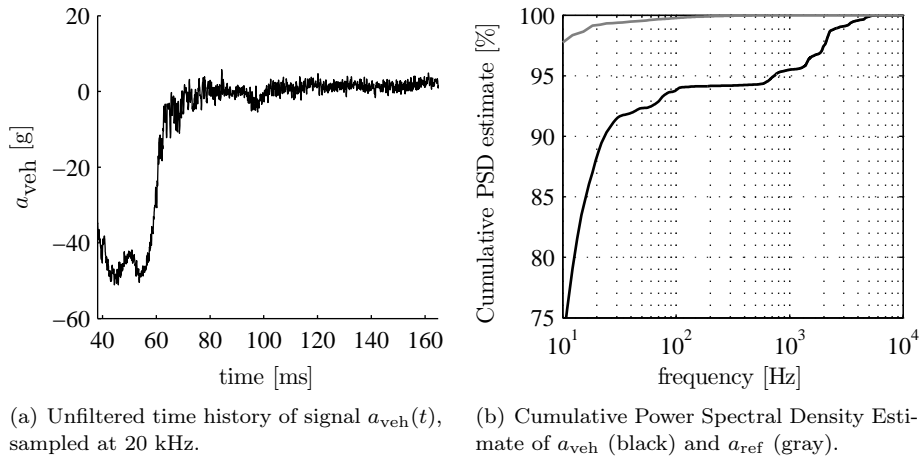


Figure 3.6 / Time and frequency domain plots of the input signals.

Now assume that the input variables consist of a single frequency ω , which lies for each variable in the expected frequency region as discussed above. This implies that, in the Laplace domain, the magnitude of these signals satisfy $|a_{\text{veh}}(j\omega)| = 50$ g, $|n_y(j\omega)| = 1$ g and $|a_{\text{ref}}(j\omega)| = 30$ g. Moreover, for this single frequency, it follows that $|z(j\omega)| = 0.5$ g. Consider the following closed-loop frequency response functions, see (3.4)-(3.5):

$$|S(j\omega)| = \frac{|z(j\omega)|}{|a_{\text{ref}}(j\omega)|}, \quad |\mathcal{P}_{12}(j\omega)S(j\omega)| = \frac{|z(j\omega)|}{|a_{\text{veh}}(j\omega)|}, \quad |T(j\omega)| = \frac{|z(j\omega)|}{|n_y(j\omega)|}$$

With these expressions, an upperbound for the magnitude of the closed-loop FRFs is found for this single frequency. Although the bounds on the time domain signals

do not reflect the bounds in the frequency domain, these upperbounds are adhered to in formulating the performance design criteria in the frequency domain. Hence:

$$\begin{aligned} |S(j\omega)| &\leq \frac{0.5}{30} = -36 \text{ dB} && \text{for } \omega \leq 2\pi 10^1 \text{ Hz} \\ |\mathcal{P}_{12}(j\omega)S(j\omega)| &\leq \frac{0.5}{50} = -40 \text{ dB} && \text{for } \omega \leq 2\pi 10^2 \text{ Hz} \\ |T(j\omega)| &\leq \frac{0.5}{1} = -6 \text{ dB} && \text{for } \omega \geq 1.2\pi 10^3 \text{ Hz} \end{aligned}$$

To ensure a stable and robust closed-loop system, the following robustness criteria are adopted

$$\text{PM} \geq 45^\circ, \quad \text{MM} \leq 3 \text{ dB}$$

with PM the phase margin and MM the modulus margin (Skogestad and Postlethwaite, 2005). These robustness margins have to account for, e.g., model mismatches between \mathcal{P} and the plant Σ .

3.3.3 Control design

The local controller \mathcal{K} is designed for the LTI model \mathcal{P} of the 50th percentile dummy, see (2.14) and Figure 2.22. The gain of the plant model is constant for low frequencies, hence a proportional-integrative action is added to increase the open-loop amplification, thereby reducing the gain of the sensitivity function (see the first and second performance criteria). To fulfill the third requirement, a first-order low-pass filter is added to the controller, to improve the high-frequency roll-off without introducing too much phase delay. The controller is scaled with a gain K to meet the criteria. The following controller closely fulfills the requirements formulated above

$$\mathcal{K}(s) = K \cdot \frac{s + 2\pi f_I}{s} \cdot \frac{1}{s + 2\pi f_{LP}} \quad (3.6)$$

with $K = 3.7 \cdot 10^5$, $f_I = 195 \text{ Hz}$ and $f_{LP} = 255 \text{ Hz}$. The open-loop transfer is given in Figure 3.7(a), and the Nyquist diagram in Figure 3.7(b). The 0 dB cross-over frequency is $f_{bw} = 3.4 \cdot 10^2 \text{ Hz}$, and the margins are exactly satisfied, i.e. MM= 3.0 dB and PM= 45°. The criterion on the sensitivity function is easily met, whereas the complementary sensitivity function is critical, and the process sensitivity criterion is not met, see Figure 3.8, and

$$\begin{aligned} |S(j\omega)| &\leq -40 \text{ dB} && \text{for } \omega \leq 2\pi 10^1 \text{ Hz} \\ |\mathcal{P}_{12}(j\omega)S(j\omega)| &\leq -38 \text{ dB} && \text{for } \omega \leq 2\pi 10^2 \text{ Hz} \\ |T(j\omega)| &\leq -6.0 \text{ dB} && \text{for } \omega \geq 1.2\pi 10^3 \text{ Hz} \end{aligned}$$

It was not possible to meet the process sensitivity criterion without violation of other criteria. The consequence is that $z(j\omega) \leq 0.63$ g, which is more than required but acceptable, also given the fact that $\max |a_{\text{veh}}(t)| = 50$ g is a conservative estimate.

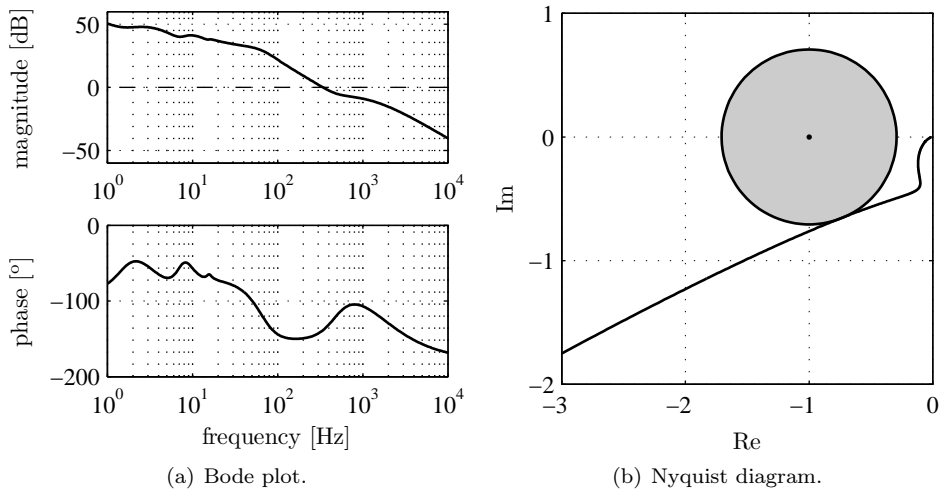


Figure 3.7 / Plots of the open-loop transfer $P_{11}(s)\mathcal{K}(s)$.

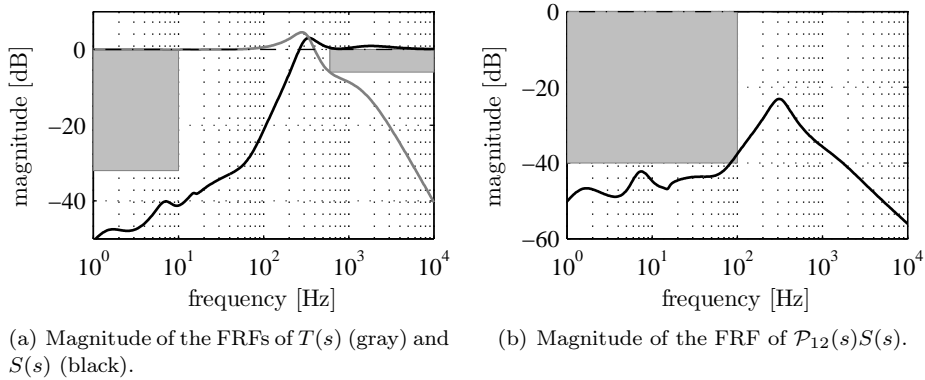


Figure 3.8 / Bode plot of the closed-loop transfer functions, with performance criteria indicated by gray blocks.

The controller in (3.6) did not meet the requirements when applied to the 5th and the 95th percentile dummy models \mathcal{P} . Indeed, it was shown in Section 2.8.4 that the gain of $\mathcal{P}_{11}(s)$ differs 20 dB at 300 Hz between the 5%-ile and the 95%-ile dummy. Different controller parameters are selected, without changing the

controller structure. For the small female dummy, the gain is lowered to $K = 8.0 \cdot 10^4$ leading to $\text{MM}=0.5$ dB, $f_{\text{bw}} = 3.0 \cdot 10^2$ Hz and a phase margin $\text{PM}=68^\circ$. For the large male dummy, the gain is to $K = 5.5 \cdot 10^5$ with $f_{\text{LP}} = 1$ kHz, leading to $\text{MM}=2.4$ dB, $f_{\text{bw}} = 3.9 \cdot 10^2$ Hz and a phase margin $\text{PM}=45^\circ$.

3.4 Setpoint Optimization

In this section, the second component of the cascade controller \mathcal{C} is designed, see Figure 3.3, namely the setpoint optimization of the MPC controller \mathcal{M} . It is shown here that the setpoint optimization problem can be written as a linear program (LP), which can be solved efficiently in limited time, see (Boyd and Vandenberghe, 2004).

3.4.1 The Finite Horizon

The setpoint optimization step solves a constrained optimization problem using a prediction of the vehicle motion. To make this problem feasible in real-time, a finite prediction horizon is introduced in the constraint equation (3.3) by using the following assumptions.

Concerning the vehicle motion, the following assumption is proposed

Assumption 3.5 / *At $t = T_e$, the vehicle has come to a full stop, i.e., the velocity of the vehicle satisfies $v_{\text{veh}}(t) = 0$ for $t \geq T_e$.*

With crash data being widely available, a value T_e can easily be chosen such that this assumption is in general satisfied.

Assumption 3.6 / *At $t = T_e$, the occupant has come close to a stop in the sense that the relative occupant velocity is within bounds $S_1 < 0 < S_2$, i.e.*

$$S_1 \leq \Delta v_{\text{spine}}(T_e) \leq S_2, \quad \Delta v_{\text{spine}}(t) = \Delta \dot{x}_{\text{spine}}(t) \quad (3.7)$$

with Δx_{spine} as in (3.1).

Assumption 3.5 implies that the vehicle has no kinetic energy after time T_e . Given that the restraint systems only dissipate energy, the occupant's kinetic energy typically decreases to zero after time T_e . If (3.7) is imposed for S_1 and S_2 sufficiently close to zero, and if

$$L_1 \leq \Delta x_{\text{spine}}(t) \leq L_2, \quad 0 \leq t \leq T_e \quad (3.8)$$

is imposed for a suitably chosen $L_1 > \bar{L}_1$ and $L_2 < \bar{L}_2$, then it is reasonable to assume that the original infinite horizon constraint in (3.3) is satisfied. Hence,

when the above assumptions hold, the infinite horizon in (3.3) can be replaced by the finite horizon constraints in (3.7) and (3.8).

The measurable variables \mathbf{v} are sampled on $[0, T_e]$ with sample time $T = T_e/N_e$, $N_e \in \mathbb{N}$, with \mathbb{N} the set of nonnegative integers. Then the measurements are available at times $t = kT$, with $k \in \mathbb{K} := \{0, 1, 2, \dots, N_e\} \subset \mathbb{N}$. The MPC controller \mathcal{M} is executed every $T_o = N_o T$ seconds on the interval $[0, T_e]$, with $N_o = N_e/\ell$, $N_o, \ell \in \mathbb{N}$. So it is executed at times $t = kT$, with $k \in \mathbb{K}_o := \{0, N_o, 2N_o, \dots, N_e\} \subseteq \mathbb{K}$. Furthermore, at time $t = kT$, $k \in \mathbb{K}$, the remaining samples will become available at times $t = (k + j)T$, with $j \in \mathbb{K}_e := \{0, 1, 2, \dots, N_e - k\} \subseteq \mathbb{K}$. See Figure 3.9 for a graphical depiction of the time line. The three sets are repeated here for future reference

$$\mathbb{K} := \{0, 1, \dots, N_e\}, \quad \mathbb{K}_e := \{0, 1, \dots, N_e - k\}, \quad \mathbb{K}_o := \{0, N_o, 2N_o, \dots, N_e\}$$

For clarity of notation, the variables in discrete time are denoted by $v[k] = v(kT)$, with $k \in \mathbb{K}$, \mathbb{K}_o or \mathbb{K}_e .

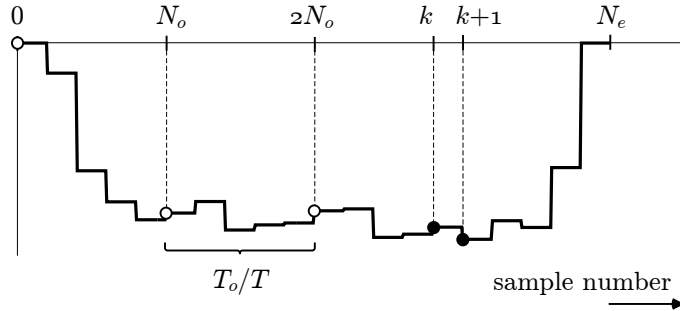


Figure 3.9 / An example of a discrete time signal. Measurements are available at discrete time instants $t = kT$ (\bullet), with $k \in \mathbb{K}$. The MPC controller \mathcal{M} is executed every T_o seconds, that is at times $t = kT$ (\circ), with $k \in \mathbb{K}_o$.

3.4.2 Optimization Problem

The optimization problem from Section 3.2.1 can now be formulated mathematically. Note that the A_{\max} criterion in (1.1) satisfies the following inequality

$$A_{\max} = \max_t \left(\min_{\tau \in [0, 3] \text{ ms}} |a_{\text{spine}}(t + \tau)| \right) \leq \max_t |a_{\text{spine}}(t)|$$

so the right hand side of this expression is an upper bound for A_{\max} . There are clear advantages in using the upper bound in the optimization problem instead of A_{\max} .

First, the implementation is much more efficient from a numerical point of view, since no extra constraint equations are required. Secondly, using A_{\max} directly in the optimization will lead to an optimal solution where one sample of a_{spine} in the 3 ms interval is zero, while the remaining samples have very high values. This solution minimizes A_{\max} , but is clearly undesirable from a control design point-of-view. It shows that the definition A_{\max} is adequate to analyze a given physical signal, but a realistic signal cannot be generated using this definition.

The upper bound of A_{\max} is also valid in discrete time, given that the sample time $T \leq 3$ ms. Suppose that Assumption 3.3 holds, then the optimal control problem formulation with constraints in (3.7) and (3.8) is given in discrete time by

$$\begin{aligned} & \min_{a_{\text{ref}}[k+j]} \quad \max_{j \in \mathbb{K}_e} \quad |a_{\text{ref}}[k+j]| && k \in \mathbb{K}_o \\ \text{subject to} \quad & L_1 \leq \Delta x_{\text{spine}}[k+j|k] \leq L_2 && \\ & S_1 \leq \Delta v_{\text{spine}}[N_e|k] \leq S_2 && \end{aligned} \quad (3.9)$$

in which Δx_{spine} and Δv_{spine} connects to a_{ref} via (3.1), (3.2), (3.7) and Assumption 3.3. The notation $\Delta x_{\text{spine}}[k+j|k]$ with $j > 0$ is used to denote the prediction of signal $\Delta x_{\text{spine}}[k+j]$ with knowledge up to time kT . Hence, the problem in (3.9) states that at every optimization instant $k \in \mathbb{K}_o$, the remaining setpoint sequence a_{ref} is chosen to minimize the maximum of $|a_{\text{spine}}|$, while satisfying constraints on the relative displacement and on the final relative velocity.

3.4.3 Formulation of Linear Constraints

To solve the problem in (3.9), the relative motions Δx_{spine} and Δv_{spine} have to be predicted on the basis of available information. It is chosen here to use a prediction model for the *absolute* chest motion, instead of the relative chest motion. This is an important choice, as will become clear in the next section.

From (3.2) and Assumption 3.3, it follows that $\dot{x}_{\text{spine}} = v_{\text{spine}}$ and $\dot{v}_{\text{spine}} = a_{\text{ref}}$. With an auxiliary state $x = [x_{\text{spine}} \ v_{\text{spine}}]^T$, two matrices A and B can be found straightforwardly such that $\dot{x}(t) = Ax(t) + Ba_{\text{ref}}(t)$. The pair (A, B) can be transformed to a discrete-time system, applying a zero-order hold to the input:

$$x[k+1|k] = \begin{pmatrix} 1 & T \\ 0 & 1 \end{pmatrix} x[k] + \begin{pmatrix} \frac{1}{2}T^2 \\ T \end{pmatrix} a_{\text{ref}}[k] = A_d x[k] + B_d a_{\text{ref}}[k] \quad (3.10)$$

When this model is executed recursively, the prediction of the relative motion can be written as

$$x[k+j|k] = \tilde{A}_d x[k] + \tilde{B}_d [a_{\text{ref}}[k] \quad a_{\text{ref}}[k+1] \quad \dots \quad a_{\text{ref}}[k+j-1]]^T$$

with $\tilde{A}_d = A_d^{(j)}$ and $\tilde{B}_d = [A_d^{(j-1)} B_d A_d^{(j-2)} B_d \dots B_d]$. Substituting A_d and B_d in this equation, the “prediction model” of the spine position and velocity is given by

$$\begin{aligned} x_{\text{spine}}[k+j|k] &= x_{\text{spine}}[k] + jTv_{\text{spine}}[k] + T^2 \sum_{i=0}^{j-1} (j-i-\frac{1}{2})a_{\text{ref}}[k+i] \\ v_{\text{spine}}[N_e|k] &= v_{\text{spine}}[k] + T \sum_{i=0}^{N_e-k-1} a_{\text{ref}}[k+i] \end{aligned} \quad (3.11)$$

with $k \in \mathbb{K}_o$, $j \in \mathbb{K}_e$. Note that the discrete-time prediction model is an unstable system, with two poles on the unit circle. However, applying the end constraint on the predicted velocity, (3.7), prevents this state to drift away. Stability of the prediction model is still not guaranteed, but the system is now made convergent. The current states of the prediction model, i.e. $x_{\text{spine}}[k]$ and $v_{\text{spine}}[k]$, are provided by an “open-loop observer”, which is also based on the same zero-order hold discrete-time system

$$\begin{aligned} x_{\text{spine}}[k] &= x_{\text{spine}}[0] + kTv_{\text{spine}}[0] + T^2 \sum_{i=0}^{k-1} (k-i-\frac{1}{2})a_{\text{ref}}[i] \\ v_{\text{spine}}[k] &= v_{\text{spine}}[0] + T \sum_{i=0}^{k-1} a_{\text{ref}}[i] \end{aligned} \quad (3.12)$$

with $k \in \mathbb{K}_o$. It is recognized that this observer is far from optimal: it is unstable, and moreover, it uses the setpoint instead of the actual spinal acceleration to estimate the current chest position and velocity. The current state could, however, also be provided by a stable observer based on measurements. Such an observer will be presented in the next chapter, but at this point, the unstable observer is used.

Before substituting (3.12) in (3.11), the initial state has to be defined:

Definition 3.7 / *At the moment of impact, i.e. at $t = 0$, the vehicle position, the vehicle velocity and the spinal position are defined as $x_{\text{veh}}[0] := 0$, $v_{\text{veh}}[0] := v_o$ and $x_{\text{spine}}[0] := 0$, respectively.*

With this definition, consider the following assumption:

Assumption 3.8 / *The relative spinal velocity at the moment of impact, i.e. at $t = 0$, is assumed to be zero. Hence with (3.7) and Definition 3.7, it follows that $v_{\text{spine}}[0] = v_o$.*

This assumption is plausible, since it is likely that an occupant or passenger braces itself before impact. The observer model in (3.12) can be substituted into the pre-

diction model in (3.11), and with Definition 3.7 and Assumption 3.8 the following equation can be obtained

$$\begin{aligned} x_{\text{spine}}[k+j|k] &= (k+j)Tv_o + T^2 \sum_{i=0}^{k+j-1} (k+j-i-\frac{1}{2})a_{\text{ref}}[i] \\ v_{\text{spine}}[N_e|k] &= v_o + T \sum_{i=0}^{N_e-1} a_{\text{ref}}[i] \end{aligned} \quad (3.13)$$

with $k \in \mathbb{K}_o$, $j \in \mathbb{K}_e$. The relative motion is now given by

$$\begin{aligned} \Delta x_{\text{spine}}[k+j|k] &= x_{\text{spine}}[k+j|k] - x_{\text{veh}}[k+j] \\ \Delta v_{\text{spine}}[N_e|k] &= v_{\text{spine}}[N_e|k] \end{aligned} \quad (3.14)$$

in which Assumption 3.5 is used to set the predicted final vehicle velocity to zero, $v_{\text{veh}}[N_e] = 0$. Note that the constraint equations in (3.9) now *linearly* depend on v_o , on the future vehicle displacement $x_{\text{veh}}[k+j]$ and on the virtual setpoint sequence $a_{\text{ref}}[i]$ for $i \in \{0, \dots, k+j-1\}$, given $j \in \mathbb{K}_e$ and $k \in \mathbb{K}_o$.

3.4.4 Linear Programming

The maximum objective in (3.9) can be rewritten to get a linear program (LP) by introducing an auxiliary variable $\gamma \geq 0$ (Boyd and Vandenberghe, 2004). This γ represents the maximum of the absolute value of $a_{\text{ref}}[k+j]$. Hence, (3.9) becomes

$$\begin{aligned} \min_{\mathbf{p}} \quad & \gamma \\ \text{subject to} \quad & -\gamma \leq a_{\text{ref}}[k+j] \leq \gamma \quad k \in \mathbb{K}_o, j \in \mathbb{K}_e \\ & L_1 \leq \Delta x_{\text{spine}}[k+j|k] \leq L_2 \\ & S_1 \leq \Delta v_{\text{spine}}[N_e|k] \leq S_2 \end{aligned} \quad (3.15)$$

where $\mathbf{p} \in \mathbb{R}^{N_e-k+2}$ contains the optimization parameters according to

$$\mathbf{p} = [a_{\text{ref}}[k] \quad a_{\text{ref}}[k+1] \quad \dots \quad a_{\text{ref}}[N_e] \quad \gamma]^T$$

The constraints are related to \mathbf{p} through (3.13)-(3.14). When the above constraint equations are written in matrix form, then (3.15) can be formulated as a standard inequality form LP

$$\begin{aligned} \min_{\mathbf{p}} \quad & \mathbf{c}^T \mathbf{p} \\ \text{subject to} \quad & H\mathbf{p} \leq \mathbf{b} \end{aligned} \quad (3.16)$$

with $\mathbf{c} = [0 \quad \dots \quad 0 \quad 1]^T \in \mathbb{R}^{N_e-k+2}$, and H and \mathbf{b} suitable vectors according to the constraint equations in (3.13)-(3.15). Note that the vector \mathbf{b}_p contains the

history of a_{ref} , the initial velocity v_o and the vehicle displacement prediction x_{veh} . The problem in (3.16) can now be efficiently and accurately solved by simplex or interior point methods (Boyd and Vandenberghe, 2004).

3.4.5 Results

The algorithm is implemented in Matlab/Simulink[®], and results are generated for $L_1 = -0.03$ m, $L_2 = 0.25$ m, $S_1 = -1$ m/s, $S_2 = 0$ m/s, $T = 0.1$ ms, $T_o = 10$ ms and $T_e = 200$ ms. At this point, it is assumed that full a priori crash information on x_{veh} is available. Later, this information will come from the second step in the RG, namely the crash prediction step as shown in Figure 3.3.

Since the computational complexity of the problem in (3.16) depends directly on the degrees of freedom in \mathbf{p} , a tractable optimization problem can be obtained by fixing the degrees of freedom to be constant over a certain number of samples. This is known as move blocking, see e.g. Cagienard et al. (2007). In (3.16), the number of parameters is reduced to 11, and the problem of finding the optimal \mathbf{p} is restated as finding the optimal $\hat{\mathbf{p}}$, where $\mathbf{p} = M\hat{\mathbf{p}}$ and $M \in \mathbb{R}^{(N_e - k + 2) \times 11}$ is the so-called blocking matrix. M is assumed to be a matrix with entries between zero and one only, such that \mathbf{p} is a linear interpolation of $\hat{\mathbf{p}}$. Note however that γ is not included in the move blocking. Correspondingly, constraint violation is checked at only 10 points on the future horizon. These problem reducing techniques save valuable computational time, while they still lead to good performance, as will be shown later on.

At every time instant kT , $k \in \mathbb{K}_o$, the optimal solution is calculated with a Linear Programming solver in Matlab², which uses the simplex algorithm. Figure 3.10 shows the outcome of the simulation for a crash pulse obtained from a 40% offset frontal impact with a small family car against a deformable barrier at 64 km/h. The top left figure shows the pulse a_{veh} (gray) and the optimal setpoint r (black). The obtained solution is near optimal as can be observed from the small peak at 20 ms, caused by the problem reduction methods described above.

The solution was found within 6 milliseconds – see figure on the top right – on an average workstation³, which is below the available time of $T_o = 10$ ms. Of course, with dedicated algorithms and hardware, this can easily be improved. The decrease in calculation times is caused by the fact that blocking matrix M decreases in size as the future horizon length decreases, although the degrees of freedom in

²LPSolve, Mixed Integer Linear Programming (MILP) solver, version 5.5 [online], <http://lpsolve.sourceforge.net/> (last access: August 2009)

³Simulations were performed on a workstation with a CPU that runs at 1.4 GHz.

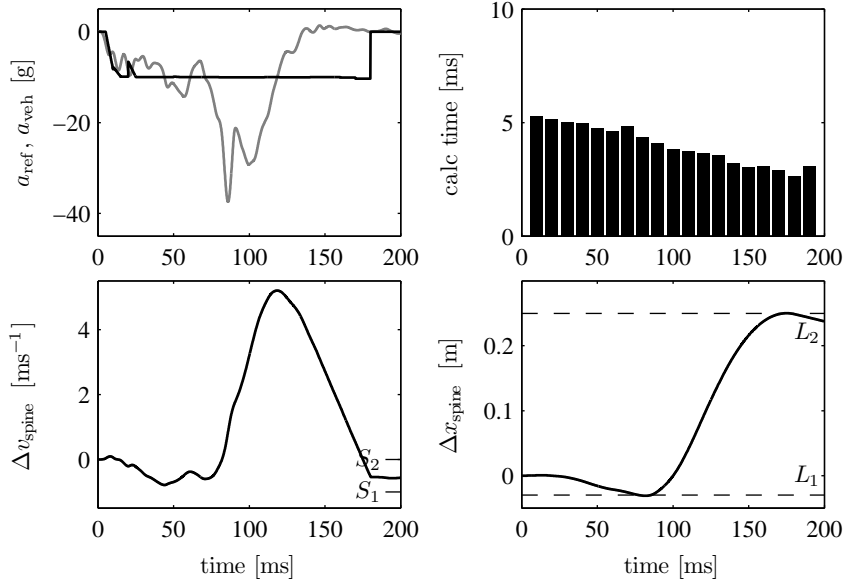


Figure 3.10 / Top left: The setpoint a_{ref} (black) for the spinal acceleration given a vehicle acceleration a_{veh} (gray), calculated with a priori crash information. Top right: Calculation times at every optimization step T_o . Bottom: The relative spinal motion does not violate the constraints.

\mathbf{p} remains constant. The bottom two figures show that the constraints are only slightly violated.

3.4.6 Conclusion

In this section, a setpoint optimization step has been developed that generates a setpoint for the primal controlled system shown in Figure 3.3. This setpoint is optimal in the sense that an upper bound on the A_{max} criteria is minimized while satisfying the constraint in (3.3). It was shown that a finite prediction horizon suffices when this constraint is replaced by (3.7) and (3.8). Using the models in (3.11) and (3.12), the constraints became linear in the optimization parameters, and the optimization problem could be written as an LP. To solve this LP, the initial vehicle velocity and a prediction of the future vehicle displacement are required. With assumed a priori knowledge of the latter, the obtained setpoint for a given crash pulse was shown to be near optimal, and it was found within a few milliseconds due to a move blocking procedure.

3.5 Prediction of Vehicle Motion

In this section, the third component of the cascade controller \mathcal{C} is designed, namely the crash prediction of the MPC controller \mathcal{M} . In (3.14), a prediction of the future vehicle displacement, $x_{\text{veh}}[k+j|k]$, is required. In this section, a method is proposed to predict this signal, and at the end of this section, the approximation error will be quantified and incorporated in the optimization problem in (3.15)

3.5.1 Objective Function

In Assumption 3.4, it has been stated that only the vehicle acceleration can be measured. This implies that a proper estimation of the position cannot be obtained by Kalman filtering techniques, since the position and velocity are both unobservable states (Skogestad and Postlethwaite, 2005). Therefore, the position is estimation by regression analysis. A vehicle displacement function, $\psi_x : \mathbb{R} \rightarrow \mathbb{R}$, is fitted to the history of x_{veh} . This function $\psi(t)$ is chosen to be twice differentiable in t , such that $\dot{\psi}$ and $\ddot{\psi}$ are the vehicle velocity and acceleration functions, respectively. The optimal fit is found by minimization of an objective function. The optimal vehicle displacement function, ψ , is then employed to predict the future vehicle displacement as follows:

$$x_{\text{veh}}[k+j|k] = \psi((k+j)T), \quad k \in \mathbb{K}_o, \quad j \in \mathbb{K}_e \quad (3.17)$$

Part of the objective function, J , consists of the sum of the squared error between the displacement history and the function evaluations ψ . The squared errors between *current* velocity and velocity function, and between the current acceleration and acceleration function are also included in J . Previously, it was assumed that the vehicle will reach zero velocity at time T_e , see Assumption 3.5. Therefore, it is required that the vehicle has zero velocity at an *additional* 10 time instants after T_e with a time separation of $\tau = 5$ ms. This objective forms the fourth and last part of J . Hence, the objective function J for $k \in \mathbb{K}_o$ reads

$$J[k] = \sum_{i=0}^k |\psi(iT) - x_{\text{veh}}[i]|^2 + \beta_1^2 |\dot{\psi}(kT) - v_{\text{veh}}[k]|^2 + \beta_3^2 \sum_{i=0}^{10} |\dot{\psi}(T_e + i\tau) - 0|^2 + \beta_2^2 |\ddot{\psi}(kT) - a_{\text{veh}}[k]|^2 \quad (3.18)$$

where $\beta_i > 0$, $i = 1, 2, 3$ are weighting constants. The objective function (3.18) requires knowledge of the current values of v_{veh} , a_{veh} , and the history of x_{veh} . According to Assumption 3.4, only the vehicle acceleration and initial velocity

are available for measurement. Therefore, again an “open-loop observer” is used similar to (3.12), hence

$$\begin{aligned} x_{\text{veh}}[k] &= 0 + kTv_o + T^2 \sum_{i=0}^{k-1} (k-i-\frac{1}{2})a_{\text{veh}}[i] \\ v_{\text{veh}}[k] &= v_o + T \sum_{i=0}^{k-1} a_{\text{veh}}[i] \end{aligned} \quad (3.19)$$

With this observer, the objective J now only depends on the measured vehicle acceleration a_{veh} , and the known initial speed v_o . Note that this discrete-time observer is marginally stable, since it is based on a double integrator so it has two poles on the unit circle. Adding the end constraint on the velocity stabilizes the second state.

3.5.2 Linear Regression

To solve the minimization of J , a polynomial basis function of order n is imposed on ψ :

$$\psi(t) = h_0 + h_1t + h_2t^2 + h_3t^3 + \dots + h_nt^n$$

with $h_i \in \mathbb{R}$, $i = 0, \dots, n$. The class of basis functions is limited by applying three constraints, using Definition 3.7:

$$\begin{aligned} \psi(0) &= x_{\text{veh}}(0) = 0 \quad \Rightarrow \quad h_0 = 0 \\ \dot{\psi}(0) &= v_{\text{veh}}(0) = v_o \quad \Rightarrow \quad h_1 = v_o \end{aligned}$$

Note that, e.g., the second through the fourth part in the objective function J could also be implemented by limiting the class of the polynomial basis function. However, this would give very complex expressions for the basis function parameters. The remaining parameters are stacked in a parameter vector $\mathbf{h} = [h_2 \ h_3 \ \dots \ h_n]^T$. The vehicle motion functions can be written linearly in \mathbf{h} as follows

$$\psi(t) = \mathbf{t}(t)\mathbf{h} + v_ot, \quad \dot{\psi}(t) = \dot{\mathbf{t}}(t)\mathbf{h} + v_o, \quad \ddot{\psi}(t) = \ddot{\mathbf{t}}(t)\mathbf{h} \quad (3.20)$$

with $\mathbf{t} : \mathbb{R} \rightarrow \mathbb{R}^{n-1}$ a vector function that is at least twice differentiable. It is given by $\mathbf{t}(t) = [t^2 \ t^3 \ \dots \ t^n]$. With (3.19)-(3.20) substituted into (3.18), the minimization of the objective function can be rewritten as a least squares problem:

$$\min_{\mathbf{h}} J[k] = \min_{\mathbf{h}} \|A_h[k]\mathbf{h} - \mathbf{b}_h[k]\|_2^2 \quad (3.21)$$

with matrices A_h and \mathbf{b}_h as follows

$$A_h[k] = \begin{bmatrix} \mathbf{t}(0) \\ \mathbf{t}(T) \\ \mathbf{t}(2T) \\ \mathbf{t}(3T) \\ \vdots \\ \mathbf{t}(kT) \\ \beta_1 \dot{\mathbf{t}}(kT) \\ \beta_2 \ddot{\mathbf{t}}(kT) \\ \beta_3 \dot{\mathbf{t}}(T_e) \\ \beta_3 \dot{\mathbf{t}}(T_e + \tau) \\ \vdots \\ \beta_3 \dot{\mathbf{t}}(T_e + 10\tau) \end{bmatrix}, \mathbf{b}_h[k] = \begin{bmatrix} 0 & 0 & 0 & \cdots & 0 & 0 \\ 0 & 0 & 0 & \cdots & 0 & 0 \\ 0 & \frac{1}{2}T^2 & 0 & \cdots & 0 & 0 \\ 0 & \frac{3}{2}T^2 & \frac{1}{2}T^2 & \cdots & 0 & 0 \\ \vdots & \vdots & \vdots & \ddots & \vdots & \vdots \\ 0 & (k - \frac{1}{2})T^2 & (k - \frac{3}{2})T^2 & \cdots & \frac{1}{2}T^2 & 0 \\ 0 & \beta_1 T & \beta_1 T & \cdots & \beta_1 T & 0 \\ 0 & 0 & 0 & \cdots & 0 & \beta_2 \\ -\beta_3 & 0 & 0 & \cdots & 0 & 0 \\ -\beta_3 & 0 & 0 & \cdots & 0 & 0 \\ \vdots & \vdots & \vdots & \ddots & \vdots & \vdots \\ -\beta_3 & 0 & 0 & \cdots & 0 & 0 \end{bmatrix} \begin{bmatrix} v_0 \\ a_{\text{veh}}[0] \\ a_{\text{veh}}[1] \\ \vdots \\ a_{\text{veh}}[k] \end{bmatrix}$$

It is well known, see, e.g., Boyd and Vandenberghe (2004), that the analytical solution to the least square problem in (3.21) is $\mathbf{h}^* = (A_h^T A_h)^{-1} A_h^T \mathbf{b}_h$, assuming A_h has full column rank. Since the first k rows of A_h have linearly independent columns and dimensions $k \times (n - 1)$, one can easily verify that A_h has full column rank for all $k \geq n - 1$. So the optimal solution exists, when there are at least as many data points available as the order of the basis function of ψ . Or in other words, the vehicle prediction can successfully be executed for the first time at $t \geq nT$. Algorithms and software for solving least-squares problems are very reliable and accurate, and embedded optimization is very well possible (Boyd and Vandenberghe, 2004).

With the optimal solution \mathbf{h}^* and equations (3.20) and (3.17), the prediction for x_{veh} reads

$$x_{\text{veh}}[k + j|k] = \mathbf{t}((k + j)T)\mathbf{h}^* + (k + j)Tv_0, \quad k \in \mathbb{K}_o, j \in \mathbb{K}_e \quad (3.22)$$

Summarizing, the vehicle prediction depends on sample time T , current time t , estimated end time T_e , initial vehicle speed v_0 , weightings β_i , polynomial order n and measurement history of a_{veh} .

3.5.3 Results

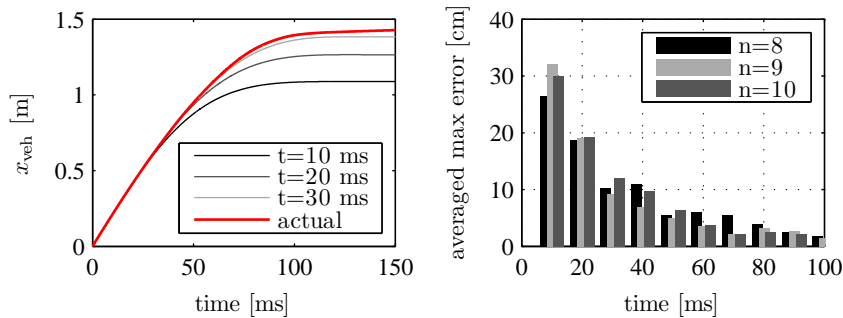
A large set of crash pulses, obtained from data from frontal EuroNCAP and US-NCAP impact tests, is used to evaluate the accuracy of the algorithm. The actual vehicle displacement is derived from the acceleration data, as an accurate vehicle position measurement during the crash was not available. The maximum of the absolute error between the predicted displacement at time $t = kT$ and the actual future vehicle displacement at that time is calculated at every optimization step T_o . This error is thus given by

$$\max_{j \in \mathbb{K}_e} |x_{\text{veh}}[k + j|k] - x_{\text{veh}}[k + j]|, \quad k \in \mathbb{K}_o \quad (3.23)$$

The error values are obtained for 19 different crash pulses and then averaged over the pulses. Figure 3.11(b) shows the error values for three different approximation orders $n = 8, 9, 10$, and for $T_o = 10$ ms, $T = 0.1$ ms, $\beta_1 = \beta_2 = 1$, $\beta_3 = 10$ and $T_e = 0.2$ s. The prediction algorithm is first executed at time $t = T_o = 100T \gg mT$, so the optimal solution exists. Each bar in the figure represents the maximum error of the prediction over the entire future horizon, predicted at the time indicated at the horizontal axis. The results show that for $n = 9$ the best results are obtained, leading to errors of less than 10 cm after 30 ms, and less than 5 cm after 50 ms. Figure 3.11(a) shows an example of the vehicle prediction, where the thick line represent the actual vehicle displacement $x_{\text{veh}}(t)$.

Given that the desired relative displacement of the chest is in the order of 25 cm, the obtained error values are acceptable after 30 ms. Especially since the setpoint optimization can adapt on-line to mismatches, as will be shown in Section 3.6 where the setpoint optimization and crash prediction are combined. Furthermore, as constraint violation is likely to occur at the end of the crash, prediction errors at the start of the crash are less critical. So, although the crashes differ substantially in magnitude, impact velocity and duration, the displacement is predicted with moderate accuracy.

In the vehicle prediction, the initial vehicle velocity v_o was obtained from integrating the measured acceleration signal. This implies that the initial estimate of v_o is *exact*. However, from (3.19) it can be observed that the displacement prediction is very sensitive to v_o : a mismatch of 1 m/s in v_o leads to an error of 10 cm after 100 ms. So, with the current proposed algorithm, the vehicle prediction will not be as accurate as sketched in Figure 3.11(b).



(a) Example of the vehicle prediction at several time instances, together with the actual vehicle displacement (thick).

(b) The maximum error according to (3.23), averaged over 19 crash pulses and for different approximation orders n .

Figure 3.11 / Results of the crash prediction algorithm.

3.6 Combined Model Predictive Controller

In this section, the results are shown for the Combined Model Predictive Controller, \mathcal{M} , which combines the setpoint optimization and the vehicle motion prediction, as depicted in Figure 3.3. To accommodate the prediction errors of the future vehicle displacement path, a robustified version of the setpoint optimization algorithm is proposed.

3.6.1 Robustness

The information about the maximum prediction error at every time instant k is shown in Figure 3.12. It is used in the setpoint optimization problem to cope with the uncertainty in the prediction. This will be done using a so-called robustness function $\epsilon : \mathbb{R} \rightarrow \mathbb{R}$. It is a function of time, and it is assumed that the maximum absolute error in the prediction of x_{veh} will be less than this function, in the sense that

$$\max_j |x_{\text{veh}}[k+j|k] - x_{\text{veh}}[k+j]| \leq \epsilon[k], \quad k \in \mathbb{K}_o, j \in \mathbb{K}_e \quad (3.24)$$

The function $\epsilon_x[k]$ decreases over time, as the maximum prediction error over 19 pulses also decreases, as can be seen in Figure 3.12. The function is chosen as

$$\epsilon[k] = \begin{cases} 0.20 - 1.33kT & \text{for } k \leq 0.15T^{-1} \\ 0 & \text{for } k > 0.15T^{-1} \end{cases} \quad (3.25)$$

and is indicated in Figure 3.12 by the black line. So (3.24) is being close to satisfied for $t \geq 30$ ms. In this function, ϵ is given in meter, and T in seconds.

The setpoint optimization algorithm is made robust against the inevitable vehicle prediction error. The robustified version of the optimization problem in (3.15) is obtained by decreasing the upper bound constraint with $\epsilon[k]$:

$$\begin{aligned} & \min_{\mathbf{p}} && \gamma \\ \text{subject to} & & -\gamma & \leq & r[k+j] & \leq & \gamma \\ & & L_1 & \leq & \Delta x_{\text{spine}}[k+j|k] & \leq & L_2 - \epsilon[k] \\ & & S_1 & \leq & \Delta v_{\text{spine}}[N_e|k] & \leq & S_2 \end{aligned} \quad (3.26)$$

for $k \in \mathbb{K}_o$, $j \in \mathbb{K}_e$. The modified constraint on the predicted Δx_{spine} guarantees that the actual relative spine displacement stays within bound L_2 . Besides, since ϵ is a decreasing function, the bound becomes less conservative as the crash progresses and more information becomes available. Note that the problem would become infeasible for $L_2 - L_1 < 0.2$. As it is more important to prevent head

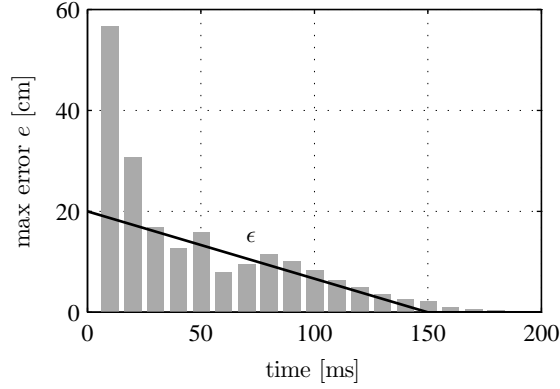


Figure 3.12 / The maximum error, according to (3.23), over the 19 pulses for $n = 9$, with robustness function ϵ , according to (3.25).

collision with the vehicle interior, it is chosen to guarantee that the upper bound is not violated. The prediction error in the final vehicle velocity can be neglected, see Assumption 3.6, and therefore the constraint on Δv_{spine} is not altered.

3.6.2 Results

The vehicle prediction is now used in the prediction model of the relative spinal displacement in (3.14). The resulting MPC controller \mathcal{M} , i.e. the robustified setpoint optimization combined with the vehicle prediction, is executed with identical setting as previously. So $T = 0.1$ ms, $T_o = 10$ ms, $T_e = 200$ ms, $L_1 = -0.03$ m, $L_2 = 0.25$ m, $S_1 = -1$ m/s, $S_2 = 0$ m/s, $n = 9$, $\beta_1 = \beta_2 = 1$ and $\beta_3 = 10$. Figure 3.13 shows the results of the MPC controller \mathcal{M} for the same EuroNCAP frontal impact pulse as in Figure 3.10. The controller starts at $t = 2T_o = 20$ ms, because the error in the vehicle prediction is too large at $t = T_o$, as can be observed in Figure 3.12, and a feasible solution could not be found. For $t < 20$ ms, the setpoint is set to $a_{\text{ref}}(t) = \alpha \cdot a_{\text{veh}}(t)$, with $0 < \alpha < 1$, as this will prevent the occupant from being pushed through the seat. A second result is shown in Figure 3.14, with the same settings but for a different crash pulse.

Obviously, the calculation times were higher than for the case in which it was assumed that full a priori knowledge of the crash is available, see Figure 3.10. The prediction step takes no more than 2 ms on the average. However, the constraints are tighter in the robustified version of (3.26), which leads in most cases to more computational effort, viz. 10 ms compared to 6 ms to find the optimal solution. In the used standard high-level computing language (Matlab[®]), solutions were hence

found within 12 ms. When the algorithms are efficiently rewritten in a middle-level language, e.g. C++, it is more than reasonable to assume that the solutions can be found within $T_o = 10$ ms, thereby meeting the real-time requirements.

The results show that the calculated setpoint, based on the vehicle prediction, is in both examples within 4 g of the optimal setpoint, obtained with full a priori crash information as in Section 3.4.5. This implies that *without* knowledge of the crash, close to optimal behavior can be predicted in terms of the injury parameter A_{\max} for the considered impact pulse.

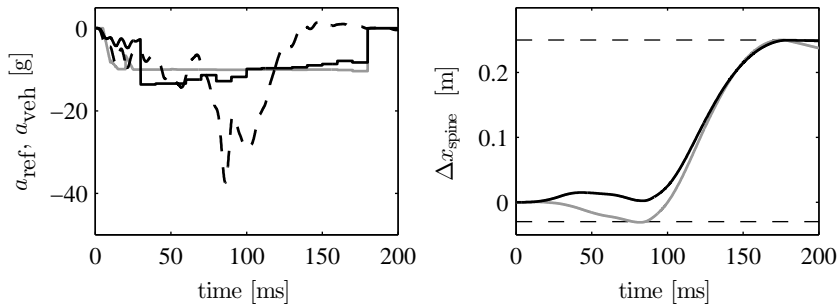


Figure 3.13 / Left: The optimal setpoint a_{ref} for the spinal acceleration with (gray) and without (black) prior knowledge of the 38 g crash pulse (dashed). Right: Corresponding relative spinal displacement.

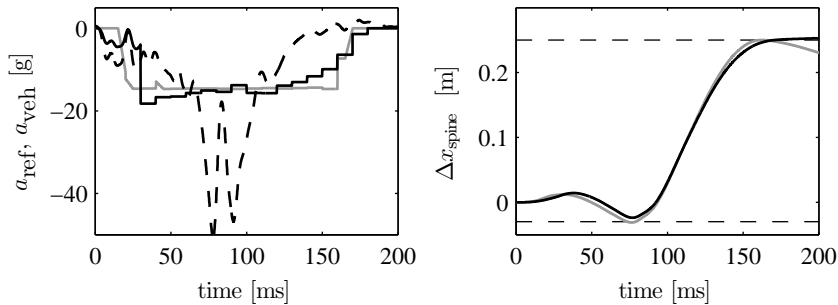


Figure 3.14 / Left: The optimal setpoint a_{ref} for the spinal acceleration with (gray) and without (black) prior knowledge of the 50 g crash pulse (dashed). Right: Corresponding relative spinal displacement.

3.7 Results with the Reference Model

In this section, the MPC cascade controller is evaluated using the primal controlled system. The primal controlled system consists of plant Σ and local controller \mathcal{K} , see Figure 3.3, and here, the model \mathcal{R} is chosen to represent system Σ . The model consists of a 50%-ile Hybrid III dummy from the MADYMO database (TNO Madymo B.V., 2005), seated in an interior compartment model, representing a small family car. The airbag system is disabled, and the conventional belt load limiter is replaced by a belt force actuator. For more details on this model, see Section 2.4.1 and Bosch-Rekvelde et al. (2005).

A simulation is performed with the reference model \mathcal{R} , and the MPC cascade controller \mathcal{C} , as depicted Figure 3.3. The control algorithm consists of the local controller \mathcal{K} from (3.6), the robustified optimization algorithm from (3.26) and the crash prediction from (3.22). Results for the controlled spinal acceleration, the required belt force and the performance variable $z = a_{\text{ref}} - a_{\text{spine}}$ are shown in Figure 3.15. Results are compared to responses from an identical occupant model with a conventional belt restraint system with a 4 kN load limiter.

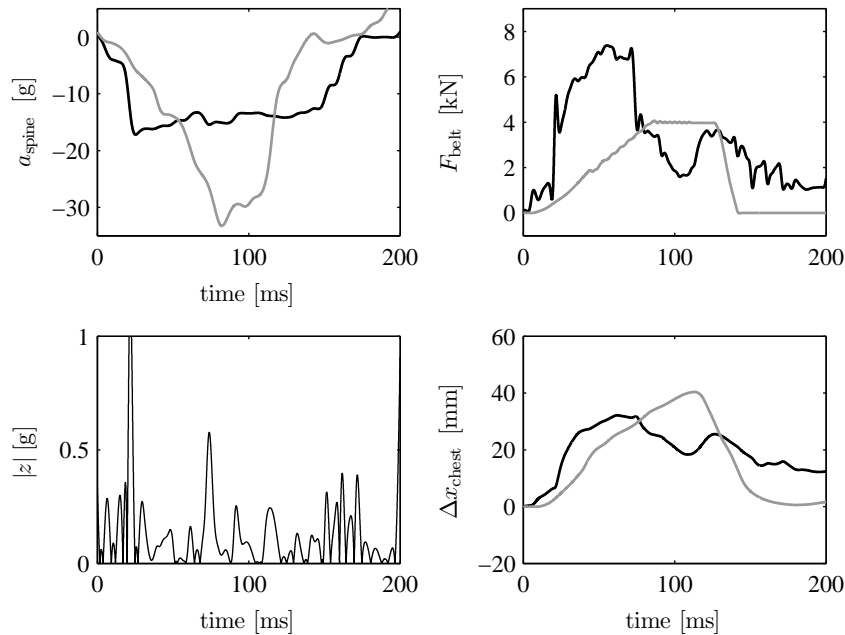


Figure 3.15 / Spinal acceleration (left) and belt force (right) from a system with a conventional restraint (gray) and a primal controlled system with the cascade MPC controller as proposed in this chapter (black).

It can be seen that the A_{\max} criterion has been reduced by approximately 45%. Moreover, the maximum tracking error is less than 1 g, which is higher than the requirement of 0.5 g, but the mean tracking error is less than 0.5 g. To emphasize the relevance of these results, note that the only inputs to \mathcal{C} are the initial vehicle velocity v_o , and the measured *current* vehicle acceleration a_{veh} , and spinal acceleration a_{spine} .

3.8 Discussion

In this chapter, a cascaded control strategy for real-time control of adaptive belt restraint systems is proposed. The control method consists of a combination of a primal controlled loop, and a Model Predictive Controller. The local controller, \mathcal{K} , gives excellent tracking properties and disturbance attenuation to the primal loop. The controller \mathcal{K} determines the belt force input based on the difference between the measured spinal acceleration, and a setpoint from the MPC controller.

The MPC controller, \mathcal{M} , finds an optimal setpoint, while satisfying constraints and without having a priori knowledge of the upcoming crash. In the algorithm, the injury criteria and the constraints are rewritten such that they depend linearly on the optimization variables. This allows writing the optimization problem as a Linear Program, which can be solved with low computational effort and which allows the MPC controller to meet real-time requirements. The controller \mathcal{M} also includes a vehicle motion estimation procedure to obtain good estimates of the vehicle position during the crash. The optimization algorithm of the controller is robustified with respect to uncertain prediction errors.

Moreover, the whole design procedure is generic in nature. For instance, it is straightforward to include multiple injury criteria in the design process. LTI models are available that approximate various thoracic injury criteria based on the crash pulse and the belt force. Adding an LTI model to the optimization objective will still lead to an LP problem, which can hence be solved efficiently. Also, the flexibility in the design of the primal controller enables to accommodate the primal controller to different plant dynamics, slow actuator dynamics, and to the filtering properties of output observer for, e.g., a_{spine} .

The performance of the overall control scheme can be improved when accurate pre-crash information systems become available in the near future. This systems could be based on lidar, radar or vision devices that detect the closing speed or impact angle, or could contain knowledge of the vehicle deformation properties from crash simulation models, see Eichberger et al. (2009). The reason is that the vehicle motion prediction can be significantly improved. This could potentially lead to a further reduction of injury risk, although the room for improvement

beyond the already achieved reduction is limited. A second improvement in the design is achieved when the (unstable) chest motion observer in (3.12) is replaced by a stable observer. Such an observer is derived in the next chapter, but using it would imply that a feedback loop is introduced from the plant Σ to the MPC controller \mathcal{M} , see Figure 3.3. This could possibly lead to stability issues, although it can be expected that no problems will arise when the settling time of the primal loop is sufficiently smaller than the execution period of the MPC controller.

In summary, the cascaded control strategy is believed to be an important step towards real-time implementation of controlled safety restraint systems. It reduces the injury criteria considerably (e.g. A_{\max} with 45%) with respect to conventional restraint systems, while still meeting the real-time computational requirements. It should be mentioned that this injury reduction is achieved with an ideal belt actuator (Assumption 3.1), a perfect sensor for the spinal acceleration (Assumption 3.2) and knowledge of the vehicle acceleration and initial velocity (Assumption 3.4). In the next two chapters, approximate solutions are presented for the first two assumptions.

4

SMART SENSORS FOR THORACIC INJURIES ESTIMATION

Abstract / This chapter presents a method to estimate the biomechanical responses of a vehicle occupant in real-time during an impact. These estimated responses are relevant to the control algorithm of the CRC system, or may be used to improve this controller. Kalman filtering is employed to estimate the state and output of the system, based on measurements of four simple, low cost sensors. Simulation results show that an estimation of the relevant thoracic injury criteria can be provided.

4.1 Introduction

In the control algorithm \mathcal{C} presented in Chapter 3, it has been assumed that the spinal acceleration could be measured in real-time. Moreover, it was discussed that the potential injury reduction with this controller could be improved when multiple IC are included, corresponding to the biomechanical responses listed in Table 1.2. However, not all of the required sensors to measure these responses do yet exist, whereas many of the available sensors are too expensive, too inaccurate or have too low a bandwidth. Automotive safety engineering would thus benefit from alternative techniques in (spatial) occupant sensing. In the next section, an overview is given of current sensor technologies, and subsequently, sensors are selected in accordance with the CRC system requirements.

This chapter is largely based on E.P. van der Laan et al. (2007b), State Estimator Design for Real-time Controlled Restraint Systems. In *Proceedings of the IEEE American Control Conference (ACC)*, New York City, NY, USA, 11-13 Jul, p. 242-247.

4.2 Vehicular Occupant Sensors

Two general requirements can be formulated on the sensors that are to be used in a CRC seat belt system. The sensors

- must be low-cost devices, since the financial margins in automotive industry are small;
- do not have to be installed or mounted by the vehicle occupant when entering the vehicle. People tend to forget to perform this action, or are simply not willing to.

Moreover, the sensors that are required can be categorized according to two main functions. The first type of sensors are called the *biomechanical sensors*, as they

- i) must provide information on the biomechanical responses a_{spine} , Δx_{ribs} , Δx_{chest} and Δx_{chest} , which could be used in the cascade controller \mathcal{C} . Since the primal controlled system with ideal sensors has a closed-loop bandwidth between 300-400 Hz, see Section 3.3.3, the sensors must have a bandwidth of around 1 kHz¹;

The second type of sensors are referred to as *classification sensors*, as they

- ii) must be able classify the operating environment during the normal driving phase, such that optimal controller parameters can be selected. In such a sensor, the bandwidth is not relevant, as the measurement can take place at anytime during the normal driving phase.

This second type follows from Section 3.3.3, in which it was shown that different local controllers have to be applied in correspondence with the various occupant sizes. Therefore, a sensor is desired that classifies the occupant during the normal driving phase, such that the suitable local controller can be selected. Secondly, in the constrained control problem given by (3.15), the constants L_1 and L_2 , which were related to the position of the seat and steering wheel, have to be chosen. A sensor that measures these positions is hence desired. Thirdly, in Chapter 3 it was assumed that a measurement of the vehicle velocity at the onset of the crash was available.

Sensors can be divided in two general classes, namely contact and non-contact sensors, also known as mechanical and spatial sensing technologies, respectively. The following paragraphs give an overview of both classes, as far as they are relevant considering the requirements listed above.

¹The sensor bandwidth is defined here as the frequency at which a sensor amplifies the measured signal with -3 dB below the average passband.

4.2.1 Spatial Sensing Technologies

Spatial sensing techniques usually monitor the presence of objects and the position of the occupant with a low update frequency. They are therefore typically employed to (statically) determine whether an occupant is in the airbag deployment zone. However, they may also be used to capture the motion of the occupant during the crash. Various technologies have been developed for spatial sensing, each with its advantages and disadvantages, see Wismans (2003). The five main technologies are summarized below, and (dis)advantages are given in Table 4.1.

Thermal infrared (IR) imaging. Research on thermal infrared imaging has focussed so far on detecting heads movements, and classification of the rear and forward facing child (Texas Transportation Institute, 2006).

Capacitive or Electric field. Kithil (1998) has developed a capacitive occupant sensing technology. A low-level electrical field is created by the device, which is changed by the presence of an occupant. Capacitive sensors can in this way determine the radial distance of the occupant from the sensor up to 0.6 m., and with an error below 2.5 mm. The system can acquire data continuously at 1 kHz. A more recent, but similar system is the Occupant Position Detection System² described by Fukui et al. (2001).

Ultrasonic. Breed et al. (2001) describe the first spatial occupant sensing system that has been released on a production vehicle. The detection system works by emitting 50 kHz sound waves from ultrasound transducers that are installed around the passenger. The sensor picks up the resulting echoes, and determines the (presence and) position of the occupant with respect to the vehicle interior. The position and velocity of the occupant can be determined with an update frequency of 100 Hz, which is sufficient during normal driving, but insufficient during the crash.

Visual Servoing. An optical video camera with stereo- or monovision can be used for so-called markerless human motion capture. The camera's images are analyzed using image-processing algorithms to determine the position of the occupant. Schoenmackers and Trivedi (2003) are able to locate the torso and head of a passenger seat occupant at 15 Hz. Since computing power is nowadays readily available at low cost, image-processing algorithms and data acquisition are also becoming faster. As an example, de Best et al. (2009) presented a vision based system that is able to measure the position of a marker at an update frequency of 1 kHz (in ideal conditions).

²Elesys Inc., Occupant Position Detection System (OPDS) [online], <http://www.elesys-na.com> (last access: August 2009)

Near infrared (IR) imaging. Near infrared imaging methods are a type of range measurement that employ mostly lasers. The lasers emit frequency modulated waves, and the delay of the beam reflected from a distant object is evaluated. The update frequency of the system can be close to 50 Hz, giving it the capability of tracking the occupant motion (Texas Transportation Institute, 2006).

Table 4.1 / Spatial Sensing Technologies

#	Technology	Advantage	Disadvantage
1	Thermal IR	lighting conditions irrelevant	low bandwidth clear line-of-sight temperature sensitive
2	Capacitative	low cost all conditions high bandwidth	limited sensing range blocked by conductives
3	Ultrasonic	lighting conditions irrelevant low cost high bandwidth	clear line-of-sight temperature sensitive interference sensitive (calibration)
4	Visual	deals with complex scenes can deal with color contrast	lighting conditions clear line-of-sight costs low bandwidth
5	Near IR	lighting conditions irrelevant compact low cost	line of sight low bandwidth

4.2.2 Mechanical Sensing Technologies

Mechanical, or contact sensing technologies are mostly used for occupant (weight) classification, but also for seat position or seat slide travel (Wismans, 2003). The seated weight sensors measure the occupant's weight to discern a small child from an adult. The airbag deployment can be adjusted accordingly, or may be disabled if a child or empty seat is detected. See for example the Delphi Passive Occupant Detection System³. Seat slide travel sensors are used to detect whether the seat is positioned far forward, which indicates that a small person is driving the vehicle and that the airbag timing should be adapted (Fleming, 2008).

³Delphi Automotive Systems Inc., Passive Occupant Detection System (PODS-B) [online], <http://www.delphi.com> (last access: August 2009)

Mechanical sensing technologies may also be used to provide indirect information on the occupant. For example, sensors that measure the belt rollout may be used to determine the forward occupant motion during a crash. The rollout sensors usually consist of a geared rotation counter that is mounted on the retractor drum (Wismans, 2003). Table 4.2 lists candidate mechanical sensors that may be used as biomechanical sensors.

Table 4.2 / Candidate mechanical sensors for sensing the biomechanical responses.

#	Sensor
1	Belt roll-out at the retractor
3	Belt slip through D-ring or buckle
4	Absolute acceleration of belt segments
5	Tension force in the seat belt segments (pillar, shoulder or lap belt)
6	Force on the belt attachments points
7	Force on the seat back or cushion
8	Friction force on the seat cushion
9	Force on the steering wheel

4.2.3 Selection of Sensors

Two types of sensors have to be selected as stated in Section 4.2, viz. biomechanical and classification sensors.

Concerning *biomechanical sensors*, the spatial sensing technologies have the advantage of being non-contact, but only capacitive sensors have a sufficient bandwidth (although current research on visual servoing is promising). The disadvantage of these capacitive sensors is their sensitivity to conductive materials (metal) in the sensing range, since these materials easily perturb the electric field. Especially during a crash event, all kinds of objects may be flying in the vehicle. It is therefore concluded that spatial occupant sensors are not (yet) applicable in a CRC systems, since they are too slow, too sensitive or easily blocked. Mechanical sensing technologies, on the other hand, offer a better perspective. Concerning the spinal acceleration, a_{spine} , it is expected that this response could be estimated with one or more acceleration sensors (#4) that are sewed in the shoulder belt segment. It is assumed that these sensors measure the (absolute) forward acceleration of the sternum, a_{ribs} . Furthermore, it is plausible that the relative displacement of the sternum, Δx_{ribs} , can be estimated from the difference between the a_{ribs} measurement and a_{veh} , the output of a vehicle acceleration sensor. To compensate for typical drift when double integrating an acceleration signal, a position sensor

should be included. Here, it is chosen to use a belt displacement sensor (#1), which yields signal x_{belt} . The belt force actuator is part of the CRC system, and since it has a local feedback controller, a sensor signal for the pillar belt force, F_{belt} , will be available (#5). Hence, it is proposed that with these four sensors for the belt force, the sternum acceleration, the belt position and the vehicle acceleration, the four biomechanical responses as listed in Section 4.2 can be estimated.

Concerning the *classification sensors*, one objective is to determine the occupant type. In a paper by van der Laan et al. (2008a), a method is proposed where the LTI occupant models from Section 2.8 are interpolated based on the total mass of the occupant, m_{occ} . The classification of the occupant during the normal driving phase is therefore based on the seated weight of the occupant, and hence a seat weight sensor system is included. Appropriate values for L_1 and L_2 are determined with a sensor for the seat slide travel, Δx_{seat} . For the initial vehicle velocity, v_o , the GPS speed estimate or the vehicle's speedometer can be used to determine the speed just before impact.

The proposed sensors are listed in Table 4.3, together with their output variable. Note that the measurable variables of system Σ are collected in variable \mathbf{v} , see Figure 1.5, so

$$\mathbf{v}(t) = [F_{\text{belt}}(t) \quad a_{\text{veh}}(t) \quad x_{\text{belt}}(t) \quad a_{\text{ribs}}(t) \quad m_{\text{occ}} \quad \Delta x_{\text{seat}} \quad v_o]^T$$

Table 4.3 / Sensors used in CRC seat belt system.

Sensor	Output	Objective
Force on seat cushion	m_{occ}	Select occupant model and local controller
Seat slide travel	Δx_{seat}	Determine constraint constants in MPC controller
Initial vehicle velocity	v_o	For vehicle prediction in the MPC controller
Belt roll-out	$x_{\text{belt}}(t)$	Estimate biomechanical responses
Acceleration of shoulder belt	$a_{\text{ribs}}(t)$	Estimate biomechanical responses
Actuator belt force	$F_{\text{belt}}(t)$	Estimate biomechanical responses
Vehicle acceleration	$a_{\text{veh}}(t)$	Estimate biomechanical responses

In the following section, a method is described that consist of model-based filtering of the measurable outputs of the system Σ , to reconstruct the biomechanical occupant responses.

4.3 The Kalman Filter

Whenever the state of a system must be estimated from noisy or uncertain sensor information, some kind of state estimator is employed to fuse the data from different sensors together to produce an accurate estimate of the true system state (Julier and Uhlmann, 1997). Kalman filtering is a common method to estimate the state of a system from available data and a model of the system (Gelb, 1974; Kalman, 1960). The Kalman filter is shortly explained below.

4.3.1 Algorithm

The algorithm for a Kalman filter can be found in standard literature, see e.g. Gelb (1974), but some elements have to be mentioned here. Consider the system Σ with $\mathbf{w} \in \mathbb{R}^2$ as input variable, see (1.4). The measurable *output* variable of this system is specified in the previous section. Note that it coincides with (2.2), so the measurable output is

$$\mathbf{y}_3(t) = [x_{\text{belt}} \quad a_{\text{ribs}}]^T \quad (4.1)$$

This system is modeled by a linear time-invariant model, see (2.14) in Section 2.8. It is governed by the stochastic, discrete-time differential equation

$$\begin{aligned} \mathbf{x}[k+1] &= A\mathbf{x}[k] + B\mathbf{w}[k] + \mathbf{n}_x[k], & \mathbf{x}[0] &= \mathbf{x}_o \\ \mathbf{y}_3[k] &= C_3\mathbf{x}[k] + D_3\mathbf{w}[k] + \mathbf{n}_y[k] \end{aligned} \quad (4.2)$$

with $\mathbf{n}_x \in \mathbb{R}^{23}$ and $\mathbf{n}_y \in \mathbb{R}^2$ the process and measurement noise, respectively. The noise signals are uncorrelated, have a statistically zero mean, and are spectrally white with a normal probability distribution⁴ $Pr(\mathbf{n}_x) \sim N(0, Q)$ and $Pr(\mathbf{n}_y) \sim N(0, R)$. The matrices Q and R are constant, diagonal, noise covariance matrices.

The Kalman filter tries to estimate the state $\mathbf{x} \in \mathbb{R}^{23}$ of this LTI model, given by $\hat{\mathbf{x}}$. Define the expected value of the error in the state estimate by an error estimate covariance matrix P

$$P[k] := E((\mathbf{x}[k] - \hat{\mathbf{x}}[k])(\mathbf{x}[k] - \hat{\mathbf{x}}[k])^T) = P^T[k]$$

hence $P \in \mathbb{R}^{23 \times 23}$. The state is estimated by minimizing the trace of this matrix, and the state estimation is achieved in two steps, the prediction and correction step.

⁴For a normal distributed, stochastic, scalar signal n , it holds that $Pr(|n| \leq \sigma) = 0.683$, with σ the standard deviation, given by the square root of the covariance.

Firstly, the state, the error covariance matrix and the output are predicted in the *prediction or time update* step:

$$\begin{aligned}\hat{\mathbf{x}}[k|k-1] &= A\hat{\mathbf{x}}[k-1] + B\mathbf{w}[k-1] \\ P[k|k-1] &= AP[k-1]A^T + Q\end{aligned}\quad (4.3)$$

with $P[0] = (\mathbf{x}_o - \hat{\mathbf{x}}[0])(\mathbf{x}_o - \hat{\mathbf{x}}[0])^T$. After this, the *correction or measurement update* follows:

$$\begin{aligned}\hat{\mathbf{x}}[k] &= \hat{\mathbf{x}}[k|k-1] + \mathcal{L}[k](\mathbf{y}_3[k] - \hat{\mathbf{y}}_3[k|k-1]) \\ \hat{\mathbf{y}}_3[k|k-1] &= C_3\hat{\mathbf{x}}[k|k-1] + D_3\mathbf{w}[k] \\ P[k] &= (I - \mathcal{L}[k]C_3)P[k|k-1]\end{aligned}\quad (4.4)$$

with $\mathcal{L} \in \mathbb{R}^{23 \times 2}$ the filter gain. Under some conditions, minimization of the trace of P yields a unique solution for \mathcal{L} :

$$\mathcal{L}[k] = P[k|k-1]C_3^T(C_3P[k|k-1]C_3^T + R)^{-1}\quad (4.5)$$

Now, if (4.2) is detectable, i.e. iff its unobservable modes are stable, then an \mathcal{L} exists that renders a stable observer (Zhou et al., 1996). Note that the elements in the filter gain \mathcal{L} express the ratio between the uncertainty in the state estimate and the uncertainty in the measurement. The combined observer estimates the output \mathbf{y} based on measurements \mathbf{w} and \mathbf{y}_3 , and reads

$$\mathcal{O}[k] : \begin{bmatrix} \hat{\mathbf{x}}[k] \\ \hat{\mathbf{y}}[k] \end{bmatrix} = \begin{bmatrix} (I - \mathcal{L}[k]C_3)A & (I - \mathcal{L}[k]C_3)B & -\mathcal{L}[k]D_3 & \mathcal{L}[k] \\ C & 0 & D & 0 \end{bmatrix} \begin{bmatrix} \hat{\mathbf{x}}[k-1] \\ \mathbf{w}[k-1] \\ \mathbf{w}[k] \\ \mathbf{y}_3[k] \end{bmatrix}\quad (4.6)$$

with \mathbf{y} given by

$$\mathbf{y} = [a_{\text{spine}} \quad \Delta x_{\text{chest}} \quad \Delta v_{\text{chest}} \quad \Delta x_{\text{ribs}} \quad x_{\text{belt}} \quad a_{\text{ribs}}]^T$$

as in (2.3). Define $\mathcal{O}(s)$ as the time-varying transfer function from measurement to estimated output

$$\mathcal{O}(s) = C(s(A - \mathcal{L}C_3) - I)^{-1}\mathcal{L}, \quad \Rightarrow \quad \hat{\mathbf{y}}(s) = \mathcal{O}(s)\mathbf{y}_3(s)$$

with $\mathcal{O}(s) \in \mathbb{R}^{6 \times 2}$. See Figure 4.1 for a layout of the Kalman filter.

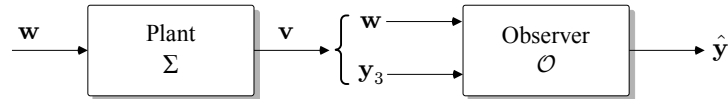
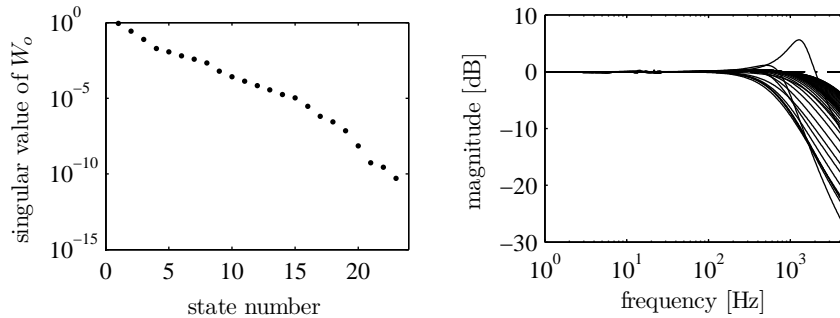


Figure 4.1 / Layout of the Kalman filter, applied to the plant Σ .

4.3.2 Filter Design

As discussed in Section 2.8, the system in (4.2) is stable, so it has no unstable modes that are unobservable. Hence, the system is detectable and a \mathcal{L} exists that renders \mathcal{O} stable. The system could, however, contain stable modes that are unobservable, hence the system's observability is evaluated. A system is called (state) observable, if the initial state can be determined from the history of the input and the measurement (Skogestad and Postlethwaite, 2005). For the linear system in (4.2), observability can be determined by a test on the pair (A, C_3) , namely, the observability grammian W_o must have full rank. Rank condition tests are not very practical for high order systems from a numerical point of view, so the singular values of W_o are determined. Each singular value is associated with a vector, that spans a subspace of the state space. The singular value is a relative measure of the observability of this subspace in the output. Intuitively formulated, a small singular value means that if the system is in this subspace, it does hardly transfer energy to the output and can hence badly be observed. In Figure 4.2(a), the singular values of the grammian W_o of the pair (A, C_3) are plotted. It shows that the singular values 21-23 have a relatively very low value, so a part of the state space could be badly reconstructed. This does not necessarily imply that the output \mathbf{y}_3 is badly estimated, as the contribution of this subspace to this output is low. However, there is no guarantee that a different linear combination of the states, e.g. $\mathbf{y} = C\hat{x}$, is properly estimated.



(a) Singular values of observability grammian W_o , associated with system (A, C_3) .

(b) Magnitude plot of the frequency response function from measured input x_{belt} to estimated output \hat{x}_{belt} .

Figure 4.2 / Properties of the Kalman filter.

In Section 3.3.2, it was proposed that the measurement noise on acceleration signals satisfies $|n_y| \leq 1$ g, so assuming a normal distribution, $3\sigma \approx 1$ g. So the variance (σ^2) of the noise on a_{spine} is taken to be $10 \text{ m}^2/\text{s}^4$. For x_{belt} , the measurement

noise is taken rather large, i.e. $|n_y| \leq 0.03$ m, so the variance is 10^{-4} m². The process noise \mathbf{n}_x is chosen rather large, with a standard deviation (RMS) value of 1.0, in appropriate SI units. Hence, the covariance matrices read

$$R = \begin{bmatrix} 1.0 \cdot 10^{-4} & 0 \\ 0 & 10 \end{bmatrix}, \quad Q = I_{23}$$

and so R^{-1} exists.

The Kalman filter gain $\mathcal{L}(t)$ is determined according to (4.5) for $\hat{\mathbf{x}}_o = \mathbf{x}_o$, which implies $P(0) = 0$. The differential equation for the error covariance matrix is solved with an Euler solver with a 0.1 ms sample time. This allows to precalculate the observer filter gain $\mathcal{L}(t)$. The filter gain is evaluated at 50 points on a 3 ms time grid, and its values are used to calculate the transfer function in (4.3.1) on the same grid. The result is graphically depicted in Figure 4.2(b), which shows the magnitude of the frequency response function from measured input x_{belt} to estimated output \hat{x}_{belt} . As shown in the figure, this specific transfer function resembles a second order low-pass filter, with a bandwidth between 0.5-5 kHz. The variations in magnitude after the bandwidth are caused by the variations in gain \mathcal{L} .

4.3.3 Results

The Kalman filter is now applied to the reference model \mathcal{R} from Section 2.4. The appropriate LTI model \mathcal{P} that has to be used in the Kalman filter algorithm in (4.6), may be selected using the seated weight sensor discussed previously. Here, the 50th percentile dummy is used as a reference model, so also the corresponding LTI model is chosen, see Section 2.8.4. The measurement outputs of \mathcal{R} are perturbed with noise \mathbf{n}_y .

The measurement signals are shown in Figure 4.3, together with the estimated output by \mathcal{O} . One can see proper estimation of the measurements. This, however, does not mean that all states are well recovered. Figure 4.4 shows the remaining 4 estimated outputs, which are a linear combination of the states and the input. The spinal acceleration and chest deflection are well estimated, but the model updates by the Kalman filter worsens the output estimates for the chest deflection velocity and sternal displacement. It is likely that this is caused by limitations of the linear model, not the Kalman filter, since other responses are well estimated. The outputs of the nonlinear reference model can not be properly estimated by a linear Kalman filter.

Many techniques exist for state estimation of nonlinear systems, and a well-known method is the Extended Kalman Filter (EKF) (Gelb, 1974).

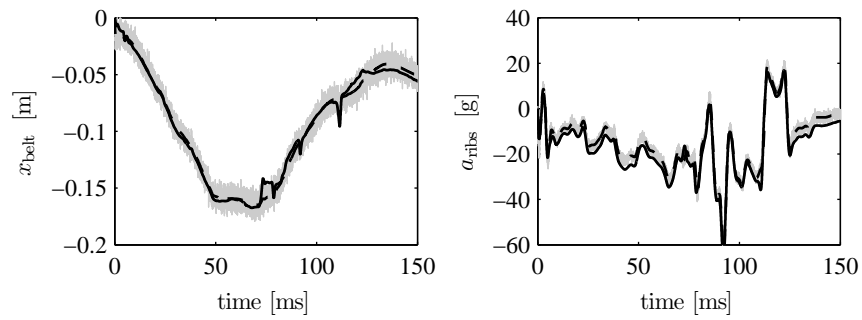


Figure 4.3 / Measured outputs of the Madymo reference model (dashed), perturbed with measurement noise (gray), and the estimated outputs by the Kalman filter (black).

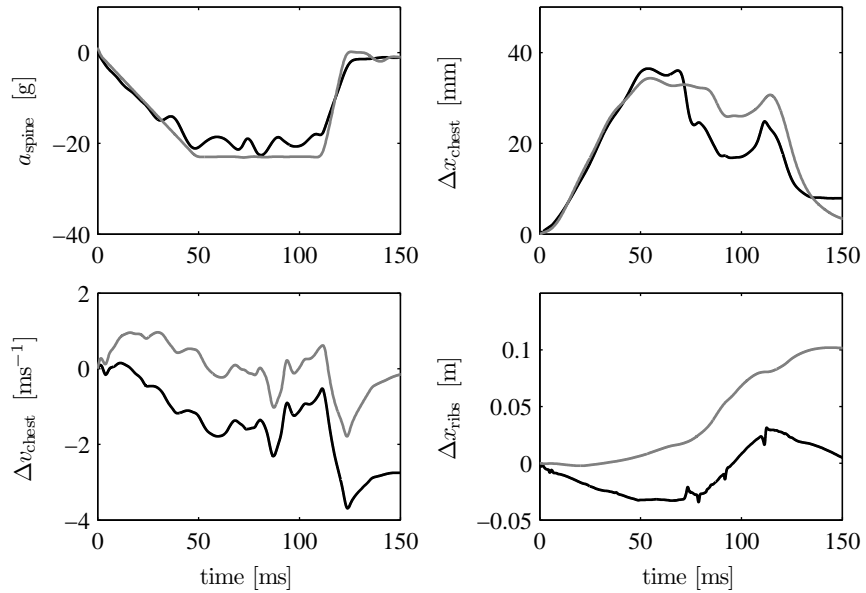


Figure 4.4 / Biomechanical responses of the Madymo reference model (gray), and the estimated outputs by the Kalman filter (black).

4.4 The Linearized Extended Kalman Filter

An Extended Kalman Filter (EKF) can be employed when the dynamics of the system to be observed are (predominantly) nonlinear. The reader can find more details on EKFs in e.g. Gelb (1974). Now consider the nonlinear design model presented in Section 2.6

$$\mathcal{D}_3 : \begin{cases} \mathbf{x}[k+1] &= \mathbf{f}(\mathbf{x}[k], \mathbf{w}[k]) + \mathbf{n}_x[k], & \mathbf{x}[k] = \mathbf{x}_o \\ \mathbf{y}_3[k] &= \mathbf{g}_3(\mathbf{x}[k], \mathbf{w}[k]) + \mathbf{n}_y[k] \end{cases}$$

with $\mathbf{n}_x \in \mathbb{R}^{28}$ and $\mathbf{n}_y \in \mathbb{R}^2$ again the process and measurement noise, respectively. The Kalman gain and error covariance matrix are found according to (4.5) and (4.3)-(4.4), respectively. Only now, the matrices A and C_3 in these equations are time-variant and are obtained as follows

$$A[k] := \left. \frac{\partial \mathbf{f}(\mathbf{x}, \mathbf{w})}{\partial \mathbf{x}} \right|_{\hat{\mathbf{x}}[k], \mathbf{w}[k]}, \quad C_3[k] := \left. \frac{\partial \mathbf{g}_3(\mathbf{x}, \mathbf{w})}{\partial \mathbf{x}} \right|_{\hat{\mathbf{x}}[k], \mathbf{w}[k]}$$

So the matrices are evaluated along the estimated state. The nonlinear model is updated by the Kalman gain in a similar way as with the linear filter, so the extended Kalman filter is given by

$$\mathcal{O}[k] : \begin{cases} \hat{\mathbf{x}}[k] &= \mathbf{f}(\hat{\mathbf{x}}[k-1], \mathbf{w}[k-1]) + \mathcal{L}[k] (\mathbf{y}_3 - \mathbf{g}_3(\hat{\mathbf{x}}[k-1], \mathbf{w}[k])) \\ \hat{\mathbf{y}}[k] &= \mathbf{g}_3(\hat{\mathbf{x}}[k], \mathbf{w}[k]) \end{cases}$$

The EKF is slightly modified however. Instead of evaluating the Jacobians every time step, constant time-invariant matrices A and C_3 are used. Calculating the Jacobians is a time-consuming process, and it is not expected that these computations can meet the real-time requirements. Hence, the resulting *linearized* Extended Kalman Filter consists of a filter gain $\mathcal{L}[k]$ that can be computed offline, given the constant matrices A , C_3 , R , and Q . In fact, it is identical to the filter gain from Section 4.3.1. So the prediction or time update step is done with the nonlinear model, and the update step is performed with the linear filter gain. Generally, this procedure yields less accurate filtering properties, as the linearization point is not as close to the actual trajectory as $\hat{\mathbf{x}}$ (Gelb, 1974).

The linearized EKF is applied to the same measurement data set as in the previous section. Results are shown in Figure 4.5 and Figure 4.6. It illustrates that the Kalman filter with the nonlinear prediction step clearly performs a more accurate estimation than the linear Kalman filter. In addition, also neck injury responses are shown. Unfortunately, the relative sternum displacement, Δx_{ribs} , is badly predicted in the region of interest, i.e. the region when the occupant is close to the steering wheel.

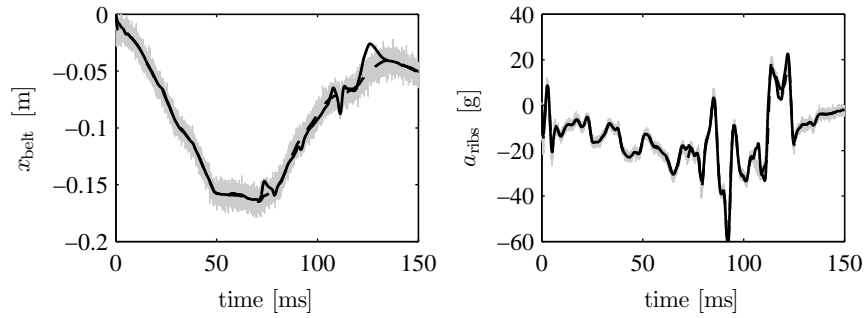


Figure 4.5 / Biomechanical responses of the Madymo reference model (gray), and the estimated outputs of the linearized EKF (black).

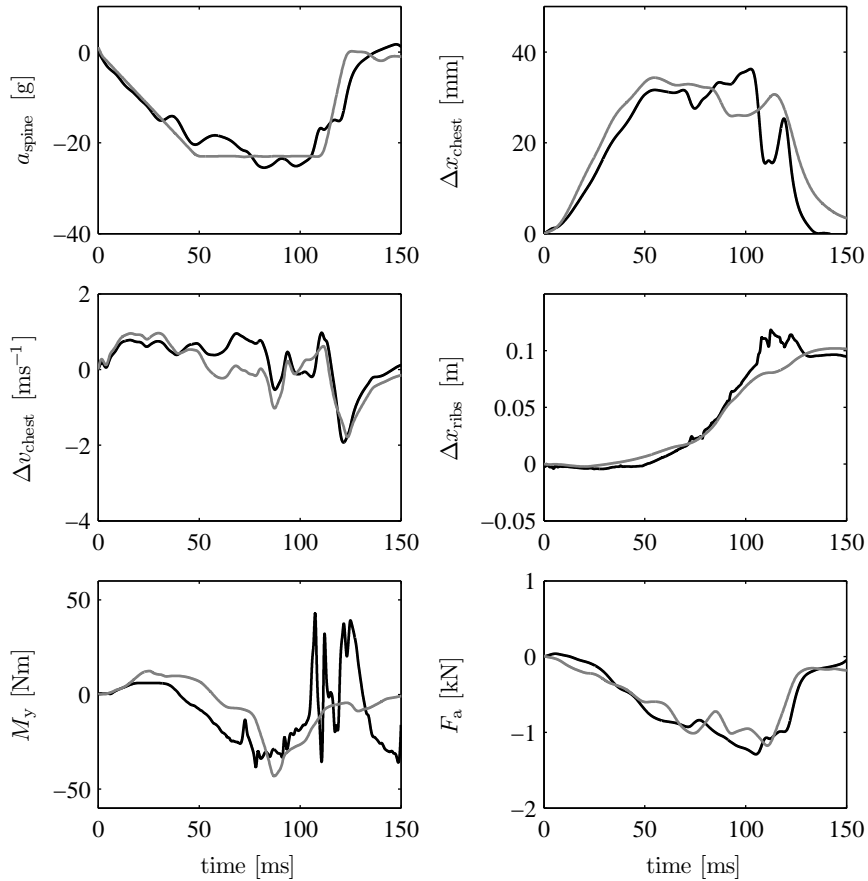


Figure 4.6 / Biomechanical responses of the Madymo reference model (gray), and the estimated outputs of the linearized EKF (black).

4.5 Discussion

In this chapter, a solution has been presented for the problem of real-time prediction of (thoracic) injuries and occupant position during a crash. It has been proposed that filtering of 4 measurable variables will help in improving the estimation of these responses.

A linear Kalman filter has been designed with the LTI model developed in Chapter 2. Its objective was to estimate the systems state vector, based on output measurements of the sternum acceleration and belt rollout, and on input measurements of the belt force and the vehicle acceleration. Results indicated that the measurement outputs were correctly updated by the filter, however, a part of the state space was not correctly reconstructed, resulting in erroneous prediction of outputs \mathbf{y}_1 and \mathbf{y}_2 . This leads to the conclusion that the prediction step in the Kalman filter should be improved. Given the nonlinearities of the system, the prediction step in the Kalman filter was performed with a nonlinear model rather than with the LTI model. The error estimate covariance matrix, however, was still determined with LTI model system matrices, to save computational time in calculating the Jacobians. This filter adjustment significantly improved the prediction of the *non-measurable* outputs.

Other methods to estimate responses of a nonlinear systems do also exist. For example, the Unscented Kalman Filter (UKF) has clear advantages over the EKF: it predicts the mean and covariance with second order accuracy, and any filter which uses the unscented transform does not require the derivation of Jacobians. So it estimates the state more accurately and it is much less difficult to implement (Julier and Uhlmann, 1997). It would therefore be interesting to implement the UKF filter on the nonlinear design model.

The estimation of the output responses is required by the CRC seat belt system, but can also be applied to various other safety systems. For example, airbag developers would largely benefit from this method of real-time spatial occupant sensing, to improve the airbag timing. Also, deflating characteristics of the airbag could be varied during the crash, based on real-time estimated neck injury criteria.

5

A SEMI-ACTIVE BELT FORCE ACTUATOR

Abstract / In this chapter, a design for a seat belt force actuator is presented. This actuator is able to continuously adapt the restraint force in the seat belt during impact, hereby offering the possibility to influence the load level on the vehicle occupant. The design consists of an electro-hydraulic cylinder, or semi-active damper, which is relatively small, has a high bandwidth, and is able to deliver large restraint forces over a long stroke. The belt force actuator is tested and partly evaluated in an experimental setup.

5.1 Introduction

In Section 1.3.3, the relation between thoracic injuries and seat belt loading during frontal impact, and the effect of either varying or various constant load levels on the thoracic injuries has been discussed. Based on these findings, it was proposed that thoracic injury mitigation can be largely enhanced when the belt loading is actively adapted. Indeed, simulation results in Chapter 2 showed that a restraint system with an ideal belt force actuator leads to a significant reduction of the (thoracic) injury criteria.

Automotive restraint suppliers and researchers have proposed several concepts to allow adaptation of the load during the crash. State-of-the-art products include

switchable or progressive load limiters^{1,2}, declining load limiters³, or reinforced braking⁴. Besides these developments, some patents for adaptive load limiters have been filed. For example, a load limiter with infinitely variable gear (Ashtiani et al., 2002; Specht, 2001), a load limiter based on deformation of a strip through a variable groove (Shiotani and Hamaue, 2004), and a load limiter which uses fluidic torque conversion (Knox, 2001) or magneto-rheological fluids (Karlo, 1998). However, no device has so far been developed that is able to effectively set the belt restraint force during the crash. This led to idea to design and construct a novel type of load limiter. The goal of this chapter is summarized as follows:

- (i) design and construct a seat belt force actuator;
- (ii) evaluate the (dynamic) characteristics of the actuator;
- (iii) design an experimental setup that represents a high speed crash environment;
- (iv) demonstrate potential injury reduction with a controlled force actuator on this experimental setup.

In the remainder of this chapter, requirements for the actuator are discussed in Section 5.2, followed by an exploration on actuator concepts in Section 5.3. The final hydraulic concept is modeled in Section 5.4, and numerical simulations aided in motivating the design choices are given. Subsequently, Section 5.5 presents the resulting actuator design. Its dynamic properties are determined by experiments, as shown in Section 5.6. An experimental sled setup is described and modeled in Section 5.7, and modifications are described as well that are required to test the force actuator. This chapter concludes with a discussion and with remarks on the actuator design that may limit its performance.

5.2 Actuator Requirements

As a starting point for the belt force actuator concept, a number of design and performance requirements is formulated. An important aspect concerns the mechanical power delivered by the actuator body, i.e. the body that is connected to the pillar belt. This power, P , is the rate at which energy is transmitted over

¹TRW Automotive Inc. [online], http://www.trw.com/sub_system/seat_belt_systems/load_limiters (last access: August 2009)

²Key Safety Systems (KSS), Inc. [online], <http://www.keysafetyinc.com/seatbelts.asp> (last access: August 2009)

³Autoliv, Inc. [online], <http://http://www.autoliv.com/wps/wcm/connect/autoliv/home/what+we+do/seatbelts/load+limiter> (last access: August 2009)

⁴Wedgetronic Seatbelt, Siemens VDO, Inc. [online], <http://www.vdo.com> (last access: January 2009)

time, and is given by the following expression $P(t) = \vec{F}(t) \cdot \vec{v}(t) = |\vec{F}(t)| \cdot |\vec{v}(t)| \cos \theta$, with \vec{F} and \vec{v} the force and velocity vectors of the actuator body, respectively, and θ the angle between the vectors. For the belt force actuator as modeled in the reference and design models, the magnitude of the force and velocity signals is given by F_{belt} and v_{belt} . As can be seen in Figure 2.1 and Figure 2.12, the force and position vectors are directed opposite, hence $\theta = -180^\circ$ and the power is $P(t) = -F_{\text{belt}}(t)v_{\text{belt}}(t)$.

Actuators that deliver negative power, $P(t) < 0$, will only dissipate energy, and do not require an external energy source. An additional energy source is undesirable considering the costs, weight, space, and practicality, and hence dissipative actuators are preferable by far. Simulation results with the actuated reference model, shown in Figure 2.9, indicate, however, that the required power is not strictly negative. To evaluate the performance of a CRC system with a strictly dissipative actuator, a simulation with the closed-loop controlled reference model is performed as in Section 2.4.5. However, the actuator body is now initially rigidly connected to the vehicle's B-pillar, and the controller is disabled. At the moment that the spinal acceleration equals the setpoint value, the actuator body is allowed to move and the controller is enabled. The results of this simulation are shown in Figure 5.1. It shows that the controller is enabled at $t = 40$ ms, and despite of some (numerical) settling behavior, the belt does not coil up. The rollout velocity is thus (almost) strictly positive, and the actuator only dissipates energy (900 J). Compared to Figure 2.9, the setpoint is slightly lower in order to satisfy the displacement constraint, hence A_{max} is slightly higher. However, it is concluded that the CRC system with an ideal, but strictly dissipative actuator yields sufficient performance.

Performance requirements are based on these simulation results. The actuator performance requirements are formulated in Table 5.1. The bandwidth follows from the closed-loop bandwidth of the primal controlled system, which was 300-400 Hz, see Section 3.3.3. Ideally, the actuator bandwidth should be factors higher to prevent that the closed-loop characteristics are affected, but it is expected that 300 Hz is still reasonable.

Table 5.1 / Belt actuator performance requirements

description	value	unit
force applied to belt	$0 \leq F_{\text{belt}} \leq 8$	kN
stroke displacement	$0 \leq x_{\text{belt}} \leq 0.50$	m
stroke speed	$0 \leq v_{\text{belt}} \leq 10$	ms^{-1}
actuator bandwidth	$f_{\text{act}} \approx 300$	Hz

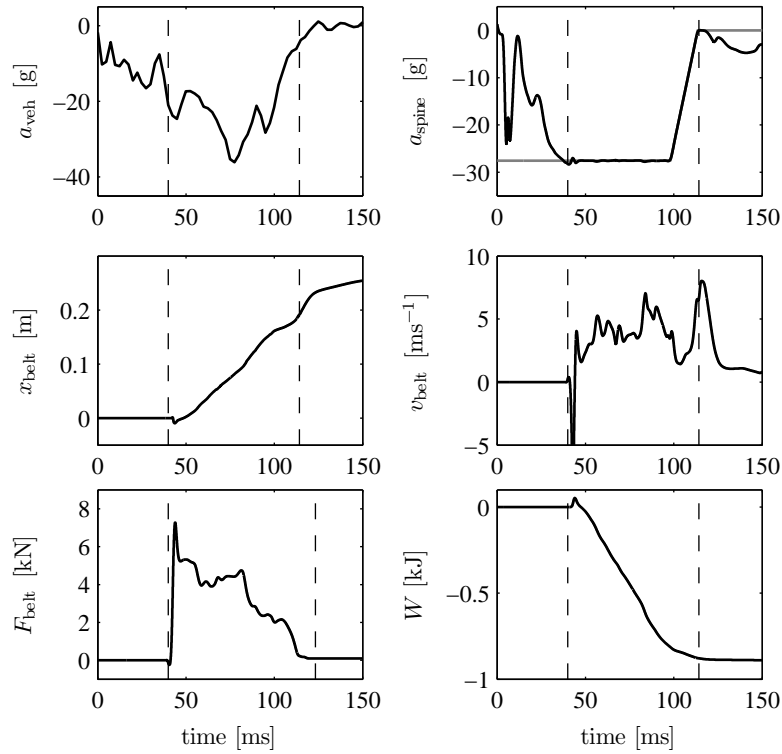


Figure 5.1 / Closed-loop simulation with the reference model \mathcal{R} , in which the actuator body is rigidly connected to the B-pillar until time $t = 40$ ms.

Other aspects have also to be taken into account in the design process, namely that the device has to be practical for use in the experimental setup, and that it could be installed in a passenger car. With these in mind, the design requirements are summarized in the following list:

- The actuator is *semi-active*, i.e., it can deliver only negative power;
- the actuator could be fitted in the B-pillar of a passenger vehicle, so dimensions should be maximum $0.2 \times 0.2 \times 0.5$ m ($w \times b \times h$);
- the duration of application is short, maximum 200 ms;
- the amount of electrical energy to control the actuator is limited (capacitors, battery);
- the device should be re-usable to perform multiple experimental tests.

5.3 Design Concept

In the section, some very general actuator design concepts are presented. It is discussed whether these concepts may be used to meet the requirements sketched in the previous section.

5.3.1 Concept Explorations

Concept 1: Electro-magnetic actuators. Electro-magnetic actuators involve a moving iron or coil, and the action is controlled by means of a control current through the coil (Blackburn et al., 1969). The solenoid, torque and force motor are examples of devices that convert electric energy to mechanical motion through electro-magnetic forces or vice-versa. Here, it is investigated if the kinetic energy from the moving iron or coil can be dissipated through dissipation of the electrical energy. The energy, E , that a coil can store is given by $E = 0.5LI^2$, with I the current in the coil, and L the inductance, given by $L = \mu_o \ell \pi (nR)^2$ (Benson, 1996), with n the number of turns per meter, ℓ the coil length and R the coil radius. Suppose that the coil is very densely packed, e.g. $n = 1500 \text{ m}^{-1}$ and has a very large volume, $R = 0.1 \text{ m}$, $\ell = 0.5 \text{ m}$. Suppose that the force on the moving core is 4 kN during 0.1 m of translation. This means that 400 J has to be dissipated, which results in an average current of 134 A through the coil (assuming no flux leakage). It is difficult to dissipate this amount of electrical energy by a resistance. This indicates that this concept is very suitable to deliver high forces, but only over short distances. This makes electro-magnetic actuators not suitable in this context.

Concept 2: Self-reinforced braking. Self-reinforced braking is proposed for use in intelligent vehicle braking systems (brake-by-wire), and aims at using minimum actuation forces to modify the braking force. The principle is based on an electric powered friction brake with self-reinforcement capabilities, see (Hartmann et al., 2002; Man Ho et al., 2006). A small wedge-shaped brake pad is squeezed between an abutment and a moving surface. Friction drags the brake pad along the surface, increasing the normal force and hence the friction force. By actuating the brake pad, the braking forces can be controlled accurately and fast. Recently, Siemens VDO has developed the Wedgetronic Seatbelt⁵, which makes it possible to seamlessly adjust the restraint force in real time, see Figure 5.2. The main problem is that friction is a very unpredictable phenomenon, especially when the system is not used for

⁵Wedgetronic Seatbelt, Siemens VDO, Inc. [online], <http://www.vdo.com> (last access: January 2009)

several years, which is likely in restraint systems. Therefore, it is concluded that this concept is less suitable to be used as a belt restraint actuator

Concept 3: Electro-hydraulic actuation. The limitations in the amount of force that can be achieved by electromechanical actuation, can be overcome by using fluid power. The stiffness of fluids is highly desirable in this application. The force in the belt is converted to fluid flow through a hydraulic cylinder, and the flow is controlled by an electro-mechanical valve. The advantage of hydraulic control is the high stiffness of the fluid, which allows redirecting forces efficiently to other locations with hardly any deformation. Also, heat is efficiently transported by the fluid, which also works as a lubricant. Since only negative power has to be delivered, there is no need for a hydraulic power supply, which strongly simplifies the design and allows small dimensions. Disadvantages are the high costs by manufacturing tolerances, limited flexibility in the design, non-linearity's, and the inertia of the fluid which may limit the bandwidth (Merritt, 1967). Also, it is difficult to predict whether seals and oil are still usable after years of inactivity. Here it is chosen to use electro-hydraulic actuation to achieve the required actuation forces. Examples of this concept in belt restraint systems are given by (Karlo, 1998; Smithson et al., 2000).



Figure 5.2 / Wedgetronic seat belt from Siemens VDO, which allows a seamlessly adjustment of the belt restraint force. Image taken from Siemens VDO, Inc.

5.3.2 Final Concept

Based on the concept explorations⁶ sketched above, the actuator design will be based on a hydraulic cylinder that functions as a controllable damper; hence there is no pressure source line. In the field of vehicle suspensions, actuators that only deliver negative power are called semi-active dampers. In the remainder of this chapter, the term *semi-active actuator* is employed.

The concept is sketched in Figure 5.3. The hydraulic fluid is present at only one side of the cylinder piston. Since no fluid is added to the cylinder, the pressure can only be varied through fluid outflow or through piston movement (given that the fluid temperature is constant). An electrically controlled servo-valve regulates the outflow of the fluid, and thereby controls the hydraulic pressure on the piston. The pressure results in a restraining force on the belted occupant, and the occupant dynamics will in its turn determine the belt displacement. The corresponding piston motion is therefore a result of the dynamical system “connected” to the semi-active actuator.

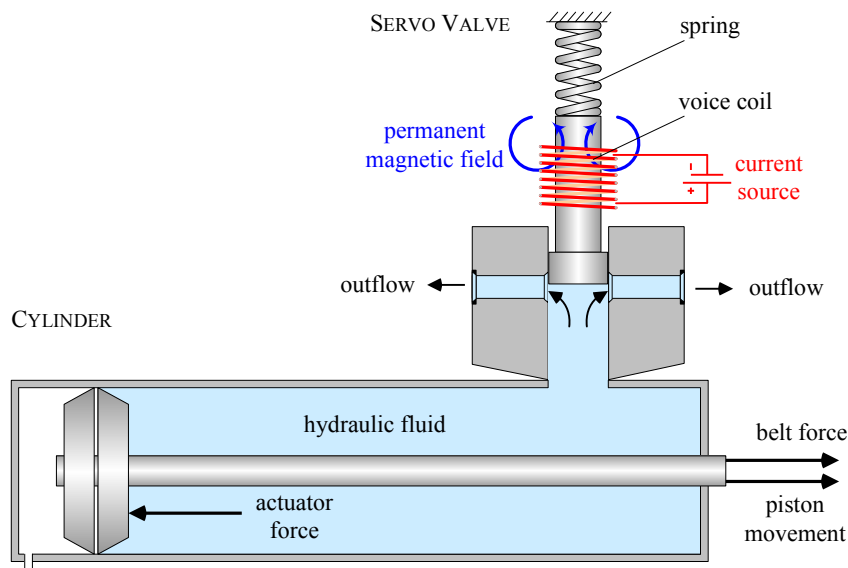


Figure 5.3 / Schematic concept of the semi-active hydraulic belt force actuator.

Hydraulic pressure sensors can be fast, cheap and small, and therefore the hydraulic pressure inside the cylinder is used as a measurement for output feedback control of the servo valve. Pressure sensors are also known to be noisy. Force, flow

⁶Personal communications with P.C.J.N. Rosielle, 2009.

or valve position sensors could also be chosen, but these sensors are more complex, slower and less practical to implement. A local controller, \mathcal{H} , actuates the servo valve according to a desired pressure, see Figure 5.4. This pressure follows from the desired *actuator force* through the piston area, A_p . Note that the actuator force does not represent the force in the belt, F_{belt} , since piston dynamics have to be taken into account. Note that the piston motion results from the occupant motion, and therefore enters the actuator system Γ as a disturbance.

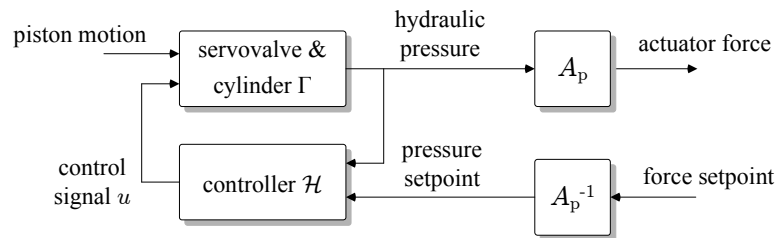


Figure 5.4 / Feedback control scheme of the belt force actuator with servo valve and hydraulic cylinder.

Reviewing the performance requirements in Table 5.1, there is a number of reasons why the servo-valve and cylinder have to be specially designed instead of using commercially available components.

Firstly, a maximum pressure of 500 bar is allowed, since too high a pressure would be demanding on the cylinder construction, seals, sensors, etcetera. Given the required maximum force of 8 kN, the piston area A_p should be at least 160 mm² to prevent over pressurizing the system. With this minimum area, the volumetric flow rate, Φ , through the valve will be at least 96 l min⁻¹ at the maximum stroke velocity. Secondly, a high bandwidth is required, i.e. around 300 Hz.

Off-the-shelf or commercially available servo-valves for pressure control have typically too low a bandwidth at these flows, around 50-80 Hz⁷. The servo-valves with a higher bandwidth, i.e. 100-200 Hz, are in general not able to handle the required flow of 100 l min⁻¹. Additionally, controller software is often integrated in the valve, which limits the flexibility in the control design. Finally, using commercially available valves and cylinders may not lead to an optimal design in terms of dimensions, manageability and suitability in the crash setup.

A large variety of servo valves exist, but most of them are based on the same concept. A spool body regulates the opening between the pressure supply and control lines, and this spool is actuated by a pilot pressure. The pilot pressure

⁷Moog Electro-hydraulic Valves [online], <http://www.moog.com/literature/ICD/technical.pdf> (last access: August 2009)

is regulated by an electronically actuated flapper. In the adopted design concept, there is no pilot pressure to move the spool body, and the spool needs to be actuated directly. A voice coil will be used to move the spool. Since the actuation period is short, i.e. less than 200 ms, high currents can be used without overheating the spool actuator. Voice coils can exert high forces over a short distance, see Section 5.3.1. A pre-loaded spring between the spool and spool housing provides an additional force to support the voice coil force, and keeps the valve closed up till a certain pressure, to prevent fluid outflow when the actuator is not used.

In conventional servo-valves, the spool body moves perpendicular to the direction of the hydraulic force. In this way, the force on the spool is taken on by the valve housing. In our concept, the spool body moves in line with the hydraulic force, thereby reducing friction between spool and housing, and allowing a much lighter construction. A light spool body increases the resonance frequency, thereby improving the dynamic behavior. Disadvantage of this concept is that higher forces are required to move the spool body, as it directly has to counteract the hydraulic force. So the presented design concept is only advantageous when the servo-valve is used during very short periods, see the third design requirement in Section 5.2. The concept is schematically shown in Figure 5.3.

In the next section, a model will be derived for the semi-active actuator. This model, \mathcal{G} , is required for 3 reasons: (i) to obtain optimal parameters that lead to an actuator design that fulfills the requirements in Table 5.1, (ii) to provide an estimate of the current for the servo valve, and (iii) to design the local controller \mathcal{H} .

5.4 Dynamic Modeling of the Hydraulic System

In this section, fundamental laws and equations are presented that govern the fluid motion and the flow through conduits and orifices.

5.4.1 Fundamental Relations for Lumped Hydraulic Systems

Analytical description of fluid flow formally requires solving a number of independent equations. However, some simplifications can be applied here (Blackburn et al., 1969; Merritt, 1967; Watton, 1989). The first fundamental equations that govern the flow of fluids, are the well-known Navier-Stokes equations, which relate the inertia and the viscous forces of the fluid. However, fluid is usually dominated by either the viscosity or the inertia (Merritt, 1967). Some empirical relations,

e.g. for orifices, may only apply to one type of flow. Then it is of more interest to determine the flow type than analytical flow patterns. It turns out that the Navier-Stokes equations are not required here.

The Reynolds number is a dimensionless quantity that can be used to determine the flow type. It is defined by

$$Re = \frac{\rho u D}{\mu} \quad (5.1)$$

with ρ the density of the fluid, u the average flow velocity, D the characteristic dimension of the flow, and μ the dynamic or absolute viscosity. A flow dominated by viscous forces is called a laminar flow, whereas inertia dominated flows are turbulent. Roughly said, a flow in pipe is turbulent for Reynolds number higher than 4000, and it is laminar for numbers below 2300.

Another fundamental equation follows from the law of conservation of mass, and it is called the *continuity equation*. It is simply given by

$$\dot{m}(t) = \sum \dot{m}_{in}(t) - \sum \dot{m}_{out}(t) \quad (5.2)$$

with m the mass inside a selected control volume V . This mass is obviously related to this volume through the density as $m = \rho V$.

In most hydraulic systems, hydraulic resistances such as orifices will dominate the restrictions from pipes and bends. Therefore the following is assumed

Assumption 5.1 / *Pressure gradients along pipes and bends are insignificant, given the large pressure drops over orifices.*

This implies that only the (empirical) relations for orifices have to be used to account for pressure variations. The following assumption is also plausible

Assumption 5.2 / *The effect of temperature variations in the fluid is neglected given the time scale of the experiment (max 0.2 s).*

This assumption implies that fluid properties like the absolute viscosity μ and density ρ can be evaluated at operating temperature T_o .

The compressibility of an hydraulic fluid combined with the mass of the mechanical components induces resonances that may limit the dynamic performance (Merritt, 1967). This *spring* effect of the fluid is characterized by the bulk modulus of the fluid, E , and appears in the so-called *equation of state*. This equation relates fluid density to pressure and temperature. For constant operating temperature T_o , an accurate approximation of the state equation is given by

$$\rho = \left(\frac{\Delta P}{E} + 1\right)\rho_o \quad \Leftrightarrow \quad \Delta P = \left(\frac{\rho}{\rho_o} - 1\right)E \quad (5.3)$$

with ΔP the pressure relative to the atmospheric pressure P_o , E the bulk modulus, and ρ_o the density of the fluid, both at P_o and T_o .

When the system dynamics are significantly slower than those caused by the pressure wave propagation, the hydraulic circuit may be considered as a system of lumped components (Watton, 1989). The frequency of the pressure waves is approximately given by

$$\frac{C_o}{2L} \approx 1.3 \text{ kHz}$$

with $C_o = \sqrt{E/\rho_o} \approx 1.3 \cdot 10^3$ m/s the speed of sound in the fluid, $L=0.5$ the (expected) length of the line, and $E \approx 1.5 \cdot 10^9$ the bulk modulus of hydraulic fluid. A lumped parameter description is valid, since the following assumption is plausible

Assumption 5.3 / *The system dynamics or main oscillations, characterized by frequency f , are significantly lower than 1.3 kHz.*

The continuity equation, the equation of state and an equation for orifices will be used in the next sections to develop a model of a lumped hydraulic system.

5.4.2 Continuity Equation

The first component of the lumped fluid circuit is the piston cylinder shown in Figure 5.5. The continuity equation (5.2) for the mass m_p inside the volume V_p reads

$$\dot{m}_p(t) = \sum \dot{m}_{\text{in}}(t) - \sum \dot{m}_{\text{out}}(t) = -\dot{m}_1(t) \quad (5.4)$$

This volume V_p is a function of piston rod motion $x_p(t)$ as

$$V_p(t) = A_p(L - x_p(t)), \quad 0 \leq x_p(t) \leq L \quad (5.5)$$

with $A_p = \frac{1}{4}\pi(d_c^2 - d_p^2)$ the effective piston area. As mentioned above, it is assumed that the pressure drop along the length of cylinder is negligible. This is plausible, given the large pressure drops that can be expected over the orifice in the system. Hence the pressure and the density are homogenous in the cylinder, and are given by P and ρ , respectively.

The mass flow \dot{m}_1 from the cylinder enters the hydraulic one-way servo valve, as sketched in Figure 5.6. The continuity equation for the mass m_s inside volume V_s reads

$$\dot{m}_s(t) = \sum \dot{m}_{\text{in}}(t) - \sum \dot{m}_{\text{out}}(t) = \dot{m}_1(t) - \dot{m}_2(t) \quad (5.6)$$

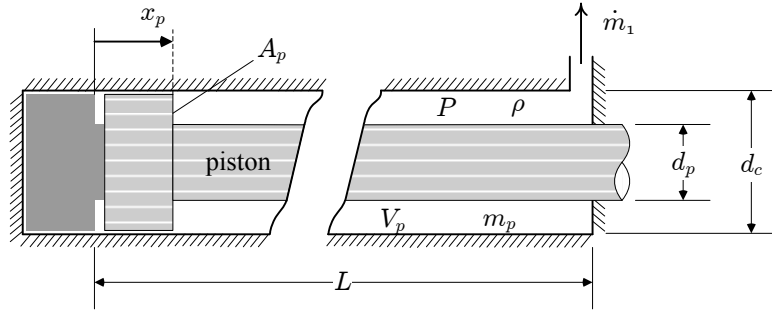


Figure 5.5 / The hydraulic cylinder.

The volume V_s represent the volume taken by the spool body, as shown in Figure 5.6 by the dashed box. It is given by

$$V_s(t) = A_s(x_o + x_s(t)), \quad x_s(t) \geq -x_o \tag{5.7}$$

with $A_s = 1/4\pi d_s^2$. Note in the figure that a stop is defined on the negative spool displacement, so that a constraint on the valve position has to be taken into account, i.e. $x_s(t) \geq -x_o$.

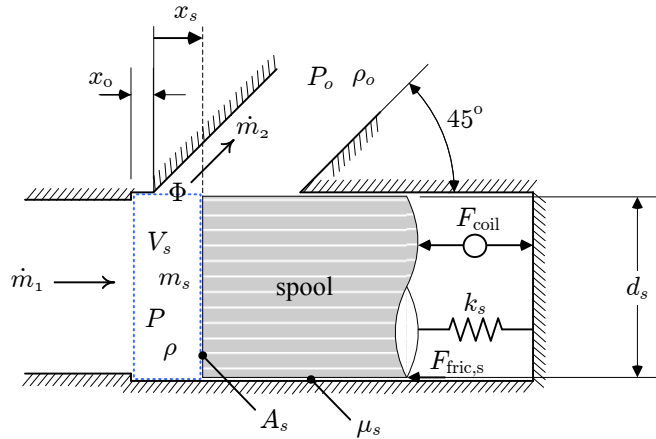


Figure 5.6 / The hydraulic one-way servo valve.

It is assumed that the pipe between the cylinder and the valve body causes no significant pressure drop, and the pressure and density in the valve body are thus also given by a uniformly distributed P and ρ , respectively. It is convenient to write the mass flow through the orifice as a function of its volumetric flow rate, Φ . Hence

$$\dot{m}_2(t) = \rho(t)\Phi(t) \tag{5.8}$$

Now define the total mass inside both volumes V_p and V_s as the state of the system, i.e. $m(t) = m_p(t) + m_s(t)$. With (5.4), (5.6) and (5.8), the differential equation for $m(t)$ reads

$$\dot{m}(t) = -\rho(t)\Phi(t) \quad (5.9)$$

Given a uniformly distributed density in both volumes, as argued, this density is

$$\rho(t) = \frac{m(t)}{V_p(t) + V_s(t)}, \quad -x_o \leq x_s(t), \quad 0 \leq x_p(t) \leq L \quad (5.10)$$

5.4.3 Flow through a Valve Orifice

The volumetric flow $\Phi(t)$ through the valve opening depends on the pressure drop over the valve $\Delta P(t) = P(t) - P_o$, the orifice area $A_{\text{ori}}(t)$, the valve geometry and the fluid and flow properties. Generally, the following (empirical) equation is used to approximate the flow through an orifice (Blackburn et al., 1969)

$$\Phi(t) = C_d A_{\text{ori}}(t) \sqrt{\frac{2\Delta P(t)}{\rho(t)}} \quad (5.11)$$

with $C_d > 0$ the dimensionless discharge coefficient, which will be discussed later. It is required that the flow is nonnegative, so $\Delta P(t) \geq 0$, since $A_{\text{ori}} \geq 0$, $\rho \geq 0$.

The valve has three identical circular return lines with diameter d_1 , which are placed under an angle of 45 degrees, as shown in Figure 5.6. In Figure 5.7, it is shown how the orifice area A_{ori} is related to the spool stroke x_s . Since the return lines are placed under an angle, the restriction area is approximately ellipsoidal (egg-shaped), with minor and major axes d_1 and $d_2 = \sqrt{2}d_1$. The maximum total orifice area A_{res} for the three outlets is given by

$$A_{\text{res}} = \max_{x_s} A_{\text{ori}} \approx 3 \left(\frac{\pi d_1 d_2}{4} \right) \quad (5.12)$$

In Figure 5.7(b), the effective orifice area A_{ori} , normalized to the maximum opening, is plotted as a function of the normalized spool stroke. The dashed line shows that there is a near linear relation between these variables, so $A_{\text{ori}} \approx A_{\text{res}} x_s / d_2$. With this approximation, the opening is

$$A_{\text{ori}}(t) \approx \xi(x_s) \frac{3}{4} \pi d_1 \quad (5.13)$$

with ξ a saturation function

$$\xi(x_s) = \begin{cases} 0 & \text{for } -x_o \leq x_s < 0 \\ x_s & \text{for } 0 \leq x_s < d_2 \\ d_2 & \text{for } d_2 \leq x_s \end{cases} \quad (5.14)$$

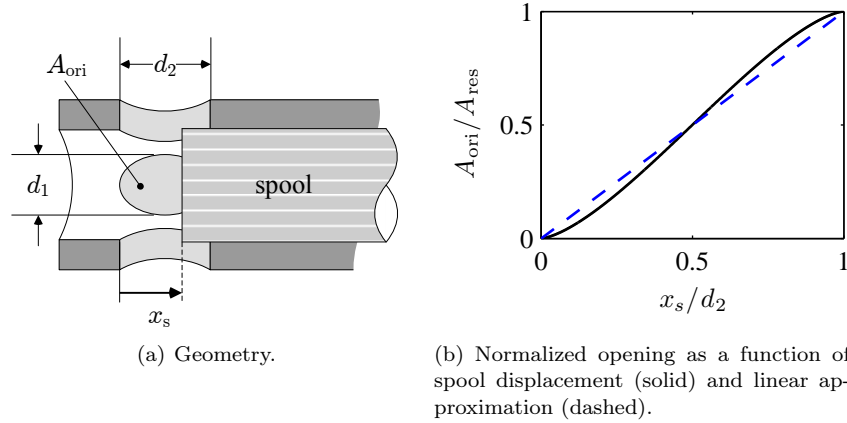


Figure 5.7 / Ellipsoidal orifice opening area.

For most orifice geometries in sliding-type control valves, the discharge coefficient C_d is approximately constant above a certain value of the Reynolds number, viz. $Re = 260$ (Blackburn et al., 1969; Merritt, 1967). The value of C_d is independent of the orifice geometry and varies between $C_d = 0.60$ and 0.65 if the orifice edges are sharp. If the edges are rounded or truncated by wear, however, the coefficient can go up to values of 0.9 . Sharp-edges orifices are thus desirable for their predictable behavior.

For subcritical values of the Reynolds number, the viscosity of the fluid dominates the flow, making it laminar. The value of C_d will drop and goes to zero for high viscous flows. For the type of valve opening presented in Figure 5.7, the characteristic dimension D is usually taken as $D = \sqrt{A_{\text{ori}}/\pi}$ (Blackburn et al., 1969), and the Reynolds number is then given by

$$Re \approx \frac{\rho\Phi(t)}{\mu\sqrt{\pi A_{\text{ori}}(t)}} \quad (5.15)$$

So a large flow rate, a small orifice opening and a low dynamic viscosity are desired for a turbulent flow, which is also intuitive. Suppose a large orifice opening, $d_1 = 5$ mm, and proper values of ρ and μ , then the flow is already turbulent at a flow rate of $\Phi = 5$ l/min. Therefore, the following is assumed

Assumption 5.4 / *The flow through the orifice is turbulent, and a constant value of $C_d = 0.625$ can be adopted for the discharge coefficient*

However, the influence of a higher C_d , caused by wear or fabrication tolerances on the orifice edges, and a lower number, caused by a laminar flow, is shown by

simulations results at the end of this section.

In the orifice flow equation (5.11), the pressure can be found from the equation of state, (5.3), and the density follows from (5.10). So then the differential equation in (5.9) becomes

$$\dot{m}(t) = -\frac{C_d A_{\text{ori}}(t) m(t)}{V_p(t) + V_s(t)} \sqrt{2E \left(\frac{1}{\rho_0} - \frac{V_p(t) + V_s(t)}{m(t)} \right)}$$

Now combining the equations (5.7) and (5.5) for the volumes, and the orifice opening equation in (5.13), yield the nonlinear differential equation

$$\dot{m}(t) = \xi(x_s) f_1(x_s, m, x_p), \quad -x_o \leq x_s(t), \quad 0 \leq x_p(t) \leq L \quad (5.16)$$

with ξ as in (5.14). The initial condition can be formulated in terms of the initial system pressure, as follows

$$m(0) = \rho_o \left(\frac{P(0) - P_o}{E} + 1 \right) \left(A_p L - A_p x_p(0) + A_s x_o + A_s x_s(0) \right) \quad (5.17)$$

When the initial pressure is atmospheric, $x_s(0) = -x_o$ and $x_p(0) = 0$, then $m(0) = \rho_o A_p L$.

The uniformly distributed relative pressure ΔP is measured, and is used by the feedback controller, as shown in Figure 5.4. It is given by

$$\begin{aligned} \Delta P(t) &= \frac{E}{\rho_o} \frac{m(t)}{(V_p(t) + V_s(t))} - E \\ &= g(x_s, m, x_p), \quad -x_o \leq x_s(t), \quad 0 \leq x_p(t) \leq L \end{aligned} \quad (5.18)$$

5.4.4 Force Equations

The pressure generated in the hydraulic system exerts a force on the piston body, $F_{\text{hyd,p}}$, obviously given by

$$F_{\text{hyd,p}} = A_p \Delta P(t) \quad (5.19)$$

This force equals *the actuator force*, that was mentioned in Section 5.3.2. The pressure also exerts a force on the spool body, $F_{\text{hyd,s}}$. As shown in Figure 5.6, the forces on the spool body are balanced as follows

$$F_{\text{hyd,s}}(t) = M_s a_s(t) + F_{\text{coil}}(t) + F_{\text{spring}}(t) + F_{\text{fric,s}}(t) \quad (5.20)$$

with $a_s = \dot{v}_s = \ddot{x}_s$, M_s the mass of the spool body, F_{coil} the force from the voice coil actuator, and

$$\begin{aligned} F_{\text{hyd},s}(t) &= A_s \Delta P(t) \\ F_{\text{spring}}(t) &= k_s(x_s(t) + x_o) + F_o, \quad -x_o \leq x_s(t) \\ F_{\text{fric},s}(t) &= \mu_s v_s(t) + F_c \text{sgn}(v_s(t)) \end{aligned} \quad (5.21)$$

The friction force on the spool body accounts for the coulomb friction and the fluid friction, caused by the oil between spool and housing. The force F_o is defined as the initial spring force when the spool is pressed against the stop, i.e. $x_s = -x_o$, and k_s is the spring stiffness.

A linear voice coil actuator is used to actuate the spool mass. This type of actuator is fast, contact-free, and is able to generate the required large forces over small displacements. Although voice coils contain nonlinearities, it is assumed here that the current is linear with the generated electromagnetic force. Moreover, it is assumed that a current amplifier is available that outputs a current linearly with a reference voltage $U(t)$. Hence the coil force, F_{coil} , is given by

$$F_{\text{coil}}(t) = K_u U(t) \quad (5.22)$$

with a constant parameter K_u that incorporates the motor constant of the voice coil and the current amplifier gain.

With (5.18), the acceleration of the spool body is now written as

$$\begin{aligned} a_s(t) &= \frac{A_s \Delta P(t) - K_u U(t) - k_s x_s(t) - \mu_s v_s(t) - F_c \text{sgn}(v_s(t))}{M_s} - \frac{k_s x_o + F_o}{M_s} \\ &= f_2(x_s, v_s, m, U, x_p), \quad -x_o \leq x_s(t), \quad 0 \leq x_p(t) \leq L \end{aligned} \quad (5.23)$$

5.4.5 Design Considerations

In this section, the equations derived previously are used to select the parameters for the cylinder and valve, based on the performance and design requirements formulated previously in Section 5.2.

The fourth design requirement stated that the amount of available electrical energy in the vehicle is limited, so it is preferable to minimize the required voice coil current. This implies minimizing the required coil force F_{coil} .

Consider a specific quasi-static situation where fluid flows through the valve, but the spool does not move, so $x_s > 0$ and $v_s = 0$. According to (5.19) and (5.20), the hydraulic piston force and coil force are then related by

$$F_{\text{coil}} \propto \frac{A_s}{A_p} F_{\text{hyd},p} \quad (5.24)$$

This expression might lead to the conclusion that in an optimal design, i.e. with a minimal coil force, the piston area is maximized and the spool area is minimized. However, this conclusion does not hold, since the areas are dependent of each other. To understand this, the following rationale is presented.

The orifice opening is made in the spool housing, and the maximum orifice diameter, d_1 , is limited by the spool circumferential πd_s , see Figure 5.7(a). So d_1 can be considered proportional to the spool diameter d_s , i.e. $d_1 \propto d_s$, or in terms of area, the maximum orifice area is proportional to the spool area

$$A_{\text{res}} \propto A_s$$

Next, compressibility of the fluid can be neglected when there is flow through the orifice, hence $\rho(t) = \rho_o$. Differentiating $m(t)$ in (5.10) with respect to time, and substituting it into (5.9) leads to $\Phi = A_p v_p$, with $v_p = \dot{x}_p$. The orifice area then relates with (5.11) to the piston area as

$$A_{\text{res}} = \frac{\Phi}{C_d} \sqrt{\frac{\rho_o}{2\Delta P}} = \frac{A_p v_p}{C_d} \sqrt{\frac{A_p \rho_o}{2F_{\text{hyd,p}}}} \propto v_p \sqrt{\frac{A_p^3}{F_{\text{hyd,p}}}} \propto A_s \quad (5.25)$$

When the last equation is inserted in (5.24), the coil force is given by

$$F_{\text{coil}} \propto \sqrt{v_p^2 F_{\text{hyd,p}} A_p} \propto \sqrt[3]{v_p^2 F_{\text{hyd,p}} A_s}$$

So it is indeed desirable to keep the spool area small. But in contrast to the former conclusion, now a *small* piston area A_p will minimize the required coil force. The piston area scales nonlinearly with the orifice area, which is proportional to the spool area. Hence, increasing the piston area, will increase the spool area even more. A small piston has the additional advantage that the actuator dimensions will become small, satisfying the second design requirement.

5.4.6 Selection of Parameters

As the hydraulic oil, type Mobil DTE-25⁸ is chosen. The properties are listed in Table 5.2. Since a turbulent flow is desired, as mentioned, an oil type is chosen with a low dynamic viscosity. It was argued in the previous section that the piston area should be small, but not smaller than 160 mm², as argued in Section 5.3.2. The minimal piston rod diameter d_p is limited by the availability of suitable rod seals, and a rod diameter of $d_p = 10$ mm is chosen. The smallest inner cylinder diameter, d_c , is also limited by fabrication requirements, and could be no smaller

⁸Exxon Mobil Corporation [online], <http://www.mobil.com> (last access: August 2009)

Table 5.2 / Hydraulic oil (Mobil DTE-25, ISO grade 46) properties at atmospheric pressure ($P_o = 10^5$ Pa)

symbol	value	unit	quantity
ρ_o	876	$\text{kg}\cdot\text{m}^{-3}$	density @ 15.6 °C
ν	44.2	mm^2s^{-1} (cSt)	kinematic viscosity @ 40 °C
μ	0.0385	Nm^{-2}s	dynamic viscosity @ 40 °C
E	$1.50\cdot 10^9$	Nm^{-2}	theoretical bulk modulus

than $d_c=18$ mm, which lead to $A_p = 175.9 > 160$ mm². The length of the cylinder chamber is $L = 500$ mm, as specified in Table 5.1.

When the desired actuator force, $F_{\text{hyd},p}$ is known, then with the chosen piston area A_p , the hydraulic pressure follows from (5.19). With the piston velocity v_p , the volumetric flow Φ can be estimated assuming incompressible flow. The obtained estimates are shown in Figure 5.8, and $F_{\text{hyd},p}$ and v_p are based on the belt force and belt rollout velocity shown in Figure 5.1. The pressure results in a hydraulic force $F_{\text{hyd},s}$ on the spool, which is also plotted in Figure 5.8.

Next, the required orifice opening A_{ori} is calculated for the given volumetric flow rate and pressure, see (5.11). Again, incompressibility is assumed, with $\rho(t) = \rho_o$. The results are shown in Figure 5.8 for three values of $C_d \in \{0.4, 0.625, 0.9\}$. For this particular simulation, a maximum orifice area of approximately 15 mm² is required for low values of C_d . To make the actuator suitable for more severe impacts, and large flows, a maximum orifice area $A_{\text{res}} = 30$ mm² is taken. With (5.12), a value of $d_1 = 3.00$ mm is chosen, which gives $d_2 = 4.24$ mm. The smallest spool diameter related to this orifice diameter is $d_s = 5.00$ mm, which lead to $A_s = 19.6$ mm². The spool position x_s can now be found with (5.13), and is plotted in the same figure. The Reynolds number is found through (5.15). The number is sufficiently high, $Re \gg 260$, to assume a constant value of $C_d = 0.625$, given that the orifice edges are sharp. To prevent leakage through the valve before use, a dead zone in the valve opening of $x_o = 1.00$ mm is chosen.

Lastly, the spring stiffness and initial spring force have to be chosen. From a control point of view, it is convenient that the resonance frequency of the system of spring and spool mass exceeds the desired closed-loop actuator bandwidth. This implies that a low spool mass and a stiff spring are desired. Given the space to install the spring, a maximum stiffness of $k_s = 8.09$ kNm⁻¹ could be chosen, according to the specifications of the manufacturer. This leads to a resonance frequency of 60-80 Hz, given a spool mass of 30-55 gr. Hence the controller has to compensate for this low resonance.

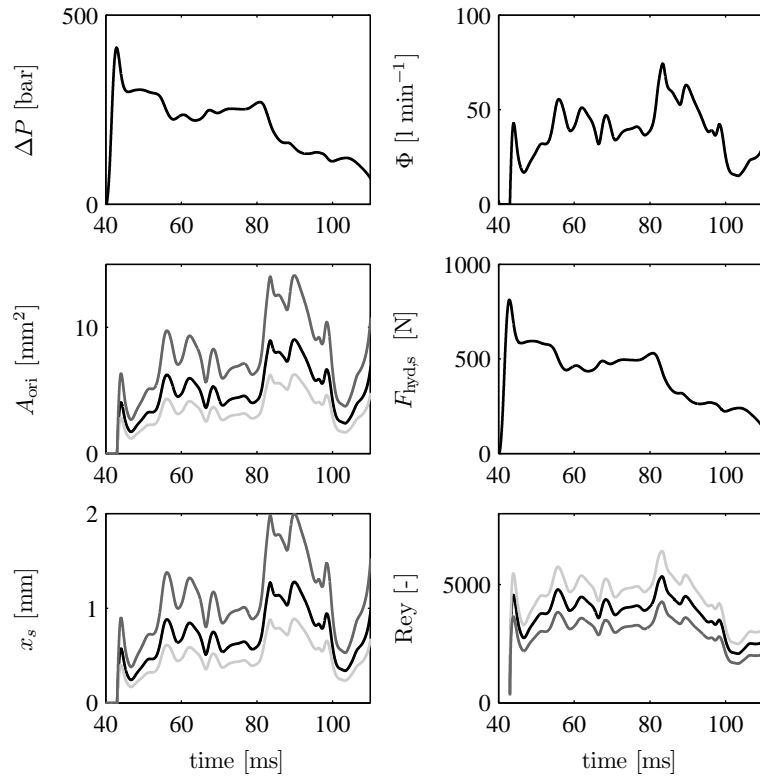


Figure 5.8 / Approximated simulation results for the desired belt force F_{belt} and piston displacement x_p given in Figure 5.1. The parameters are listed in Table 5.3, but C_d is also given the value 0.4 (dark gray) and 0.9 (light gray).

Without actuation of the voice coil, the force on the spool upon opening of the valve is $k_s x_o + F_o$. As a safety precaution, it would be desirable if the valve opens at a belt force of around 1 kN, i.e. a hydraulic force on the spool body of 112 N. With $k_s x_o = 8.09$ N, this leads to a $F_0 \approx 100$ N or a initial spring compression of around 13 mm.

All parameters are listed in Table 5.3, which also shows the masses of the piston and valve bodies. They are not known exactly at this point, but are obtained from the subsequent section, and listed in this table for completeness.

Table 5.3 / Actuator parameters.

symbol	value	unit	quantity
d_p	10.0	mm	piston diameter
d_c	18.0	mm	inner diameter cylinder
A_p	176	mm ²	effective piston area
L	500	mm	length cylinder chamber
M_p	1.66	kg	mass of the piston
M_s	35.0	g	mass valve
d_s	5.00	mm	diameter valve
A_s	19.6	mm ²	spool area
C_d	0.625	-	Discharge coefficient of the valve
d_1	3.00	mm	diameter outlet channel
d_2	4.24	mm	diameter outlet channel
A_{res}	30.0	mm ²	maximum orifice area
k_s	8.09	kNm ⁻¹	spring stiffness
x_o	1.00	mm	offset

5.4.7 Nonlinear State Equations and Simulations

The differential equations for the hydraulic semi-active actuator are combined into a nonlinear model, \mathcal{G} . The inputs to the model are the current through the voice coil, U , and the piston position x_p . The controlled output is the hydraulic pressure, ΔP . The state of the model is collected in the column vector $[x_s \ v_s \ m]^T$. With the equations from the previous sections, the nonlinear state space equations read

$$\mathcal{G} : \begin{cases} \dot{m}(t) &= f_1(x_s, m, x_p)\xi(x_s), & -x_o \leq x_s(t), 0 \leq x_p(t) \leq L \\ \dot{x}_s(t) &= v_s \\ \dot{v}_s(t) &= f_2(x_s, v_s, m, U, x_p) \\ \Delta P(t) &= g(x_s, m, x_p) \end{cases} \quad (5.26)$$

The functions ξ , f_1 , f_2 and g are previously given in (5.14), (5.16), (5.23) and (5.18), respectively.

With model \mathcal{G} , the required voice coil force can be determined given a desired pressure and piston position. With an estimate of the required voice coil force F_{coil} , the voice coil parameters and current amplifier can be selected.

It is chosen to control the model with output feedback, in which the voltage U is provided by the output feedback controller. Since the voice coil characteristics

are unknown at this point, $K_u = 1$ is taken in (5.22), and the control effort will in fact represent the voice coil force $U = F_{\text{coil}}$. The linear feedback controller is represented by a transfer function $\hat{\mathcal{H}}(s)$. Its output is based on the error between the measured pressure, ΔP , and the desired pressure profile ΔP_{ref} , see the scheme in Figure 5.4. The controller differs from $\mathcal{H}(s)$, which is the controller that will be implemented on the system, and will provide voltage U in stead of the force F_{coil} .

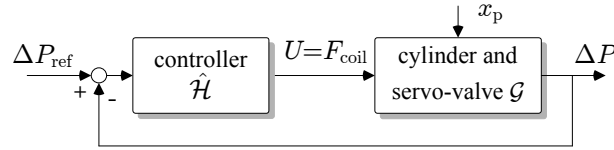


Figure 5.9 / Control scheme to determine an estimate for F_{coil} .

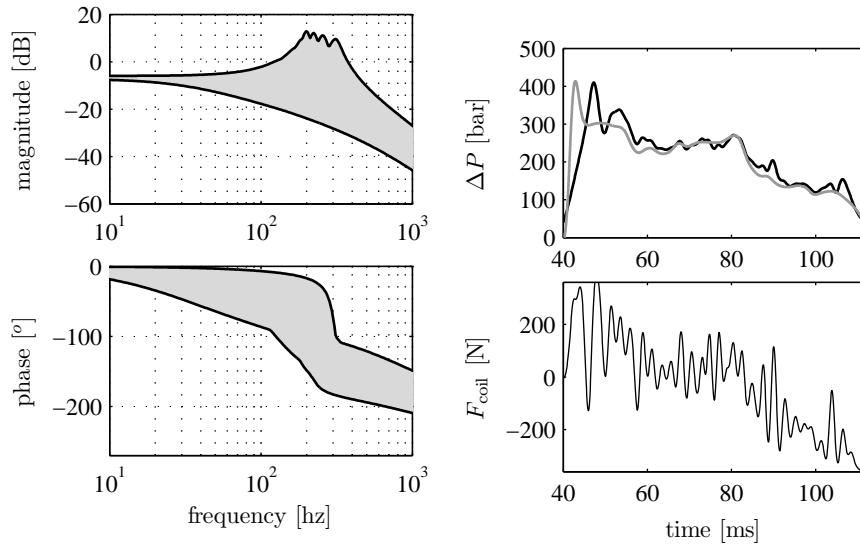
The controller is designed with a linearized model of \mathcal{G} , obtained from a first order Taylor approximation of the nonlinear model in (5.26), see Section 2.8.1. A grid of operating points is used to perform the linearization, and since v_s and U do not appear in the Jacobians, the following operating points were chosen $\bar{x}_s \in \{1, 2, 3, 4\}$ mm, $\bar{x}_p \in \{0, 0.1, 0.2, 0.3\}$ m, and a pressure $\Delta \bar{P} \in \{50, 150, \dots, 450\}$. This result in a *family* of 80 third order LTI models, each with two inputs and one output. The transfer function corresponding to input U is given by $\hat{\mathcal{G}}(s)$

$$\hat{\mathcal{G}}(s) = \Delta P(s)(F_{\text{coil}}(s))^{-1} \quad (5.27)$$

The frequency response function of this transfer function is derived on the entire grid of operating points. The upper and lower bounds on the magnitude and phase vectors of these FRFs are plotted in Figure 5.10(a).

Based on $\hat{\mathcal{G}}(s)$, the feedback controller $\hat{\mathcal{H}}(s)$ is designed, consisting of a lead filter and a proportional-integral controller. This specific controller is only used in the simulations to determine an estimate of F_{coil} , and will not be implemented on the real apparatus. To prevent confusion, the controller or open-loop systems are not plotted in a diagram.

A closed-loop simulation is performed with controller $\hat{\mathcal{H}}(s)$ and the nonlinear model (5.26), see Figure 5.9. The hydraulic pressure and piston position as shown in Figure 5.1 are used as the setpoint ΔP_{ref} and disturbance x_p , respectively. The results are shown in Figure 5.10(b), which illustrates that the desired pressure is not very accurately tracked by the control system. Especially the rise time is too low, but this is not caused by a sluggish controller. In fact, the spool body is in that phase against spool stop $x_s = x_o$, and the pressure cannot be increased by the valve. Pressure decrease can be realized sufficiently fast, however. Note that the voice coil has to generate a force of maximum 300 N. This requirement is used in the design of the voice coil, which is presented in the next section.



(a) Bode plot with the upper and lower bounds of the family of FRFs, corresponding to transfer function $\hat{G}(s)$.

(b) Closed-loop simulation results with the nonlinear model. Top: the desired (gray) and controlled (black) output. Bottom: the required voice coil force.

Figure 5.10 / LTI model and simulation results.

5.5 Actuator Design

Based on the design parameters from the previous section, the hydraulic cylinder is designed and constructed by the Gemeenschappelijke Technische Dienst (GTD/TNO/TUE), the Netherlands.

5.5.1 Valve Design

The valve design is shown in Figure 5.11. Indicated in the figure are the valve body, the outlet channels, the voice coil and permanent magnets, and the spring. The spring can easily be replaced by an opening on the left. Note that the spool body is not supported by bearings or a guidance, but it is constrained by the fitting in the housing. To prevent the spool body from going askew, much effort has been put in keeping the manufacturing tolerances low. Fluid from the cylinder enters the valve at the top through a conical shaped hole. The fluid leaves the valve via the three outlet channels, from where it is led to a reservoir (not shown). The permanent magnets are little cubes that are fitted in holes on the bottom. The

coil is spun around a drum, and glued to the valve body with the drum removed. The coil moves in a very narrow slit between two steel pole pieces. The design leads to an estimated theoretical motor constant of 11.0 N/A, which is calculated in Appendix B. With a maximum voice coil force of 300 N, see Figure 5.10(b), the maximum required current is 30 A. More details on the valve design are shown in Figure B.2, also in Appendix B.

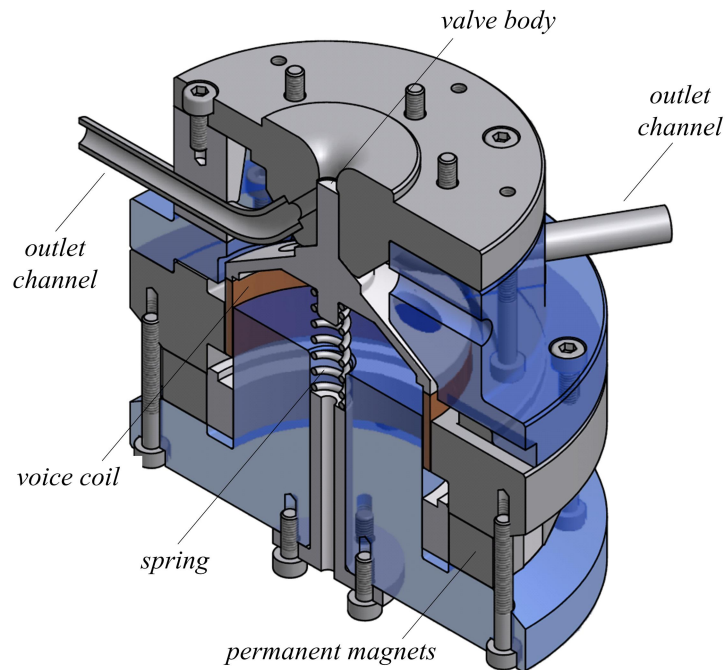


Figure 5.11 / Design of the servo-valve.

5.5.2 Cylinder Design

The cylinder design is shown in Figure 5.12. On the left side of the cylinder, a rotational joint is used to attach the cylinder to the surroundings, allowing two rotational degrees of freedom. The belt is connected to the other end of the piston. During operation, the cylinder aligns itself to the line of force and no momentum will be applied to the piston. A curved tube is shown in the figure, which is used to fill the cylinder with fluid after operation. In the top part, the outlet opening is shown, which leads the fluid to the valve body. In Figure 5.13, a drawing is shown of the cylinder and valve assembled.

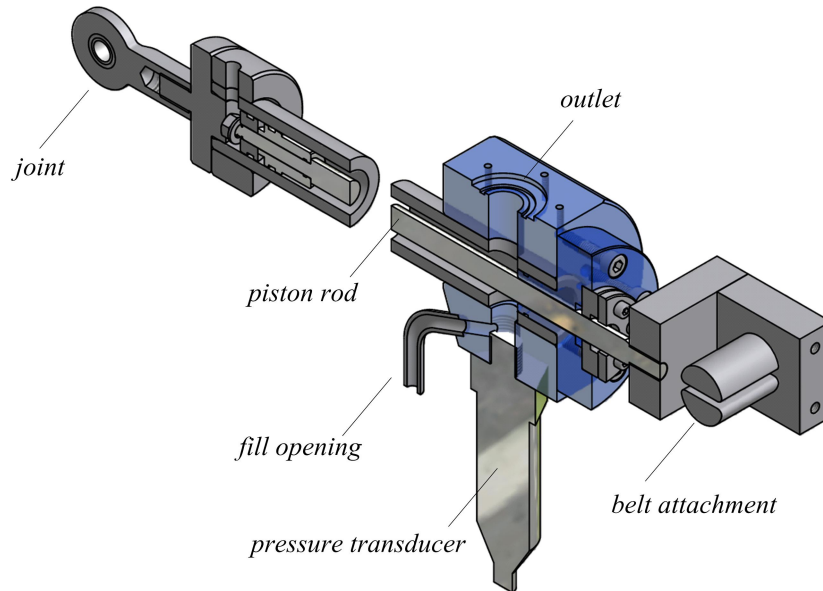


Figure 5.12 / Design of the hydraulic cylinder.

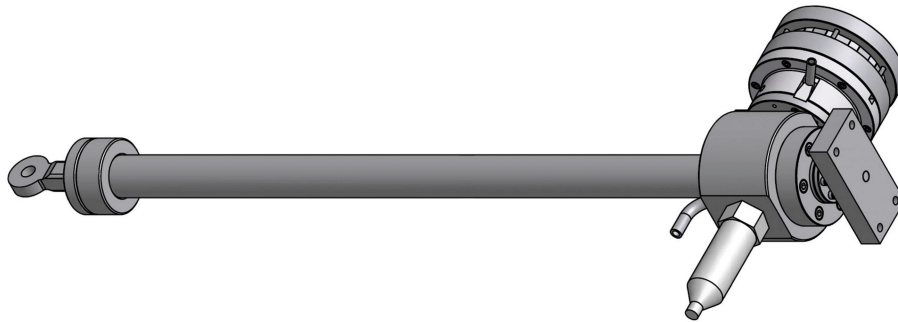
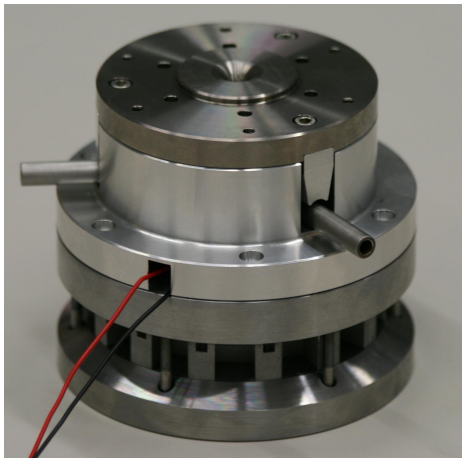


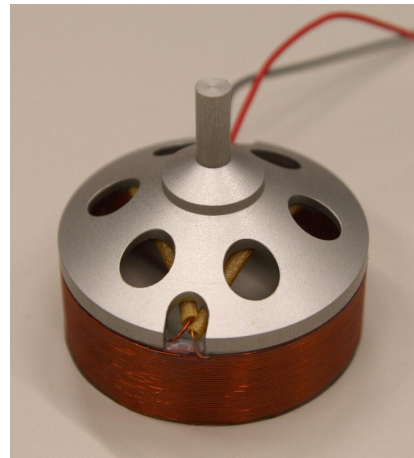
Figure 5.13 / Design of the actuator, consisting of cylinder and servo-valve.

The length of the device, defined from joint to belt attachment, is 72 cm. The width and height of the cylinder *without* the pressure sensor and reservoir is 8.5 cm by 15 cm respectively. These dimensions make it possible to mount this belt actuator in the B-pillar of a passenger vehicle. In Figure 5.14, pictures are shown of the valve parts. On the left side, the assembled valve housing is shown. On the right side, the valve body with the coil is shown. In Figure 5.15, the assembled actuator is shown. The three valve outlets are connected to a small reservoir by flexible tubes. After every experiment, this reservoir is emptied. At the bottom

of the cylinder, next to the pressure sensor, a quick-release connector is used for filling of the cylinder after every experiment. This greatly limits the amounts of air that will be carried along with the fluid during filling. At the front, an attachment for the belt can be seen, which is constructed such that the belt aligns with the piston rod. After every experiment, the belt is replaced.



(a) The servo valve with outlets, but without the permanent magnets.



(b) The spool body glued to the coil.

Figure 5.14 / Valve parts.

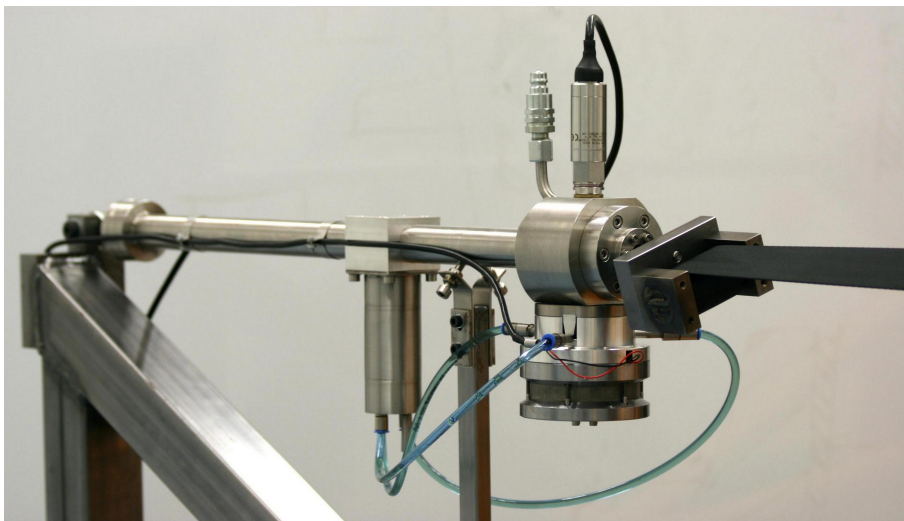


Figure 5.15 / The assembled belt force actuator.

5.5.3 Data Acquisition and Control Hardware

The current through the valve, $I(t)$, is provided by a current amplifier, which takes a voltage $U(t)$ as input. The gain of the amplifier is roughly 4, so with the voice coil motor constant derived above, it follows that K_u has a theoretical value of 44 N/V. The current amplifier is an analog servo amplifier from Elmo, see Table 5.4. It has a current feedback loop with a bandwidth up to 4 kHz, and the linearity is within 0.4 A. The particular amplifier can output 20 A continuously, and a peak current of 30 A is allowed. Voltage comes from two DC voltage sources that are placed in series, and are able to deliver 104 V at 30 A.

A pressure sensor is placed opposite to the outlet, as shown in Figure 5.12. Different types of pressure sensors are available. Here, it is chosen to use a transducer (opposed to a transmitter) and an instrumentation amplifier. Most pressure transducers are either piezoelectric or piezo-resistive. The former are very suitable for high pressure applications, but not for static measurements. For the best frequency response from a pressure sensor, an unamplified piezo-resistive transducer has to be used that provides a mV output directly from a strain gauge bridge. The PDCR 4000 series transducer from GE Sensing (Drück) is chosen, a high performance sensor with good linearity and accuracy. As shown in Figure 5.10(b), the maximum pressure inside the cylinder is approximately 400 bar. The PDCR 4000 has a range of 350 bar, although this can be extended to 700 bar without any noticeable effect. It should also be noted that these sensors can take mechanical shocks up till 1000 g without affecting the performance. An HBM measurement amplifier is used to convert the sensor output to a manageable signal.

For the data acquisition and control, a dSpace real-time I/O system is used⁹. ControlDesk is used as the interface between the dSPACE processor and a workstation. The software for the system is written in Matlab/Simulink[®]. The data acquisition as well as the control software runs at a sample frequency of 10 kHz.

Table 5.4 / Actuator equipment

Instrument	Manufacturer	Type
Pressure transducer	GE Sensing	PDCR4000, 350 bar
Measurement amplifier	HBM	MGCplus
Current amplifier	Elmo Motion Control	VIOLIN 20/100
DC Power Supply	Delta Elektronika	2 x SM52-30
Data Acquisition	dSPACE	DS1103

⁹dSpace, Inc. [online], <http://www.dspaceinc.com> (last access: August 2009).

5.6 Identification and Control Design

In this section, the dynamic characteristics of voice coil and the semi-active damper are identified. Based on this identification, a local controller \mathcal{H} is designed, and the performance of the actuator is evaluated with closed-loop experiments.

5.6.1 Identification of the Voice Coil

The dynamic behavior of the voice coil actuator is important for the overall control performance of the belt force actuator. In this section, the static and dynamic behavior of the voice coil is analyzed, without hydraulic oil in the system. The absence of oil may influence the friction between spool body and housing, so small amounts of oil are added to the valve during the experiments.

The force applied to the valve body cannot be measured directly in a non-contact way. Since the mass of the valve is accurately known, its acceleration is used to determine the resultant force on the body. The motion of the valve body is measured with a laser vibrometer (Polytec OFV 3000). The working principle of this sensor is based on the Doppler effect, so the output is in fact a velocity. Measurements are performed at 4 kHz sampling frequency with a TueDACS MicroGiant data acquisition and control system¹⁰, connected to a Linux OS via USB.

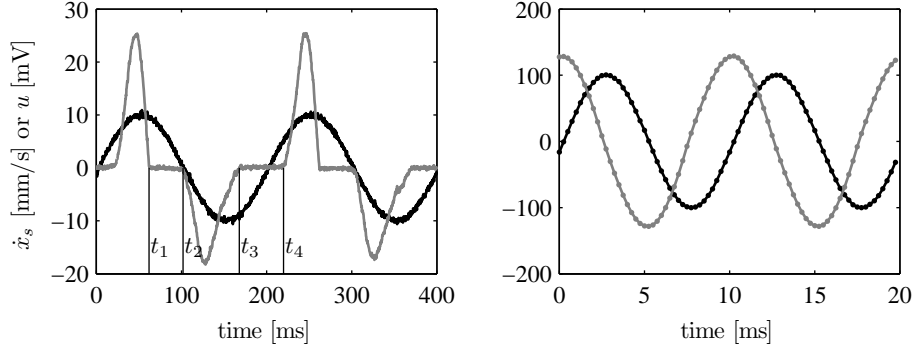
The equation of motion for the valve body is given in (5.23). Since there is no hydraulic pressure ΔP , only the voice coil can move the spool. To be able to move the spool in absence of hydraulic forces, the spring k_s in this experiment is taken to be much less stiff than the original spring. The spring that is used in this experiment has an estimated stiffness of $\check{k}_s \approx 0.4 \text{ kNm}^{-1}$, and $\check{F}_o \approx 7.2 \text{ N}$. Without hydraulic pressure, the equation of motion reads

$$M_s \ddot{x}_s(t) + \mu_s \dot{x}_s(t) + F_c \cdot \text{sgn}(\dot{x}_s(t)) + \check{k}_s(x_s(t) + x_o) + \check{F}_o = K_u U(t)$$

For $\mu_s > 0$, $F_c > 0$, this system is stable. So for a constant input, $U(t) = U^* > 0$, an equilibrium will set at position x_s^* , and hence $U^* = \frac{\check{k}_s(x_s^* + x_o) + \check{F}_o}{K_u}$. Deviations on this constant voltage and equilibrium position are denoted by $\Delta U(t) = U(t) - U^*$ and $\Delta x_s(t) = x_s(t) - x_s^*$, respectively. With $\Delta \dot{x}_s = \dot{x}_s$ and $\Delta \ddot{x}_s = \ddot{x}_s$

$$M_s \Delta \ddot{x}_s(t) + \mu_s \Delta \dot{x}_s(t) + F_c \cdot \text{sgn}(\Delta \dot{x}_s(t)) + \check{k}_s \Delta x_s(t) = K_u \Delta U(t) \quad (5.28)$$

¹⁰TueDACS, trademark of the Experiment Automation Group at the Eindhoven University of Technology [online], <http://www.tuedacs.nl> (last access: August 2009)



(a) A 5 Hz sinusoidal input $\Delta U(t)$ with an amplitude of 10 mV.

(b) A 100 Hz sinusoidal input $\Delta U(t)$ with an amplitude of 100 mV.

Figure 5.16 / The measured velocity $\dot{x}_s(t)$ of the valve body (gray), for different sinusoidal inputs $\Delta U(t)$ (black).

Experimental results with $\Delta U(t) = 0.01 \sin(10\pi t)$ are shown in Figure 5.16(a), where the input is a 5 Hz sine with a 10 mV amplitude. In the period $t_1 \leq t \leq t_2$, the velocity of the valve is zero, hence $\Delta \ddot{x}_s(t) = \Delta \dot{x}_s(t) = 0$ and $\Delta x_s(t_1) = \Delta x_s(t_2)$. At the beginning and end of this period, the Coulomb friction component is given by $F_c \cdot \text{sgn}(\Delta \dot{x}_s(t_1)) = F_c$ and $F_c \cdot \text{sgn}(\Delta \dot{x}_s(t_2)) = -F_c$. Note the asymmetry in the response, which is caused by dependence of the voice coil motor constant on the current, see Appendix B. The Coulomb friction is calculated in the period $t_3 \leq t \leq t_4$, hence

$$F_c = K_u \frac{\Delta U(t_4) - \Delta U(t_3) - \ddot{k}_s(\Delta x_s(t_4) - \Delta x_s(t_3))}{2} = 7.2 \cdot 10^{-3} K_u$$

So 7.2 mV input voltage is required to overcome the friction. With an expected value of $K_u \approx 40$, the Coulomb friction is low, $F_c < 0.3$ N.

The Coulomb friction induces a nonlinearity, but this can be neglected if the forces on the body are much larger than the friction forces. The system is therefore excited with a sinusoidal with an amplitude of 100 mV at a frequency of 100 Hz. As shown in Figure 5.16(b), the Coulomb friction is not influencing the valve motion in this case. More specifically, for input amplitudes larger than 50 mV, the friction is not noticeable.

After these fixed frequency measurements, the dynamic response of the voice coil is analyzed. Noise with a frequency content up till 1.8 kHz is superposed on the sinusoidal input from Figure 5.16(b). Together with the measured velocity signal, frequency response data is generated. It is plotted in Figure 5.17 in a Bode plot,

which shows the magnitude and phase of the frequency response data.

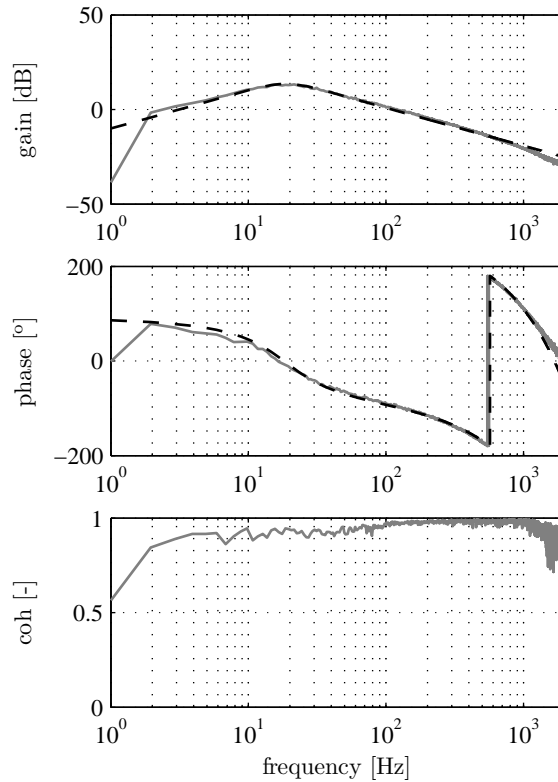


Figure 5.17 / Measured frequency response data (gray), and fitted frequency response function (black, dashed) of the transfer from input voltage ΔU to spool velocity Δv_s .

Also shown is the coherence plot, which defines to what extent the measured output is a linear map of the considered input. Measurement noise, process noise, an insufficient rich input signal, and non-linearities cause that the coherence will deviate from the value 1. The coherence plot indicates that at least for frequencies higher than 10 Hz, the system behaves linearly and Coulomb friction can be ignored. Therefore, the system described by (5.28) can be represented by the following transfer function

$$\frac{\Delta v_s(s)}{\Delta U(s)} = \frac{sK_u/M_s}{s^2 + \mu_s/M_s s + \check{k}_s/M_s} e^{-\tau s}$$

with $M_s = 35 \cdot 10^{-3}$ kg, $\Delta v_s(s)$ the Laplace transfer of the output velocity $\Delta \dot{x}_s$, and τ the time delay caused by the data acquisition and control. To find the values

for K_u , μ_s and \check{k}_s , the magnitude of this frequency response *function* is fitted to magnitude of the frequency response *data*, and the fit is shown in Figure 5.17 as the black dashed line. Next, the time delay τ is found by fit of the phase data. The parameters that result from this fit are given in Table 5.5. Note that the updated Coulomb friction coefficient is given by $F_c = 0.18$ N.

With a sample frequency of 4 samples per millisecond during the experiment, the time delay is roughly two samples. Note that the gain K_u is almost half of the expected value, so the motor constant of the voice coil is much lower than designed: 6.0 N/A against 13.3 N/A. This implies that the maximum coil force is 180 N instead of 300 N.

5.6.2 Identification of the Hydraulic Actuator

In this section, identification experiments are described that are carried out with the valve mounted on the cylinder. These experiments are performed to determine the dynamic behavior of the semi-active actuator. The cylinder is filled with hydraulic oil, and placed in a Zwick universal testing machine. This machine is capable of performing accurate tensile tests, and is equipped with load cells and extensometers. The advantage of experimenting with the actuator in a testing machine first, is the fact that the environment is well conditioned and forces can be accurately measured. Figure 5.18 shows the actuator mounted in the testing machine.

Since the hydraulic pressure induces a larger force on the valve, the stiff spring that was presented in Table 5.3 is mounted in the valve. According to the specifications of the manufacturer, $k_s = 8.09$ kN/m and after assembly, the spring shortening is measured to be around 15.5 mm, so it is estimated that $F_0 = 15.5 \cdot 8.09 \approx 125$ N.

Model Matching in the Time Domain

The testing machine is capable of moving with a maximum velocity of 1000 mm/min. According to the model presented in (5.26), the inputs of the system are the voltage $U(t)$, and the piston position $x_p(t)$. The piston starts to accelerate at a rate of 1.5 mm/s², until it reaches a constant speed of 15 mm/s. During this piston movement, the pressure increases until the valve opens. At this point, an equilibrium is set, in which the pressure remains approximately constant. A voltage is applied 5.0 seconds after the pressure reaches 40 bar, at which the valve is partly open. A sinusoidal signal with a frequency of 1 Hz and 0.5 V peak-to-peak is applied during 10 seconds. The voltage, and the piston position and velocity are shown in Figure 5.19.

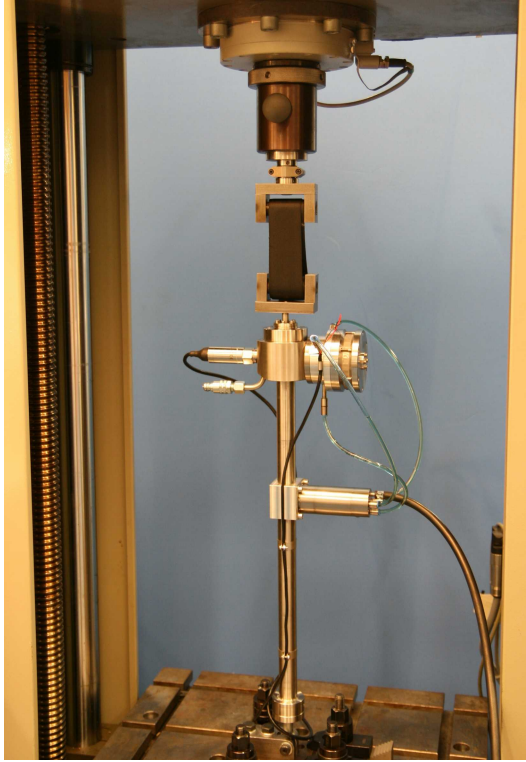


Figure 5.18 / Belt force mounted in a Zwick universal testing machine for identification experiments.

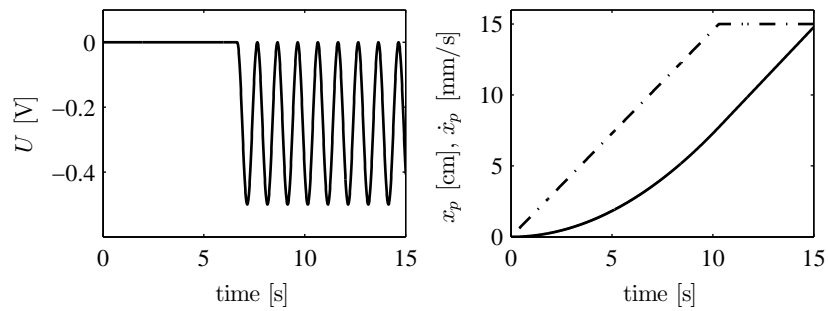


Figure 5.19 / Inputs to the actuator system. On the left, the voltage $U(t)$ applied to the current amplifier, and on the right the piston position (solid). Also shown is the piston velocity (dash-dotted).

The equations of the model in (5.26) are solved for the measured inputs. The

initial values of the 3 states of the model are given by $x_s(0) = -x_o$, $\dot{x}_s(0)$, and $m(0) = 77.5$ g. This value is calculated with (5.17), given the initial (measured) pressure $\Delta P(0) = 24.2$ bar. The simulation results with the model are shown in Figure 5.20. The measured pressure, filtered with CFC600, is given by the gray line. Furthermore, the flow through the orifice is calculated according to (5.11), and the spring force using (5.21). Noticeable is that the valve opens only several μm , which leads at the given pressure to sufficient flow through the orifice.

The excellent fit in the pressure results is obtained by slightly adapting two *uncertain* model parameters, i.e. the effective bulk modulus E_f , and the initial spring force F_0 . The effective bulk modulus will always be lower than its theoretical value, $E = 1.5 \cdot 10^9$ Nm^{-2} , because of air being inevitably trapped in the fluid. It is found that $E_f = 0.35 \cdot 10^9$ Nm^{-2} . The initial spring force is found to be $F_0 = 114$ N, so the initial spring compression is 1.4 mm less than measured, which is plausible. All parameters are listed in Table 5.5.

Table 5.5 / Parameters of the voice coil.

symbol	value	unit	quantity
K_u	24	[N/V]	motor constant and current amplifier gain
μ_s	5.1	[Ns/m]	viscous friction coefficient
\tilde{k}_s	0.48	[kN/m]	stiffness of temporary spring
k_s	8.09	[kN/m]	stiffness of spring
τ	0.45	[ms]	time delay
F_c	0.18	[N]	friction force
E_f	$1.5 \cdot 10^9$	Nm^{-2}	effective bulk modulus
F_o	114	N	initial spring force

Identification in the Frequency Domain

In the second experiment, the input-output behavior is analyzed in the frequency domain. In the field of system identification, this is often done by applying a random signal with a known mean value and variance to the input, which approximates a white noise signal (constant spectral power in the frequency domain). Other methods are analyzing step or impulse responses of the system. Here, a multi-sine input is applied to the system, given by

$$U(t) = \sum_{i=1}^n A_i \sin(2\pi f_i t + \phi_i)$$

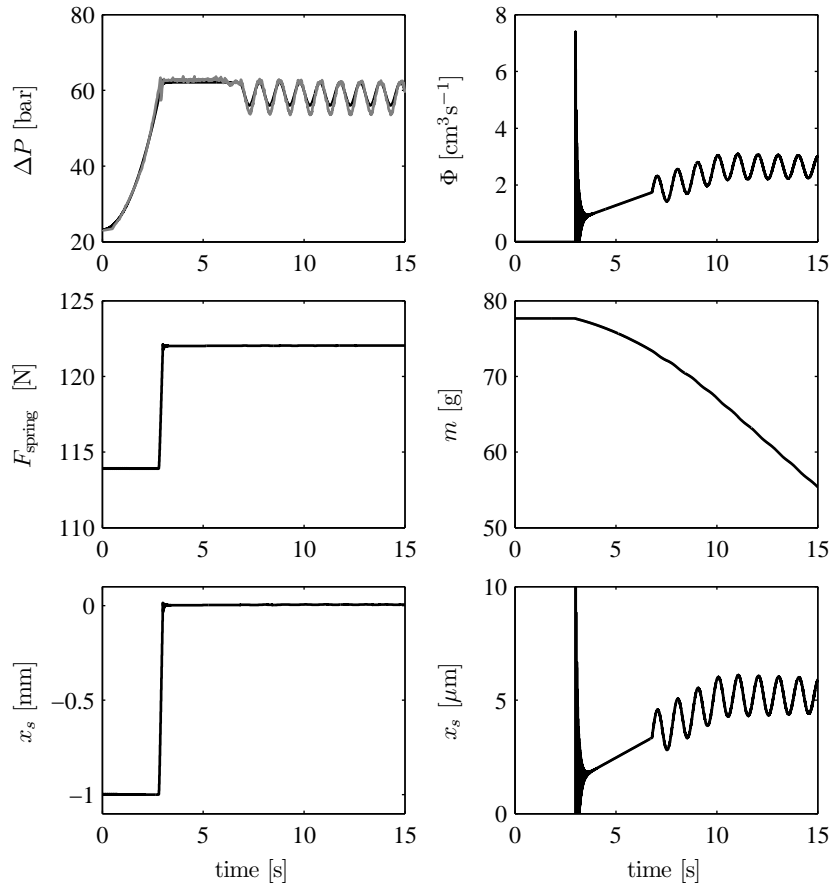


Figure 5.20 / Results of the actuator model for the inputs plotted in Figure 5.19, together with the measured pressure (gray). The figures on the bottom row are both spool displacements, but with a different scale.

with the individual frequencies and phase shifts given by

$$\phi_i = -\frac{i(i-1)\pi}{n}, \quad f_i = \ell_i f_{\min} \text{ with } \ell_i \in \mathbb{N}$$

This particular phase shift is called the Schroeder phase, and ensures a low crest factor. This factor is defined as the ratio between peak and rms value of a signal in the frequency band of interest. For a multisine signal with Schroeder phase, it is typically 1.7 (Pintelon and Schoukens, 2001). The advantages of the multisine approach over the more common approaches in system identification, e.g. step or impulse responses, are (Pintelon and Schoukens, 2001)

- the signal is periodic in $1/f_{\min}$, so for time-invariant systems, the estimation can be averaged and will converge to a mean estimation;
- the user is free to choose the frequencies f_i , given that they are multiples of f_{\min} ;
- the signal power of every individual sinusoidal can be freely chosen.

The frequency region of interest is around the desired bandwidth, 300 Hz, and around the expected actuator resonance, i.e. 77 Hz. Therefore, it is chosen to apply a multisine with $t \in [0, 10]$ s, $f_{\min} = 10$ Hz, $n = 25$, $\ell_i = (2i - 1)$, such that $f_n = 490$ Hz. The amplitude A_i is chosen to be low at low frequencies, since the input results in an acceleration of the spool body, and the spool displacement is limited by the available space. The input signal is shown in Figure 5.21, in the time and frequency domain.

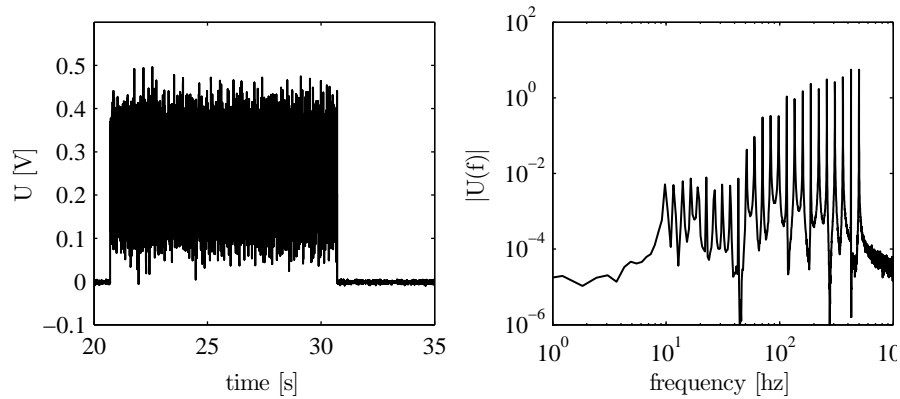


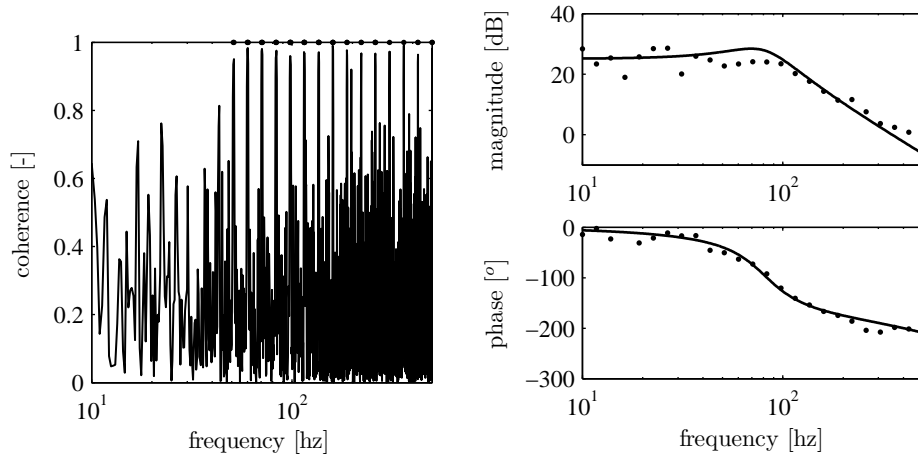
Figure 5.21 / The time signal and the spectral density of the multisine input.

The coherence plot is shown in Figure 5.22(a), which shows that the system is not sufficiently excited at low frequencies, but higher input amplitudes were not possible as mentioned above. After averaging of the responses to improve the signal-to-noise ratio, the frequency response is derived at points f_i and shown in Figure 5.22(b), indicated by dots.

For the frequency points with a coherence higher than 0.9, a fit is made using the transfer function model $\hat{\mathcal{G}}(s)$ from (5.27), see Section 5.4.7. In this third order LTI model, now the obtained parameters from Table 5.5 are incorporated, i.e. $K_u = 24$ N/V, $\mu_s = 5.1$ Ns/m, $\tau = 0.45$ ms, and an effective bulk modulus $E_f = 0.35 \cdot 10^9$ Nm⁻². The resulting LTI model is given by the transfer function

$$\mathcal{G}(s) = \Delta P(s)(U(s))^{-1}$$

The FRF is fitted to the magnitude of the complex frequency response data, since the transfer function depends on the operating point used in the linearization, as shown in Figure 5.10. The fit is shown in Figure 5.22(b) by the solid line.



(a) Coherence plot from input voltage U in Figure 5.21 to the measured pressure ΔP .

(b) Estimated frequency response data for the frequency points f_i (dotted). The solid line is an FRF fit corresponding to the third order transfer function $\mathcal{G}(s)$.

Figure 5.22 / Results of the multisine experiment.

The multisine experiments are performed at one constant velocity of the piston, i.e. $\dot{x}_p = 900$ mm/min, which implies that the spool position is more or less constant during these tests. From the modeling of the system in Section 5.4.7, it became clear that the linear approximations depend on the operating point. The multisine experiments are therefore also performed at different piston velocities, resulting in higher flows and hence a different mass m , valve position x_s , and piston position x_p at the time of the multisine input. The FRF of a transfer function $\mathcal{G}(s)$ is again fitted to the frequency response data, and the results are shown in Figure 5.23.

5.6.3 Control Design

The transfer functions $\mathcal{G}(s)$ from the fitted frequency response functions are employed to design a controller for pressure control, \mathcal{H} . Since the pressure transducer has a very high bandwidth, the measurement data is very noisy and a second order

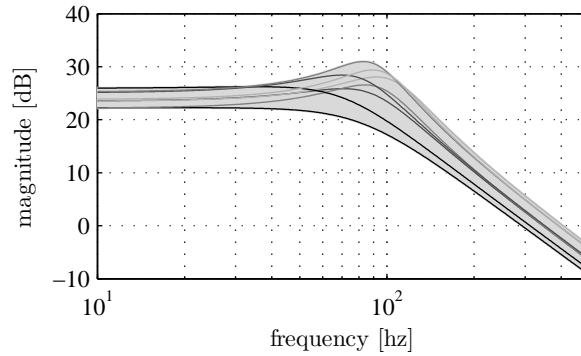


Figure 5.23 / Fitted FRFs of $\mathcal{G}(s)$ on frequency response data from 8 multisine experiments with piston velocities of 500, 750, 900 and 1000 mm/min (from black to light gray, respectively).

Butterworth filter is used as an output filter. It is given by \mathcal{H}_{BW}

$$\mathcal{H}_{\text{BW}} = \frac{\omega_r^2}{s^2 + \sqrt{2}\omega_r s + \omega_r^2}$$

with a cutoff frequency of $\omega_r/2\pi = 200$ Hz. A feedback controller, \mathcal{H}_{FB} , is used for robust stability and closed-loop linearization, and a feedforward controller, \mathcal{H}_{FF} , is added for performance. The resulting controller is \mathcal{H} , see Figure 5.24 and compare it to Figure 5.4.

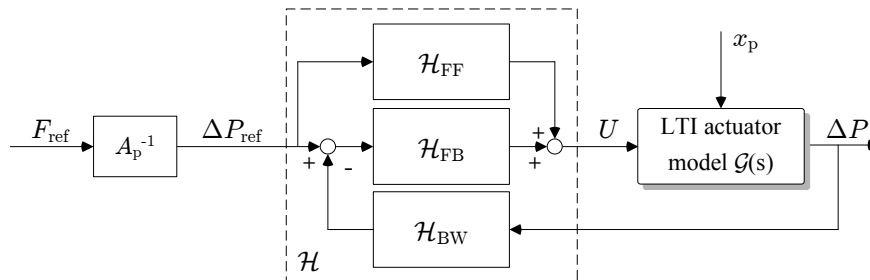


Figure 5.24 / Control layout of belt force actuator.

The FRFs of the transfer function $\mathcal{H}_{\text{BW}}(s)\mathcal{G}(s)$ are shown in Figure 5.25(a), with the mean of the FRFs drawn by a black line. In the control design, the upper and lower bounds of the magnitude of the FRFs are used, to provide a controller that is robustly stable for the system's nonlinearities. As required in Table 5.1, the closed-loop system should have a bandwidth or cross-over frequency of $f_{\text{act}} \approx 300$ Hz. Moreover, it should provide closed-loop robustness through a phase margin

$PM > 50^\circ$ and a modulus margin $MM < 6$ dB. The feedback controller \mathcal{H}_{FB} consists of a proportional integrator and a skew notch to give phase lead. The Bode plot of this controller is illustrated in Figure 5.25(b). The open-loop transfer function, $\mathcal{H}_{FB}\mathcal{H}_{BW}(s)\mathcal{G}(s)$, is shown in Figure 5.26 in a Bode plot and a Nyquist diagram. It can be observed that the cross-over frequency or bandwidth is 260 Hz, the modulus margin $MM = 5.7$ dB, and the phase margin $PM = 57^\circ$.

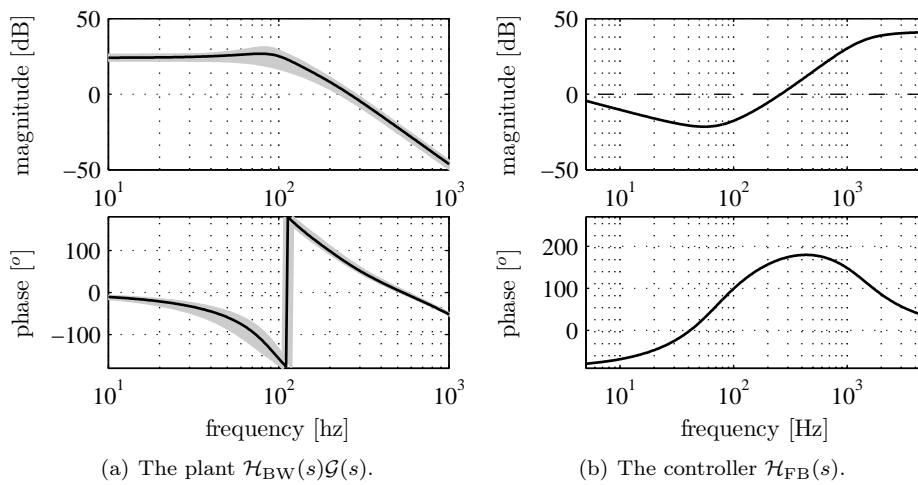


Figure 5.25 / Bode plots of the transfer functions of the plant and controller.

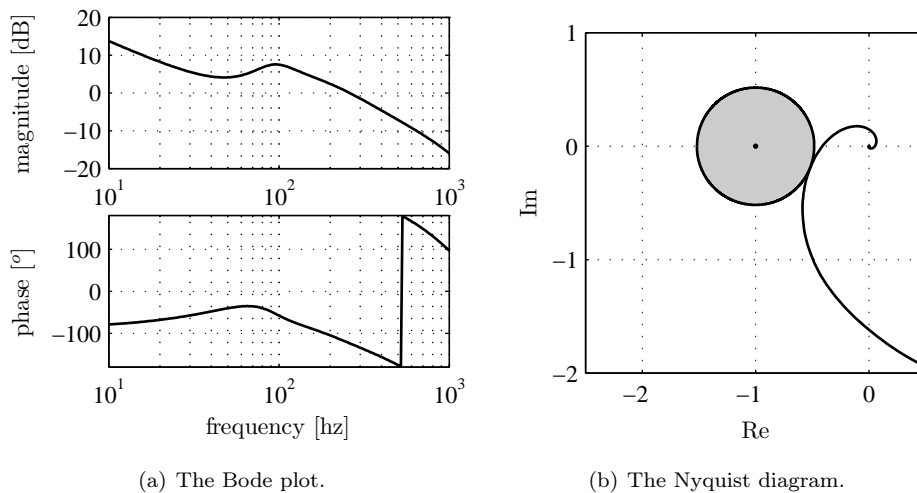


Figure 5.26 / The open-loop transfer functions $\mathcal{H}_{FB}\mathcal{H}_{BW}(s)\mathcal{G}(s)$.

The feedforward controller \mathcal{H}_{FF} consists of a stiffness and a mass feedforward term, based on the inverse of the plant model in Figure 5.25(a). The feedforward term of the control effort in the Laplace domain is given by

$$\mathcal{H}_{\text{FF}}(s) = \frac{U_{\text{FF}}(s)}{\Delta P_{\text{ref}}(s)} = 2.0 \cdot 10^{-7} s^2 + 0.080$$

5.6.4 Closed-loop Experiments

Closed-loop experiments are performed with the semi-active belt force actuator placed in the universal testing machine. The piston moves at a speed of 1000 mm/min. At a certain time instance during the piston movement, a setpoint for the pressure is superposed on the current pressure, and the controller \mathcal{H} is activated. In Figure 5.27, three examples are shown of the closed-loop results, for sinusoidal setpoints of 5 Hz and 10 Hz, and a trapezium-shaped setpoint. Tracking errors are small, e.g. for the sinusoidal input an error reduction of -20 dB at 10 Hz.

It is noticeable that the system behaves differently between decreasing and increasing the pressure. This is best seen in the third row in the figure, where the tracking error during pressure increase stays within 0.2 bar, while it exceeds 1 bar during decrease. The current variations are too small to cause significant variations in the motor constant, see Figure B.1. Moreover, applying a sinusoidal input voltage in open-loop did not show the high-frequency oscillations during the pressure decrease phase, hence, the behavior is caused by the controller and not by the mechanics.

5.6.5 Performance Specifications

After the design, construction and identification process, it can be concluded that the design and performance requirements are partly met.

During the movement of the piston, a pressure drop is generated across the valve. According to Table 5.1, the maximum piston velocity is 10 m/s, and when incompressibility is assumed, this gives a maximum flow of $1.76 \cdot 10^{-3} \text{ m}^3\text{s}^{-1}$. This flow corresponds to a pressure of 38 bar at full valve opening, see (5.11). When it is desired to increase the pressure, the valve needs to be closed. According to (5.23), a negative spool acceleration requires that the coil and spring force together exceed the hydraulic force (ignoring friction forces). The motor constant of the voice coil is found to be 6 N/A, which implies that the coil force is $F_{\text{coil}} \leq 180 \text{ N}$. The spring force during full valve opening is $F_{\text{spring}} = 156 \text{ N}$. The hydraulic spool force should thus be less than 336 N, in order to be able to close the valve, which equals an

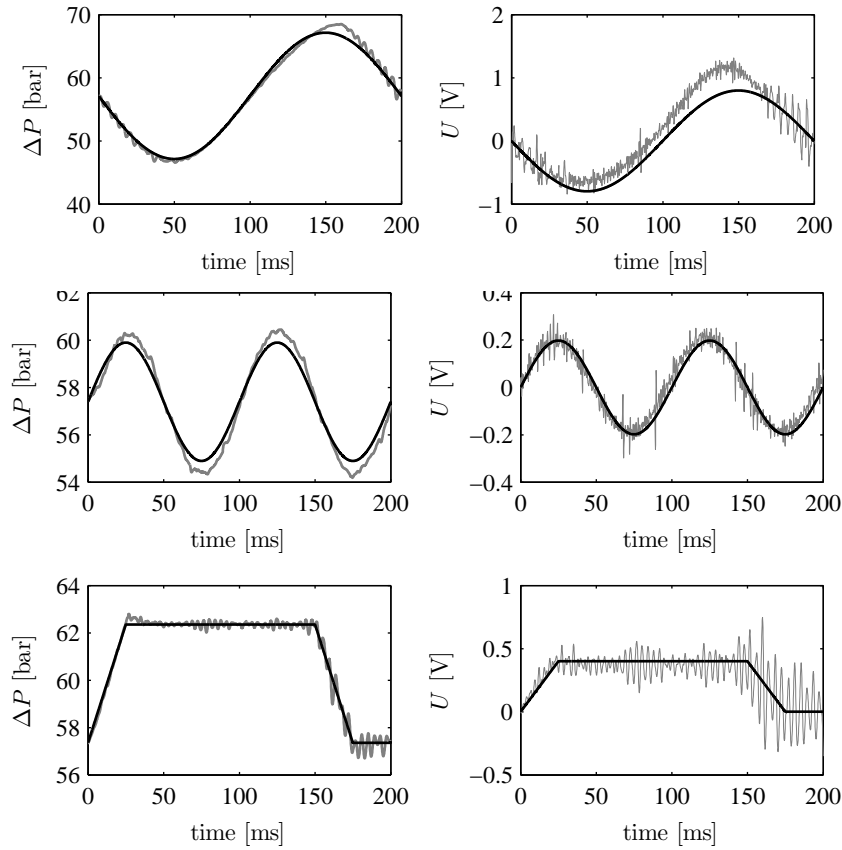


Figure 5.27 / Closed-loop experimental results with the belt-force actuator in a universal testing machine.

actuator force of $336A_p/A_s = 3.0$ kN. Hence, during a piston velocity of 10 m/s, the force can be prescribed between 0.67-3.0 kN.

The cross-over bandwidth was found to be around 260 Hz, which is close to the performance requirement of 300 Hz. Also, the required maximum stroke and stroke velocity can be realized. The performance specifications are summarized in Table 5.6.

Reviewing the design requirements in Section 5.2, it is concluded that these requirements are met. The actuator is semi-active, and given its dimensions of 72x8.5x15 cm could be well fitted in a vehicle's B-pillar. The device is used only during maximum 200 ms, which allows sending high currents through the voice coil. The energy needed to actuate the voice coil can be obtained from a capacitor.

Table 5.6 / Realized actuator performance specifications

description	value	unit
force applied to belt	$0 \leq F_{\text{hyd,p}} \leq 3$	kN
stroke displacement	$0 \leq x_{\text{belt}} \leq 0.50$	m
stroke speed	$0 \leq v_{\text{belt}} \leq 10$	ms^{-1}
actuator bandwidth	$f_{\text{act}} \approx 260$	Hz

Finally, the device is made re-usable, by mounting a quick-release connector to fill the cylinder, and collecting the outflow in a reservoir. At the time of writing, the coil and valve bodies are not impact-proof.

5.7 Towards Closed-loop Sled Experiments

An experimental setup is developed to test the actuator and to evaluate the performance in terms of thoracic injury reduction. Since (commercial) full-scale sled tests with dummies are expensive (10-30 k€), a simple in-house sled setup is used to demonstrate the concept of controlled restraint systems.

5.7.1 Introduction

The experimental setup merely serves to demonstrate the principle of a continuous controlled belt actuator in a high speed crash environment, where impact forces and the time scale have similar magnitudes as in real-world frontal impacts. It is not meant to accurately mimic the dummy or occupant behavior in an actual crash scenario. Since it will be quite laborious to seat an entire dummy or other anthropomorphic device on this sled, only the occupant's thorax is used. The thorax is represented by a single mass, *the torso body*, with one degree-of-freedom.

The objective of the proposed controlled restraint system is to minimize the peak deceleration of this mass during impact, analogous to the 3ms chest acceleration exceedence or the A_{max} criterion for a dummy or occupant. It is recognized that this criterion is not accepted as a good injury predictor for the human body in impact, see Section 1.2.2. However, if satisfactory results are obtained for this criterion, then it is safe to assume that the actuator is capable to influence more accepted thoracic injury criteria.

It should be noted here that the sled experiments described in this section showed that the actuator is yet not impact-proof, and the final closed-loop experiments could not be performed.

5.7.2 The Sled Setup

A sled test setup has been built previously, and used in various research projects at the University of Technology Eindhoven, see e.g. (Egberts, 1996; Witteman, 1999). The sled is shown in Figure 5.28. The setup has previously been used to study deformation of various crumple components, with the goal to improve the vehicle's front-end structure. However, in this study the crumple components serve to apply a deceleration to the moving cart.

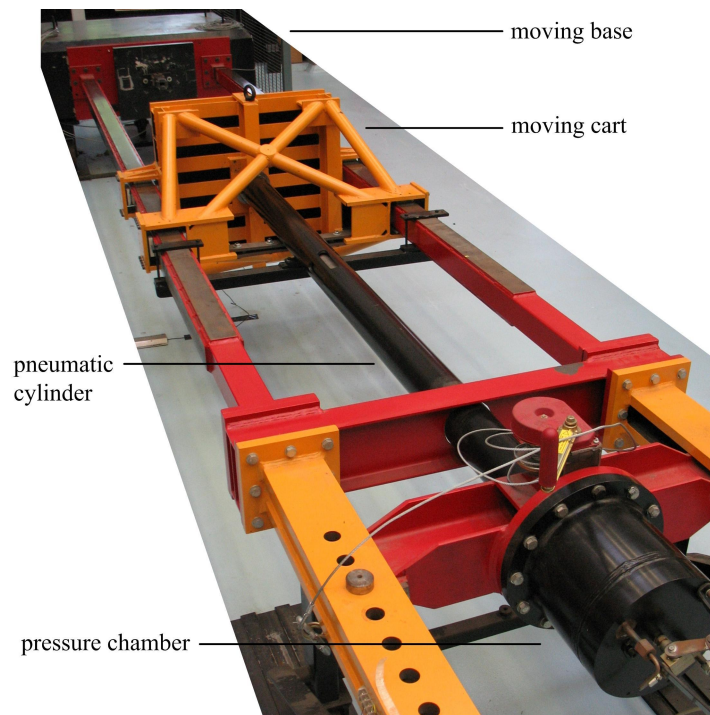


Figure 5.28 / The experimental sled setup.

As shown in Figure 5.28, the construction consists of two parallel bars with a length of approximately 6 m. They are connected at one end to a large mass on wheels (1700 kg), the *moving base*, and at the other end to a large pneumatic cylinder. This cylinder is connected to a pressure chamber with a volume of 2 l, which can be pressurized up to 100 bar. When the pressure from the chamber is released into the cylinder, the piston of the cylinder extends and accelerates a moving mass (218 kg), the *cart*. With the bars as a guidance, the cart moves with high velocity towards the moving base. The cart impacts against a deformable steel crumple component, which through plastic deformation dissipates the kinetic energy of the

cart. The entire construction is placed on wheels, so the reaction forces during acceleration and deceleration are not transferred to the surroundings.

The setup is capable of accelerating the cart up to a speed of 15 ms^{-1} (54 kmph). The type of crumple component, the cart mass and the chamber pressure will determine the shape and duration of the crash pulse at impact. In Figure 5.29, a typical crumple component, *viz.*, a welded, rectangular steel profile, is shown before and after the deformation. When the profile is slightly deformed *before* impact, a regular deformation pattern can be observed as shown in the picture, see also (Witteman, 1999).

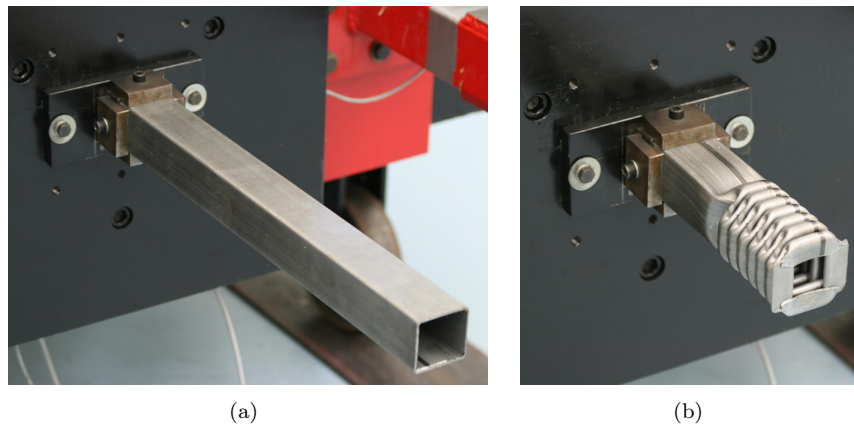


Figure 5.29 / The crumple component before (a) and after (b) impact.

Crash pulses measured in frontal crash procedures with passenger vehicles, e.g. EuroNCAP or USNCAP, generally have a duration of 80-200 ms and a mean acceleration of 6-18 g's, see (Agaram et al., 2000; Huang, 2002; Wood, 2003). This implies that the mean impact velocity ranges between $5\text{-}36 \text{ ms}^{-1}$. Various chamber pressures and crumple components have been tested to obtain an acceleration pulse of the cart, a_{cart} , that roughly has a duration of 80 ms and a mean of 10 g. With a cart of 218 kg, a pressure of 30 bar and a crumple components of $50 \times 50 \times 1.5 \text{ mm}$ (width, height, thickness), deceleration pulses are obtained as shown in Figure 5.31(a). The velocity just before impact is 9 ms^{-1} , and with a crash duration of 80 ms, the mean acceleration is roughly -11 g. The crumple components are pre-crumpled before they are used in the actual tests, since this prevents force peaks when the cart hits the tube.

Acceleration sensors are added to the cart and to the moving base. These piezoresistive accelerometers from Entran, model EGCS-S425, are widely used in auto

safety testing¹¹. Dynamic characteristics are presented in Figure 5.30, which shows a bandwidth of more than 1 kHz. This implies that measurement noise up till 1 kHz is not attenuated.

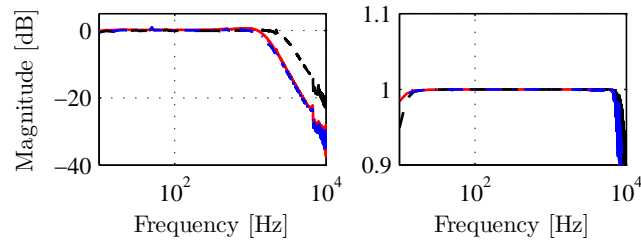
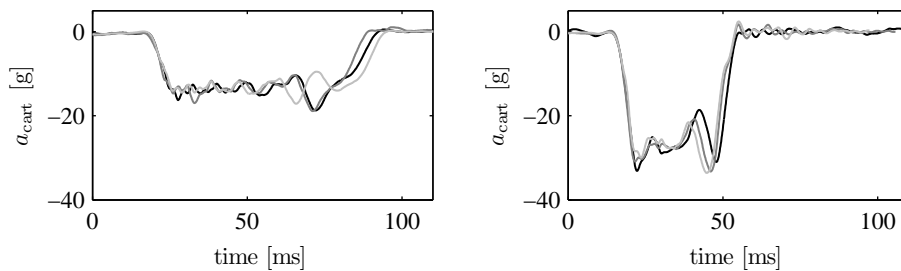


Figure 5.30 / Calibration (left) and coherence (right) plots of three Entran vibration sensors.

Moreover, a velocity sensor is added to measure the relative velocity between base and cart just before impact. The sensor is based on a linear optical encoder, with the optical device mounted on the base and a rail with slits mounted on the cart.

When the torso mass and other structural elements are added to the moving cart, it is expected that the higher cart mass will result in an increased crash duration and a lower mean acceleration. Therefore, a stiffer crumple bar is chosen, resulting in higher deceleration values than desired, see Figure 5.31(b). Multiple tests with identical settings are performed, and one can see in the figures that reproducibility is sufficient.



(a) Crumple component thickness of 1.5 mm (b) Crumple component thickness of 2.0 mm

Figure 5.31 / Example of cart deceleration pulses (CFC60) obtained with crumple components of various thicknesses.

¹¹Measurement Specialties, Entran Vibration Sensors [online] <http://www.meas-spec.com/> (Last access: January 2009).

5.7.3 Control Objective

As mentioned previously in this chapter, it is not possible to mount a dummy or other anthropomorphic device on the cart. Therefore, it is chosen to use a simple representation of the human torso: a sliding mass of 30 kg, which roughly approximates the mass of the thorax for averaged sized humans and dummies (Lobdell, 1973; Neathery and Lobdell, 1972). The mass has one degree of freedom, in the direction of the cart movement. Figure 5.32 shows the setup conceptually. In this figure, the absolute accelerations of the torso body, the cart and the moving base are indicated by a_{torso} , a_{cart} and a_{base} respectively. As presented in Figure 5.24, the actuator applies a force $F_{\text{hyd,p}}$ to the actuator body.

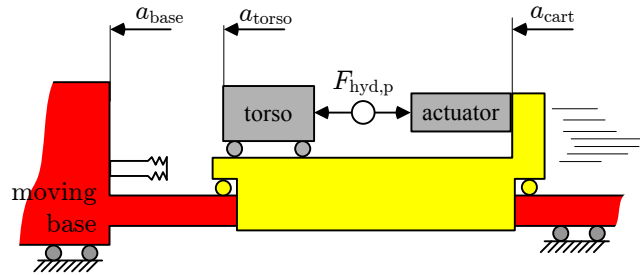


Figure 5.32 / Conceptual representation of the sled with the torso dummy mounted on the cart.

The concept is constructed as shown in Figure 5.33. The torso mass is placed in the center of the cart, and is guided by steel profiles. These profiles support the impact plate as well. A conventional vehicular seat belt is used to transfer the restraint force from the actuator to the torso mass. The seat belt is attached to base plate, runs over the torso body via a slit, and through a conventional D-ring to the actuator. The sled with torso body is shown in Figure 5.34.

The acceleration of the torso body is controlled by an outer feedback controller, \mathcal{F} . Based on the error between an acceleration setpoint, a_{ref} , and the measured acceleration, it determines the belt force setpoint, F_{ref} . This setpoint is given to the actuator controller, \mathcal{H} , which provides input U to the actuator such that $|F_{\text{ref}} - F_{\text{hyd,p}}|$ is minimized, see Figure 5.24. The control scheme is sketched in Figure 5.35, where the block belt force actuator represents Figure 5.24. The piston position x_p is a state of the sled system, and is a disturbance input to the actuator.

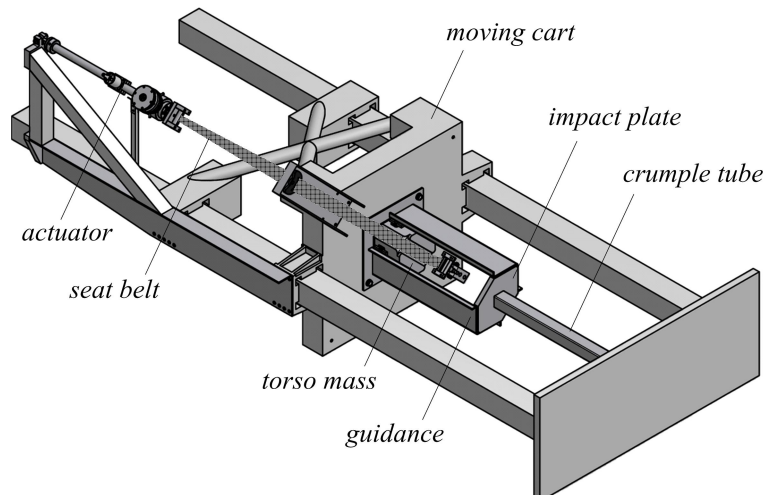


Figure 5.33 / Moving cart with an additional torso mass mounted on the base plate between the guidance bars. A seat belt is used to transfer the load to the actuator during impact.

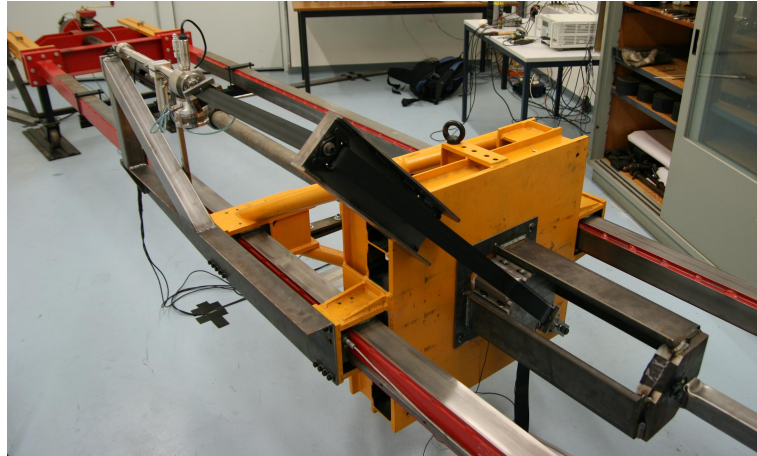


Figure 5.34 / Final sled setup with sliding torso body and belt force actuator.

5.7.4 Modeling of the Sled

The design of the controller \mathcal{F} is based on a dynamical model of the system. A simple two-dimensional model of the sled setup and torso mass has been developed, see Figure 5.36. Modeling in two dimensions seems appropriate, since the belt

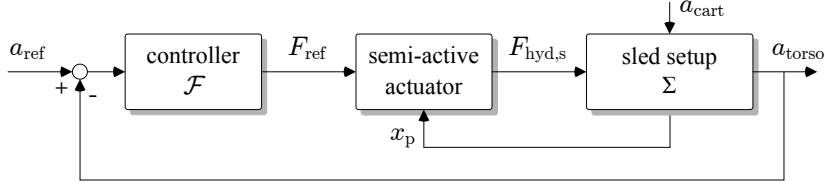


Figure 5.35 / Closed-loop configuration for control of the torso body acceleration.

roughly runs in a single plane. The cart is considered as a moving frame and is given a forced motion, x_{cart} . The torso body is mounted on this frame, and has mass M_t . It is connected via a belt to the second body, the piston with mass M_p . The belt is modeled as a linear visco-elastic element, with parameters k and d . The belt runs from the piston body over the D-ring pulley to the torso, and via two frictionless pulleys to the cart. Coulomb friction with coefficient μ is defined in the D-ring pulley, since this friction force is expected to be considerable, see e.g. TNO Madymo B.V. (2005). Since the torso body runs very smoothly over its guidance, no friction is modeled between torso and cart body.

The system has two degrees of freedom, Δx_{torso} and x_p , with $\Delta x_{\text{torso}} = x_{\text{torso}} - x_{\text{veh}}$. The cart acceleration, a_{cart} , acts as a disturbance on the system, and the control input is given by the hydraulic piston force $F_{\text{hyd,p}}$. The nonlinear equations of motion of this system are derived using Euler-Lagrange's equations (Schiehlen, 1990).

Consider the model shown in Figure 5.36 in the Cartesian frame $\{O, \vec{e}\}$, with $\vec{e} = [\vec{e}_1 \ \vec{e}_2]^T$ a column of two orthogonal vectors of unit length. The two degrees of freedom are represented by two generalized coordinates, $q_1 = \Delta x_{\text{torso}}$ and $q_2 = x_p$, as shown in the figure. The generalized coordinates are stacked in a vector $\mathbf{q} = [q_1 \ q_2]^T$. The initial conditions are given by $\mathbf{q}(0) = \mathbf{0}$. Constraints on the displacement result in the requirement $\mathbf{q} > \mathbf{0}$. The Euler-Lagrange equations, also presented in Section 2.6.3, read

$$\frac{d}{dt} \left(T_{,\dot{\mathbf{q}}} \right) - T_{,\mathbf{q}} + V_{,\mathbf{q}} = (\mathbf{Q}^{\text{nc}})^T \quad (5.29)$$

The position vectors to the center of gravity of the torso and actuator body are given by resp. $\vec{r}_1 = \mathbf{r}_1^T \vec{e}$ and $\vec{r}_2 = \mathbf{r}_2^T \vec{e}$, with

$$\mathbf{r}_1 = \begin{bmatrix} x_{\text{cart}}(t) + l_4/2 + q_1 \\ l_3 + l_2/2 \end{bmatrix}, \quad \mathbf{r}_2 = \begin{bmatrix} x_{\text{cart}}(t) - (l_5 - q_2) \\ l_1 + l_2 + l_3 \end{bmatrix} \quad (5.30)$$

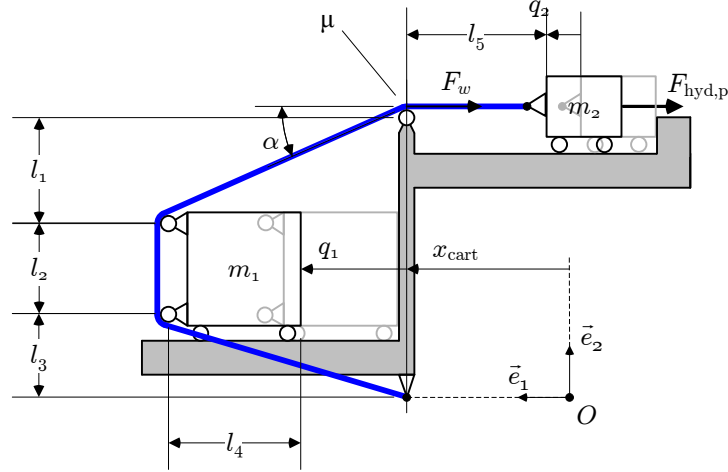


Figure 5.36 / Model of the torso and actuator.

The total kinetic energy T is given by

$$T = \frac{1}{2} \sum_{i=1}^2 m_i \dot{\mathbf{r}}_i^T \dot{\mathbf{r}}_i = \frac{1}{2} m_1 (\dot{x}_{\text{cart}}(t) + \dot{q}_1)^2 + \frac{1}{2} m_2 (\dot{x}_{\text{cart}}(t) + \dot{q}_2)^2 \quad (5.31)$$

Now it is easy to see that

$$\frac{d}{dt} \left(T, \dot{\mathbf{q}} \right) - T, \mathbf{q} = \dot{\mathbf{q}}^T \begin{bmatrix} m_1 & 0 \\ 0 & m_2 \end{bmatrix} + \begin{bmatrix} m_1 \\ m_2 \end{bmatrix}^T \ddot{x}_{\text{cart}} \quad (5.32)$$

The potential energy function V is the sum of the internal and the potential energy:

$$V = g \sum_{i=1}^2 m_i \mathbf{r}_i^T \vec{e}_2 + \frac{1}{2} k \varepsilon^2 \Rightarrow V, \mathbf{q}(\mathbf{q}) = k \left(\frac{\partial \varepsilon}{\partial \mathbf{q}} \right) \varepsilon$$

with k the stiffness of the belt and ε the belt elongation. Here, it is assumed that the belt can be described by linear, elastic behavior. This is plausible when it is also assumed that the elongation during the entire experiment is *strictly* increasing. The elongation is given by $\varepsilon(\mathbf{q}) = \ell(\mathbf{q}) - \ell(\mathbf{0})$, with ℓ the length of the belt:

$$\ell(\mathbf{q}) = l_2 + \sqrt{l_3^2 + (l_4 + q_1)^2} + \sqrt{l_1^2 + (l_4 + q_1)^2} + l_5 - q_2$$

In this system, the nonconservative forces comprise of the externally applied force $F_{\text{hyd,p}}$, the friction force F_w (in the D-ring), and the damping force in the belt. The damping is merely used to make the system under-damped, such that eventual

oscillations caused by the belt elasticity are attenuated. The generalized damping force is given by

$$\mathbf{Q}_d^{\text{nc}}(\mathbf{q}, \dot{\mathbf{q}}) = -d \left(\frac{\partial \varepsilon}{\partial \mathbf{q}} \right)^T \dot{\varepsilon}$$

with d the belt damping coefficient. The friction force F_w is modeled similar to Section 2.6.3, i.e.

$$F_w(q_1) = (1 - e^{-\mu\alpha}) F_{\text{belt}}$$

with α the wrapped angle between the two belt segments on the pulley, and μ the Coulomb friction coefficient. The force in the belt is given by the belt elongation ε , according to $F_{\text{belt}} = k\varepsilon + d\dot{\varepsilon}$. The actuator cannot retract the piston, so $\dot{q}_2 > 0$, and it can be assumed that the friction force is always positive. The wrapped angle is a function of the first generalized coordinate according to $\alpha(q_1) = \arctan((l_4 + q_1)l_1^{-1})$. The relative displacement of the belt with respect to the pulley surface is given by $\kappa(q_1) = \varepsilon + q_2$. The nonconservative friction force follows from the virtual work $\mathbf{Q}_f^{\text{nc}}\delta\mathbf{q} = F_w\delta\kappa$. Hence

$$\mathbf{Q}_f^{\text{nc}}(q_1) = \left[(1 - e^{-\mu\alpha}) \frac{\partial \varepsilon}{\partial q_1} \quad 0 \right]^T (k\varepsilon + d\dot{\varepsilon})$$

Finally, the applied force $F_{\text{hyd,p}}$ works on the system as

$$\mathbf{Q}_u^{\text{nc}} = [0 \quad -1]^T F_{\text{hyd,p}}$$

The total nonconservative forces and potential energy are now

$$\begin{aligned} \mathbf{Q}^{\text{nc}} - V_{,\mathbf{q}}^T &= \mathbf{Q}_d^{\text{nc}}(\mathbf{q}, \dot{\mathbf{q}}) + \mathbf{Q}_f^{\text{nc}}(q_1) + \mathbf{Q}_u^{\text{nc}} - V_{,\mathbf{q}}(\mathbf{q})^T \\ &= [0 \quad -1]^T F_{\text{hyd,p}} - \left[e^{-\mu\alpha} \frac{\partial \varepsilon}{\partial q_1} \quad 1 \right]^T (k\varepsilon + d\dot{\varepsilon}) \end{aligned}$$

Using (5.29), the equations of motion read

$$\begin{aligned} \ddot{\mathbf{q}} &= \begin{bmatrix} 0 \\ -\frac{1}{m_2} \end{bmatrix} F_{\text{hyd,p}} - \begin{bmatrix} e^{-\mu\alpha} \frac{\partial \varepsilon}{\partial q_1} \\ \frac{1}{m_2} \end{bmatrix} (k\varepsilon + d\dot{\varepsilon}) - \begin{bmatrix} 1 \\ 1 \end{bmatrix} \ddot{x}_{\text{cart}} \\ &\text{with } \mathbf{q} > \mathbf{0}, \quad \mathbf{q}(0) = \dot{\mathbf{q}}(0) = \mathbf{0} \end{aligned}$$

The constraints on the displacements, i.e. $\mathbf{q} > \mathbf{0}$, are implemented in the simulation model by the so-called *bouncing ball* principle:

$$\dot{q}_i(t) = \begin{cases} \dot{q}_i(t) & q_i(t) \geq 0 \\ -0.7\dot{q}_i(t) & q_i(t) < 0 \end{cases}$$

for $i = 1, 2$. It ensures that the constraints are close to satisfied when the simulation step time is sufficiently small. The outputs of the model are the torso acceleration a_{torso} , and the force in the belt, F_{belt} . They are given by

$$a_{\text{torso}} = \ddot{q}_1 + a_{\text{cart}} = -\frac{e^{-\mu\alpha}}{m_1} \frac{\partial \varepsilon}{\partial q_1} (k\varepsilon + d\dot{\varepsilon})$$

$$F_{\text{belt}} = k\varepsilon + d\dot{\varepsilon}$$

The model parameters and their values are listed in Table 5.7.

Table 5.7 / Sled model parameters.

symbol	value	unit	description
m_1	30	kg	mass torso body
m_2	1.656	kg	mass actuator body
μ	0.1	-	Coulomb friction coefficient
k	52.5	kN	belt stiffness
d	250	Ns	belt damping coefficient
l_1	0.60	m	height D-ring
l_2	0.20	m	height torso
l_3	0.30	m	attachment point
l_4	0.13	m	depth torso
l_5	0.5	m	length belt between D-ring and piston body

The model, referred to by \mathcal{S} , is governed by the following differential equations:

$$\mathcal{S} : \begin{cases} \begin{bmatrix} \Delta \dot{v}_{\text{torso}} \\ \dot{v}_p \end{bmatrix} = \begin{bmatrix} 0 \\ -m_2^{-1} \end{bmatrix} F_{\text{hyd,p}} - \begin{bmatrix} \frac{e^{-\mu\alpha}}{m_1} \frac{\partial \varepsilon}{\partial \Delta x_{\text{torso}}} \\ m_2^{-1} \end{bmatrix} (k\varepsilon + d\dot{\varepsilon}) - \begin{bmatrix} 1 \\ 1 \end{bmatrix} a_{\text{cart}} \\ \begin{bmatrix} a_{\text{torso}} \\ F_{\text{belt}} \end{bmatrix} = \begin{bmatrix} -\frac{e^{-\mu\alpha}}{m_1} \frac{\partial \varepsilon}{\partial \Delta x_{\text{torso}}} \\ 1 \end{bmatrix} (k\varepsilon + d\dot{\varepsilon}) \end{cases} \quad (5.33)$$

With $\Delta x_{\text{torso}} \geq 0$, $x_p \geq 0$ and $v_p = \dot{x}_p$, $\Delta v_{\text{torso}} = \Delta \dot{x}_{\text{torso}}$.

The seat belt is an important element in the setup, and the system dynamics properties are to a large extent determined by the belt characteristics. To determine the properties of the seat belt, a number of experiments is performed on a universal testing machine, with a sample of belt with an average length of 500 mm. In Figure 5.37, belt measurement results are shown that are performed to estimate belt stiffness k . A preload force of 1000 N is applied to remove possible slack in the system. After pretensioning, strain is applied to the belt at a rate of 10, 100, 333 and 1000 mm/min. The tension force and belt length are measured, and the force and relative elongation are plotted in Figure 5.37. One can see that

the strain rate has no significant influence, at least up till the maximum strain rate of the machine.

It is noticeable that the belt returns to its original length when unloaded, so at least part of the material deforms elastically. A part of the belt deforms plastically during loading. Therefore, a belt damping coefficient d is added to account for the energy dissipation of the plastic deformation, and ensure that oscillations are dampened.

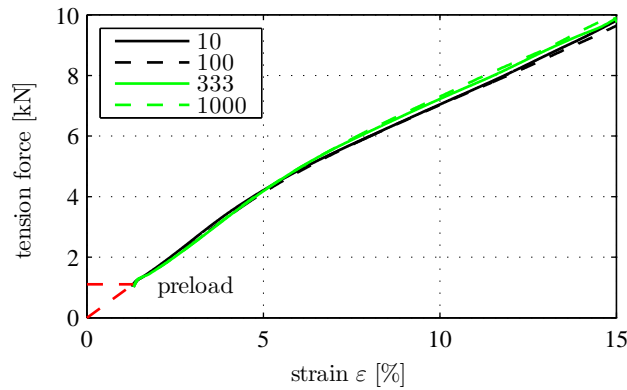


Figure 5.37 / Measurement of relative belt elongation versus tension force, measured at a constant velocity of 10-1000 mm/min.

The belt type in the measurement is identical to the belt that will be used in the sled setup, i.e. a so-called 12% polyester belt¹². One can see that the belt is indeed elongated 12% at 10 kN of tension. Now define the stiffness of the belt *per unit of length* as K . Two points in the measurement data are used to find an estimate

$$K = \frac{F_2 - F_1}{\varepsilon_2 - \varepsilon_1} = \frac{4.195 - 0}{0.050 - 0.0} \approx 84 \text{ kN}$$

with ε the strain. When the initial length of the belt ℓ_o is known, the stiffness can be easily calculated, $k = K/\ell_o$.

The stiffness k of the length of belt used in the setup is simply given by

$$k = \frac{K}{\ell_o} = \frac{84 \cdot 10^3}{1.6} = 52.5 \text{ kN/m}$$

¹²The % number is used by automotive restraint suppliers to reflect the relative belt elongation at a tensile force of 10 kN

5.7.5 Experimental Validation

The sled model presented above is validated with a simple experiment. The actuator is removed, so the belt is fixed to the cart structure. In the equations of motion of the model \mathcal{S} in (5.33), this leads to $\dot{v}_p(t) = 0$, and the only input is now the measured cart acceleration pulse, a_{cart} . The damping coefficient is given a relatively small value, whereas the D-ring friction coefficient is known from Section 2.6.2.

A belt force transducer is placed on the belt near the actuator attachment point. This sensor, a Messring DK-11-31-00, is shown in Figure 5.38 and is commonly used in safety crash tests. The measured belt tension force F_{belt} and torso acceleration a_{torso} are compared with the model output force as a validation.



Figure 5.38 / The Messring belt force transducer.

An experiment is performed with a pneumatic chamber pressure of 30 bar, and a crumple component of $50 \times 50 \times 1.7$ mm. The resulting cart acceleration and deceleration, and absolute cart velocity are shown in Figure 5.39.

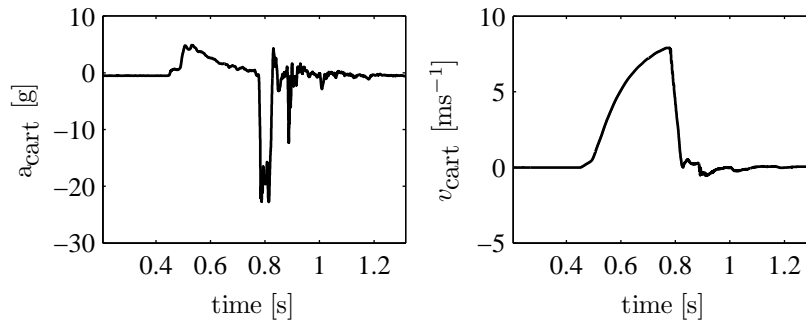


Figure 5.39 / Measured cart acceleration (left) and velocity (right).

The simulation and experimental results are shown in Figure 5.40. It indicates that the belt forces matches very accurately, in timing as well as in magnitude. The measured force signal has a dominant 50 Hz noise signal, probably caused by insufficient shielding from power lines. Also the torso acceleration matches quite well, hence the model is a useful representation of the sled setup.

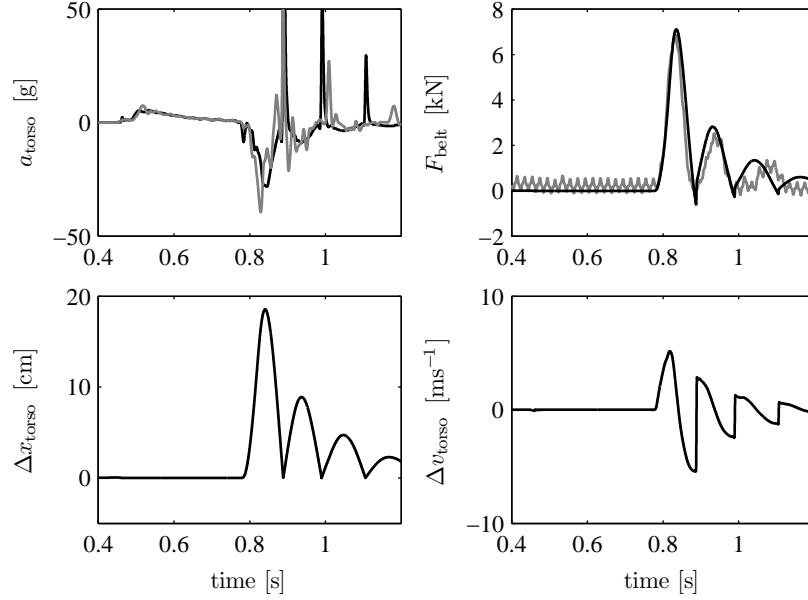


Figure 5.40 / Motion of the torso body and belt tension force of the experiment (gray) and the model (black), all filtered with CFC60.

5.7.6 Control Scheme

The approach for the closed-loop experiments, in which the actuator is used to control the torso acceleration during an impact, is presented here. The scheme in Figure 5.24 for the actuator control is combined with the sled control scheme shown in Figure 5.35. The combined control scheme is illustrated in Figure 5.41, where a boundary is indicated between the real and numerical world. Note that a filter is added on the measured torso acceleration signal, since the sensors have a high bandwidth and are noisy. This filter is given by

$$\mathcal{F}_{\text{BW}} = \frac{\omega_r^2}{s^2 + \sqrt{2}\omega_r s + \omega_r^2}$$

with $\omega_r/2\pi = 200$ Hz.

When the constructed actuator is modified such that it can withstand impact tests, the ability of the actuator to mitigate thoracic injuries can be evaluated in an experimental setup, according to this control scheme.

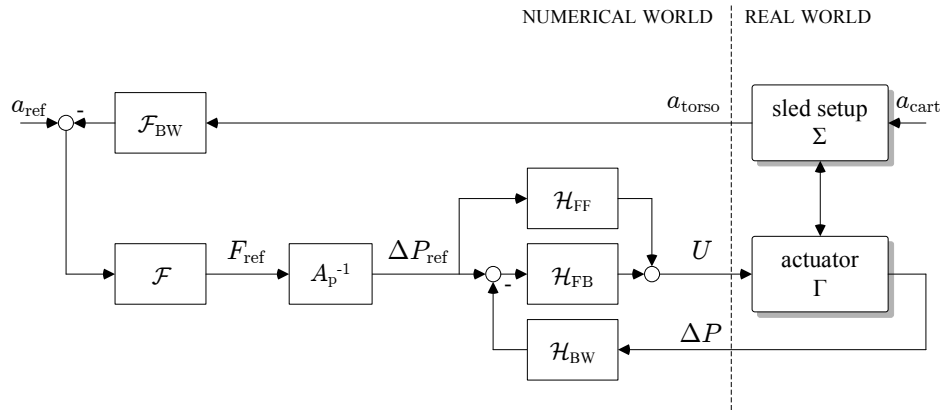


Figure 5.41 / Closed-loop configuration of the sled experiment with the belt force actuator.

5.7.7 Conclusion

In the previous section, an experimental sled setup has been presented. This setup was used to impact a moving cart against a deformable element at high speed. The obtained crash pulses of the cart were reproducible over multiple tests, and their pulse shape roughly resembles real-world crash pulses. A sliding mass has been added to the cart to represent the human thorax. Moreover, a model of the setup has been developed for control design purposes, and this model has been validated with experimental tests. Experimental tests with the actuator mounted on the setup indicated that the actuator is not yet impact-proof, as the voicecoil breaks down from the valve body for reasons that are unclear.

5.8 Discussion

In this chapter, a belt force actuator has been designed, constructed and experimentally evaluated. The performance and design requirements for the actuator have been formulated using closed-loop simulation results with the Madymo reference model. It was possible to perform a closed-loop simulation in which the belt rollout velocity was (almost) strictly positive, at the cost of slightly increased injury criteria. This implies that a semi-active actuator can be used, i.e. an actuator that is strictly dissipative. This result led to a actuator design concept based on a hydraulic cylinder. A model of the hydraulic actuator has been developed, to i) determine the required dimensions, ii) assess the performance, and iii) to design a controller. The actuator is constructed, and identification experiments have been performed to determine the actual performance specifications. One finding is that the maximum force that can be applied is lower than specified, viz. 3 kN instead of 8 kN. Subsequently, closed-loop experiments with the actuator in a universal testing machine are performed, from which was observed that the closed-loop (tracking) performance is according to the specifications. The research objective to test the actuator under impact conditions is not yet achieved.

6

CONCLUSIONS AND RECOMMENDATIONS

Abstract / The main ideas and results that have been presented in this thesis are summarized. Furthermore, recommendations and directions for future research on controlled seat belt systems are proposed.

6.1 Conclusions

In this thesis, a study is presented on continuous restraint control systems for passenger vehicles. This type of systems allow the optimization of injury mitigation for each specific accident situation separately, rather than applying a methodology that has been optimized for a specific accident situation such as prescribed by crash regulations. This type of integrated safety measures is an important part of the future vehicle safety technology, and significant developments in this field are required (Passive Safety Network, 2004). The main objective for this research has been to design an actuator and a system that prescribes the belt force in a conventional 3-point seat belt arrangement, such that thoracic injuries sustained by a vehicle occupant are mitigated. Moreover, no major assumptions are allowed that would hinder the actual implementation of this system in a vehicle. The scope of this research objective was limited to adult front-seat occupants, involved in a frontal impact with a passenger car, and to three thoracic injury criteria.

In this section, the conclusions are presented with respect to this research objective, following the outline of Chapters 2-5.

Modeling for Control Design

In Chapter 2, it has been recognized that low-order occupant models are essential in the development of restraint control systems. Control design models have been developed via a multi-fidelity approach, using a sensitivity analysis of a complex crash victim simulation model. A two-dimensional model is constructed that consists of 11 rigid bodies and has 14 degrees of freedom. Various validation studies are performed, in which simulation results of the design models are compared with responses from experimentally validated Madymo models. These studies are done for a broad range of frontal crash scenarios, and for three different adult Hybrid III dummies, i.e. the 5th, the 50th and the 95th percentile. Subsequently, the design models have been linearized to yield a set of linear time-invariant crash victim simulation models.

Although only three design models have been developed, the models can be easily interpolated based on a measurable parameter, e.g., the total body mass of the occupant. This is also described in Section 4.2.3. The interpolated model can then be used in the observer or to select the corresponding controller gains.

Moreover, the models are based on the Hybrid III dummies. The 50th male dummy is likely to be replaced in the near future by the more humanlike THOR dummy. The THOR dummy has improved biofidelity and includes multipoint sensing for advanced injury assessment. However, it is expected that the HIII and THOR dummy differ primarily in complexity, but the most basic features and components will be alike. This implies that the developed design models, which also include only the most basic elements of the HIII dummy, will also be suitable for the THOR dummy.

Current crash victim simulation models are very complex, highly non-linear and have typically many degrees of freedom. However, relevant phenomena concerning thoracic injury mechanisms could be accurately described by the developed design models, despite the imposed limitations on the complexity and non-linearities. The validation studies showed that the design model generates the biomechanical responses related to injury predictors for the chest and neck region remarkably well. Even the linear time-invariant models are well suited to predict spinal accelerations and chest compressions. This leads to the conclusion that thoracic injury mechanisms in severe frontal impact can be captured by some simple relations, although the large amount of non-linearities present in common CVS models, such as discontinuities, hysteresis, and geometry, suggest otherwise. On the other hand, it became clear that the linear visco-elastic belt model was too elementary to accurately simulate the belt rollout. The belt rollout largely influences the occupant displacement during impact, which was thus also not predicted very precisely in some cases.

Model Predictive Control Strategy

In Chapter 3, a cascaded control strategy for real-time control of belt restraint systems is proposed. The control method consists of a combination of a primal controlled loop and an MPC controller. The primal controlled loop has excellent tracking properties and disturbance attenuation, enforced by a local feedback controller. The MPC controller finds an optimal setpoint for the primal loop, while satisfying constraints and without a priori knowledge of the upcoming crash. The latter is achieved by a procedure to obtain an estimate of the vehicle motion during the crash. This procedure is based on extrapolation of data that is fitted to the crash measurement history. The optimization algorithm of the MPC controller is robustified with respect to inevitable vehicle motion prediction errors.

The whole proposed design procedure is generic in nature. For instance, it is straightforward to include multiple injury criteria in the optimization problem, on the condition that these criteria depend linearly on the belt force and crash pulse. Also, the flexibility in the design of the primal loop enables to tailor the primal controller to different plant dynamics, without the need for adjusting the MPC controller. Concluding, the cascaded control strategy is believed to be an important step towards real-time implementation of controlled safety restraint systems. It reduces the injury criteria considerably (e.g. A_{\max} with 45%) with respect to conventional restraint systems, while still meeting the real-time computational requirements.

Smart Sensors for Thoracic Injury Estimation

In Chapter 4, a solution has been presented for the problem of real-time prediction of (thoracic) injuries and occupant position during a crash. It has been proposed that filtering of four measurable variables will help in improving the estimation of these responses. These measurable variables have been selected after a study on available vehicle sensor technologies. Sensors are selected that measure the acceleration of a belt segment that lies over the thorax, that measure the belt rollout, the vehicle acceleration, and the belt force in the pillar belt. A linear Kalman filter has been designed, with the objective to estimate the state of the design model. The simulation results indicated that the measurement outputs were correctly updated by the filter, however, a part of the state space was not correctly reconstructed, resulting in an inaccurate prediction of the thoracic injuries and occupant position. This led to the conclusion that the prediction step in the Kalman filter should be improved, and the prediction was subsequently performed with the nonlinear design model. The extended Kalman filter significantly improved the prediction of the *non-measurable* model outputs.

It has been difficult to select sensors that provide information on biomechanical occupant responses. Responses like spinal acceleration and chest compression had to be estimated, without mounting sensors in or on the occupant. This limitation greatly reduces the possibility of an accurate estimation. It was chosen to use sensors that provide information on the belt motion and force, which require that the belt and belt friction model used in the observer should be very accurate. With the proposed belt model, this requirement is not met.

Semi-Active Belt Force Actuator

In Chapter 5, a belt force actuator has been designed, constructed and evaluated. The performance and design requirements for the actuator have been formulated using closed-loop simulation results with the complex Madymo model. It was possible to perform a closed-loop simulation, in which the belt rollout velocity was directed opposite to the belt force (almost) during the entire crash. This implies that a semi-active actuator can be used, i.e. an actuator that is strictly dissipative. This result led to a design concept based on a hydraulic cylinder with an electro-hydraulic servo-valve. A model of the hydraulic actuator has been developed, such that the required dimensions could be determined, the performance could be evaluated by simulations, and a controller could be designed. The actuator is constructed, and identification experiments have been performed to determine the performance specifications. One finding is that the maximum force that can be applied is lower than specified, namely 3 kN instead of 8 kN. Subsequently, closed-loop experiments with the actuator in a universal testing machine have been performed, from which was observed that the closed-loop (tracking) performance is according to the specifications. Moreover, an experimental sled setup is described, which can be used to assess the capability of the belt force actuator to reduce thoracic injuries during an impact. However, the coil and valve body were not able to withstand the impact forces. Although the experiments in the universal testing machine indicate that the actuator is able to mitigate thoracic injuries, this could not yet be validated by sled impact experiments.

6.2 Recommendations

In this section, some recommendations for future research are listed.

- In the design models, the belt displacement and sternal displacement did not match very well in some crash scenarios, as the belt rollout is very sensitive to the seat belt characteristics. The linear visco-elastic belt model used in the design model may be too elementary, and it would be very useful to improve this model, e.g. by including different loading and unloading paths and by reconsidering the friction models. Especially since the belt rollout is used to estimate injury responses, see Chapter 4, attention should be directed towards a more accurate belt model.
- The initial belt geometry and initial dummy geometry are identical in both design and reference model, hence similar trends in the responses could have been expected. To conclude on the accuracy of the models, it will be relevant to investigate the sensitivity of the responses to mismatches in the initial posture or belt placement.
- The performance of the vehicle prediction algorithm in the MPC controller could be improved. Pre-crash information systems may provide valuable data that will improve the prediction of the crash pulse. Moreover, the unstable observer that estimates the vehicle displacement during the crash is very sensitive to the initial velocity estimation, and the observer could be improved when responses from a velocity and/or position sensor is included.
- A second improvement in the MPC controller concerns the unstable open-loop observer. This observer is employed to estimate the occupant position based on the setpoint for the spinal acceleration. The position estimation is likely to drift, and this could be prevented when the occupant position is provided by the stable observer from Chapter 4.
- The MPC controller can be made versatile, when multiple injury criteria are included in the objective function. Additionally, the actuator force and belt rollout responses can be included, e.g. to ensure that the actuator will only have to dissipate energy. In Chapter 2, a linear relation was found between the injury responses and the inputs, hence it is straightforward to extend the LP problem in Chapter 3 with other objective functions.
- Concerning the observer in Chapter 4, other methods to estimate responses of a nonlinear systems do also exist, e.g. the Unscented Kalman Filter (UKF). It has clear advantages over the extended

Kalman filters, as it generally estimates the states more accurately, and it does not require online computation of the Jacobians. It would therefore be interesting to apply an UKF filter to the nonlinear design model.

- The estimation of the output responses from the observer is required by the CRC seat belt controller, but can also be used for various other safety systems. For example, airbag restraint developers would largely benefit from this method of real-time spatial occupant sensing to select the airbag deployment timing. Also, deflating characteristics of the airbag could be varied during the crash, based on real-time estimated neck injury responses.
- A belt force actuator has been developed that is able to prescribe belt forces up till 3 kN with a high bandwidth. This semi-active actuator should be tested, for instance in the sled setup described in Section 5.7, to evaluate the ability to reduce thoracic injuries during a (high-speed) impact. When these experiments are successful, the next step would be to mount the device in a vehicle that is used in full-scale sled tests. The performance of the actuator and control system can then be tested on a real-world dummies, which - when successful - would clearly mark the next step in automotive research on safety restraint systems.

A

DESIGN MODEL

The derivation of the Euler-Lagrange equations for relatively simple systems, approximately 1-15 bodies, is performed with a toolbox developed in Matlab[®]. This toolbox allows to easily and quickly define a 2-dimensional mechanical dynamic system. The algorithms in the toolbox symbolically derive the kinetic and potential energy functions, and the vector of nonconservative forces. The generated state space equations can be solved of Matlab or in Simulink. It also includes a linearization of the equations of motion, and a visual animation of the system. Although other toolboxes can also be used, e.g. Matlab's SimMechanics, the toolbox used here provides a lot of flexibility.

The dummy model parameters are listed in the tables below, and the symbols can be found in Figure A.1.

Table A.1 / Body parameters of the three design models, see Figure A.1.

	Mass				Mom. of Inertia		
	5 th	50 th	95 th		5 th	50 th	95 th
m_1	8.92	12.53	13.02	I_1	0.165	0.426	0.421
m_2	8.04	14.80	19.74	I_2	0.087	0.217	0.256
m_3	10.45	17.96	24.91	I_3	0.059	0.104	0.206
m_4	0.38	0.64	1.12	I_4	0.005	0.010	0.010
m_5	9.37	12.86	15.06	I_5	0.102	0.140	0.183
m_6	1.00	1.50	2.25	I_6	0.010	0.020	0.020
m_7	5.02	8.18	11.36	I_7	0.036	0.082	0.114
m_8	2.42	4.62	5.32	I_8	0.036	0.092	0.101
m_9	3.51	4.41	4.86	I_9	0.016	0.022	0.024
m_{10}	0.01	0.01	0.01	I_{10}	0.000	0.000	0.000
m_{11}	0.70	0.93	0.80	I_{11}	0.003	0.005	0.005

Table A.2 / Design model parameters, see Figure A.1.

	Initial condition				Dimension		
	5 th	50 th	95 th		5 th	50 th	95 th
q_1	-0.999	-1.068	-0.866	c_1	0.390	0.486	0.515
q_2	0.252	0.372	0.292	c_2	0.196	0.264	0.242
q_3	-0.367	-0.621	-0.658	c_3	0.340	0.400	0.413
q_4	0.066	0.084	0.091	c_4	0.177	0.203	0.211
q_5	-1.360	-1.481	-1.479	c_5	0.151	0.170	0.176
q_6	0.098	0.118	0.138	c_6	0.117	0.125	0.134
q_7	0.178	0.192	0.212	c_7	0.090	0.120	0.116
q_8	-0.278	-0.463	-0.455	c_8	0.335	0.380	0.401
q_9	0.631	0.483	0.375	c_9	0.183	0.220	0.220
q_{10}	1.275	1.161	1.091	c_{10}	0.045	0.062	0.061
q_{11}	-2.174	-2.259	-2.357	c_{11}	0.055	0.072	0.072
q_{12}	0.859	0.968	0.999	c_{12}	0.126	0.143	0.143
q_{13}	-1.137	-0.945	-0.722	c_{13}	0.049	0.052	0.051
q_{14}	1.512	1.512	1.501	c_{14}	0.196	0.253	0.258
				c_{15}	0.111	0.125	0.130
				c_{16}	0.056	0.067	0.056

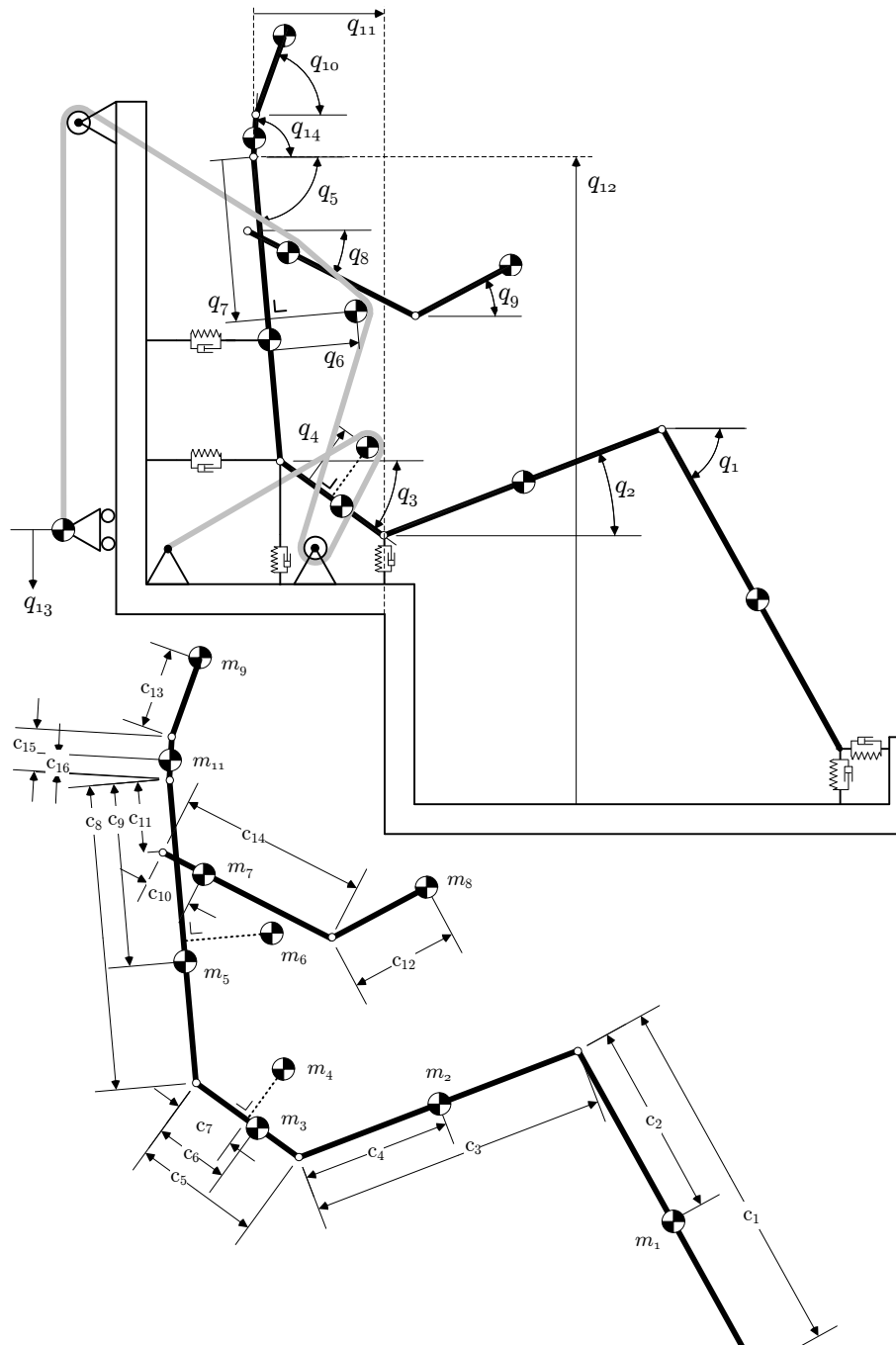


Figure A.1 / Body parameters of the design model.

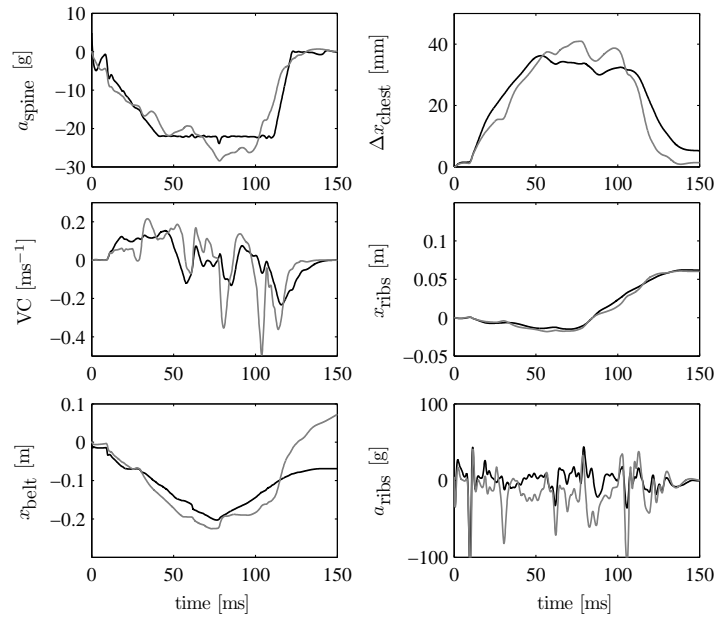
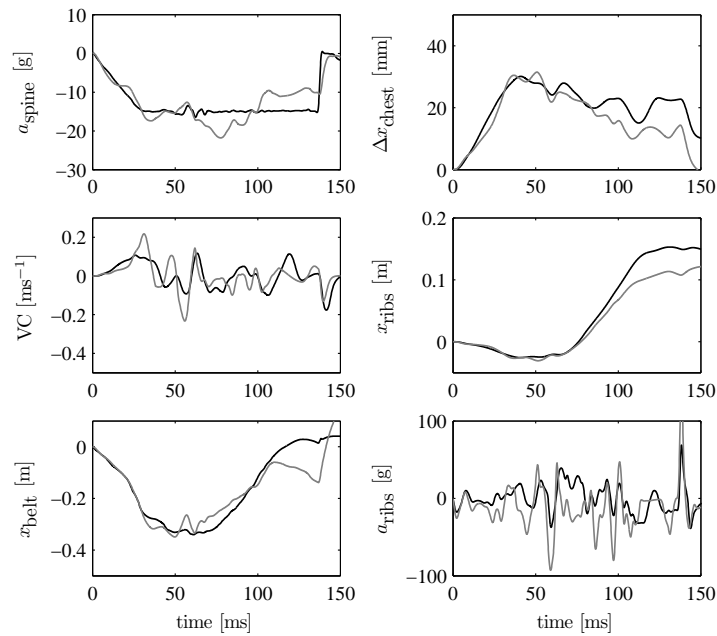
(a) 5th percentile(b) 95th percentile

Figure A.2 / Results of two design model dummies.

B

ACTUATOR DESIGN

Voice Coil Design

An intrinsic property of a permanent magnet is the remanence B_r , which induces a flux density in the magnet, B_m , that depends on the magnetizing force, H_m . Ideally, the flux density and magnetizing force in the magnet are related by

$$B_m = \mu_o H_m + B_r$$

with $\mu_o = 4\pi \cdot 10^7$ the permeability of free space. The magnetic flux, Φ , induced by the permanent magnets, runs through two steel pole pieces, that are separated by an air gap. In the air gap, the flux density is given by $B_g = \mu_o H_g$. From the conservation of flux, the flux densities in the air gap and the magnet are related through their surface area's, A_g and A_m , respectively. Ignoring the flux leakage, it follows $A_m B_m = A_g B_g$.

The magnet's magnetizing force, H_m , exerts a magnetomotive force, $F_m = H_m l_m$, with l_m the length of the flux vector through the magnet. From the conservation of magnetomotive forces, this force has to equal the force drop over the rest of the magnetic circuit. The force drop over the steel poles can be neglected, given the very low reluctance to magnetic flux, but the force drop over the air gap is given by $F_g = H_g l_g$, with l_g the length of the air gap. The voice coil is also part of the magnetic circuit, and exerts a magnetomotive force that hinders the magnetic flux from the permanent magnet. This force is given by $F_v = NI$, with I the current and N the number of turns. Hence the conservation of forces leads to $F_m + F_g + F_v = 0$, so $H_m l_m + H_g l_g + NI = 0$. Combining this relation with the

equations for the flux densities, yields an expression for the flux density in the gap width

$$B_g = \frac{B_r - \mu_o NI/l_m}{l_g/l_m + A_g/A_m}$$

So increasing the gap width or gap area decreases this density, but selecting small magnets increases it. In the present design, $l_m = 25.0$ mm, $l_g = 2.00$ mm, $A_g = 1.51$ cm² and $A_m = 1.47$ cm², $B_r = 1.30$ T. The coil has $N = 150$ turns and a diameter of 24 mm, leading to a wire length $L_d = 11.3$ m. This leads to a flux density in the air gap of $B_g = 1.17 - 6.81 \cdot 10^{-3}I$ T. The motor constant of the voice coil is estimated by $B_g L_d = 13.3 - 0.0770I$ N/A. When the current changes between -30 A to 30 A, the motor constant changes from 15.6 to 11.0 N/A, almost by 30%. In Figure B.1, the coil force is plotted as a function of the current, given by $F_{\text{coil}}(t) = 13.3I(t) - 0.0770I^2(t)$.

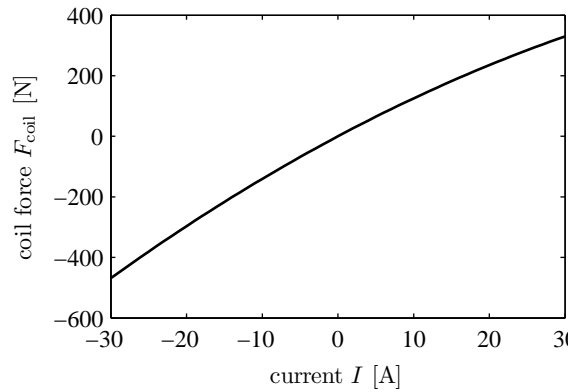


Figure B.1 / Voice coil force as a function of the current.

Valve Design

In Figure B.2, and exploded view is shown of the servo-valve body.

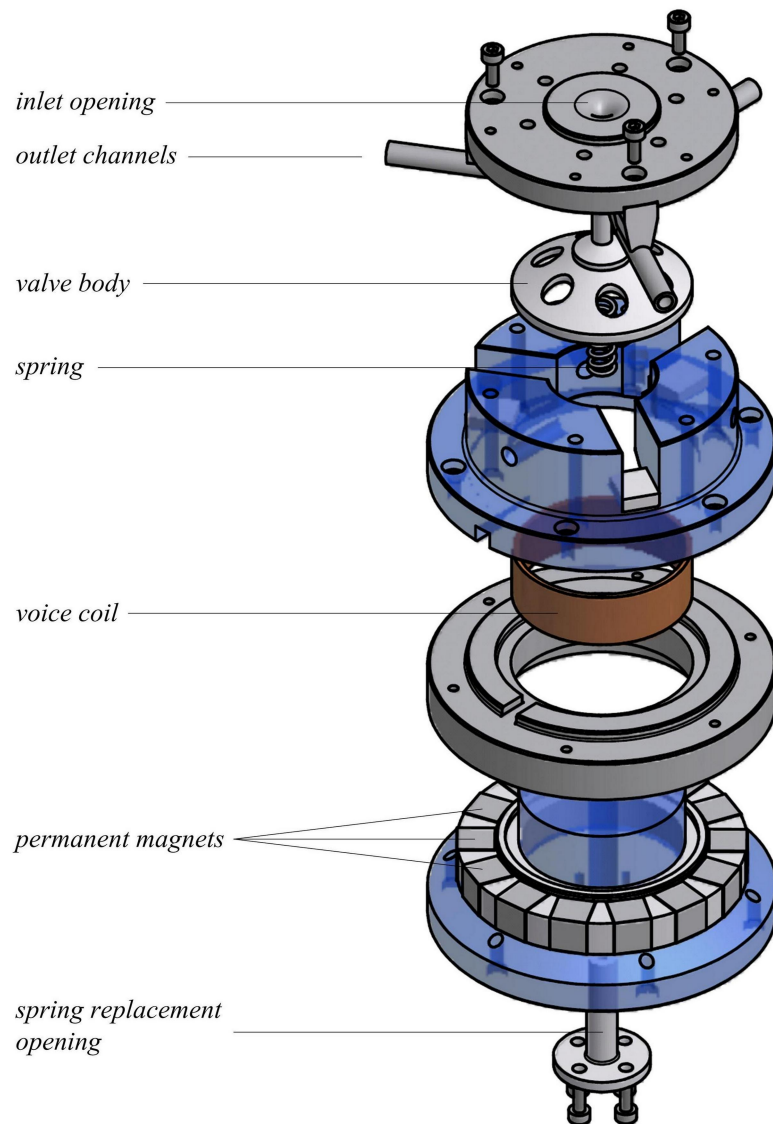


Figure B.2 / Exploded view of the servo-valve body.

BIBLIOGRAPHY

- Adomeit, H.D., Wils, E., and Heym, A. (1997). Adaptive Airbag-Belt-Restraints—An Analysis of Biomechanical Benefits. In *Proceedings of the SAE International Congress and Exposition*, 24-27 Feb, Detroit, MI, USA, paper nr. 970776 in *SAE Technical Papers*, p. 163–177.
- Agaram, V., Xu, L., Wu, J., Kostyniuk, G., and Nusholtz, G. (2000). Comparison of Frontal Crashes in Terms of Average Acceleration. In *Proceedings of the SAE 2000 World Congress*, 6-9 Mar, Detroit, MI, USA, paper nr. 2000-01-0880 in *SAE Technical Papers*, p. 1–21.
- Ashtiani, M., Sickson, R.P., Oliver, M.L., and Kruckemeyer, W.C. (2002). Variable load limiting restraint retractor. Patent no: US6481659, 19 Nov.
- Bemporad, A. (1998). Reference Governors for Constrained Linear System. *IEEE Transactions on Automatic Control*, 43(3), p. 415–419.
- Bemporad, A., Casavola, A., and Mosca, E. (1997). Nonlinear Control of Constrained Linear Systems via Predictive Reference Management. *IEEE Transactions on Automatic Control*, 42(3), p. 340–349.
- Bemporad, A., Heemels, W.P.M.H., and de Schutter, B. (2002a). On hybrid systems and closed-loop MPC systems. *IEEE Transactions on Automatic Control*, 47(5), p. 863–869.
- Bemporad, A., Morari, M., Dua, V., and Pistikopoulos, E.N. (2002b). The explicit linear quadratic regulator for constrained systems. *Automatica*, 38(1), p. 3–20.
- Benson, H. (1996). *University Physics*. John Wiley & Sons, Inc., New York City, NY, USA, revised edition.
- Berthet, F. and Vezin, P. (2006). Review of the Thorax Injury Criteria. Deliverable Report D514A - Part A AP-SP51-0038B, Integrated Project on Advanced Protection Systems (APROSYS).
- de Best, J.J.T.H., van de Molengraft, M.J.G., and Steinbuch, M. (2009). Direct Dynamic Visual Servoing at 1 kHz by using Product as 1.5 D Encoder. In *Proceedings of the International Conference on Control and Automation (ICCA)*, 9-11 Dec, Christchurch, New Zealand, p. in press.
- Blackburn, J.F., Reethof, G., and Shearer, J.L. (1969). *Fluid Power Control*. The MIT Press, Cambridge, MA, USA, 3rd edition.
- Bosch-Rekveltdt, M., Brandse, J., Couper, G., Morris, R., and Neale, M. (2005). Development and application of generic restraint numerical models for parametric investigations of selected impact scenarios. Technical Report R6 and R7, PRISM.
- Bosgra, H. (2004). Physical Modelling for Systems and Control. Lecture Notes, Delft University of Technology, the Netherlands.
- Boyd, S.P. and Vandenberghe, L. (2004). *Convex Optimization*. Cambridge University Press, UK.

- Breed, D.S., Summers, L., Carlson, J., and Koyzreff, M. (2001). Development of an Occupant Position Sensor System to Improve Frontal Crash Protection. In *Proceedings of the 17th International Technical Conference on the Enhanced Safety of Vehicles (ESV)*, 4-7 Jun, Amsterdam, The Netherlands, paper nr. 325, p. 1–10.
- Cagienard, R., Grieder, P., Kerrigan, E.C., and Morari, M. (2007). Move blocking strategies in receding horizon control. *Journal of Process Control*, 17(6), p. 563 – 570.
- Cesari, D. and Bouquet, R. (1994). Comparison of Hybrid III and human cadaver thorax deformations. In *Proceedings of the 38th Stapp Car Crash Conference*, 31 Oct - 4 Nov, Fort Lauderdale, FL, USA, paper nr. 942209 in *SAE Technical Papers*, p. 65–76.
- Cheng, Z.Q., Pelletiere, J.A., Rizer, A.L., and Pilkey, W.D. (2005). Limiting performance analysis of biomechanical systems for optimal injury control – Part 2: Applications. *International Journal of Crashworthiness*, 10(6), p. 579–587.
- Clute, G. (2001). Potentials of adaptive load limitation: presentation and system validation of the adaptive load limiter. In *Proceedings of the 17th International Technical Conference on the Enhanced Safety of Vehicles (ESV)*, 4-7 Jun, Amsterdam, The Netherlands, paper nr. 194, p. 113–134.
- Committee on Injury Scaling (2008). Abbreviated Injury Scale (AIS) 2005: update 2008. Manual, Association for the Advancement of Automotive Medicine (AAAM), Barrington, IL, USA.
- Cooper, J., Lemmen, P., and van Schie, C. (2004). Effectiveness of real time control for active restraint systems in frontal crashes. In *Proceedings of Airbag 2004*, 29 Nov - 1 Dec, Karlsruhe, Germany, p. 1–7.
- Crandall, J.R., Bass, C.R., Pilkey, W.D., Miller, H.J., Sikorski, J., and Wilkins, M. (1997). Thoracic response and injury with belt, driver side airbag and force limited belt restraint systems. *International Journal of Crashworthiness*, 2(1), p. 119–132.
- Crandall, J.R., Cheng, Z., and Pilkey, W.D. (2000). Limiting performance of seat belt systems for the prevention of thoracic injuries. *Journal of Automobile Engineering*, 214(2), p. 127–139.
- Economic Commission for Europe (2007). Uniform provisions concerning the approval of vehicles with regard to the protection of the occupants in the event of a frontal collision. Technical Report R94, United Nations.
- Egberts, T.L.T.M. (1996). Ontwerp van een botsproefopstelling voor voertuigcomponenten (Dutch). Technical Report WOC/VT/R/96.01, Eindhoven University of Technology, The Netherlands.
- Eichberger, A., Wallner, D., Hirschberg, W., and Cresnik, R. (2009). A situation based method to adapt the vehicle restraint system in frontal crashes to the accident scenario. In *Proceedings of the 21th International Technical Conference on the Enhanced Safety of Vehicles (ESV)*, 15-18 Jun, Stuttgart, Germany, paper nr. 91, p. 1–11.
- Eppinger, R., Sun, E., Bandak, F., Haffner, M., Khaewpong, N., Maltese, M., Kuppa, S., Nguyen, T., Takhounts, E., Tannous, R., Zhang, A., and Saul, R. (1999). Development of Improved Injury Criteria for the Assessment of Advanced Automotive Restraint Systems - II. Supplement to NHTSA Docket No. 1998-4405-9, NHTSA, US DoT.
- EuroNCAP (2008). Assessment Protocol and Biomechanical Limits. v4.2, European New Car Assessment Protocol (EuroNCAP), Brussels, Belgium.
- European Commission for Energy and Transport (2009). EU energy and transport in figures 2009. Technical Report ISBN: 978-92-79-10728-3, Office for the Official Publications of the European Communities, Luxembourg.

- Fleming, W.J. (2008). New Automotive Sensors - A Review. *IEEE Sensors Journal*, 8(11), p. 1900–1921.
- Foret-Bruno, J.Y., Trosseille, X., Le Coz, J.Y., Bendjellal, F., Steyer, C., Phalempin, T., Villeforceix, D., Dandres, P., and Got, C. (1998). Thoracic Injury Risk in Frontal Car Crashes with Occupant Restrained with Belt Load Limiter. In *Proceedings of the 42nd Stapp Car Crash Conference*, 2-4 Nov, Tempe, AZ, USA, paper nr. 983166 in *SAE Technical Papers*, p. 1–21.
- Foret-Bruno, J.Y., Trosseille, X., Page, Y., Huère, J.F., Le Coz, J.Y., Bendjellal, F., Diboine, A., Phalempin, T., Villeforceix, D., Baudrit, P., Guillemot, H., and Coltat, J.C. (2001). Comparison of Thoracic Injury Risk in Frontal Car Crashes for Occupant Restrained without Belt Load Limiters and Those Restrained with 6 kN and 4 kN Belt Load Limiters. In *Proceedings of the 45th Stapp Car Crash Conference*, 15-17 Nov, San Antonio, Texas, USA, paper nr. 2001-22-0009 in *SAE Technical Papers*.
- Fukui, T., Koyota, K., Isonaga, K., Kamiji, K., and Ino, T. (2001). Occupant position detection system (OPDS) for side airbag system. *JSAE Review*, 22(1), p. 69 – 74.
- Garcia, C.E., Prett, D.M., and Morari, M. (1989). Model predictive control: Theory and practice – A survey. *Automatica*, 25(3), p. 335–348.
- Gawronski, W.K. (2004). *Advanced Structural Dynamics and Active Control of Structures*. Springer-Verlag, New York, NY, USA.
- Gelb, A. (1974). *Applied Optimal Estimation*. The MIT Press, Cambridge, MA, USA.
- Gilbert, E.G. and Kolmanovsky, I. (2002). Nonlinear tracking control in the presence of state and control constraints: a generalized reference governor. *Automatica*, 38(12), p. 2063 – 2073.
- Gordon, T.J. and Hopkins, R. (1997). Parametric Identification of Multibody Models for Crash Victim Simulation. *Multibody System Dynamics*, 1, p. 85–112.
- Habib, M.S. (2001). Active control of vehicle occupant’s motion in front- and rear-end collisions. In *Proceedings of the Automotive and Transportation Technology Congress and Exhibition*, 1-3 Oct, Barcelona, Spain, paper nr. 2001-01-3430 in *SAE Technical Papers*, p. 1–9.
- Håland, Y. (2006). The Evolution of the Three Point Seatbelt - from Yesterday to Tomorrow. In *Proceedings of the Conference of the International Research Council on the Biomechanics of Impact (IRCOBI)*, 22-24 Sep, Madrid, Spain, p. 3–16.
- Hartmann, H., Schautt, M., Pascucci, A., and Gombert, B. (2002). eBrake - The Mechatronic Wedge Brake. In *Proceedings of the 20th Annual Brake Colloquium And Exhibition*, 11-14 Oct, Phoenix, AZ, USA, paper nr. 2002-01-2582 in *SAE Technical Papers*, p. 1–6.
- Hesseling, R.J. (2004). *Active restraint systems; feedback control of occupant motion*. PhD thesis, Technische Universiteit Eindhoven, the Netherlands.
- Hesseling, R.J., Steinbuch, M., Veldpaus, F.E., and Klisch, T. (2006a). Feedback control of occupant motion during a crash. *International Journal of Crashworthiness*, 11(1), p. 81–96.
- Hesseling, R.J., Steinbuch, M., Veldpaus, F.E., and Klisch, T. (2006b). Identification and control of a vehicle restraint system. *Proceedings of the Institution of Mechanical Engineers, Part D: Journal of Automobile Engineering*, 220, p. 401–413.
- van den Hof, P. M. J. (2006). System Identification. Lecture Notes, Delft University of Technology, the Netherlands.

- Holding, P.N., Chinn, B.P., and Happian-Smith, J. (2001). An evaluation of the benefits of active restraint systems in frontal impacts through computer modelling and dynamic testing. In *Proceedings of the 17th International Technical Conference on the Enhanced Safety of Vehicles (ESV)*, 4-7 Jun, Amsterdam, The Netherlands, paper nr. 328, p. 1-9.
- Horsch, J.H., Melvin, J.W., Viano, D.C., and Mertz, H.J. (1991). Thoracic injury assessment of belt restraint systems based on Hybrid III chest compression. In *Proceedings of the 35th Stapp Car Crash Conference*, 18-20 Nov, San Diego, CA, USA, paper nr. 912895 in *SAE Technical Papers*, p. 85-108.
- Huang, M. (2002). *Vehicle Crash Mechanics*. CRC Press, USA, 1st edition.
- Huang, S.C. (1995). Biomechanic modeling and simulations of automobile crash victims. *Computers and structures*, 57(3), p. 541-549.
- Huston, R.L. (1987). Crash victim simulation: Use of computer models. *International Journal of Industrial Ergonomics*, 1(4), p. 285-291.
- Huston, R.L. (2001). A review of the effectiveness of seat belt systems: design and safety considerations. *International Journal of Crashworthiness*, 6(2), p. 243-251.
- IIHS (2008). Frontal Offset Crashworthiness Evaluation: Guidelines for Rating Injury Measures. Version XIII, Insurance Institute for Highway Safety (IIHS), Arlington, VA, USA.
- Iyota, T. and Ishikawa, T. (2003). The Effect of Occupant Protection by Controlling Airbag and Seatbelt. In *Proceedings of the 18th International Technical Conference on the Enhanced Safety of Vehicles (ESV)*, 19-22 May, Nagoya, Japan, paper nr. 198, p. 1-10.
- Julier, S.J. and Uhlmann, J.K. (1997). A New Extension of the Kalman Filter to Nonlinear Systems. In *Proceedings of the 11th International Symposium on Aerospace/Defence Sensing, Simulation and Controls (AeroSens)*, Orlando, FL, USA, p. 182-193.
- Kallieris, D., Mattern, R., Rizzetti, A., and Del Conte-Zerial, P. (1998). Prediction of thoracic injuries in frontal collisions. In *Proceedings of the 16th International Technical Conference on the Enhanced Safety of Vehicles (ESV)*, 31 May - 4 Jun, Windsor, Canada, paper nr. 98-S7-O-04, p. 1550-1563.
- Kalman, R.E. (1960). A new approach to linear filtering and prediction problems. *Journal of Basic Engineering*, 82(1), p. 35-45.
- Karlow, J.P. (1998). Variable level seatbelt energy management device. Patent no: US6019392, 1 Feb.
- Katoh, H. and Nakahama, R. (1982). A study on the ride-down evaluation. In *Proceedings of the 9th International Technical Conference on the Enhanced Safety of Vehicles (ESV)*, 1-4 Nov, Kyoto, Japan, p. 190-195.
- Kawaguchi, K., Kaneo, N., Iwamoto, T., Fukushima, M., Abe, A., and Ogawa, S. (2003). Optimized Restraint Systems for Various-Sized Rear Seat Occupants in Frontal Crash. In *Proceedings of the SAE 2003 World Congress*, Mar, Detroit, MI, USA, paper nr. 2003-01-1230 in *SAE Technical Papers*, p. 1-10.
- Kent, R.W., Crandall, J.R., Rudd, R.W., and Lessley, D. (2002). Load distribution-specific viscoelastic characterization of the Hybrid III chest. In *Proceedings of the SAE 2002 World Congress*, 4-7 Mar, Detroit, MI, USA, paper nr. 2002-01-0024 in *SAE Technical Papers*, p. 1-12.
- Kent, R.W., Viano, D.C., and Crandall, J.R. (2005). The Field Performance of Frontal Air Bags: A Review of the Literature. *Traffic Injury Prevention*, 6(1), p. 1-23.

- Kent, R.W., Balandin, D.V., Bolotnik, N.N., Pilkey, W.D., and Purtsezov, S.V. (2007). Optimal control of restraint forces in an automobile impact. *Journal of Dynamic Systems Measurement and Control*, 129(4), p. 415–424.
- King, A.I. (2000). Fundamentals of Impact Biomechanics: Part 1 - Biomechanics of the Head, Neck, and Thorax. *Annual Review of Biomedical Engineering*, 2(1), p. 55–81.
- King, A.I. (2004). Vehicle Crashworthiness and Occupant Protection. Prasad, P. and Belwafa, J.E. (editor). Chapter: Injury Biomechanics from Head to Foot, p. 269–352. American Iron and Steel Institute (AISI), Southfield, MI, USA.
- Kithil, P.W. (1998). Capacitive Occupant Sensing. In *Proceedings of the International Body Engineering Conference and Exposition*, Detroit, MI, USA, paper nr. 982292 in *SAE Technical Papers*.
- Knox, M.J. (2001). Adaptive variable load limited for primary occupant safety restraint. Patent no: WO0151321, 12 Jan.
- van der Laan, E.P., Veldpaus, F.E., and Steinbuch, M. (2007a). Control Oriented Modeling of Vehicular Occupants and Restraint Systems. In *Proceedings of the Conference of the International Research Council on the Biomechanics of Impact (IRCOBI)*, 19-21 Sep, Maastricht, the Netherlands, p. 47–58.
- van der Laan, E.P., Veldpaus, F.E., and Steinbuch, M. (2007b). State Estimator Design for Real-time Controlled Restraint Systems. In *Proceedings of the American Control Conference (ACC)*, 11-13 Jul, New York City, NY, USA, p. 242–247.
- van der Laan, E.P., Veldpaus, F.E., and Steinbuch, M. (2008a). LPV Modeling of Vehicle Occupants. In *Proceedings of the 9th International Symposium on Advanced Vehicle Control (AVEC)*, 6-9 Oct, Kobe, Japan, p. 620–625.
- van der Laan, E.P., Luijten, H.J.C., Veldpaus, F.E., Heemels, W.P.M.H., and Steinbuch, M. (2008b). Reference Governors for Controlled Belt Restraint Systems. In *Proceedings of the International Conference on Vehicular Electronics and Safety (ICVES)*, 22-24 Sep, Columbus, OH, USA, p. 114–119.
- van der Laan, E.P., de Jager, B., Veldpaus, F.E., Steinbuch, M., van Nunen, E., and Willemsen, D. (2009a). Continuous Restraint Control Systems: Safety Improvement for Various Occupants. In *Proceedings of the 21th International Technical Conference on the Enhanced Safety of Vehicles (ESV)*, 15-18 Jun, Stuttgart, Germany, paper nr. 44, p. 1–11.
- van der Laan, E.P., Veldpaus, F.E., de Jager, B., and Steinbuch, M. (2009b). Control Oriented Modeling of Occupants in Frontal Impacts. *International Journal of Crashworthiness*, 14(4), p. 323–337.
- van der Laan, E.P., Heemels, W.P.M.H., Luijten, H.J.C., Veldpaus, F.E., and Steinbuch, M. (2009c). Reference Governors for Controlled Belt Restraint Systems. *Vehicle System Dynamics*, p. *in press*.
- Lobdell, T.F. (1973). Impact response of the human thorax. In *Proceedings of the Symposium on Human Impact Response, Human Impact Response: Measurement and Simulation*, p. 201–245, General Motors Research Laboratories.
- Maciejowski, J.M. (2001). *Predictive control with constraints*. Prentice-Hall, Harlow, UK.
- Mackay, M. (1994). Smart seat belts - Some population considerations applied to intelligent restraint systems. In *Proceedings of the SAE International Congress and Exposition*, 28 Feb - 3 Mar, Detroit, MI, USA, paper nr. 940531 in *SAE Technical Papers*, p. 13–22.

- Mackay, M., Parkin, S., and Scott, A. (1994). Intelligent Restraint Systems - What Characteristics Should They Have? In *Proceedings of the Joint AAAM-IRCOBI Conference*, Lyon, France, *Advances of Occupant Restraint Technologies*, p. 113–126.
- Man Ho, L., Roberts, R., Hartmann, H., and Gombert, B. (2006). The Electronic Wedge Brake - EWB. In *Proceedings of the 24th Annual Brake Colloquium and Exhibition*, Grapevine, TX, USA, paper nr. 2006-01-3196 in *SAE Technical Papers*, p. 1–10.
- Mayne, D.Q., Rawlings, J. B., Rao, C.V., and Scolaert, P.O.M. (2000). Constrained model predictive control: stability and optimality. *Automatica*, 36(6), p. 789–814.
- McHenry, R.R. (1963). Analysis of the dynamics of automobile passenger-restraint systems. In *Proceedings of the 7th Stapp Car Crash Conference*, 11-13 Nov, Playa Del Rey, CA, USA, *SAE Technical Papers*.
- Merritt, H.E. (1967). *Hydraulic Control Systems*. John Wiley & Sons, Inc., New York City, NY, USA.
- Mertz, H.J., Horsch, J., Horn, G., and Lowne, R.W. (1991). Hybrid III sternal deflection associated with thoracic injury severities of occupants restrained with force-limiting shoulder belts. In *Proceedings of the SAE International Congress and Exposition*, 25 Feb - 1 Mar, Detroit, MI, USA, paper nr. 910812 in *SAE Technical Papers*, p. 105–119.
- Mertz, H.J., Williamson, J.E., and van der Lugt, D.A. (1995). The effect of limiting shoulder belt load with airbag restraint. In *Proceedings of the SAE International Congress and Exposition*, 27 Feb-2 Mar, Detroit, MI, USA, paper nr. 950886 in *SAE Technical Papers*, p. 185–192.
- Miller, H.J. (1996). Restraint Force Optimization for a Smart Restraint System. In *Proceedings of the SAE International Congress and Exposition*, 26-29 Feb, Detroit, MI, USA, paper nr. 960662 in *SAE Technical Papers*, p. 79–84.
- Morari, M. and Lee, J.H. (1999). Model predictive control: past, present and future. *Computers and Chemical Engineering*, 23(4-5), p. 667–682.
- Morgan, R.M., Eppinger, R.H., and Haffner, M.P. (1994). Thoracic Trauma Assessment Formulations for Restrained Drivers in Simulated Frontal Impacts. In *Proceedings of the 38th Stapp Car Crash Conference*, 31 Oct - 4 Nov, Fort Lauderdale, FL, USA, paper nr. 942206 in *SAE Technical Papers*, p. 15–34.
- Musiol, J.A., Norgan-Curtiss, L.M., and Wilkins, M.D. (1997). Control and application of intelligent restraint systems. In *Proceedings of the SAE International Congress and Exposition*, 24-27 Feb, Detroit, MI, USA, paper nr. 971052 in *SAE Technical Papers*, p. 1–8.
- NHTSA (1998). Federal Motor Vehicle Safety Standard (FMVSS). Part 571, Crashworthiness, NHTSA, US DoT, Washington, DC, USA.
- NHTSA (2001). Fifth / Sixth Report to Congress Effectiveness of Occupant Protection Systems and Their Use. Technical Report DOT HS 809 442, NHTSA, US DoT.
- Nahum, A. and Melvin, J. (1993). *Accidental Injury Biomechanics and Prevention*. Springer-Verlag, New York, NY, USA.
- National Center for Statistics and Analysis (2009). Traffic Safety Facts, data from 2007. Technical Report DOT HS 810 993, NHTSA, US DoT.
- Neathery, R.F. (1975). Prediction of thoracic injury from dummy responses. In *Proceedings of the 19th Stapp Car Crash Conference*, San Diego, CA, USA, paper nr. 751151 in *SAE Technical Papers*, p. 295–316.

- Neathery, R.F. and Lobdell, T.E. (1972). Mechanical Simulation of Human Thorax under Impact. *SAE Technical Papers*, paper nr. 730982, p. 451–466.
- Nirula, R. and Pintar, F.A. (2008). Identification of vehicle components associated with severe thoracic injury in motor vehicle crashes: A CIREN and NASS analysis. *Accident Analysis & Prevention*, 40(1), p. 137 – 141.
- Office of Crashworthiness Standards (1996). Laboratory Test Procedure for the United States New Car Assessment Programme (USNCAP). Frontal Impact Testing Protocol, NHTSA, US DoT, Washington, DC, USA.
- Passive Safety Network (2004). Roadmap of Future Automotive Passive Safety Technology Development. Technical Report, European Enhanced Vehicle Safety (EEVC).
- Paulitz, T.J., Blacketter, D.M., and Rink, K.K. (2006). Constant Force Restraints For Frontal Collisions. *Proceedings of the Institution of Mechanical Engineers, Part D: Journal of Automobile Engineering*, 220(9), p. 1177–1189.
- Pintelon, R. and Schoukens, J. (2001). *System Identification: A Frequency Domain Approach*. IEEE Press, New York, NY, USA.
- Prasad, P. (1984). A overview of major occupant simulation models. *SAE Technical Papers*, paper nr. 840855, p. 1–10.
- Prasad, P. (1997). Crashworthiness of transportation systems: structural impact and occupant protection. Ambrósio, J.A.C. and Pereira, M.S. (editor). Chapter: Occupant simulation models: experiment and practice, p. 209–220. Kluwer Academic Publishers, Dordrecht, the Netherlands.
- Prasad, P. and Chou, C.C. (1989). A review of mathematical occupant simulation models. *Crashworthiness and occupant protection in transportation*, 1(1), p. 95–112.
- Safety Test Instrumentation Standards Committee (1996). SAE J1727: Injury Calculations Guidelines. Technical Report, Society of Automotive Engineers (SAE), Warrendale, PA, USA.
- SafetyNet (2009). Annual Statistical Report 2007 – based on data from the CARE/EC database. Technical Report, European Road Safety Observatory (ERSO).
- Saltelli, A., Tarantola, S., Campolongo, F., and Ratto, M. (2004). *Sensitivity Analysis in Practice: A guide to assessing scientific models*. John Wiley & Sons, West Sussex, UK.
- Schiehlen, W. (1990). *Multibody Systems Handbook*. Springer-Verlag, Berlin, Germany.
- van Schijndel-de Nooij, M. and Wismans, J.S.H.M. (2008). APROSYS: Advances in secondary safety research. *International Journal of Crashworthiness*, 13(6), p. 591–598.
- Schoenmackers, T.D. and Trivedi, M.M. (2003). Real-time stereo-based vehicle occupant posture determination for intelligent airbag deployment. In *Proceedings of the IEEE Intelligent Vehicles Symposium (IVS)*, 9-11 Jun, p. 570–574.
- Seiffert, U. and Wech, L. (2007). Automotive Safety Handbook. Chapter: Occupant Protection, p. 151–182. Society of Automotive Engineers (SAE), Warrendale, PA, USA, 2nd edition.
- Shin, H.S., Yeo, T.J., and Ha, W.P. (2007). The numerical study for the adaptive restraint system. In *Proceedings of the SAE 2007 World Congress*, 16-19 Apr, Detroit, MI, USA, paper nr. 2007-01-1500 in *SAE Technical Papers*, p. 1–10.
- Shiotani, M. and Hamaue, T. (2004). Seat belt retractor. Patent no: EP1468883 A1, 15 Apr.
- Skogestad, S. and Postlethwaite, I. (2005). *Multivariable Feedback Control*. John Wiley & Sons, West Sussex, UK, 2nd edition.

- Smithson, A., Blackadder, D., Taylor, J., Andrew, D., Joe, H., and Andrew, P. (2000). Load limiting device for a seat belt. Patent no: US6183015, 6 Feb.
- Society of Automotive Engineers (SAE) (1995). SAE J211/1: Instrumentation for impact test – Part 1 – Electronic instrumentation. Technical Report, Safety Test Instrumentation Standards Committee, Warrendale, PA, USA.
- Specht, M. (2001). Seat belt retractor with a load limiter. Patent no: EP1661777 A1, 1 Nov.
- TNO Madymo B.V. (2005). Madymo Manual. Version 6.3, TNO Road-Vehicles Research Institute, Delft, The Netherlands.
- Texas Transportation Institute (2006). Automated Vehicle Occupancy Technologies Study. Draft Synthesis Report, U.S. Department of Transportation, College Station, TX, USA.
- Tøndel, P., Johansen, T.A., and Bemporad, A. (2003). An algorithm for multi-parametric quadratic programming and explicit MPC solutions. *Automatica*, 39(3), p. 489 – 497.
- Twisk, D., Spit, H.H., Beebe, M., and Depinet, P. (2007). Effect of Dummy repeatability on numerical model accuracy. In *Proceedings of the AeroTech Congress & Exhibition*, Sep, Los Angeles, CA, USA, paper nr. 20071415 in *SAE Technical Papers*, p. 1–6.
- Viano, D.C. (1995). Restraint Effectiveness, Availability and Use in Fatal Crashes: Implications to Injury Control. *The Journal of Trauma: Injury, Infection, and Critical Care*, 38(4), p. 538–546.
- Viano, D.C. and Lau, I.V. (1983). Role of impact velocity and chest compression in thoracic injury. *Aviation, Space, and Environmental Medicine*, 54, p. 16–21.
- Viano, D.C., King, A.I., Melvin, J.W., and Weber, K. (1989). Injury Biomechanics Research: an essential element in the prevention of trauma. *Journal of Biomechanics*, 22(5), p. 403–417.
- Watton, J. (1989). *Fluid Power Systems*. Prentice-Hall, UK.
- Wismans, J.S.H.M. (2003). State-of-the-art report: Smart Restraint Systems. Task 5 report, European Vehicle Passive Safety Network.
- Wismans, J.S.H.M. (2007). Secondary Safety Research Action Plan - Updated Roadmap. Technical Report D40, Advanced Passive Safety Network (ASPN).
- Wismans, J.S.H.M., Janssen, E.G., Beusenbergh, M., Koppens, W.P., Happee, R., and Boven-deerd, P.H.M. (2000). Injury Biomechanics. Lecture Notes, Technische Universiteit Eindhoven, the Netherlands.
- Wismans, J.S.H.M., Happee, R., and van Dommelen, J.A.W. (2005). Impact biomechanics: from fundamental insights to applications. M. Gilchrist (editor). Chapter: Computational human body models, p. 417–429. Springer-Verlag, Ireland.
- Witteman, W.J. (1999). *Improved Vehicle Crashworthiness Design by Control of Energy Absorption for Different Collision Situations*. Ph.D. thesis, Technische Universiteit Eindhoven.
- Wood, D.P. (2003). Velocity changes, mean accelerations and displacements of some car types in frontal collisions. *International Journal of Crashworthiness*, 8(6), p. 591–603.
- World Health Organization (2009). *Global status report on road safety: time for action*. WHO Press, Geneva.
- Yeh, I., Kachnowski, B., and Subbian, T. (2005). Optimization of a Vehicle Restraint System Using a Genetic Algorithm. In *Proceedings of the SAE 2005 World Congress*, 11-14 Apr, Detroit, MI, USA, paper nr. 2005-01-1227 in *SAE Technical Papers*, p. 1–8.
- Zhou, K., Doyle, J.C., and Glover, K. (1996). *Robust and Optimal Control*. Prentice-Hall, Upper Saddle River, NJ, USA.

SUMMARY

Seat Belt Control From modeling to experiment

In the last decades, vehicle safety has improved considerably. For example, major improvements have been made in the area of the structural crashworthiness of the vehicle, various driver assistance systems have been developed, and enhancements can be found in the restraint systems, the final line of defense in occupant protection.

Despite this increase of vehicle safety measures, many fatalities still occur in road transportation. Regarding the unavoidable crashes, a significant amount can be attributed to the fact that the seat belt system does not perform optimally. No crash event or occupant is identical, yet conventional seat belts are – in general – not able to adjust their characteristics accordingly. The system is therefore optimal for only a limited number of crash scenarios and occupant types. With the current sensor and processor technology, it is possible to develop a seat belt system that continuously adapts to the actual crash and occupant conditions. Such a device is referred to as a Continuous Restraint Control (CRC) system, and the work presented in this thesis contributes to the development of this type of systems.

The main idea of seat belt control is to add sensors and actuators to the seat belt system. The force in the seat belt is prescribed by the actuator during the crash, such that the risk of injuries are minimized given the current impact severity and occupant size. This concept poses several technological challenges, which are in this thesis divided into four research topics.

Although many sensor technologies exist nowadays, so far no useful methods have been proposed to measure the occupant injury responses in real-time. These responses are essential when deciding on the optimal belt force. In this thesis, a solution has been presented for the problem of real-time estimation of (thoracic) injuries and occupant position during a crash. An estimation is performed using model-based filtering of a small number of readily available and cheap sensors. Simulation results with a crash victim model indicate that the injury responses can

be estimated with sufficient accuracy for control purposes, but that the estimation heavily depends on the accuracy of the model used in the filter.

A numerical controller uses these estimated injury responses to compute the optimal seat belt force. In this computation, it has to be taken into account that the occupant position is constrained during the crash by the available space in the vehicle, since contact with the interior may result in serious injury. The controller therefore has to predict the future occupant motion, using a prediction of the future crash behavior, a choice for the future seat belt force, and a model of the vehicle-occupant-belt system. Given the type of control problem, a Model Predictive Control (MPC) approach is used to develop the controller. Simulation results with crash victim models indicate that using this controller lead to a significant injury risk reduction for the thorax, given that an ideal belt actuator is available.

The injury estimator, the prediction and control algorithm proposed in the foregoing are designed with simple mathematical models of occupant, seat belt and vehicle interior. It is therefore recognized that such accurate, manageable models are essential in the development of CRC systems. In this thesis, models of various complexities have been constructed that represent three types of widely used crash test dummies. These models are validated against both numerical as experimental data. The conclusion of this validation is that in frontal crashes, the neck and thoracic injury criteria can well be described by linear (time-invariant) models. However, when the models are to be improved, more attention can be given to the modeling of the chest and seat belt.

The severity and duration of a typical impact require a seat belt actuator with challenging specifications. For example, it has to deliver very high forces over a large stroke, it must have a high bandwidth, and must be small enough to be fitted in a vehicle post. These devices do not yet exist. In this thesis, a semi-active belt actuator concept is presented. It is based on a pressure-controlled hydraulic valve, which regulates the belt force through an hydraulic cylinder. The actuator is designed and constructed at the TU/e, and evaluated experimentally. Moreover, a moving sled setup has been developed which allows testing the actuator under impact conditions. Experimental results show that the belt actuator meets the requirements, except for the maximum force. The actuator can therefore at this point be used to prescribe belt forces in a safety belt in low-speed impacts.

SAMENVATTING

Verkeersveiligheid is in de laatste decennia aanzienlijk verbeterd. Innovaties zijn doorgevoerd op het gebied van de crashbestendigheid van voertuigen, er zijn verschillende systemen ontwikkeld die de bestuurder ondersteunen in gevaarlijke situaties, en er zijn aanpassingen doorgevoerd in de restraint systemen, zoals de autogordel en airbags.

Ondanks deze toename van verkeersveiligheid vallen er nog steeds veel dodelijke verkeersslachtoffers. Wat betreft de onvermijdelijke botsingen, kan een deel hiervan worden toegeschreven aan het feit dat de autogordel geen optimale bescherming biedt. Geen botsing of inzittende is gelijk, en de conventionele autogordel is in het algemeen niet in staat zich hieraan aan te passen. De eigenschappen van de conventionele gordel worden ontworpen voor slechts een beperkt aantal botsingen en een gemiddelde inzittende.

Met de huidige technologie kan een gordelsysteem ontwikkeld worden die zich tijdens de botsing continu aanpast aan de toestand van de inzittende en het verloop van de botsing. Dit type restraint systemen wordt een Continuous Restraint Control (CRC) systeem genoemd, en het onderzoek in dit proefschrift draagt bij aan de ontwikkeling hiervan. In het voorgestelde gordelsysteem zijn sensoren en een actuator toegevoegd aan de huidige conventionele autogordel. Op basis van sensorinformatie over de toestand van het voertuig en de inzittende, past de actuator de kracht in de autogordel zodanig aan dat het risico op letsel geminimaliseerd wordt. Dit concept brengt enkele technologische uitdagingen met zich mee, die in dit proefschrift als vier deelproblemen worden behandeld.

Hoewel er tegenwoordig veel typen sensoren bestaan, zijn er nog geen bruikbare technologieën ontwikkeld waarbij de mate van letsel tijdens de botsing gemeten kan worden. Deze letselresponsies zijn essentieel voor het bepalen van het optimale gordelkracht. In dit proefschrift wordt een oplossing gepresenteerd voor het probleem van het schatten van de letselresponsies, met name aan de borstkas, en van de positie van de inzittende tijdens de botsing. Deze schatting wordt uitgevoerd door middel van een model-gebaseerde signaal filtering van enkele sensorensignalen. Resultaten met een crash simulatie model laten zien dat de letselresponsies geschat

kunnen worden met voldoende nauwkeurigheid voor de regelaar, maar dat deze schatting erg afhangt van de nauwkeurigheid van het model.

Een numerieke regelaar gebruikt de geschatte letselresponsies om de optimale gordelkracht te bepalen. Hierbij moet rekening gehouden worden met het feit dat de bewegingsruimte van de inzittende tijdens de botsing beperkt is, want contact met het stuur of andere delen van het voertuig kan namelijk tot ernstig letsel leiden en moet vermeden worden. De regelaar voorspelt daarom wat de toekomstige beweging van de inzittende is. Hierbij wordt gebruik gemaakt van een voorspelling van het toekomstige verloop van de botsing, een keuze voor het profiel van de toekomstige gordelkracht, en een model van het voertuig-inzittende-gordel. Voor dit regelaarprobleem is een aangepaste Model Predictive Control (MPC) aanpak gebruikt. Resultaten met een crash simulatie model laten zien dat met deze regelaar een significante reductie van risico op letsel aan de borstkas gehaald kan worden, gegeven dat een ideale gordelactuator beschikbaar is.

De schatter, de voorspeller en de regelaar zijn ontworpen met eenvoudige numerieke modellen van het voertuig-inzittende-gordel systeem. Nauwkeurige, hanteerbare modellen zijn daarom essentieel voor de ontwikkeling van CRC systemen. In dit proefschrift zijn modellen ontwikkeld met verschillende complexiteit, die staan voor drie typen veelgebruikte crash test dummies. Deze modellen zijn zowel numeriek als experimenteel gevalideerd. Hieruit is gebleken dat letselresponsies van de borstkas en de nek door frontale botsingen goed kunnen worden beschreven door lineaire tijds-invariante modellen. De modellen kunnen verbeterd worden door meer aandacht te besteden aan het model van de borstkas en gordel.

De hevigheid en duur van een frontale botsing met hoge snelheid vereisen een gordelactuator met uitdagende specificaties. Er moeten grote krachten geleverd kunnen worden over een grote slag en met een hoge bandbreedte, en daarnaast moet de actuator in de deurstijl ingebouwd kunnen worden. Een gordelactuator is ontworpen gebaseerd op een semi-actieve hydraulische damper, en deze is op de TU/e gebouwd en experimenteel geëvalueerd. De actuator bestaat uit een hydraulische cilinder, en de gordelkracht wordt gevarieerd door middel van een hydraulische klep met drukregeling. Daarnaast is een sledebaan ontwikkeld om de gordelactuator te testen onder omstandigheden zoals in een botsing. De experimentele resultaten tonen aan dat de gordelactuator aan de eisen voldoet, behalve wat betreft de maximaal te leveren kracht.

DANKWOORD

The best dissertation is a done dissertation.
(Joan Bolker)

Ruim 4 jaar geleden heb ik de keuze gemaakt om te gaan promoveren, uit interesse voor de wetenschap, om meer kennis te vergaren en vanwege het boeiende onderwerp. Op dat moment wist ik niet dat promoveren voor mij vooral een persoonlijke ontwikkeling zou zijn. De grote mate van zelfstandigheid geeft je de vrijheid zelf je onderzoek vorm te geven, maar maakt ook dat je erg op jezelf bent aangewezen. Een goede begeleiding is daarin essentieel, en gelukkig heeft een aantal mensen deze taak voortreffelijk op zich genomen.

Maarten, je hebt mij in de afgelopen tijd enorm weten te stimuleren en motiveren, en het is fijn om te werken met iemand die interesse heeft in zowel de mens als in de onderzoeker. Je hebt het aangedurfd iemand met een biomedische achtergrond in een “harde” regeltechnische groep te zetten, wat (voor mij) een erg goede keus is geweest, daarvoor dank.

Frans, je hebt me gedurende vele jaren week in week uit geweldig geholpen. Ik heb je bereidheid om elke keer mijn stukken kritisch door te lezen erg gewaardeerd. Met name je kennis van modelvorming, je vermogen een gedachte in één mooie Engelse zin te verwoorden, je oog voor detail, je interesse in het onderwerp, de gezelligheid en de befaamde Rode Pen hebben bijgedragen tot het werk wat er nu ligt.

Bram, ondanks het feit dat je er pas in een laat stadium bij betrokken bent als copromotor, heb ik in korte tijd veel van je geleerd, bedankt. Je bent bijzonder scherpzinnig, kritisch, en je hebt zowel oog voor detail als voor het geheel. Tijdens onze besprekingen betekende jouw opmerking “ik snap dit denk ik niet” slecht nieuws voor mij; uiteindelijk bleek dat ik het zelf niet goed had begrepen en jij veel beter!

Maurice, allereerst bijzonder bedankt voor de goede gesprekken en adviezen. Daarnaast heb ik veel geleerd van je vastberadenheid om door te willen dringen tot kern van het probleem, en om zaken heel precies geformuleerd te krijgen.

Verder wil ik Edward Holweg en Paul van den Bosch bedanken voor de tijd die zij hebben vrijgemaakt om zich in dit onderwerp te verdiepen, en om in mijn commissie plaats te nemen.

De collega's bij TNO die mij tijdens de afgelopen jaren hebben begeleid wil ik hartelijk bedanken voor hun kennis van voertuigveiligheid, en voor het werk wat zij hebben verzet. Jac Wismans, Johan Jacobs, Gabriella Griotto (grazie), Cees van Schie, Paul Lemmen, Arjan van Leijsen, Ellen van Nunen en Dehlia Willemsen, top! And of course, Sri, Kristy, Matt, thank you for the great time I had at CHOP.

Veel nuttig werk is de afgelopen jaren verricht door mijn afstudeerders, Gil Reyes Orozco, Bas de Waal en Hanri Luijten. Bedankt voor jullie inzet. Uiteraard was ook de technische staf onmisbaar, zowel van de TU/e: Ruud van den Bogaert, Jan de Vries en Erwin Meinders, als van de GTD: Erwin Dekkers, Patrick de Laat en Gerrit Fimerius. Bedankt allen! Dank ook aan de secretaresses Lia, Petra en Caroline, voor hun werk om de zaak soepel te laten verlopen, het organiseren van de DCT-uitjes en 24-uurs meetings, en alle andere zaken die voor ons vaak onzichtbaar zijn. En hier als laatste, maar je stond wel aan het begin van mijn promotie, Herr Doctor Rogier, deze promotie was onder andere jouw idee, en je proefschrift en hulp in de eerste maanden hebben me een vliegende start gegeven, herzlichen Dank dafür.

De vakgroep heb ik als één van de prettigste zaken tijdens mijn promotie ervaren. Wouters en Brunuh, als roomies van het eerste uur, ik heb met jullie fantastische vakanties en conferenties gehad, veel gesport en gefeest, en jullie hebben me ook enorm geholpen met basis regeltechniek. Tnx! Ditzelfde geldt voor alle andere collega's: Alex, Apostolis, Beast, Buxus, Donkers, Eloisa, Fix, Gnaus, prof. Hamers, Hofmeister, Jan, Jeroen, JvH, Linda, Mallon, Bierlager, Melly, Niels, René, Rick, Rob, Smackdown, TAC, Tim, T. Ohmi, Wevers, en vele anderen. Daarnaast heb ik bijzonder veel plezier beleefd aan het tennis, en niet alleen vanwege het spelletje. Bedankt Carlo, Chantal, Julienne en Mirjam!

Als laatste wil ik mijn vrienden bedanken, de VGSEi'ers en de Gran Doradogangers, voor jullie interesse en gezelligheid. Een bijzondere dank aan Floor, Tine en Dik, Lette en Jan Willem voor de voorbije 10 jaar van steun, zonder jullie was ik niet wie ik nu ben. Karijn en haar familie, erg bedankt voor jullie liefde en adviezen. Als laatste komt wie er als eerste hoort, mijn familie. Pa en Ma, Annette, Machtelt en Jan Anne, Wendelmoet en Ale, jullie liefde, betrokkenheid en onvoorwaardelijke steun zijn onmisbaar geweest.

Dit dankwoord bewijst maar eens dat een promotie helemaal geen eenzame tijd hoeft te zijn!

CURRICULUM VITAE

Ewout van der Laan was born on November 22nd, 1978 in Borne, the Netherlands. After finishing his secondary education at Het Noordik in Almelo in 1997, he started his study Biomedical Engineering at the Technische Universiteit Eindhoven (TU/e), where he received his M.Sc. degree (cum laude) in 2004. His traineeships were carried out at the TU/e and at the Georgia Institute of Technology (GeorgiaTech), Atlanta, USA. His master's thesis was entitled "Development of a smart positioning sensor for the plasma needle" and was performed at the TU/e. After his study, Ewout worked for 6 months as a visiting scientist in the Control Systems Technology Group at the department of Mechanical Engineering of the TU/e. Since 2005, Ewout has been working as a Ph.D. student in the same group on the topic of "Seat Belt Control" in cooperation with TNO Science and Industry, resulting in this thesis.

